FLORIDA STATE UNIVERSITY

COLLEGE OF ARTS AND SCIENCES

Characterizing the Diurnal Variations over Florida

By

CARLY D. NAROTSKY

A dissertation submitted to the
Department of Earth, Ocean, and Atmospheric Science
in partial fulfillment of the
requirements for the degree of
Doctor of Philosophy

2025

Carly Narotsky defended this dissertation on April 21, 2025.

The members of the supervisory committee were:

Vasubandhu Misra
Professor Directing Dissertation

Sachin Shanbhag
University Representative

Mark Bourassa
Committee Member

Alyssa Atwood
Committee Member

Zhaohua Wu
Committee Member

Jeffrey Chagnon
Committee Member

The Graduate School has verified and approved the above-named committee members, and certifies that the dissertation has been approved in accordance with university requirements.

ACKNOWLEDGMENTS

Thank you to my loved ones, family, and friends, for their unwavering support. A huge thank you to my major professor, Dr. Vasubandhu Misra, for his guidance throughout the preparation of this dissertation and through the degree program. I also thank my committee members listed above, as well as Dr. Ronald E. Doel, who also served on my committee, for their valuable contributions to this research over the years. Finally, a special thank you to my undergraduate professors in the Atmospheric Sciences Department at the University of North Carolina Asheville (Drs. Douglas K. Miller, Christopher M. Godfrey, Christopher C. Hennon, and Huo-Jin (Alex) Huang) for instilling in me a love of atmospheric science, inspiring me to pursue graduate school in the subject, and encouraging me every step of the way.

TABLE OF CONTENTS

LIST OF FIGURES

Figure 5.112. The responses of the diurnal cycles of surface temperature, specific humidity, and precipitation in Florida during June—November to concurrent weak *interannual component* of the Bermuda High Index.

ABSTRACT

Late afternoon thunderstorms are an almost-daily occurrence in Florida summers, particularly in peninsular Florida (PF). The almost-daily afternoon rains have an abrupt onset in May or June and an abrupt demise in September or October. These routine thunderstorms typically result from the afternoon sea breezes, a feature of the diurnal cycle. Indeed, the portion of summer rainfall that is explained by the diurnal cycle is larger for PF than anywhere else in the southeast US. PF owes this distinction to its peninsular geography in the subtropical latitudes. The peninsula promotes the formation of two opposing seas breeze cells which often merge in the late afternoon, amplifying convection.

There are three main objectives of the dissertation. The first objective is to characterize the phase and amplitude of the diurnal cycle variations of surface meteorology variables at 30 observational stations in the Florida Automated Weather Network (FAWN). This diurnal cycle analysis employs Ensemble Empirical Mode Decomposition (EEMD) to isolate the diurnal mode of variability. Results toward this objective consistently show the famous late-afternoon maximum in precipitation during the summer months. The second objective of the dissertation is to verify the diurnal cycle variations in the 102-year dynamically downscaled Florida Climate Institute-Florida State University Land-Atmosphere Reanalysis for the Southeastern United States (FLAReS1.0) at 10 km grid resolution using the diurnal cycle variations observed in FAWN as the verification data. This verification reveals strengths of FLAReS1.0 as well as biases regarding the Florida diurnal cycle.

The dissertation culminates in an analysis of the low frequency variability of the diurnal cycle over the 20th century in FLAReS1.0. The diurnal cycle is analyzed over the phases of ENSO, the strengthening and weakening of the North Atlantic Subtropical High or so-called Bermuda High, and the Atlantic-Pacific inter-basin SST contrast. We find strong associations between these interannual climate modes and the diurnal amplitudes of surface temperature, specific humidity, and precipitation across Florida.

CHAPTER ONE

INTRODUCTION

1.1 Florida summer precipitation

Peninsular Florida (PF) experiences a distinct wet season during boreal summer. Each spring there is an abrupt onset marked by relatively higher daily rain rates which are sustained through the summer and have an abrupt demise in autumn (Misra et al. 2018). Low-level horizontal convergence resulting from the afternoon sea breezes on the east and west sides of PF accounts for much of the almost-daily summer afternoon thunderstorm activity (Byers and Rodebush 1948; Frank et al. 1967). Plus, outflows from previous storms frequently trigger new growth (Cooper et al. 1982). Bastola and Misra (2013) show that the diurnal variations explain a large portion of the boreal summer and fall precipitation in PF, and particularly in south Florida. Additionally, an analysis of the diurnal cycle of rainfall by Schwartz and Bosart (1979) revealed afternoon maxima across most of PF.

The southeast US, which includes PF, has the strongest local diurnal maximum of rainfall in CONUS (Carbone and Tuttle 2008). Dai et al. (1999) show that the pattern of diurnal cycle precipitation in the southeast US during summer is characterized by a strong late afternoon maximum. They also find that the pattern of diurnal cycle precipitation during summer is stable interannually throughout the US, whereas diurnal cycle winter precipitation has high interannual variability. So, late afternoon rain events in summer are common across the southeast US and are not unique to Florida. However, PF is uniquely positioned to boost its diurnal scale precipitation. The peninsular geography of PF plays a role in amplifying convection from the sea breezes. Xian and Pielke (1991) simulated sea breeze circulations in a two-dimensional hydrostatic model with different-sized landmasses. They found that the optimal width of a strip of land to maximize sea breeze convergence is 150 km. At this width, the two sea breeze cells from the two sides of the land merge together in the late afternoon. Coincidentally, the width of most of PF is not much larger than 150 km, and the merging of the east and west coast sea breeze fronts does occur, amplifying convection. Blanchard and Lopez (1985) classified three types of summer convection in south Florida, all involving the merging of the east and west coast sea breeze fronts. For two

of the types, convection becomes strongest at 1500–1800 EDT. In the third type, convection peaks earlier in the day.

Similarly, panhandle Florida also experience sea breeze thunderstorms aligned along its coast (Misra et al. 2011). These thunderstorms like over PF peak in the afternoon. The positioning of the Bermuda High in the boreal summer season that shifts further to the west and slightly equatorward compared to the annual mean (Davis et al. 1997) sets up the background wind in the panhandle region to be southerly or southwesterly. As the temperature contrast between the warm land surface and comparatively cooler Gulf of Mexico builds up during the day, these thunderstorms mature from the convergence of this background flow along the panhandle Florida coast in late afternoon (~1600 LST; Misra et al. 2011).

1.2 Diurnal variations

Diurnal variability includes semidiurnal oscillations as well as diurnal oscillations. Dai and Wang (1999) identified the semidiurnal and diurnal pressure oscillations using global surface pressure data from 7500 land stations from 1976-1997. They found that in some regions, the diurnal oscillation (24-hour harmonic) dominates, and the semidiurnal oscillation (12-hour harmonic) dominates in others. The spatial variations of the diurnal pressure oscillation correlate significantly with the spatial variations in the diurnal temperature range at the surface, suggesting that sensible heating from the land surface is a major forcing for the diurnal pressure oscillation. Forcings responsible for the semidiurnal tides include downward propagation of longwave radiation from tropospheric water vapor and stratospheric ozone, clouds' reflection and absorption of solar radiation, and latent heating in convective precipitation.

Dai et al. (1999) studied the diurnal cycles of precipitation, surface pressure, and static energy over the contiguous United States in observations and a regional climate model simulation. Over the time period 1963—1993, the summertime diurnal maximum of precipitation in the southeast US occurs around 1800 LST, on average. In Florida, the summertime diurnal maximum of precipitation occurs slightly earlier, around 1700 or 1600 LST, and the amplitude of the precipitation is considerably larger, on average, than it is in the rest of the southeast US. Watters and Battaglia (2019) fit harmonics to the diurnal cycle of precipitation in the Integrated Multi-satellitE Retrievals for GPM (IMERG) precipitation product derived from the Global Precipitation Measurement (GPM) constellation, which has 0.1°× 0.1° and half-hour resolution. They found that the summertime diurnal cycles of precipitation occurrence and

accumulation over land are dominated by the 24-hour harmonic. In Florida, during all seasons of the year except December-February, the phase of the 24-hour harmonic is 15-18 LST and the amplitude is high. In December-February, diurnal precipitation has peaks at morning and night and the amplitude is low.

1.3 Large-scale influences and predictability of Florida seasonal variations

Over Florida, the diurnal variations of precipitation dominate in the boreal summer season relative to other parts of the year (Bastola and Misra 2013). However, their study also identifies that the diurnal variations of precipitation contribute significantly to the seasonal precipitation throughout the year. However, the background winds and the SST of the surrounding oceans play a significant role in the modulation of the diurnal cycle. A clear evidence of this is in the seasonal variations of the diurnal cycle (Bastola and Misra 2013). Many observational and numerical modeling studies have also demonstrated the large-scale influence on the diurnal variations (Augustine and Caracena 1994; Tuttle and Davis 2006; Misra et al. 2011; Trier et al. 2017).

The North Atlantic Subtropical High (NASH), also known as the Bermuda High or the Azores High, plays a crucial role in shaping the regional climate of the Southeastern United States (SEUS; Misra et al. 2011; Misra 2020). This high-pressure system is a semi-permanent feature in the Earth's atmospheric circulation. During the boreal winter season, the NASH is commonly referred to as the Azores High, as it is typically centered around the Azores Islands. In contrast, during the boreal summer season, it is known as the Bermuda High, as its center shifts westward towards Bermuda. Despite these seasonal variations in position, the subtropical high remains present throughout the year. While the NASH is considered permanent due to its year-round presence, it exhibits significant seasonal variability in terms of size and intensity. This variability makes the NASH a semi-permanent or quasi-permanent feature in the atmosphere.

The seasonal cycle of the NASH is depicted in Figure 1.1, showcasing the varying structure of this feature throughout the year. During the boreal summer season, a single maximum central pressure is observed over the North Atlantic (Figure 1.1c). In contrast, during the winter season, the high pressure system splits into dual maxima, with one located over the eastern US and the other over the eastern Atlantic and North Africa. Research by Davis et al. (1997) highlights the asymmetric nature of the seasonal evolution of NASH. For instance, the center of

the Azores High shifts significantly westward from January to March (within 2 months), while it gradually moves eastward from July to January (over 6 months). Additionally, the secondary maximum of high pressure in the eastern US tends to migrate southwestward from August to January of the following year. Davis et al. (1997) also note that the most significant movement occurs as the center of this secondary maximum shifts from southwestern Pennsylvania to northern Georgia between late October and early November. Figure 1.1 further illustrates the presence of closed subtropical Mean Sea Level Pressure (MSLP) contours throughout the year. The Sea Surface Temperature (SST) also exhibits distinct seasonality, with meridional gradients prevailing in the winter (Figure 1.1a) and spring (Figure 1.1b) seasons. Conversely, in the boreal summer (Figure 1.1c) and fall (Figure 1.1d) seasons, the zonal SST gradient becomes more prominent compared to other times of the year.

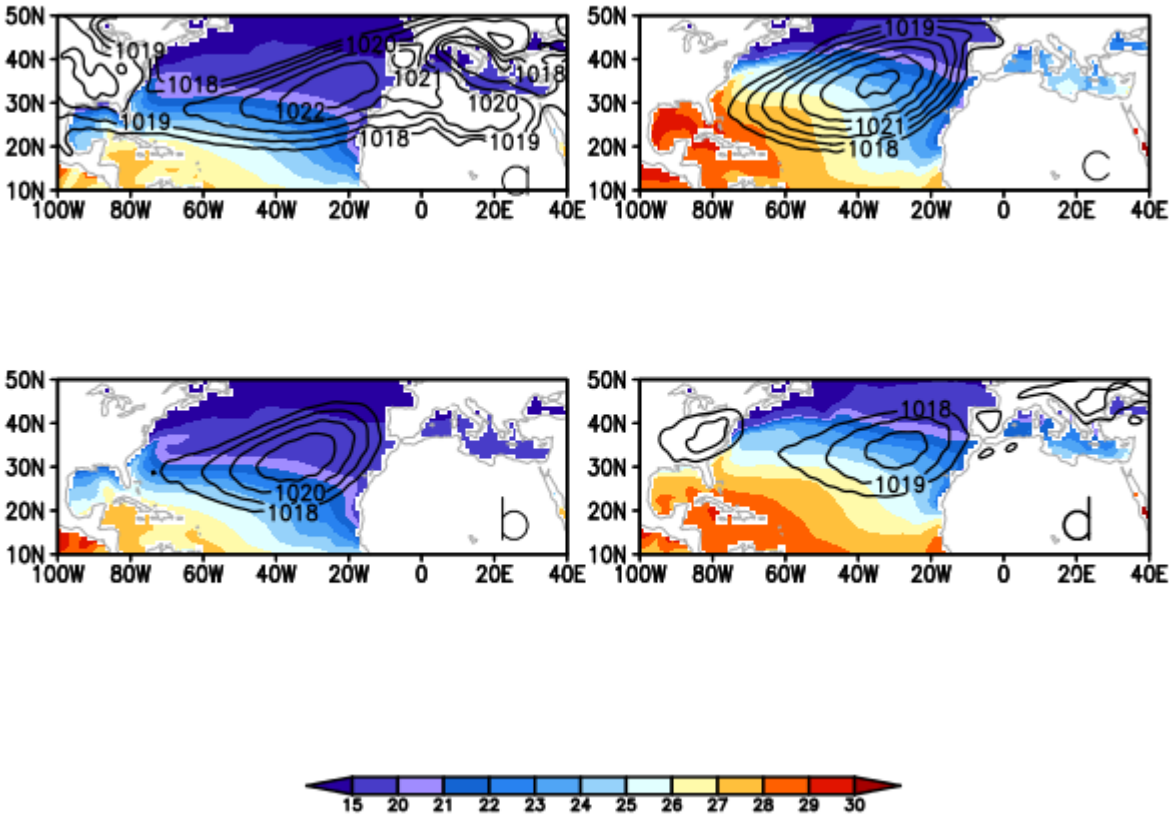

Figure 1.1.1. The climatological mean sea level pressure (contoured; hPa) and SST (°C); shaded for (A) DJF, (B) MAM, (C) JJA, and (D) SON seasons. The data is from the Climate Forecast System Reanalysis (CFSR; Saha et al., 2010) and the climatology is computed over the period of 1980–2009. From Misra (2020).

Although El Niño and the Southern Oscillation (ENSO) has an overbearing impact on the winter season in Florida (Ropelewski and Halpert 1986, 1987; Misra et al. 2017), its influence in the boreal summer season is comparatively weaker (Misra and DiNapoli 2013). However, the significant influence of ENSO on the seasonal Atlantic tropical cyclone activity cannot be ignored. The tropical Atlantic basin is impacted by ENSO in a remote manner through changes in its vertical shear, which is influenced by the shift in the Walker circulation. During El Niño years, the Walker circulation shifts slightly eastward and weakens, leading to an increase in upper-level westerlies over the tropical Atlantic. This intensified upper-level westerlies during El Niño, combined with low-level easterlies, further enhances the vertical wind shear in the tropical Atlantic, ultimately reducing tropical cyclone (TC) activity in the season (Gray 1984). Specifically, over the Caribbean region west of 60W, the low-level easterly trade winds strengthen compared to La Niña years, intensifying the vertical shear and impacting TC activity in the region during El Niño years (Klotzbach 2011). Interestingly, ENSO has minimal influence on the low-level trade winds in the eastern tropical Atlantic (east of 60W). On the other hand, La Niña years are associated with an increased likelihood of an active TC season due to reduced vertical shear from the modulation of upper-level westerlies. In contrast, Misra and DiNapoli (2013) found minimal influence on the wet season variations of Florida that coincide with the boreal summer season.

Several studies have demonstrated that tropical Pacific SST anomalies (SSTAs) can impact U.S. precipitation variability, east of the Rockies during the boreal summer season through changes in the Walker circulation. For example, Weaver et al. (2009) and Krishnamurthy et al. (2015) have highlighted that the interannual variation of the North American Low-Level Jet (NALLJ), a key driver of U.S. warm-season (April-September) rainfall variability, can be influenced by tropical Pacific SSTAs from mid-summer to early fall (July-September). Additionally, Mo et al. (2009) found that the decadal frequency of U.S. drought in mid-summer to early fall is significantly affected by tropical Pacific SSTAs, with the influence of Atlantic SSTAs being relatively minor. Several studies have suggested that variability in the Atlantic Warm Pool (AWP) and associated Sea Surface Temperature Anomalies (SSTAs) in the Gulf of Mexico (GoM), Caribbean Sea (CS), and western tropical North Atlantic could be significant drivers of U.S. summer to mid-fall precipitation variability, particularly in the southern United

States. These studies have examined both interannual and decadal timescales, highlighting the impact of warm AWP SSTAs on precipitation patterns. Research by Wang et al. (2006, 2008), Wang & Lee (2007), Misra et al. (2011), Misra & Li (2014), Liu et al. (2015), and others has shown that warm AWP SSTAs can lead to decreased precipitation in the southern United States, while cold AWP SSTAs have the opposite effect. This relationship is attributed to the weakening of the NASH during periods of warm AWP SSTAs, causing a shift in the NASH that reduces the supply of warm and moist air from the Gulf of Mexico into the United States.

Overall, the variation of the summer to fall season US hydroclimate, east of the Rockies is a response to the complex interactions between the tropical Pacific and Atlantic SSTs. Kim et al. (2017) suggests that the US precipitation in late summer to midfall (August-October) is a result of the Gill type atmospheric response to convective activity in the Caribbean region. They further suggest that this convective activity in the Caribbean Sea is triggered by the contrast between the inter-ocean basin gradient of SST between tropical Atlantic and the Pacific. This SST gradient influences both the Caribbean LLJ and the North American LLJ, thus affecting the hydroclimate over US, east of the Rockies.

Although the diurnal variations explain much of the summer precipitation during the Peninsular Florida wet season (PFWS), the larger scales also influence the PFWS. Large-scale circulations in the atmosphere and ocean dictate the onset and demise of the PFWS. For instance, an analysis of the seasonal cycle of the upper ocean circulations and upper ocean heat content of PF's surrounding oceans using ocean heat transport, SST, and the depth of the 26°C isotherm showed that the onset of the PFWS accompanies the seasonal warming of the surrounding oceans and the strengthening of the Loop Current (Misra et al. 2018). Likewise, the demise of the PFWS occurs with a weakening of the Loop Current and a reduction in upper ocean heat content (Misra et al. 2018). Although the Loop current is irregular, Hall and Leben (2016) show that the Loop current shedding events are most likely to occur in August and September, with another smaller seasonal peak in February and March. Through bathymetry sensitivity experiments with models, Misra and Mishra (2016) show the profound influence of the strengths of the Loop and Florida currents on the duration of the PFWS and its total seasonal precipitation; a weaker current system reduces the duration of the wet season and its seasonal precipitation accumulation. Additionally, tropical cyclones contribute to PFWS rainfall and may sometimes trigger the abrupt demise of the PFWS (Misra et al. 2018). An analysis of the wind field revealed a shift in

wind patterns at the onset and demise of the PFWS as well. At and prior to onset date, the 850 hPa level winds over PF are mostly northerlies and northwesterlies, but during the PFWS, the southerlies and southwesterlies that comprise the western edge of the North Atlantic subtropical high (NASH) prevail over PF (Misra et al. 2018).

The climatological onset and demise dates of the PFWS over 1948–2005 are May 21st and October 10th, respectively (Misra et al. 2018). These dates have large interannual variability; the standard deviation for the onset and demise dates are 15 and 16 days, respectively (Misra et al. 2018). As a result of this, there is considerable interannual variability in the length of the PFWS. Seasons with early onset dates, late demise dates, or that are longer than normal tend to correspond with positive seasonal rainfall anomalies (Misra et al. 2018). Therefore, predicting the onset and demise dates of the PFWS is useful for anticipating seasonal rainfall anomalies.

1.4 Can models simulate the diurnal cycle in Florida?

There are several studies that have examined the diurnal variations of the CMIP6 models (e.g., Wu et al. 2019; Wang and Clow 2020; Christopolous and Schneider 2021, Tang et al. 2021, Watters and Battaglia 2019, Wang et al. 2021; Lee and Wang 2021; Chen et al. 2022). Across generations of model development, three persistent errors with diurnal variation of precipitation have been observed: 1) too-early precipitation peak over ocean with the observed peak in the early morning, 2) too-early precipitation peak over land with the observed peak in the late afternoon, and 3) missing nocturnal precipitation peak over some regions. This is also observed in the CMIP6 models (Lee and Wang 2021). However, some modest improvement of CMIP6 relative to CMIP5 is noted (Tang et al. 2021; Lee and Wang 2021). For example, the phase lag between diurnal peak of precipitation and insolation has improved. Furthermore, better treatments of interactions between convection and boundary layer processes, convective triggering and closure functions have led to better simulation of nocturnal peak in precipitation over certain regions (Tang et al. 2021).

Watters et al. (2021) examined the fidelity of the representation of the June-August diurnal cycle of precipitation in the ERA5 reanalysis as well as three climate models: NCAR-CESM2, CNRM-CM6.1, and CNRM-ESM2.1. They found that ERA5 overestimates the diurnal amplitude of summertime precipitation over land in comparison to IMERG precipitation observations coarsened to the spatial and hourly resolution of ERA5 and the CMIP6 models. Dai and Trenberth (2004) evaluated the performance of version 2 of the Community Climate System

Model (CCSM2) in simulating the diurnal cycle globally using 3-hourly data. They found that CCSM2 captures the diurnal amplitude and phase (peak time of day) of surface air temperature over land and simulates a realistic pattern of rainy days over land during the warm season. However, in these simulations, warm season daytime moist convection over land starts prematurely and plateaus in the afternoon when it should be peaking according to observations. The premature start of convection reduces the intensity of the convection while extending its duration. Similarly, Dai et al. (1999) found that the NCAR regional climate model (RegCM) overestimates precipitation frequency and underestimates precipitation intensity. This study evaluated the RegCM using three cumulus schemes (Grell, Kuo, and CCM3), and found that moist convection starts too early and occurs too often in all three schemes. Liang et al. (2004) demonstrate the importance of cumulus schemes in climate model simulations of the diurnal cycle of US summer precipitation. The late-afternoon peaks in precipitation in the southeast US are best depicted in model simulations that use the Kain-Fritsch scheme rather than the Grell scheme, which performs better in some other regions. The Kain-Fritsch scheme works well for the southeast US where convection is largely governed by the near-surface forcing.

It is important and relevant to understand the diurnal variations of precipitation over Florida given that diurnal variability represents a fundamental mode of climate variability (Yang and Slingo 2001) and the fact that Florida shows a very strong diurnal cycle, persistent throughout the year but strongest in the summer (Bastola and Misra 2013). The ubiquity of the diurnal variations in the global tropics and at higher latitudes in the summer season fit with the importance of the diurnal scales to the global climate. This study examines the diurnal variations from in-situ observations followed by an analysis of the diurnal cycle over Florida from a 103-year dynamically downscaled data at 10 km grid resolution forced by atmospheric reanalysis and observed SST (Misra and DiNapoli 2012). The findings of this study could be used to understand the deficiencies in the diurnal cycle of precipitation in the model and potential ways to rectify them. It may be argued that although the results of this study are specific to Florida, the fundamental processes of the diurnal cycle could still be generally applicable to other regions.

CHAPTER TWO

OBJECTIVES

This research work is motivated by the availability of high temporal resolution in situ data across Florida that resolves both diurnal and semi-diurnal variations of some surface meteorological variables. Given the paucity of such high quality observations the analysis of this unique set of observations for the diurnal variations over Florida for a period of 16 years by the Florida Automated Weather Network (FAWN) provides a good opportunity to understand the diurnal variations. Furthermore, given the robust seasonal hydroclimate of Florida that is representative of similar regimes spread across the trade wind belt region, some of the conclusions drawn from the study could be made broadly applicable. Similarly, the availability of 102 years of dynamically downscaled data in the form of **F**lorida Climate Institute-Florida State University **L**and-**A**tmosphere **Re**analysis for the **S**outheastern United States at 10-km resolution (FLAReS1.0) offers an opportunity to verify with FAWN and explore low-frequency variations associated with NASH, ENSO, and inter-ocean basin SST variations. Therefore, the three primary objectives of this dissertation are:

1. Characterizing the diurnal variations of surface meteorology from station data across Florida from 2005-2020
2. Validation of the diurnal variations in the dynamically downscaled **F**lorida Climate Institute-Florida State University **L**and-**A**tmosphere **Re**analysis for the **S**outheastern United States at 10-km resolution (FLAReS1.0)
3. Characterize the interannual variability of the diurnal cycle in Florida over the 20th century.

Objective 1 is concerned with diagnosing the phase (peak time of day) and amplitude (magnitude of the variable at its peak time) of the diurnal mode in seven surface meteorology variables at each of the 30 Florida Automated Weather Network (FAWN) sites that were in operation for the period 2005–2020. Ensemble Empirical Mode Decomposition (EEMD) is performed on 1-month periods of 15-minute observations of each variable from the FAWN data. Thereafter, the lead/lag relationships between the variables are computed, and the peak times are diagnosed for each variable. Additionally, the amplitudes of the variables at their peak times are

computed. This work demonstrates the seasonality of the diurnal cycle in Florida and illuminates differences in the diurnal cycle amongst regions within Florida. This analysis is performed for the diurnal component alone, and for the combined diurnal component plus the semi-diurnal component as well.

The diurnal scale variations represent a fundamental mode of variability of our climate system. Diurnal variations are generated from diurnally varying solar heating that affects near the surface, through the depths of the troposphere and in the stratosphere that manifest as pronounced oscillations with periods of 24 h (diurnal) and 12 h (semi-diurnal). These periodic oscillations that appear in the upper atmosphere are also called atmospheric tides (Chapman and Lindzen 1970). Often, the fidelity of climate models and reanalyses is assessed in its ability to represent the diurnal scales owing to its feature of being a fundamental mode of variation of the climate system (e.g., Lin et al. 2000, Trenberth et al. 2003, Dai and Trenberth 2004, Lee et al. 2007).

Although solar radiation is the primary driver of these oscillations, the proper interaction of land-atmosphere-ocean-cryosphere is essential for achieving correct amplitude and phase of these oscillations (Yang and Slingo 2001). For example, owing to different heat capacities of land and ocean, the diurnal variability over these surfaces acquires very different characteristics. Many earlier studies showed that the convective or precipitation maximum tended to occur in the early morning over the open oceans and in the late afternoon/early evening over land (e.g., Gray and Jacobson 1977; McGarry and Reed 1978; Albright et al. 1981). However, some studies also showed an afternoon maximum in precipitation and cloudiness over the oceans (e.g., McGarry and Reed 1978; Augustine 1984; Shin et al. 1990). One of the earliest studies of diurnal variations of convection in the global tropics was conducted based on brightness temperature over a period of ~16 years (Yang and Slingo 2001). This study confirmed the findings of many of the earlier, regional studies conducted over a limited time interval. But the study also highlighted significant spatial heterogeneity in diurnal variations, with ocean and land diurnal variation of brightness temperature contrast leading these differences.

In this study we validate the FLAReS1.0 using FAWN as the validation dataset (Objective 2). This is a prelude to Objective 3, which examines the low-frequency variability of the diurnal scales in FLAReS1.0.

In contrast to validation studies of diurnal variations of precipitation, there are far fewer studies that examine the low frequency variations of the diurnal scales. This is partly because of

the absence of long periods of data sets at hourly or sub-hourly scales until recently. Now, with many of the satellite based precipitation datasets available at least at hourly or less time interval for nearly two decades, there is some uptick in some of these studies of low frequency modulation of diurnal precipitation (e.g., Rauniyar and Walsh 2011; Peatman et al. 2014; Bai and Schumacher 2022). Many of these studies suggest the modulation of MJO on the diurnal scales and vice versa. For example, Tian et al. (2006) found that diurnal amplitude of convective cloud amount increases or decreases both over land and ocean during the active or suppressed phases of the MJO. But Rauniyar and Walsh (2011) indicate that rainfall during the active or suppressed MJO peaks two hours later or earlier than the diurnal cycle of precipitation in the boreal winter. Bai and Schumacher (2022) find that the diurnal rainfall anomalies during MJO are asymmetrical around the topography of the Maritime Continent region because of the corresponding asymmetrical convergence by the MJO winds. There are however much fewer studies that examine the interannual variability of diurnal variations (e.g., Qian et al. 2010; Misra 2010; Misra 2009; Surendra and Walsh 2013). These studies are either model based or on an extremely limited time-period of rainfall datasets resolving diurnal scales, which questions the robustness of their results. Given that diurnal scales, especially in the tropics is so dominant it is easy to conceive their importance in the local manifestation of global teleconnections. Misra (2010) show from a multi-decadal global model integration that there is a local amplification of the remote ENSO signal over equatorial Africa by the additive influence caused by phase locking of the local diurnal cycle with the seasonal cycle and the interannual signal associated with ENSO. Similarly, over equatorial Amazon, Misra (2009) finds there is a local amplification of the ENSO signal by the local modulation of the diurnal variation of moisture flux convergence. Surendra and Walsh (2013) suggest from their observational work that oceanic regions display an increase in the mean rainfall of the Maritime Continent region in correspondence with an increased diurnal amplitude of rainfall during La Niña seasons. However, the precipitation in the islands of the Maritime Continent display a very heterogeneous response with many of them displaying more rainfall during El Niño. They attribute this feature to corresponding variations in the diurnal variation of rainfall.

In this study, we are using the hourly data from FLAReS1.0 to isolate the diurnal scales and examine its low frequency variation with regard to ENSO variability, variability of the Bermuda High, and the inter-basin SST gradient between the tropical Atlantic and tropical Pacific Ocean.

CHAPTER THREE

DATASETS

3.1 Florida Automated Weather Network (FAWN)

The Florida Automated Weather Network (FAWN) is a network of surface meteorology observing stations in Florida. In 1996, the National Weather Service discontinued the service of collecting data in rural locations and issuing agricultural forecasts and advisories to Florida growers. The lack of rural weather data contributed to an apparent warm bias in temperature forecasts. FAWN was initiated in 1997 in response to a freeze event that caught Florida growers by surprise and cost an estimated $300 million in damage (Lucien and Love 1997). Sites were established quickly, and by 2002 the network was comprised of 33 stations (Lusher et al. 2009). In 2025, FAWN is comprised of 47 stations that continue to provide representative weather data to Florida growers.

At each FAWN site, several parameters are measured, including air temperature at 2 and 10m AGL, soil temperature at 10 and 60cm below the surface, pressure, solar radiation, wind speed and direction, and rainfall amount. This data is collected every 15-minutes, retrieved, and stored on data servers at the University of Florida. The collected data are compared to a standard range of acceptable values before becoming accessible via the FAWN website: http://fawn.ifas.ufl.edu/tour/tech_info.php.

We use data provided by Peeling et al. (2023) that follows from the observations made in 30 FAWN stations across Florida that were operational throughout 2005–2020 (Figure 3.1). We analyze seven surface meteorological variables observed in these stations: downwelling solar radiation (W/m^2), 2 m air temperature (K), 10 m air temperature (K), relative humidity ($\%$), wind speed *(mph*), dew point temperature (K), and precipitation (mm). The temporal gaps in the observational data are filled in a variety of ways depending on the length of the gap following Peeling et al. (2023). These data filling techniques range from linear interpolation for short gaps (< 6 hours) to replacing with outside data source such as the hourly Automated Surface Observing System (ASOS) station data provided by the National Centers for Environmental Information (Peeling et al. 2023). If the ASOS station data are not available for a particular location, then the data gaps are filled using the data from the closest FAWN station. Peeling et al. (2023) have conducted extensive validation tests of the gap filled dataset to confirm insignificant

differences in the differential statistics between the raw and the filled FAWN datasets over these 30 stations across Florida.

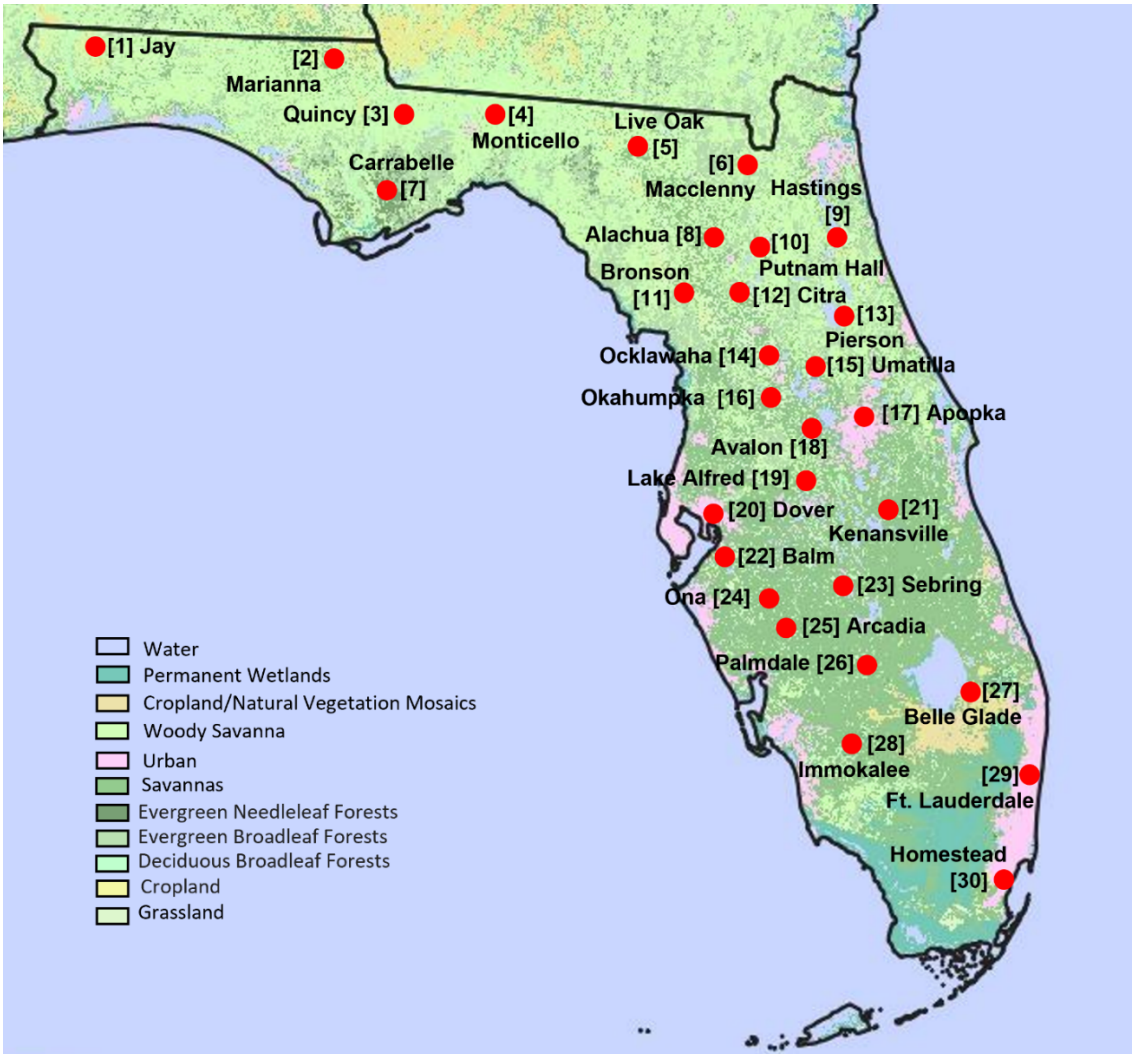

Figure 3.1.1. The distribution of the Florida Automated Weather Network (FAWN) stations across Florida. From Peeling et al. (2023).

3.2 Florida Climate Institute-Florida State University Land-Atmosphere Reanalysis for the Southeastern United States at 10-km resolution (FLAReS1.0)

FLAReS1.0 is a high-resolution dataset created by dynamically downscaling the 20th Century Reanalysis (20CR; Compo et al. 2010) to produce a 10-km dataset covering the southeastern United States (DiNapoli and Misra 2012; Misra et al. 2012). This process involves using a regional climate model with global reanalysis data as boundary conditions and applying scale selective bias correction (Kanamaru and Kanamitsu 2007).

Specifically, the Regional Spectral Model (RSM) was utilized as the regional climate model for FLAReS1.0, with UK Met Office daily SST boundary conditions as lower boundary forcing. The scale selective bias correction in RSM adjusts the rotational component of the wind spectrally for wavelengths ≥ 500km and ensures that the average temperature perturbation over the regional domain is zero at each time step, reducing climate drift in the model. The 20CR forcing at the lateral boundaries was updated every 6 hours.

FLAReS1.0 was generated in three streams with a 5-year overlap to prevent spin-up issues for the period of 1901-2005. The domain of FLAReS1.0 can be seen in Figure 3.2.1, and further details on the RSM configuration and model physics for FLAReS1.0 are available in DiNapoli and Misra (2012). Extensive verification of FLAReS1.0 has shown that the dataset has reasonable climatological bias, accurately representing the seasonality of surface meteorological variables and various weather extremes such as tropical cyclones, cold frontal passages, and sea breeze events (DiNapoli and Misra 2012).

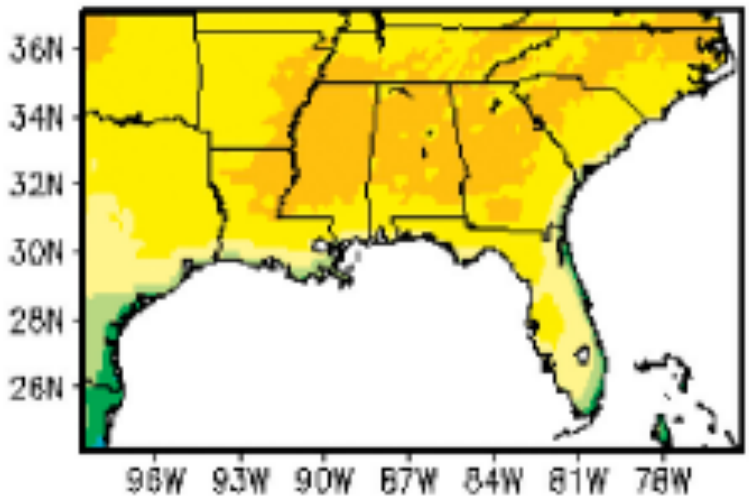

Figure 3.2.1. The domain of FLAReS1.0. From DiNapoli and Misra (2012).

CHAPTER FOUR

METHODOLOGY

4.1 Diurnal analysis of observations

Characterizing the diurnal cycle of meteorological variables requires first decomposing the timeseries into its constituent modes of variability and isolating the diurnal mode. To accomplish this, we employ Ensemble Empirical Mode Decomposition (EEMD), a noise-assisted data analysis method introduced by Wu and Huang (2009). EEMD is an effective technique for separating a signal into its component scales. The technique involves perturbing the data with white noise for several trials and sifting to make the different scale signals sort into several Intrinsic Mode Functions (IMFs). IMF1 isolates the highest frequency scale followed by IMF2, which has the second highest frequency scale in the time series and so on. The added white noise does not survive the averaging process involved in EEMD, leaving only the discrete oscillatory components of the original timeseries. An example of an original timeseries and its decomposition into IMFs is shown in Figure 4.1. The input data to the EEMD are 15-minute observations of the seven surface meteorology variables: solar radiation down, 2 m air temperature, 10 m air temperature, wind speed, dew point temperature, relative humidity, and precipitation from the gap filled datatsets following Peeling et al. (2023).

Performing the EEMD technique on a month of 15-minute observations reveals that the diurnal mode is represented by IMF5 and the semi-diurnal mode is represented by IMF4 (Figure 4.2). The following analysis is performed on the IMF5 signal alone, as well as on the sum IMF4+IMF5. For ease of explanation, the methodology is described using the IMF5 signal alone. The results of both analyses are discussed in Chapter 5.

The next step after conducting the EEMD and isolating the diurnal and semi-diurnal modes is to identify the lead/lag relationships between the seven variables. This is accomplished by computing the correlations of the IMF5 component of all variables with each other at lead/lag times ranging from +3 days to -3 days (Figure 4.3). The x-locations of the peaks in the correlation plot (marked with red dashed lines) mark the lead/lag time between the two variables. The magnitudes of the peaks in the correlation plots are correlation values that represent the strengths of the lead/lag relationships between the two variables. Table 1 is the illustration of the lead/lag relationships obtained from such an exercise and their corresponding correlation values

(i.e., the strength of the relationships). We note that these lead/lag relationships do not imply causal relationships but merely illuminate the timings of the variables in the diurnal cycle in relation to each other.

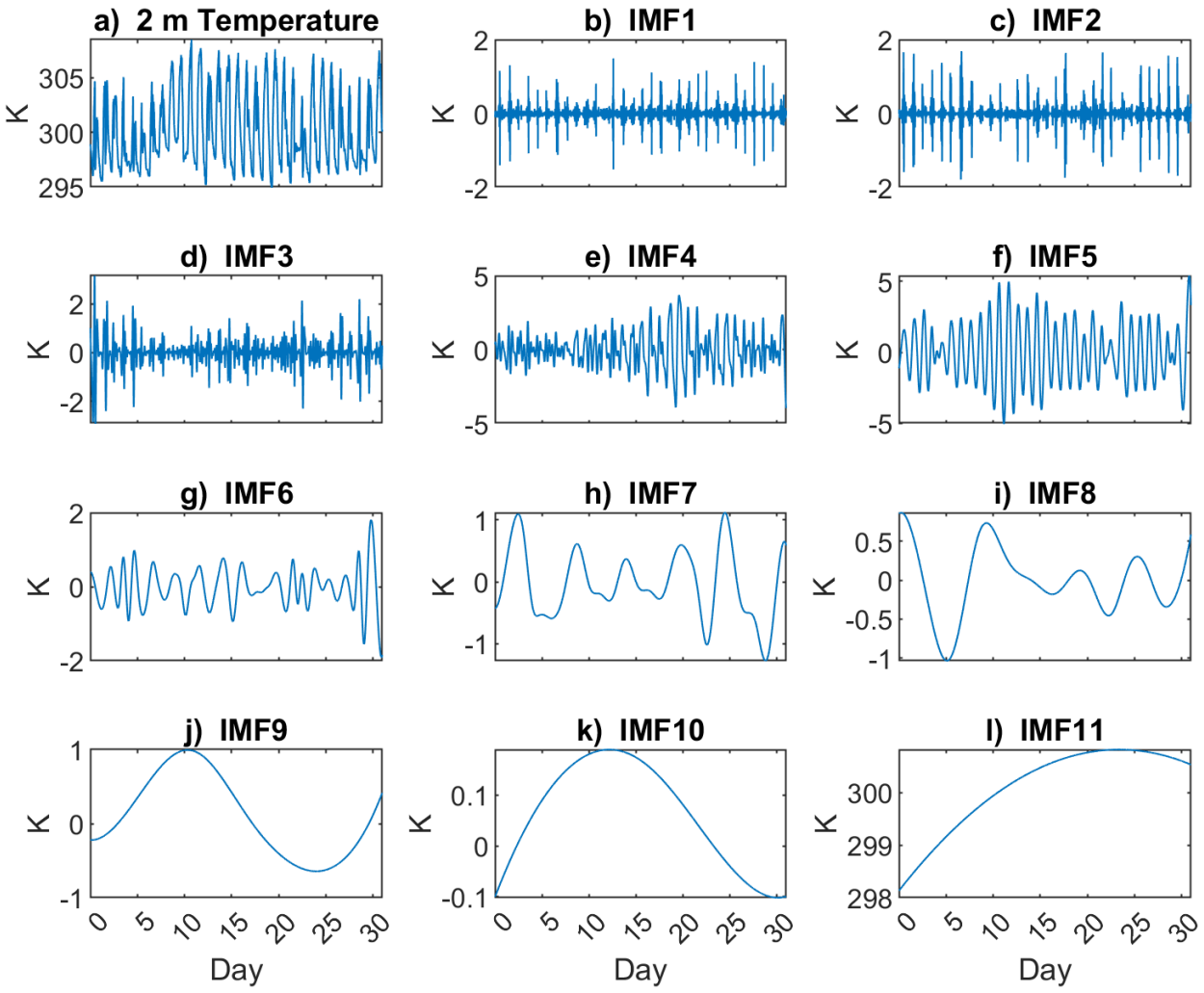

Figure 4.1.1. An illustration of the Ensemble Empirical Mode Decomposition (EEMD) showing a) the original timeseries at 15-minute intervals at FAWN Citra in July 2020 and b-l) its decomposition to constituent Intrinsic Mode Functions (IMFs).

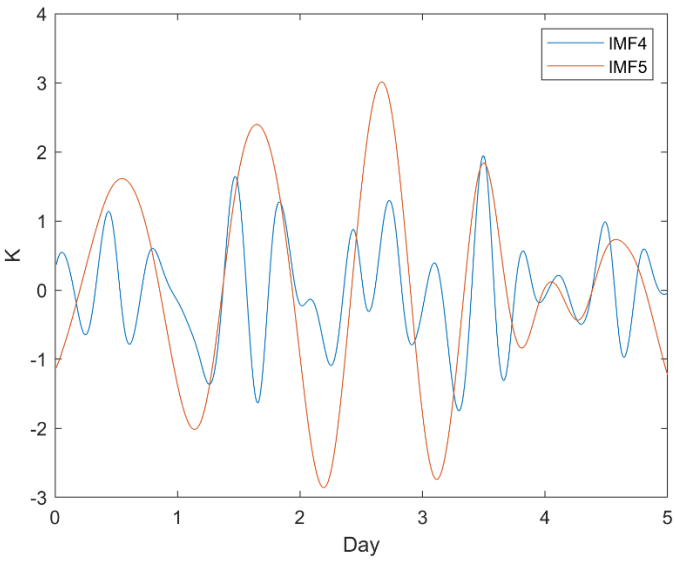

Figure 4.1.2. The semidiurnal component (IMF4) and the diurnal component (IMF5) of 2 m Temperature at FAWN Citra on 1--5 July 2020. The IMF4 and IMF5 signals were obtained by performing Ensemble Empirical Mode Decomposition on the 2 m Temperature observations at FAWN Citra over the entire month of July 2020.

Variable 1	**Variable 2**	**Lag Time between Variables 1 and 2 (hours)**	**Correlation value**
2 m Temperature	10 m Temperature	0	0.993
10 m Temperature	Solar Radiation	2	0.947
2 m Temperature	Solar Radiation	1.5	0.943
Solar Radiation	Relative Humidity	9.5	0.941
10 m Temperature	Relative Humidity	11.5	0.934
2 m Temperature	Relative Humidity	11.5	0.928
Wind Speed	Solar Radiation	2	0.892
Wind Speed	Relative Humidity	12	0.877
Wind Speed	2 m Temperature	0.5	0.872
Wind Speed	10 m Temperature	0.5	0.871
10 m Temperature	Dew Point	4	0.643
2 m Temperature	Dew Point	4	0.638
Solar Radiation	Dew Point	2.5	0.614
Wind Speed	Dew Point	4.5	0.587
Dew Point	Relative Humidity	7	0.583
Precipitation	Wind Speed	3	0.153
Precipitation	10 m Temperature	4	0.127
Precipitation	2 m Temperature	4	0.121
Precipitation	Solar Radiation	4	0.089
Precipitation	Dew Point	6	0.085
Relative Humidity	Precipitation	4.5	0.082

Table 1. The lead/lag time between each pair of variables and the relative strengths of their relationships from July 2020 at FAWN Citra station.

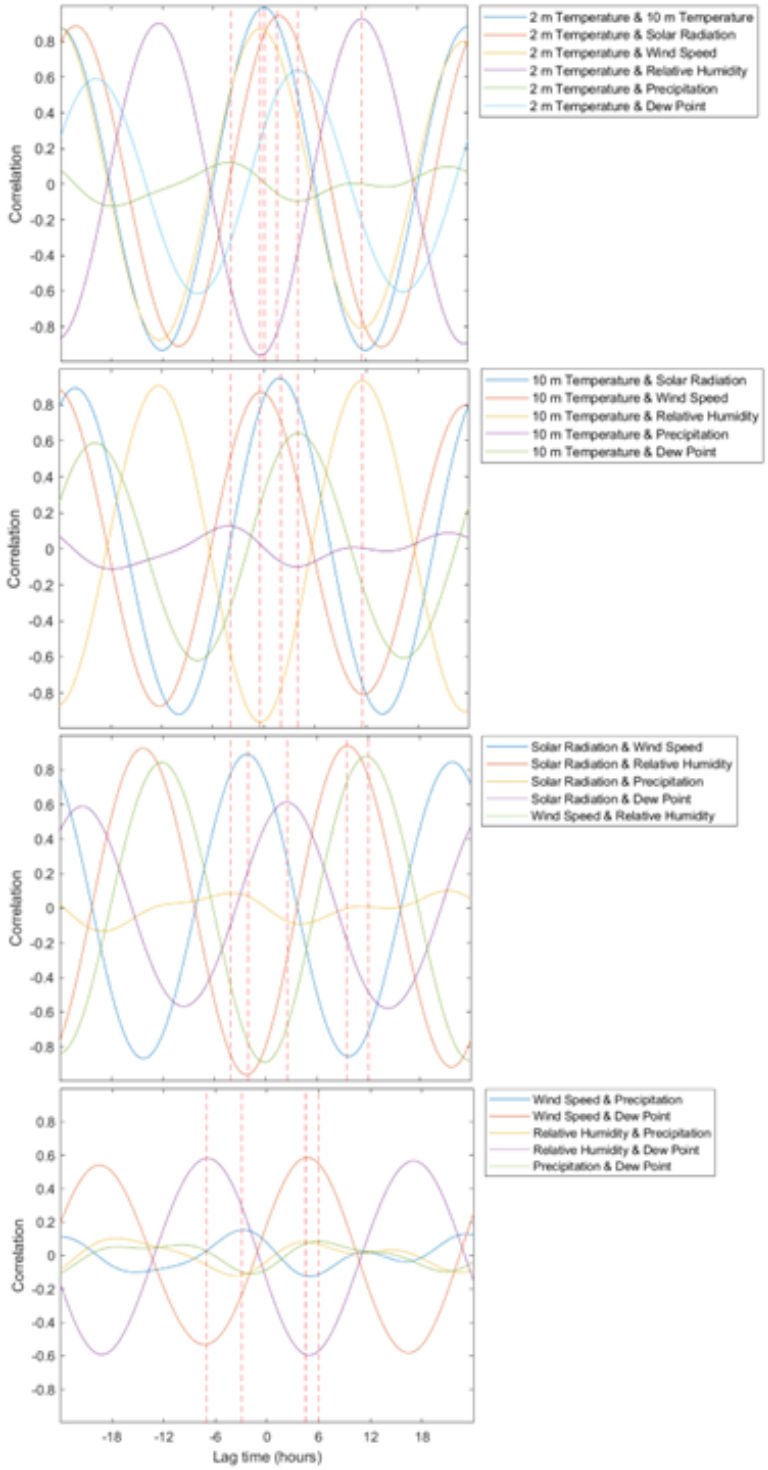

Figure 4.1.3. Correlations between the IMF5 components (i.e., the diurnal mode) of each pair of variables at lead/lag times ranging from -3 days to +3 days from July 2020 at FAWN Citra station. Red dashed lines mark the lead/lag time between the pair of variables. All 21 pairs of the seven variables are plotted.

Equipped with the lead/lag relationships between the variables and the relative strengths of these relationships, we diagnose the diurnal phase of each variable at a particular FAWN station during a month of the year. This is performed by identifying the time of day (in local solar time) of the diurnal peak of each variable. The focus of this study is on the timing of the diurnal maxima. Because we have isolated the diurnal scale using EEMD, the diurnal variations follow a sinusoidal pattern, meaning that the diurnal minima occur twelve hours before and after the diurnal maxima, and to plot them would be to provide redundant information. The procedure begins by recognizing that solar radiation peaks at solar noon at the station during the time period. Next, we identify the variable with the strongest lead/lag relationship (i.e., highest correlation coefficient) with solar radiation. If the variable lags solar radiation, we add the lag time to the solar radiation peak time. If the variable leads solar radiation, we subtract the lag time from the solar radiation peak time. At this point in the procedure, the peak time of two out of seven variables have been diagnosed. To diagnose a third variable, we identify the variable with the strongest lead/lag relationship (i.e., highest correlation coefficient) to the variable that was just previously diagnosed, and then diagnose its peak time by adding or subtracting the lag time appropriately. The same steps are then repeated to diagnose the peak time of a fourth variable. At this point, three variables remain undiagnosed. For each of these three undiagnosed variables, we find its strongest (i.e., highest correlation value) lead/lag relationship to any already-diagnosed variable, and then diagnose its peak time by adding or subtracting the lag time appropriately. The result of this procedure is a depiction of the time of diurnal maximum (i.e., the phase) of each variable at a particular FAWN station during a particular time period; Figure 4.4 is shown as an example of this.

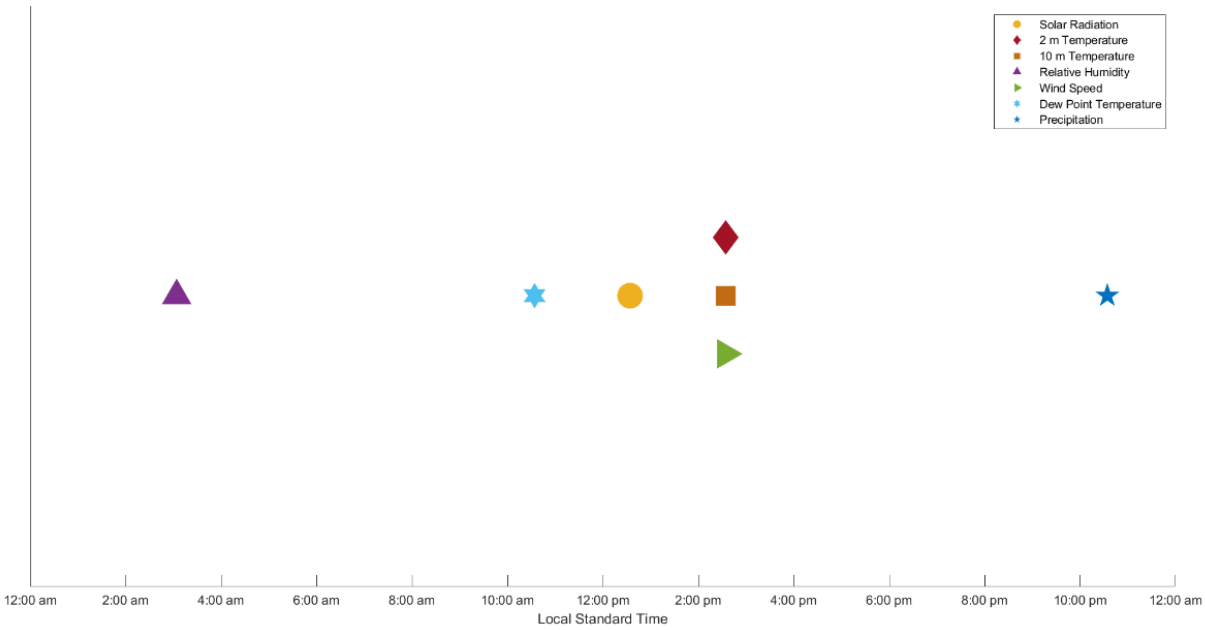

Figure 4.1.4. A depiction of the time of diurnal maximum of each variable from July 2020 at FAWN Citra station.

We diagnose the amplitude of the diurnal maximum of each variable with the following procedure. The first step is to calculate the mean of the raw data over the selected month. The next step is to identify the amplitude of each peak in the IMF5 timeseries for the selected month. The number of peaks in the IMF5 signal is equal to the number of days in the month. We average the amplitudes of the IMF5 peaks, and then add this value to the mean of the raw data from the selected month.

To summarize the diurnal cycle at a single station over several years, we calculate the climatological circular mean over 16 years of the phase and the climatological mean of the amplitude of each variable at its diurnal maximum. The phase climatology must be computed using a circular mean rather than a simple mean due to the circular nature of the diurnal phase data. The formula for circular mean is as follows:

Given n angle observations $x_1, \ldots, x_n$ measured in radians, their circular mean is:

$$Arg\left((1/n)\sum_{k=1}^{n} e^{ix_k}\right)$$

Where i is the imaginary unit and Arg z gives the principal value of the argument of complex number z, restricted to the range $[0,2\pi]$.

These climatological values are plotted using quiver arrows; the direction of the arrow represents the phase (time of day) of the diurnal maximum, and the magnitude of the arrow

represents the amplitude of the variable at its diurnal maximum. The amplitudes have been normalized over all months and all stations in the analysis to enable inter-seasonal and inter-station comparisons. The normalization formula is as follows:

$$z_i = (x_i - \min(x)) / (\max(x) - \min(x))$$

where:

- z_i: The i^{th} normalized value in the dataset
- x_i: The i^{th} value in the dataset
- min(x): The minimum value in the dataset
- max(x): The maximum value in the dataset

In addition, the variances over the 16 years of data of the phase and of the amplitude are calculated at each station for each month for each variable. Results for relative humidity and 10 m Temperature are not shown here due to their strong relationships to 2 m Temperature. Solar radiation is not shown because, in the calculation of the phase relationships between the variables, it simply reaches its diurnal maximum at solar noon.

4.2 Validation of downscaled data

To isolate the diurnal variability over Florida in FLAReS1.0, we employ the methodology following Misra and Jayasankar (2024), which is a variant of the Multi-dimensional Ensemble Empirical Mode Decomposition following Wu et al. (2009). This methodology is described below:

A dataset like X(*t,s*) that varies in space (*s*) and time (*t*) can be decomposed into *m* modes of Empirical Orthogonal Functions (EOFs) as:

$$X(t,s) = \sum_{m}^{K} r_m(s) q_m(t)$$

Where r_m and q_m are EOFs and Principal Components (PCs). In the case of precipitation, we choose to retain the first 10 (=K) PCs as the variance explained by successive EOFs began to asymptote.

We then conduct an EEMD on the first 10 PCs. EEMD is a data adaptive signal processing technique, where it decomposes the timeseries into complete sets of near orthogonal components called Intrinsic Mode Functions (IMFs).

We then use these diurnal IMF (component 3) of the PCs to obtain the diurnal anomalies ($X'(t,s)$) as:

$$X'(t,s) = \sum_{m=1}^{K} r_m(s) q_m^f(t)$$

Where, $q_m^f(t) = IMF_m^3(t)$. This reconstructed surface temperature anomaly (X') is shown for a sample grid point for one month to show the isolation of the diurnal component in Figure 4.2.1.

These reconstructed anomalies were computed month by month for the most recent 15-year period of the FLAReS1.0 dataset (1990-2004). From the reconstructed hourly diurnal anomalies, the diurnal maxima and minima are identified, including their amplitude and phase. To prevent any blips in the reconstructed anomalies from having undue influence on the analysis, diurnal maxima or minima whose amplitudes are below the 20th percentile of the entire year are excluded from the analysis. Of the diurnal maxima and minima whose amplitudes exceed the 20th percentile, the phase (time of day of the diurnal maximum or minimum) is stored and sorted into bins of 2-hour width (i.e., 00:00—2:00 LST, 2:00—4:00 LST, … , 20:00—22:00 LST, 22:00—24:00 LST). The monthly mode of the diurnal phase is computed, and stored only if its count is greater than three. This monthly diurnal phase is identified for the diurnal maxima and minima of surface temperature, specific humidity, and precipitation. Of the diurnal maxima and minima whose amplitudes exceed the 20th percentile, the monthly mean is computed and then added to the monthly mean of the variable itself. Specific humidity is converted to dew point temperature using the following empirical formula introduced by Bolton (1980), which is accurate to within 0.1% over the temperature range -30°C ≤ T < 35°C:

$$e_s(T) = 611.2\, e^{\frac{17.67 T_c}{T_c + 243.5}}$$

Where $e_s(T)$ is the saturation vapor pressure in Pascals, and T_C is the temperature in °C. Before using the Bolton formula, the ambient vapor pressure e is computed using the formula:

$$q = \frac{\varepsilon e}{p - (1 - \varepsilon) e}$$

Where q is the specific humidity, p is the ambient air pressure, and ε=0.622 is the ratio between the gas constant of dry air and the gas constant of water vapor. The dew point temperature is the temperature which one has to plug into the Bolton (1980) formula to yield a saturation vapor pressure equal to the actual vapor pressure. Therefore, with a known vapor pressure (which was obtained from a known specific humidity and a known air pressure), we solve the Bolton (1980)

formula for T_C, which is the dew point temperature. The hourly air pressure data comes from FLAReS1.0.

The phase and amplitudes of the diurnal maxima and minima of surface temperature, dew point temperature, and precipitation from FLAReS1.0 are compared to their observed counterparts. Specifically, they are computed at the grid points containing each of the 30 FAWN stations and directly compared to the diurnal cycle at each of the FAWN stations. Correlation, root-mean-square error (RMSE), and interannual standard deviations are computed as well.

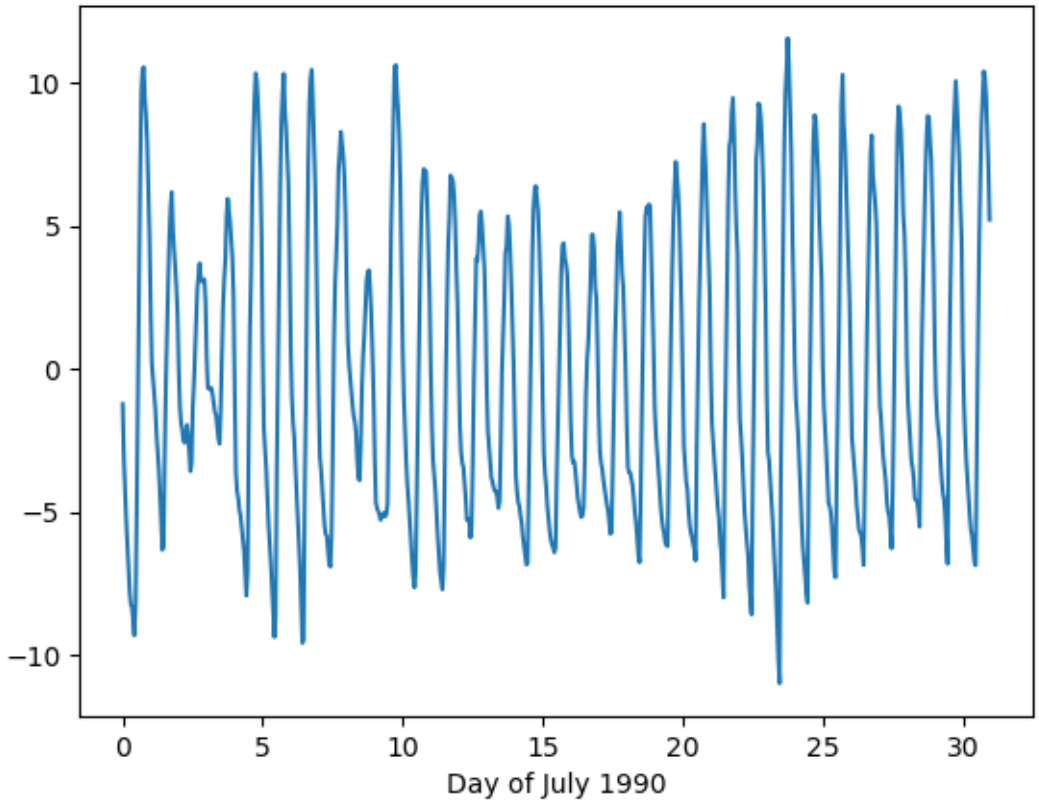

Figure 4.2.1. Reconstructed diurnal anomalies of 2 m temperature at a single grid point in July 1990 from FLAReS1.0.

4.3 Low frequency variability of diurnal variation in FLAReS1.0

Like the methodology for the FLAReS1.0 validation against FAWN station observations, we isolate the diurnal variability over Florida in FLAReS1.0 over 1903—2004 by employing the methodology following Misra and Jayasankar (2024), which is a variant of the Multi-dimensional Ensemble Empirical Mode Decomposition following Wu et al. (2009). The methodology is comprised of EOF analysis and performing EEMD on the Principal Components.

The hourly diurnal anomalies are reconstructed using IMF3 from the EEMD analysis. Figure 4.6 shows these reconstructed diurnal anomalies of precipitation over five days at (28.5052°N, 278.6532°E), which is Orlando, Florida.

The reconstructed diurnal anomalies are converted from UTC time to LST time at each grid point using the longitude at that point. Local maxima and minima are then located in the time series. Local maxima and minima are stored only if their amplitude exceeds the 20th percentile. The diurnal phase of these local maxima and minima are sorted into 2-hour bins (i.e., 00:00—2:00 LST, 2:00—4:00 LST, … , 20:00—22:00 LST, 22:00—24:00 LST). Of the bins, the monthly mode is computed, and it is stored as the diurnal phase only if its count is greater than three. For diurnal amplitude, we take the mean of the amplitudes above the 20th percentile for each variable and month.

To identify associations between interannual climate modes and the diurnal cycle in Florida, correlations are computed between each climate mode index and the diurnal maximum and minimum phase and amplitude of surface temperature, specific humidity, and precipitation. The interannual climate modes used in this analysis are ENSO, the Atlantic-Pacific interbasin SST gradient (following Kim et al. 2020), and the Bermuda High Index. For ENSO, we use the Nino3.4 SST index from the NOAA Extended Reconstructed SST V5 dataset (ERSSTv5; Huang et al. 2017). The Nino3.4 SST index is the most strongly ENSO-related SST region with respect to its strength of association with other ENSO-related anomalies and to its teleconnections to remote climate anomalies (Bamston et al. 1997). The Atlantic-Pacific interbasin SST gradient is the area-averaged SST in the tropical Atlantic (80°W to 40°W and 10°N to 25°N) minus the area-averaged SST in the tropical Pacific (160°E to 160°W and 0°N to 10°N). The SST dataset used is ERSSTv5 (Huang et al. 2017). The Bermuda High Index is the MSLP difference between 90°W, 30°N (near New Orleans, Louisiana) and 78°W, 30°N (a marine location east of Jacksonville, Florida) from FLAReS1.0. Motivated by the notion that there is noise in the Nino3.4 SST index (Hanley et al. 2003), we isolate the interannual component of all three climate modes using EEMD, and then compute the correlations between the *interannual component* of each climate mode index and each of the diurnal cycle characteristics (i.e., the diurnal maximum and minimum phase and amplitude of surface temperature, specific humidity, and precipitation). By computing these correlations with the raw climate mode indices as well as the *interannual components* of the climate mode indices, we determine which responses of the

Florida diurnal cycle are associated with the interannual scale and which responses are influenced by other scales of variability.

In months when and regions of Florida where the diurnal maximum amplitude is positively correlated to an index like ENSO or BHI, ***and*** the diurnal minimum amplitude is negatively correlated to the same index, we say that the diurnal amplitudes of that variable are enhanced. Likewise, in months when and regions of Florida where the diurnal maximum amplitude is negatively correlated to an index, ***and*** the diurnal minimum amplitude is positively correlated to the index, we say that the diurnal amplitudes are suppressed. Similarly, for diurnal phase, if both the diurnal maximum and diurnal minimum phase are positively correlated to a climate mode index, that is strong evidence that the diurnal cycle gets shifted later when that index is high, and that the diurnal cycle gets shifted earlier when that index is low.

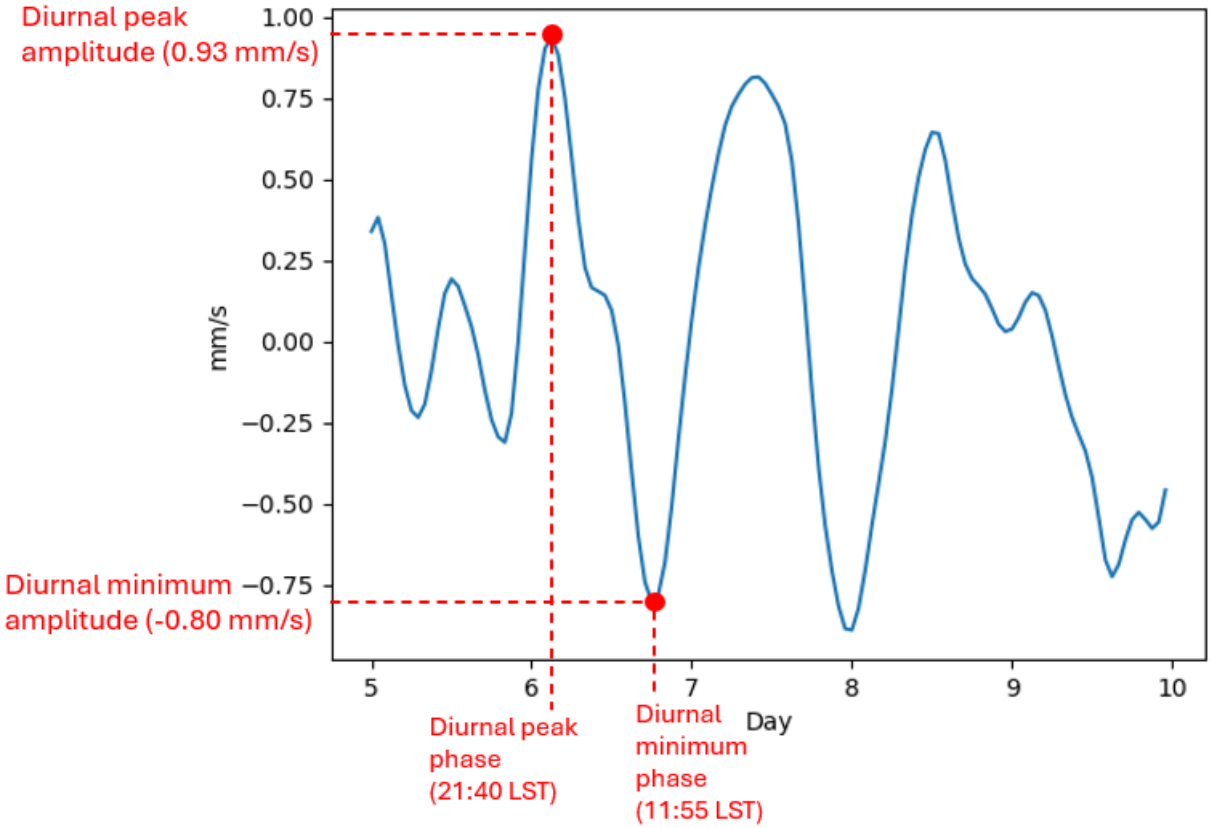

Figure 4.6. Reconstructed diurnal anomalies of precipitation rate from FLAReS1.0 in July 6—10, 1950, at Orlando, Florida. The diurnal peak amplitude, diurnal minimum amplitude, diurnal peak phase, and diurnal minimum phase are labeled.

CHAPTER FIVE

RESULTS

5.1 Characterizing the diurnal cycle at FAWN stations

5.1.1 The diurnal mode (IMF5)

At all stations and all times of the year, the climatological diurnal peak of temperature is in mid-afternoon, usually around 14:30 Local Solar Time (LST; Figures 5.1.1-12). The variance of this time of temperature's diurnal peak across the sixteen years 2005–2020 is small; only a few minutes (Figure 5.1.13a). The variance across 2005–2020 of the amplitude of temperature at its diurnal peak is small during summer and larger in winter (Figure 5.1.14a).

Wind speed tends to have its diurnal peak in the early afternoon, an hour or two before the diurnal peak of temperature, at most stations during autumn, winter, and spring (Figures 5.1.1-4 and 5.1.10-12). The exceptions to this rule include some stations in panhandle Florida which have wind speed reaching its diurnal maximum in the morning in autumn and winter (5.1.10-12). In summer (Figures 5.1.6-8), wind speed peaks in the mid-afternoon to either coincide with the diurnal peak of temperature or occur shortly after it. The variance of the diurnal phase of wind speed is less than three square hours at all stations in all months (Figure 5.1.13b). The variance of the amplitude of wind speed at its diurnal peak varies between stations, but at most stations, it is lowest during August–December, and slightly higher during January--June (Figure 5.1.14).

Dew point temperature, a measure of water vapor content, has its diurnal maximum at varying times of day through the annual cycle. In winter, at most stations, dew point temperature reaches its diurnal maximum in the mid-afternoon, coinciding with the diurnal peak of surface temperature (Figures 5.1.1 and 5.1.11--12). In February, this remains true at most stations across Florida, except for some in central Florida (Figure 5.1.2). In spring, dew point temperature reaches its diurnal maximum in the pre-dawn morning at many stations in central Florida, and mid- to late-morning in south-central Florida, while there is no clear signal in north Florida nor south Florida (Figures 5.1.3--5). In summer, dew point temperature reaches its diurnal maximum in the morning across Florida, with large amplitude at all stations (Figures 5.1.6--8). The diurnal peak of dew point temperature occurs earlier in the morning in parts of central Florida than the rest of Florida during summer (Figures 5.1.6--8). As the summer evolves, the diurnal peak of

dew point temperature shifts slightly later across Florida (Figures 5.1.6—8). In August, the peak time of dew point temperature is still mid-morning in central Florida but occurs in the early afternoon at many other stations (Figure 5.1.8). In September, the diurnal peak amplitude of dew point temperature is still as large as it was in summer, before noticeably reducing in October (Figures 5.1.6—10). However, in September, the diurnal maximum phase and amplitude look homogeneous across north Florida for the first time since February (Figure 5.1.2--9). In October, the diurnal maximum of dew point temperature occurs in the mid-afternoon in north Florida and the early afternoon in most of peninsular Florida, except for a few stations in central Florida that have the diurnal maximum of dew point temperature in the morning (Figure 5.1.10). Finally, in November, the diurnal peak occurs in the afternoon across Florida, but slightly earlier in the afternoon in south Florida (Figure 5.1.11). The interannual variance of the phase of the diurnal peak of dew point is large at some stations, particularly in the winter and spring (Figure 5.1.13c), suggesting that the window for the diurnal peak of dew point temperature spans several hours during winter and spring. Amongst most stations, the variance of the phase of the diurnal peak of dew point is lowest during the summer (Figure 5.1.13c), suggesting a summertime narrowing of the window for the diurnal peak of dew point temperature. The seasonality of the variance of the amplitude of the dew point at its diurnal peak is remarkably consistent across stations; the variance is quite low from May–September, is higher in autumn, winter, and spring, and is largest in February (Figure 5.1.14c).

Precipitation has a large amplitude at its diurnal peak in June-September (Figure 5.1.6-9), and a much smaller diurnal amplitude during the other times of year (Figures 5.1.1-5 and Figures 5.1.10-12). In June-September, precipitation has its diurnal peak in the late afternoon (17:00-18:00 LST) at most stations (Figures 5.1.6-9). A notable exception is Carabelle, on the panhandle coast, which has its summertime diurnal maximum precipitation occurring at various times of the day and night throughout the summer (Figures 5.1.6-9). The variance of the diurnal phase is relatively low in June–September, compared to the other times of year, during which it is remarkably high (Figure 5.1.13d). This suggests that in June–September, precipitation is likely to arrive predictably around the same time each day. In the other months of the year, the variance of the phase is high, suggesting that if precipitation occurs on a particular day, it may occur at nearly any time. The variance of the amplitude of precipitation at its diurnal peak is largest in June–September at most stations (Figure 5.1.14). The amplitude of the diurnal scale precipitation

is quite small outside of the summer season (Figures 5.1.1-5 and 5.1.10-12), suggesting that the precipitation that does occur during these months may not be captured by the diurnal mode.

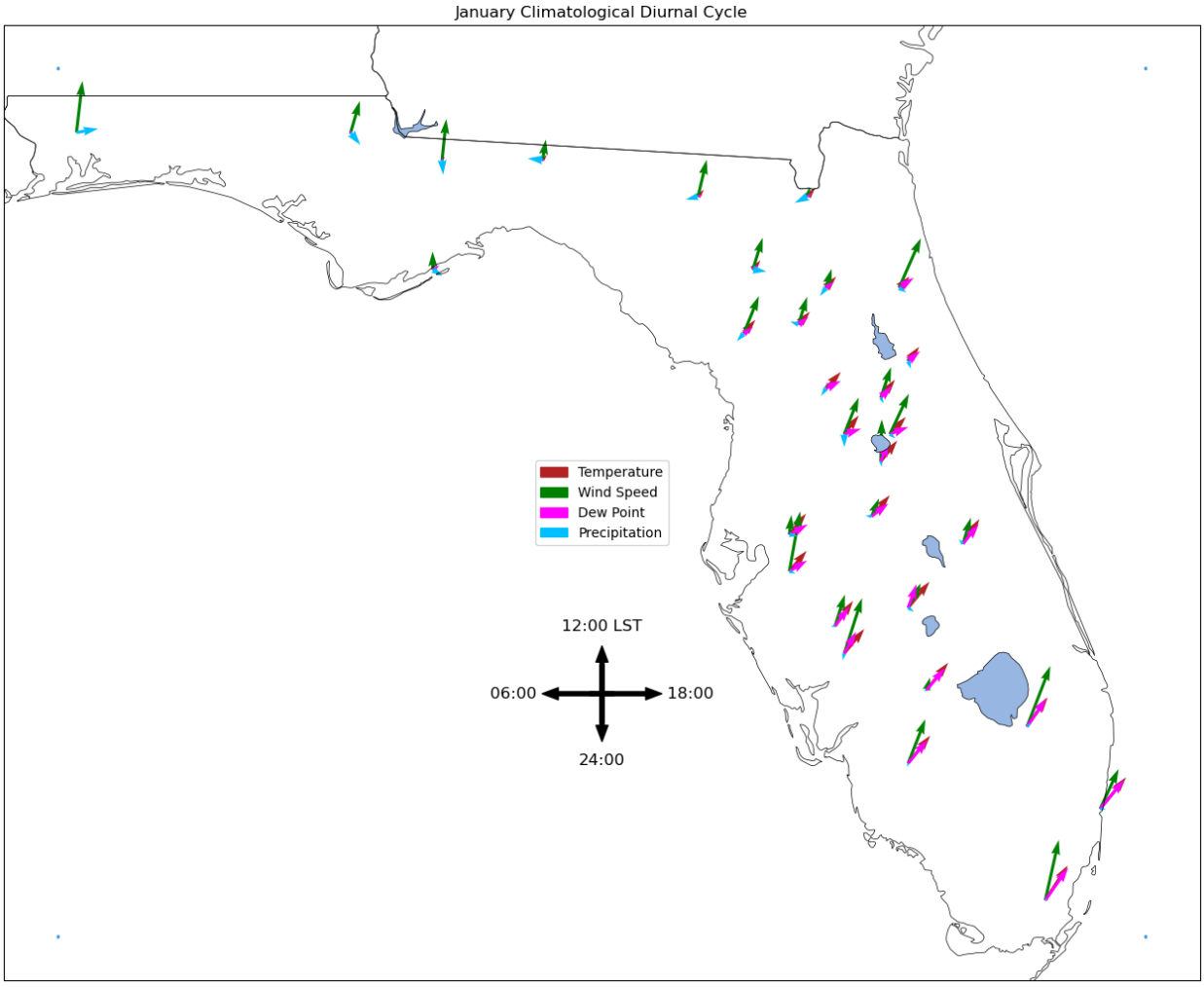

Figure 5.1. The January climatological phase (direction of arrow; Local Solar Time) and amplitude (length of arrow) of the diurnal maxima of surface temperature (red), wind speed (green), dew point temperature (magenta), and precipitation (blue) from the diurnal component (IMF5).

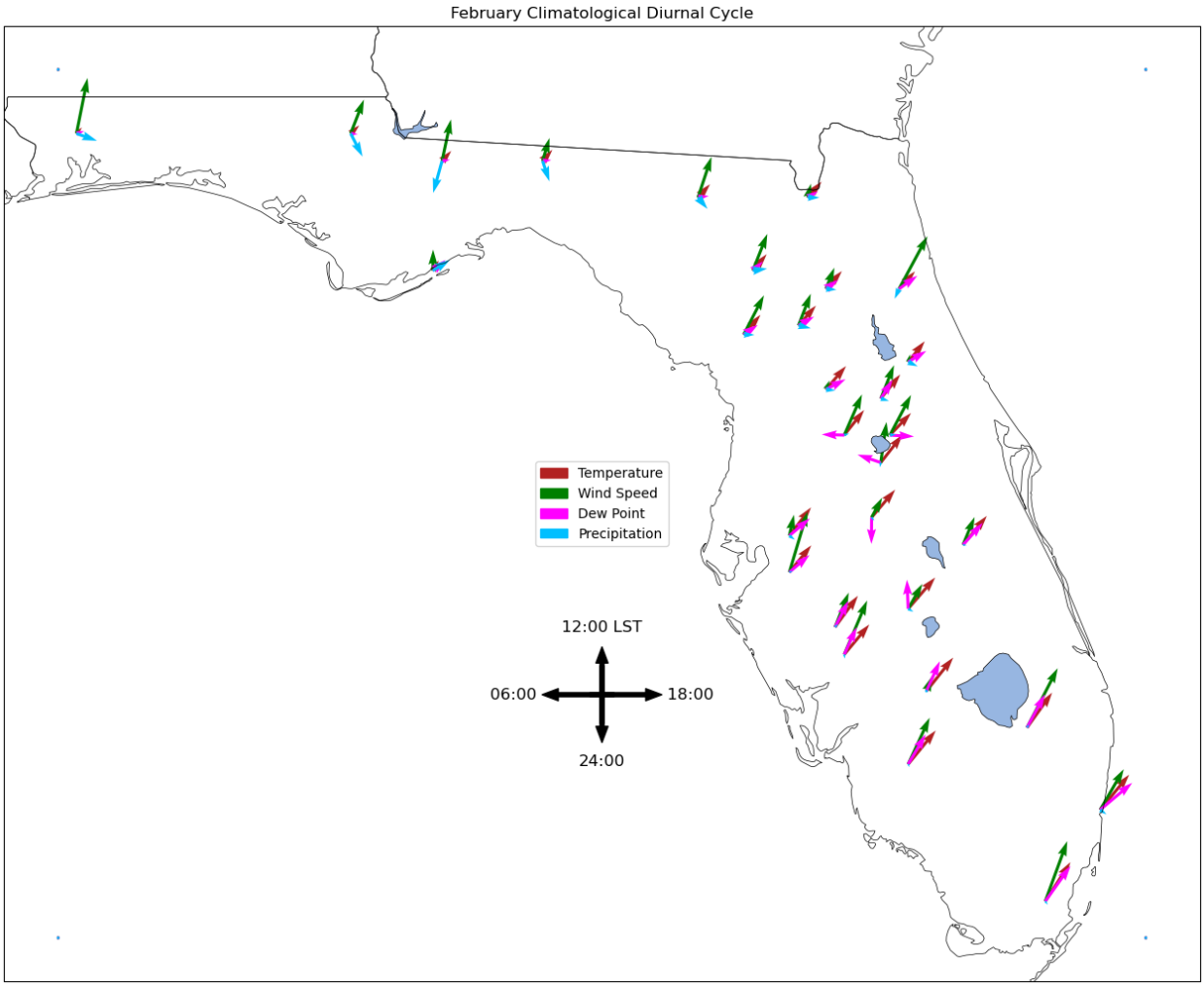

Figure 5.2. The February climatological phase (direction of arrow; Local Solar Time) and amplitude (length of arrow) of the diurnal maxima of surface temperature (red), wind speed (green), dew point temperature (magenta), and precipitation (blue) from the diurnal component (IMF5).

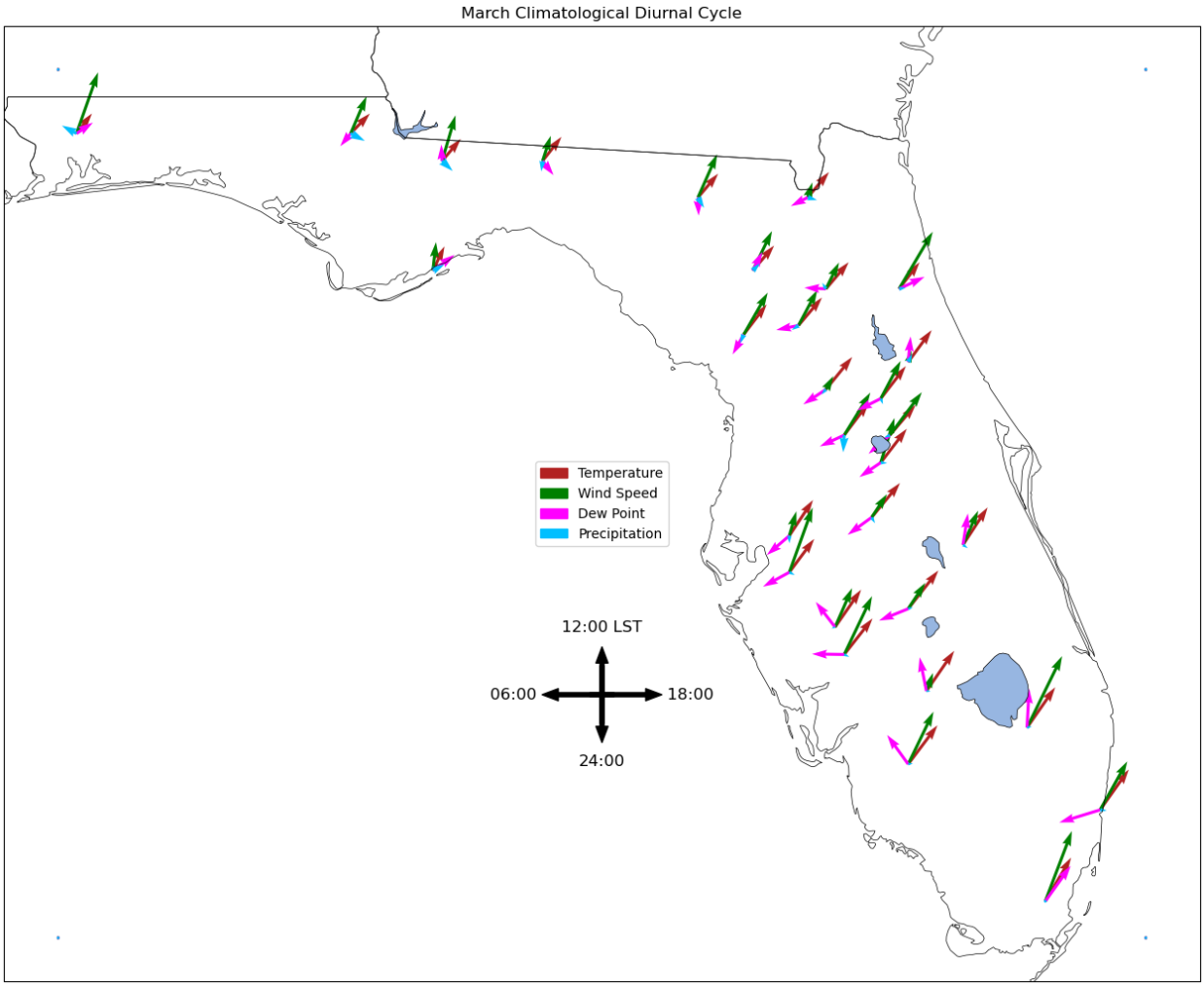

Figure 5.3. The March climatological phase (direction of arrow; Local Solar Time) and amplitude (length of arrow) of the diurnal maxima of surface temperature (red), wind speed (green), dew point temperature (magenta), and precipitation (blue) from the diurnal component (IMF5).

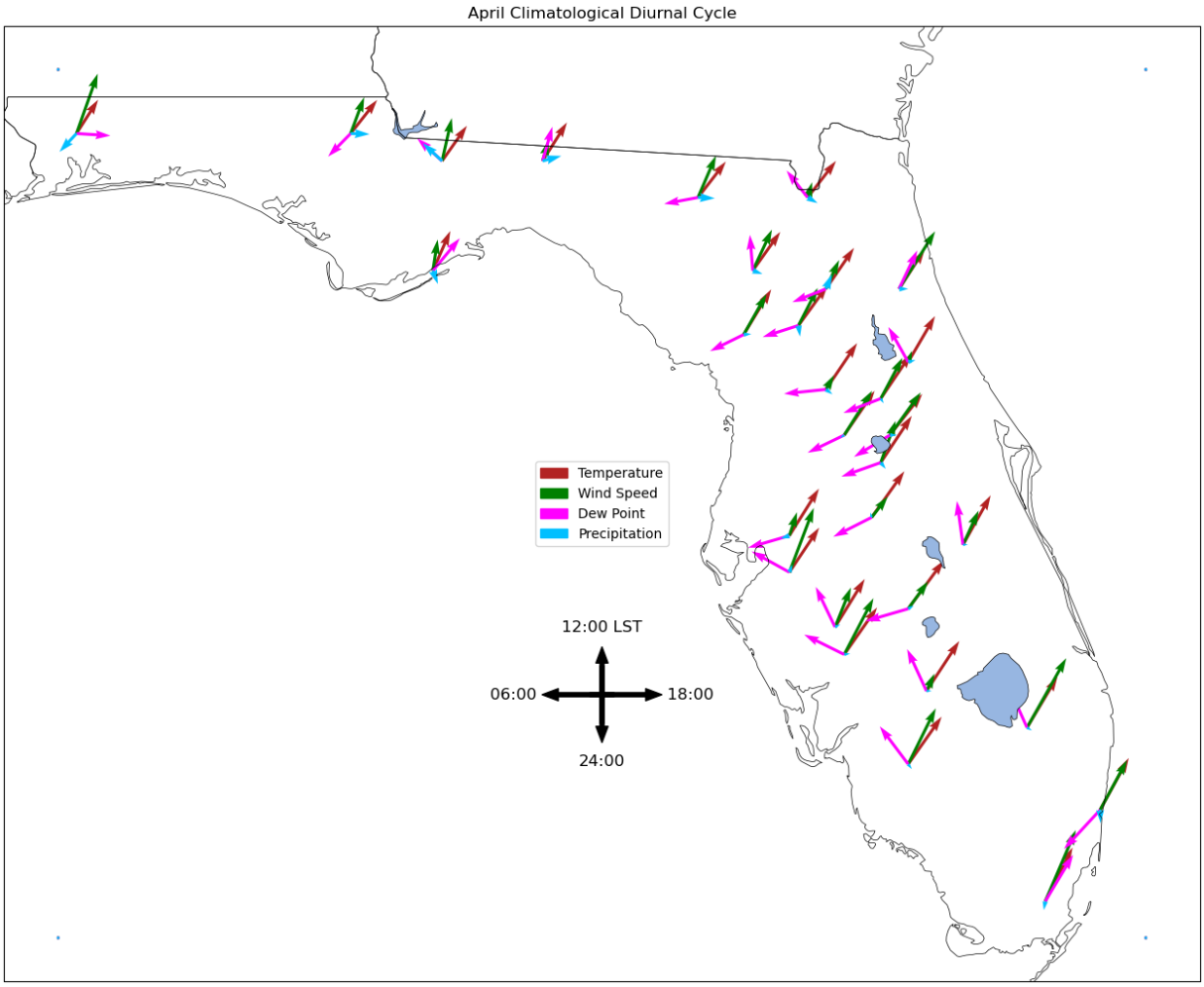

Figure 5.4. The April climatological phase (direction of arrow; Local Solar Time) and amplitude (length of arrow) of the diurnal maxima of surface temperature (red), wind speed (green), dew point temperature (magenta), and precipitation (blue) from the diurnal component (IMF5).

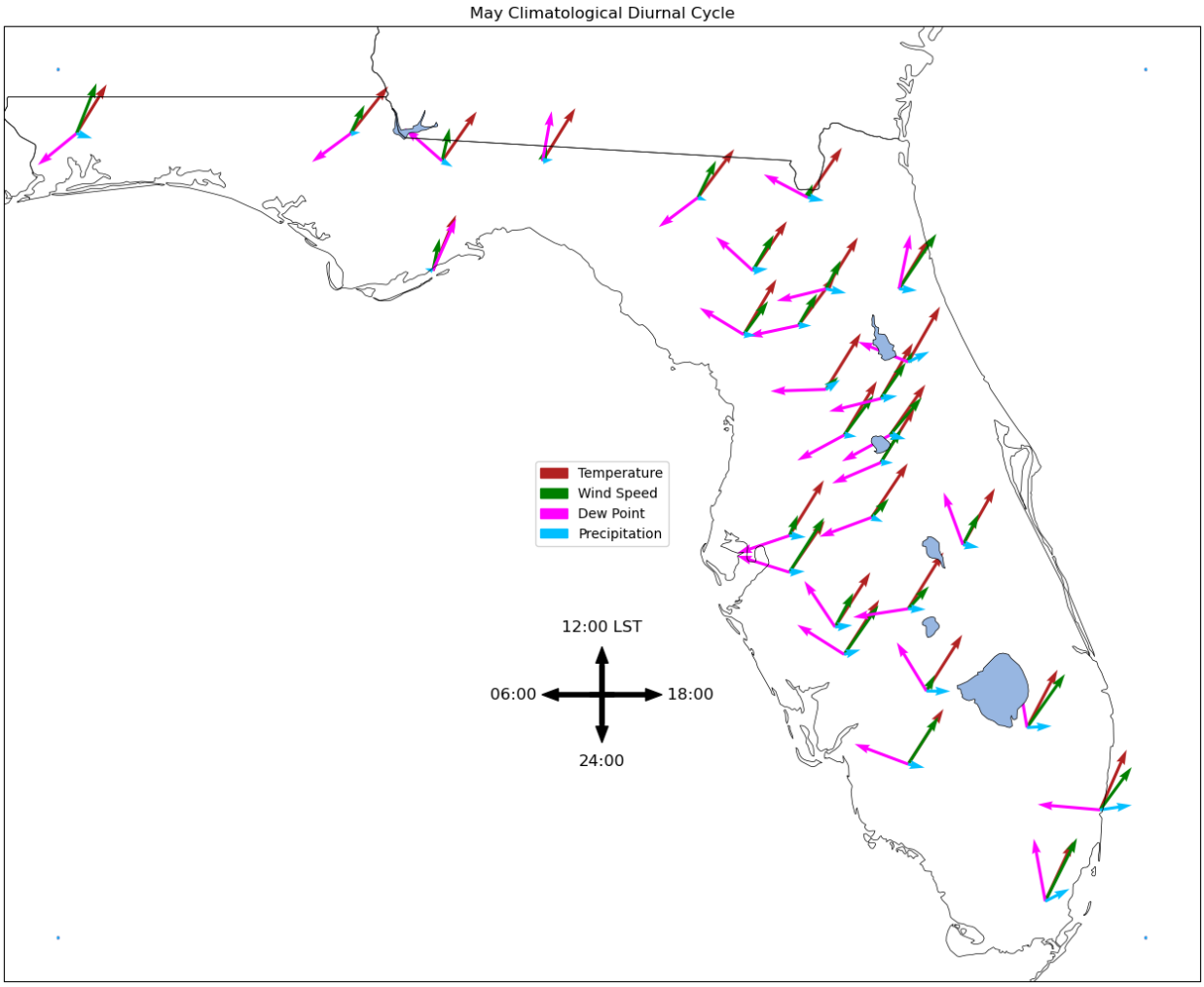

Figure 5.5. The May climatological phase (direction of arrow; Local Solar Time) and amplitude (length of arrow) of the diurnal maxima of surface temperature (red), wind speed (green), dew point temperature (magenta), and precipitation (blue) from the diurnal component (IMF5).

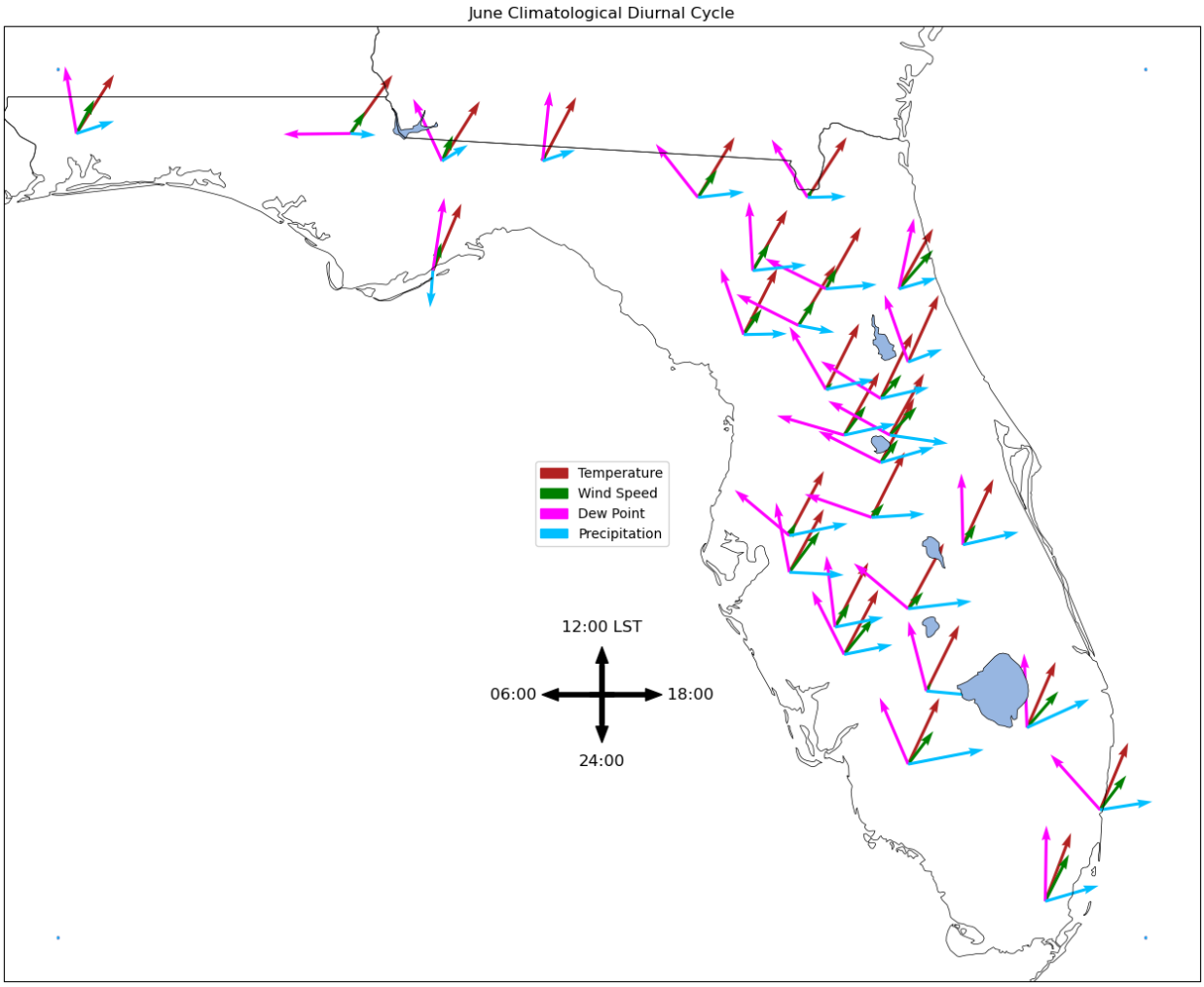

Figure 5.6. The June climatological phase (direction of arrow; Local Solar Time) and amplitude (length of arrow) of the diurnal maxima of surface temperature (red), wind speed (green), dew point temperature (magenta), and precipitation (blue) from the diurnal component (IMF5).

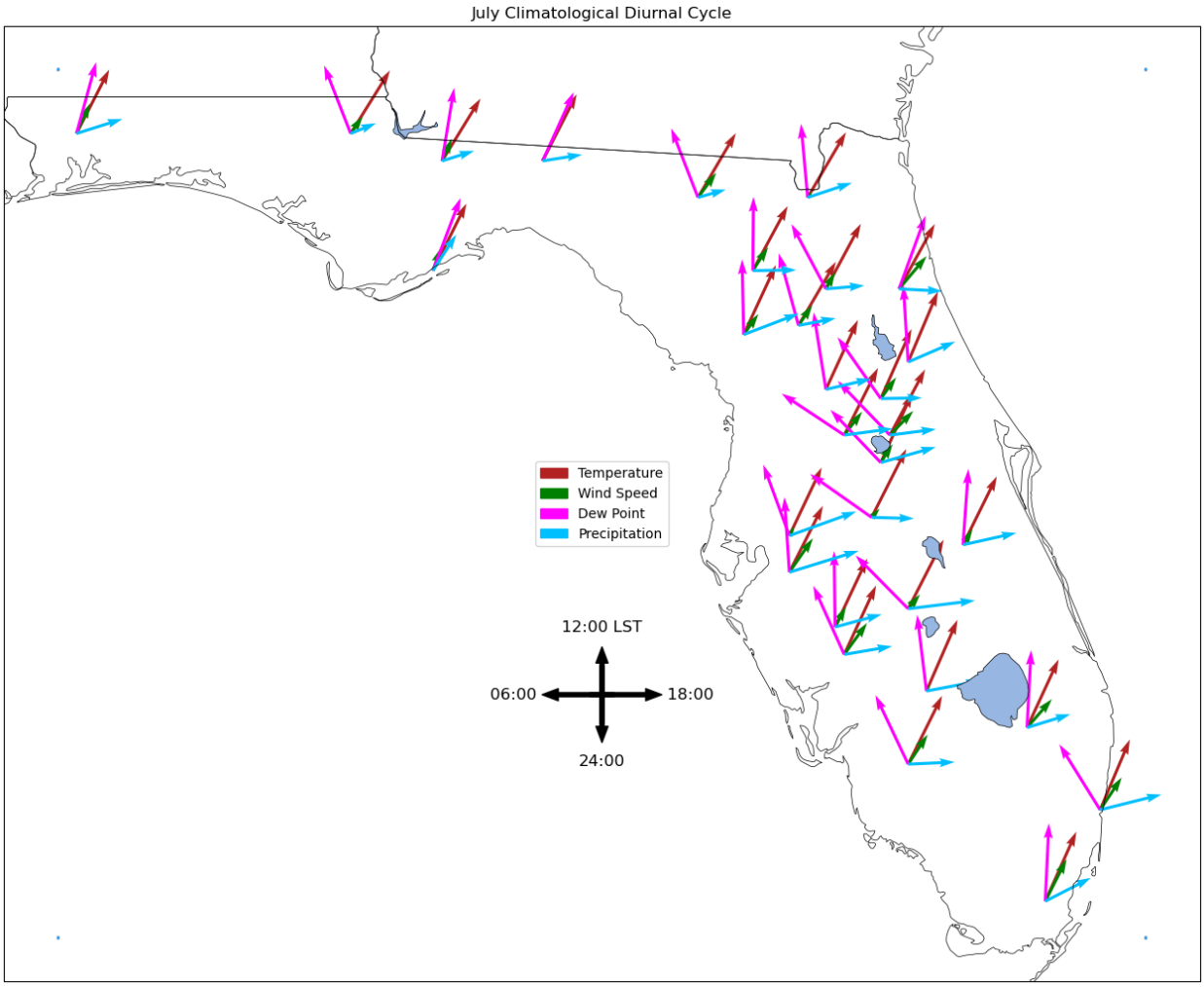

Figure 5.7. The July climatological phase (direction of arrow; Local Solar Time) and amplitude (length of arrow) of the diurnal maxima of surface temperature (red), wind speed (green), dew point temperature (magenta), and precipitation (blue) from the diurnal component (IMF5).

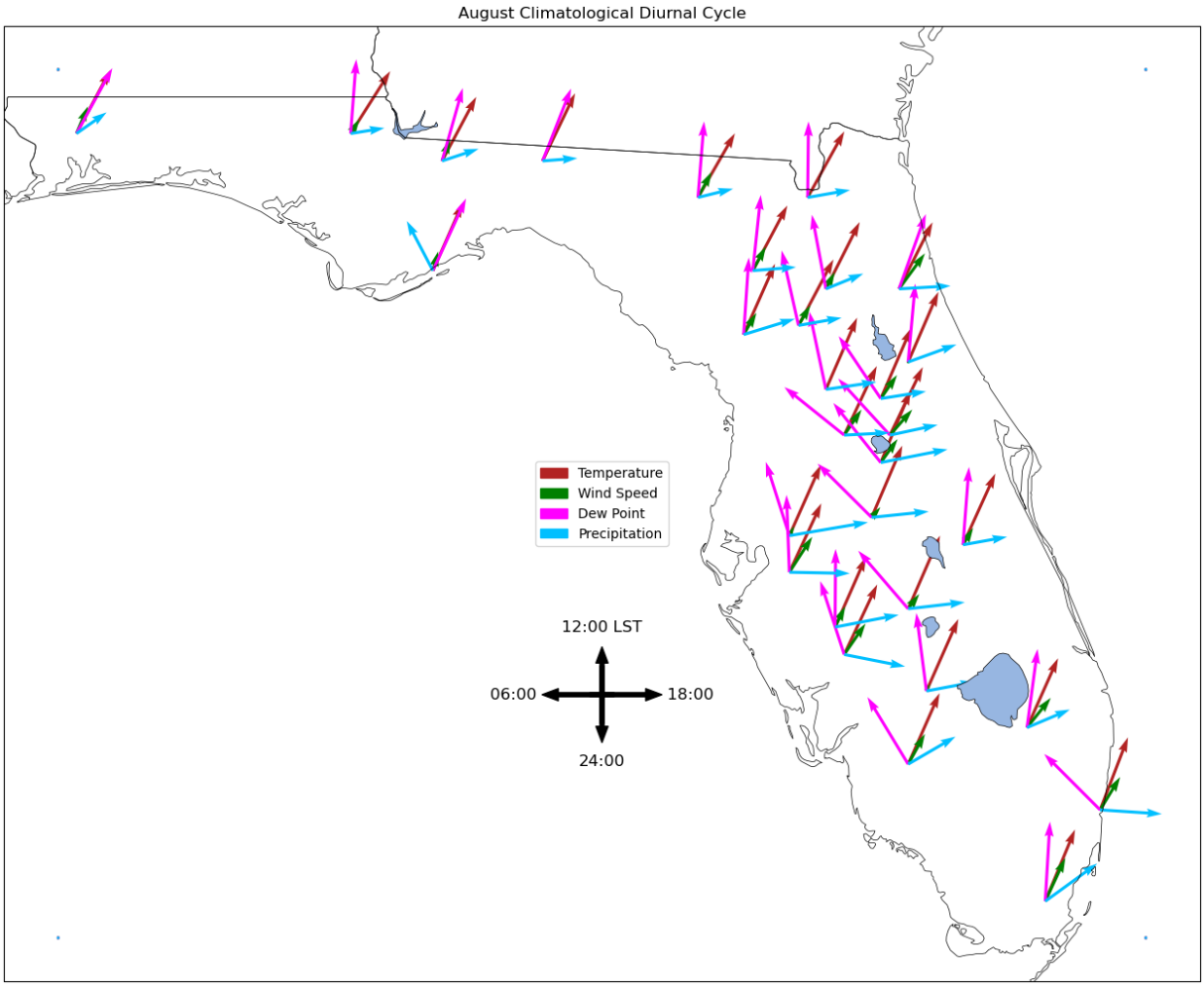

Figure 5.8. The August climatological phase (direction of arrow; Local Solar Time) and amplitude (length of arrow) of the diurnal maxima of surface temperature (red), wind speed (green), dew point temperature (magenta), and precipitation (blue) from the diurnal component (IMF5).

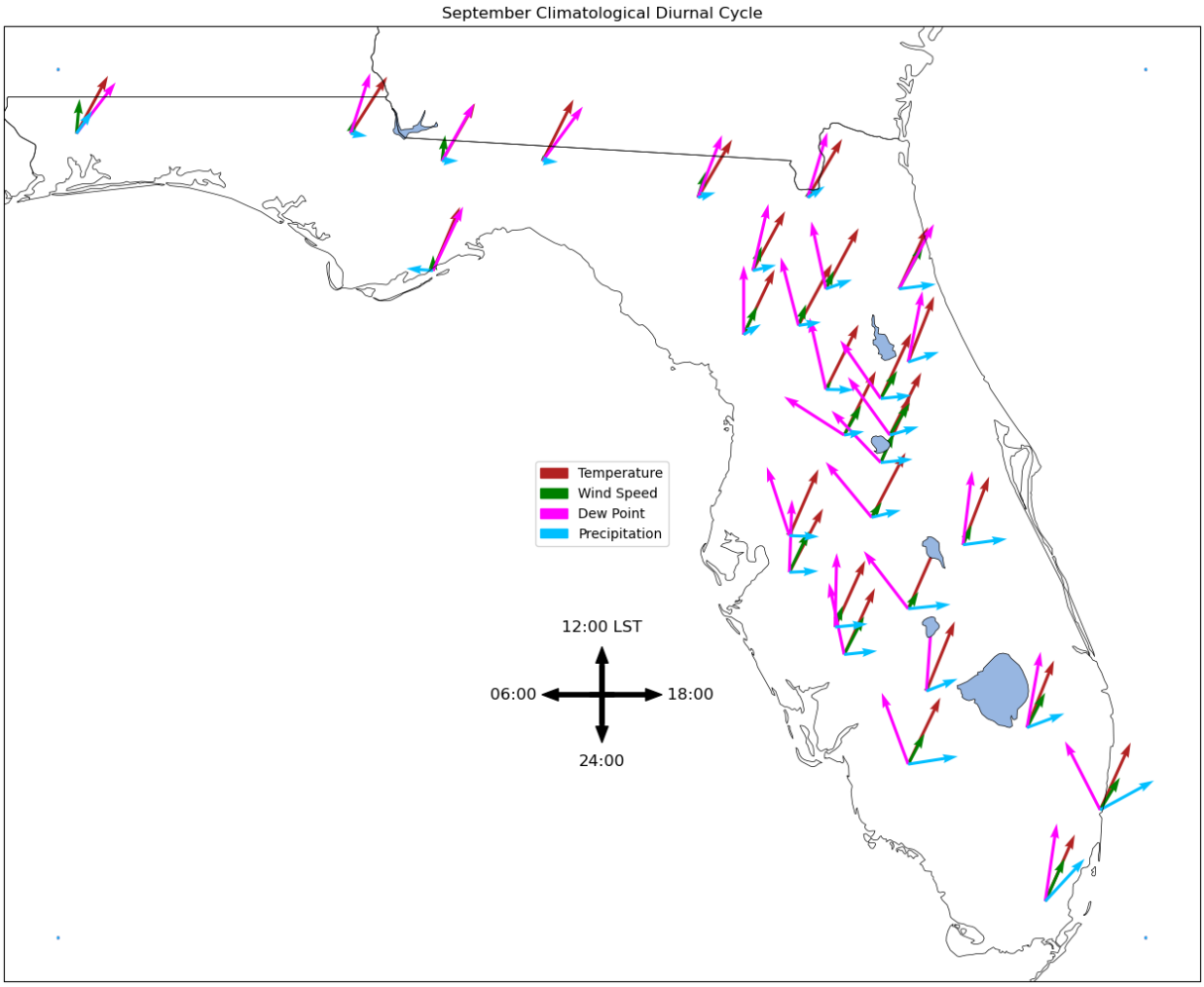

Figure 5.9. The September climatological phase (direction of arrow; Local Solar Time) and amplitude (length of arrow) of the diurnal maxima of surface temperature (red), wind speed (green), dew point temperature (magenta), and precipitation (blue) from the diurnal component (IMF5).

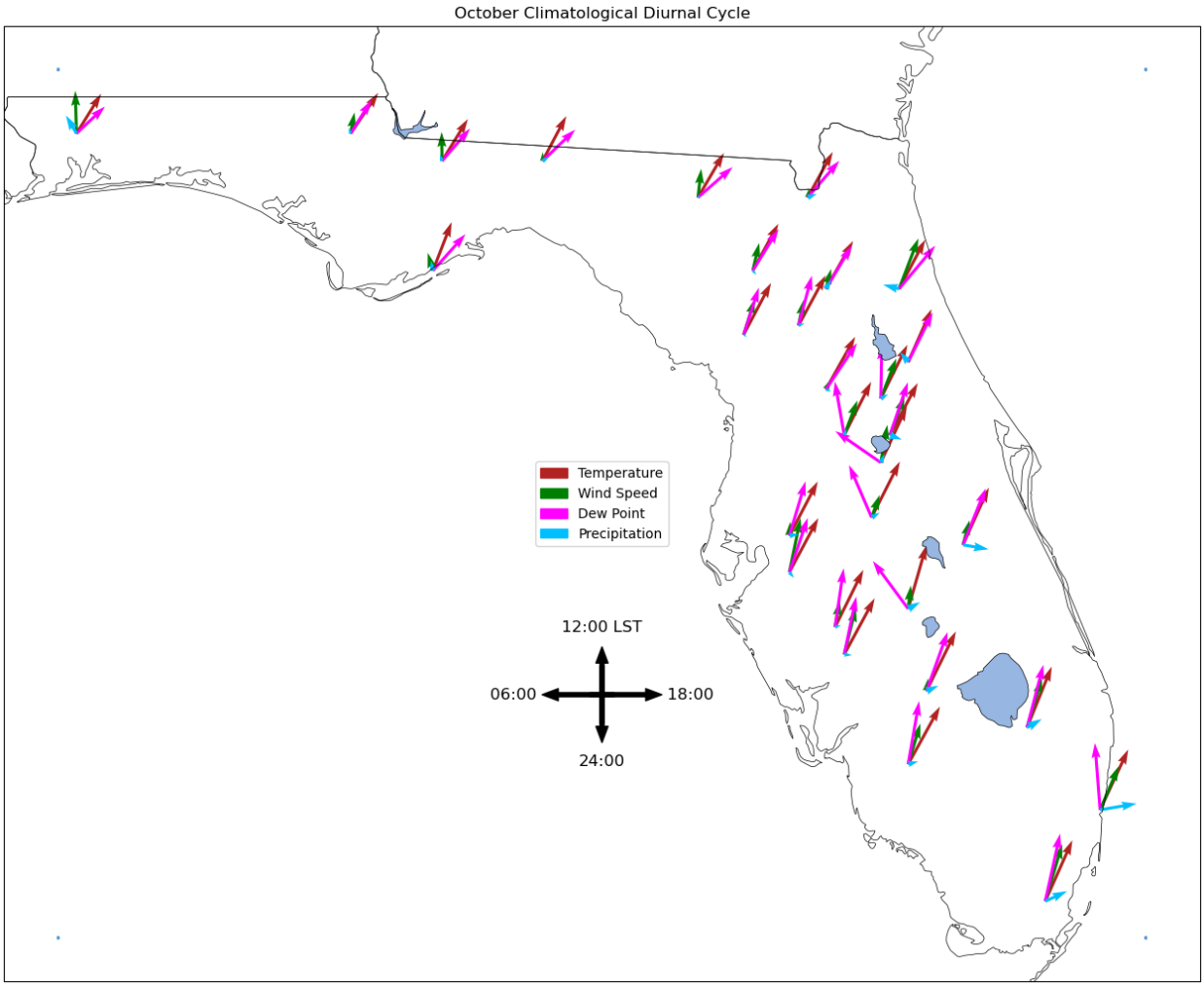

Figure 5.10. The October climatological phase (direction of arrow; Local Solar Time) and amplitude (length of arrow) of the diurnal maxima of surface temperature (red), wind speed (green), dew point temperature (magenta), and precipitation (blue) from the diurnal component (IMF5).

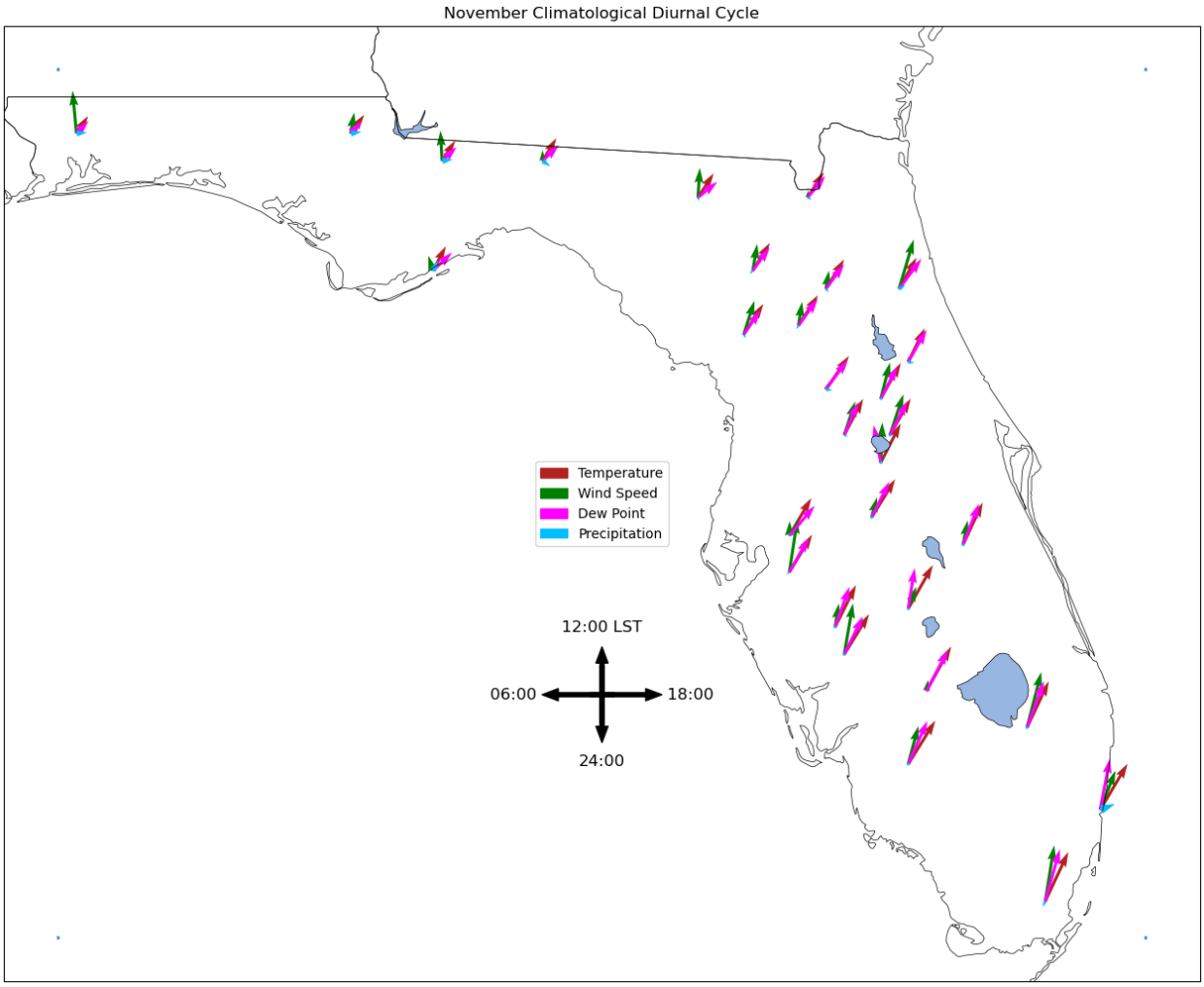

Figure 5.11. The November climatological phase (direction of arrow; Local Solar Time) and amplitude (length of arrow) of the diurnal maxima of surface temperature (red), wind speed (green), dew point temperature (magenta), and precipitation (blue) from the diurnal component (IMF5).

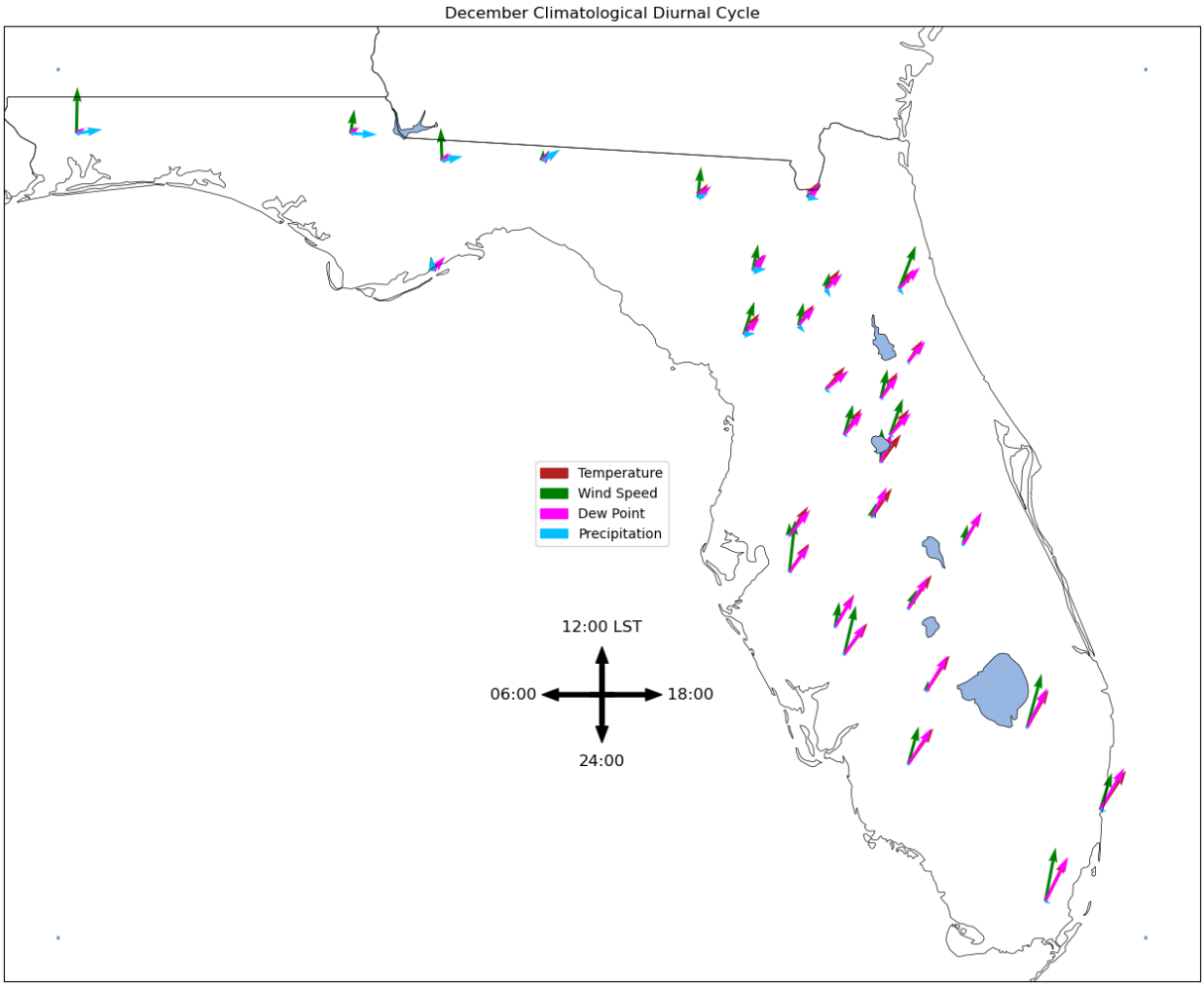

Figure 5.12. The December climatological phase (direction of arrow; Local Solar Time) and amplitude (length of arrow) of the diurnal maxima of surface temperature (red), wind speed (green), dew point temperature (magenta), and precipitation (blue) from the diurnal component (IMF5).

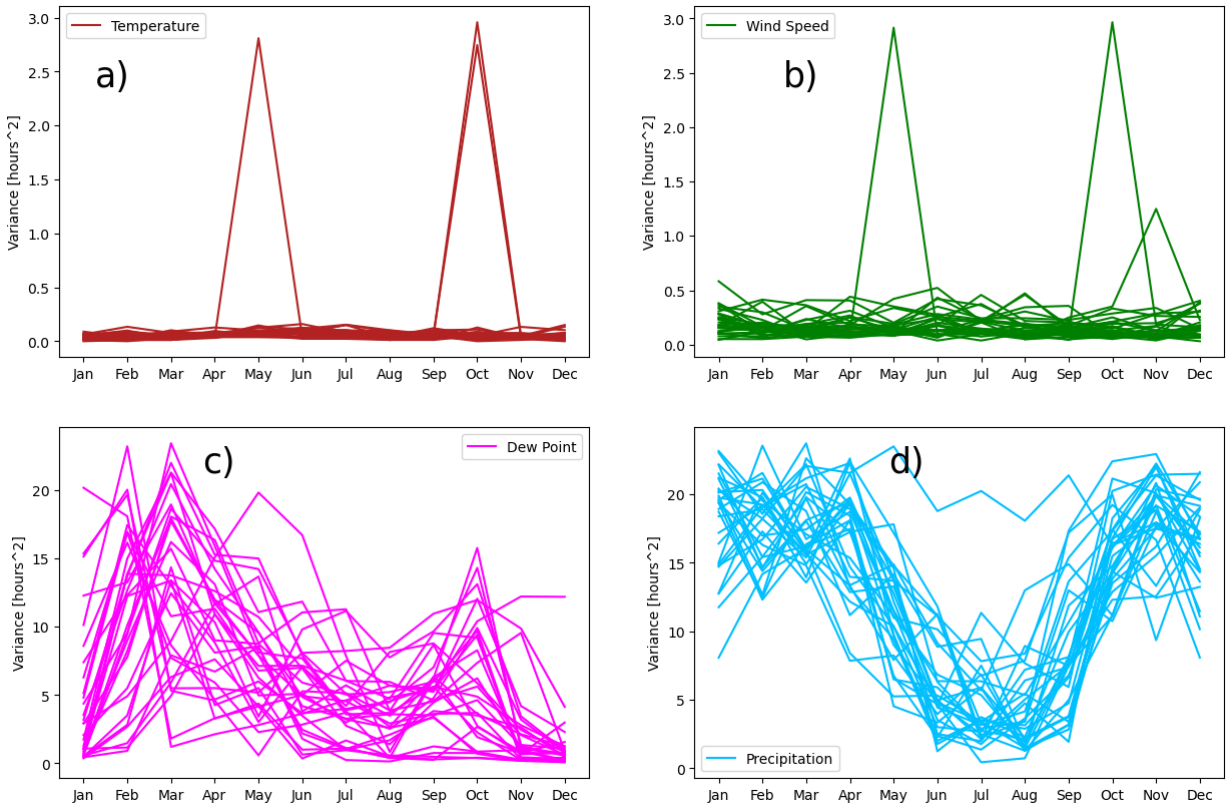

Figure 5.13. The variances of the phase (time of day) of the diurnal maxima of IMF5 (the diurnal component) of temperature (red), wind speed (green), dew point temperature (magenta), and precipitation (blue) during each month of the year. Each line represents one station.

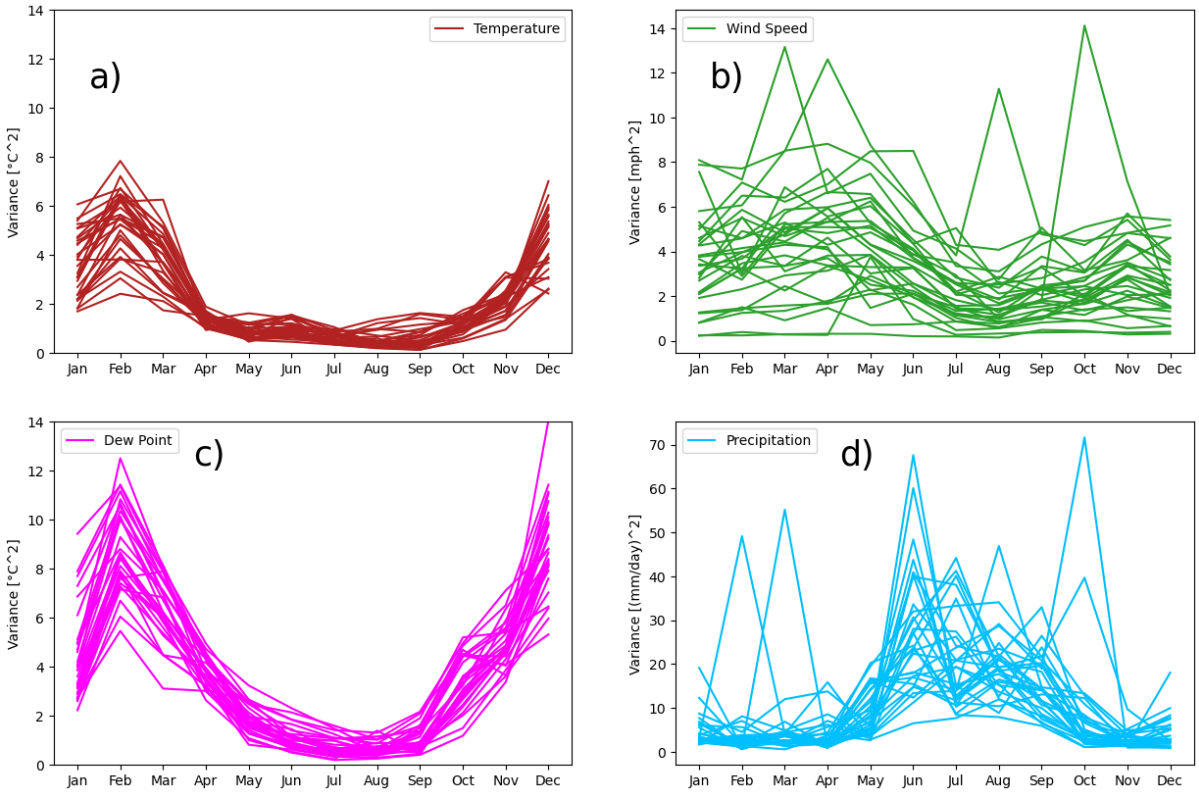

Figure 5.14. The variances of the amplitude of the diurnal maxima of IMF5 (the diurnal component) of temperature (red), wind speed (green), dew point temperature (magenta), and precipitation (blue) during each month of the year. Each line represents one station.

5.1.2 The semidiurnal mode + the diurnal mode (IMF4+IMF5)

The analyses for IMF4+IMF5 show that the climatological diurnal peak of temperature is in the early to mid-afternoon around 14:00 LST, and slightly earlier during summer. (Figures 5.1.15-26). This is slightly earlier than the results from IMF5 alone (Figures 5.1.1-12). The variance of the time of temperature's diurnal peak across the sixteen years 2005–2020 is very small for most stations and most months; only a few minutes (Figure 5.1.27a), which is consistent with the results from IMF5 alone (Figure 5.1.13a). The variance across 2005–2020 of the amplitude of temperature at its diurnal peak is small during summer and larger in winter (Figure 5.1.28a), which is also consistent with the results from IMF5 (Figure 5.1.14a).

In all months of the year and all regions of Florida, the diurnal phase and amplitude of wind speed from IMF4+IMF5 are nearly identical to those of IMF5 alone (Figures 5.1.15-26). For the IMF4+IMF5 analysis, the variance across 2005–2020 of the diurnal phase of wind speed is less than three square hours at all stations in all months (Figure 5.1.27b), which is consistent with the IMF5 analysis. Similarly, the variance of the amplitude of wind speed at its diurnal

maximum is lowest during August–December at most stations (Figure 5.1.28b), which is consistent with the IMF5 analysis.

The diurnal cycle of dew point temperature as represented by IMF4+IMF5 is generally like that of IMF5 alone. However, there are some differences. Notably, from the IMF4+IMF5 analysis, some stations have the diurnal maximum of dew point temperature overnight, whereas the diurnal maximum occurred during the day in the IMF5 counterpart. This is the case at stations in central Florida in February and March, and in north Florida in March, April, and May (Figures 5.1.16-19). In most months of the year, there are minor shifts (i.e., 1-3 hours) of the diurnal peak time of dew point temperature at a few stations. The only month that has no substantial differences between the IMF5 version and the IMF4+IMF5 version of the diurnal cycle of dew point temperature is June (Figure 5.1.20). The interannual variance of the diurnal phase of dew point temperature is higher at most stations in July—December in the IMF4+IMF5 analysis (Figure 5.1.27c) compared to the IMF5 analysis (Figure 5.1.13c). Surprisingly, there is a systematic shift in the climatological circular mean peak phase of dew point temperature during those months to be slightly earlier in the IMF4+IMF5 analysis (Figures 5.1.21-26) compared to the IMF5 analysis (Figures 5.1.7-12).

For precipitation, there are marked differences between the results of the analysis of IMF4+IMF5 and the analysis of IMF5 alone. Most notably, the interannual variance of the phase of precipitation during June--September is much higher at several stations in the IMF4+IMF5 analysis (Figure 5.1.27d) compared to that of the IMF5 analysis (Figure 5.1.13d). Therefore, the climatological circular means shown in Figures 5.1.20-23 become less meaningful. With that caveat in mind, the June-September circular means of the diurnal phase of precipitation from the IMF4+IMF5 analysis show minor (i.e., 1-3 hours) shifts (Figures 5.1.20-23) compared to those from the IMF5 analysis (Figures 5.1.6-9). In June, at several stations, the diurnal peak of precipitation occurs 2-3 hours later in the evening in the IMF4+IMF5 analysis (Figure 5.1.20) compared to the corresponding IMF5 analysis (Figure 5.1.6). In July, at several stations, the shift is only one hour later in the afternoon or evening in the IMF4+IMF5 analysis (Figure 5.1.21) compared to the IMF5 analysis (Figure 5.1.7). In August and September, the diurnal maximum of precipitation occurs about one hour earlier in the afternoon at several stations across Florida in the IMF4+IMF5 analysis (Figures 5.1.22-23) compared to the IMF5 analysis (Figures 5.1.7-8).

Additionally, the summertime diurnal maximum amplitude of precipitation is suppressed in the IMF4+IMF5 analysis (Figure 5.1.28d) compared to the IMF5 analysis (Figure 5.1.14d).

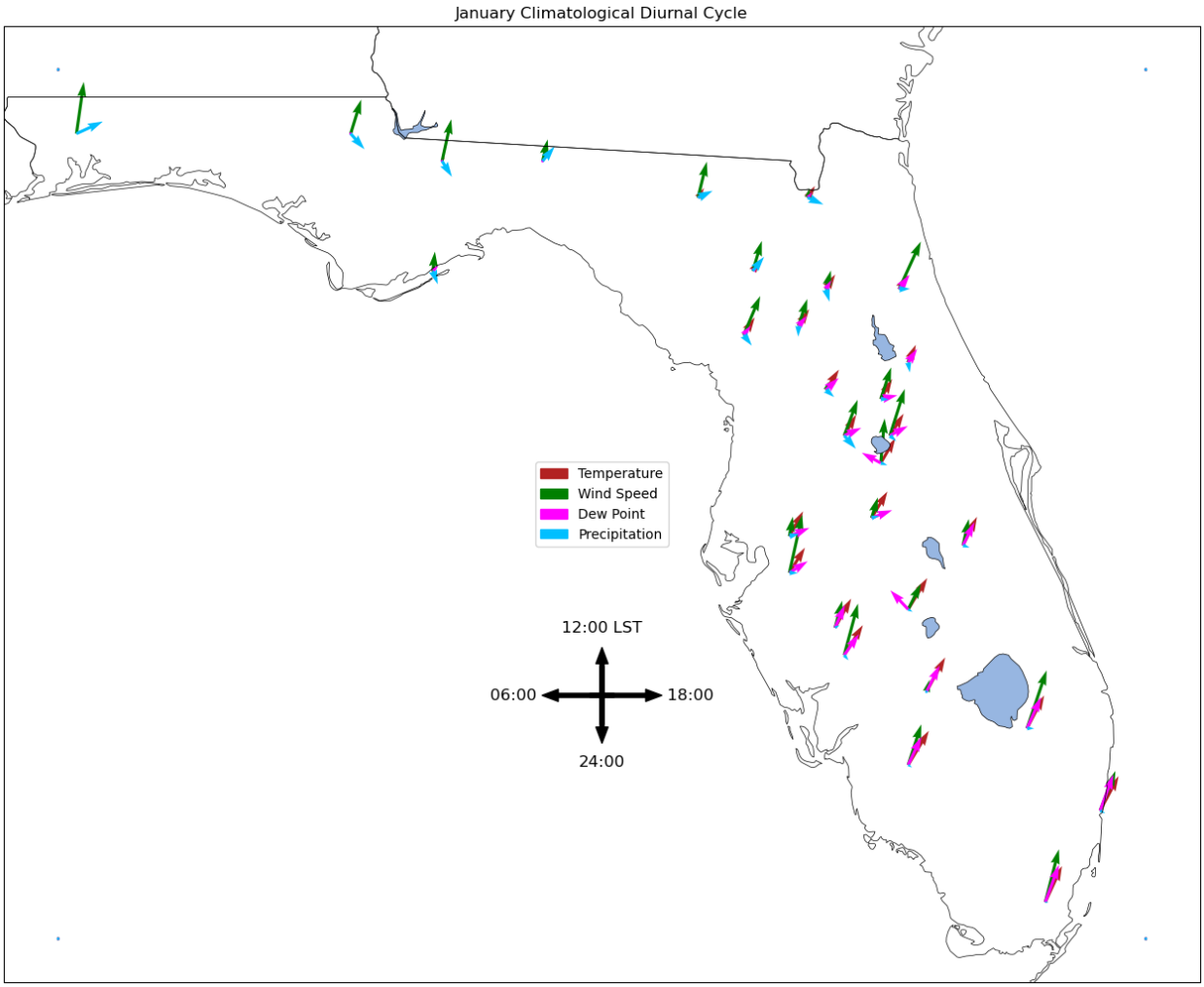

Figure 5.15. The January climatological phase (direction of arrow; Local Solar Time) and amplitude (length of arrow) of the diurnal maxima of surface temperature (red), wind speed (green), dew point temperature (magenta), and precipitation (blue) from the sum of the semidiurnal and diurnal components (IMF4+IMF5).

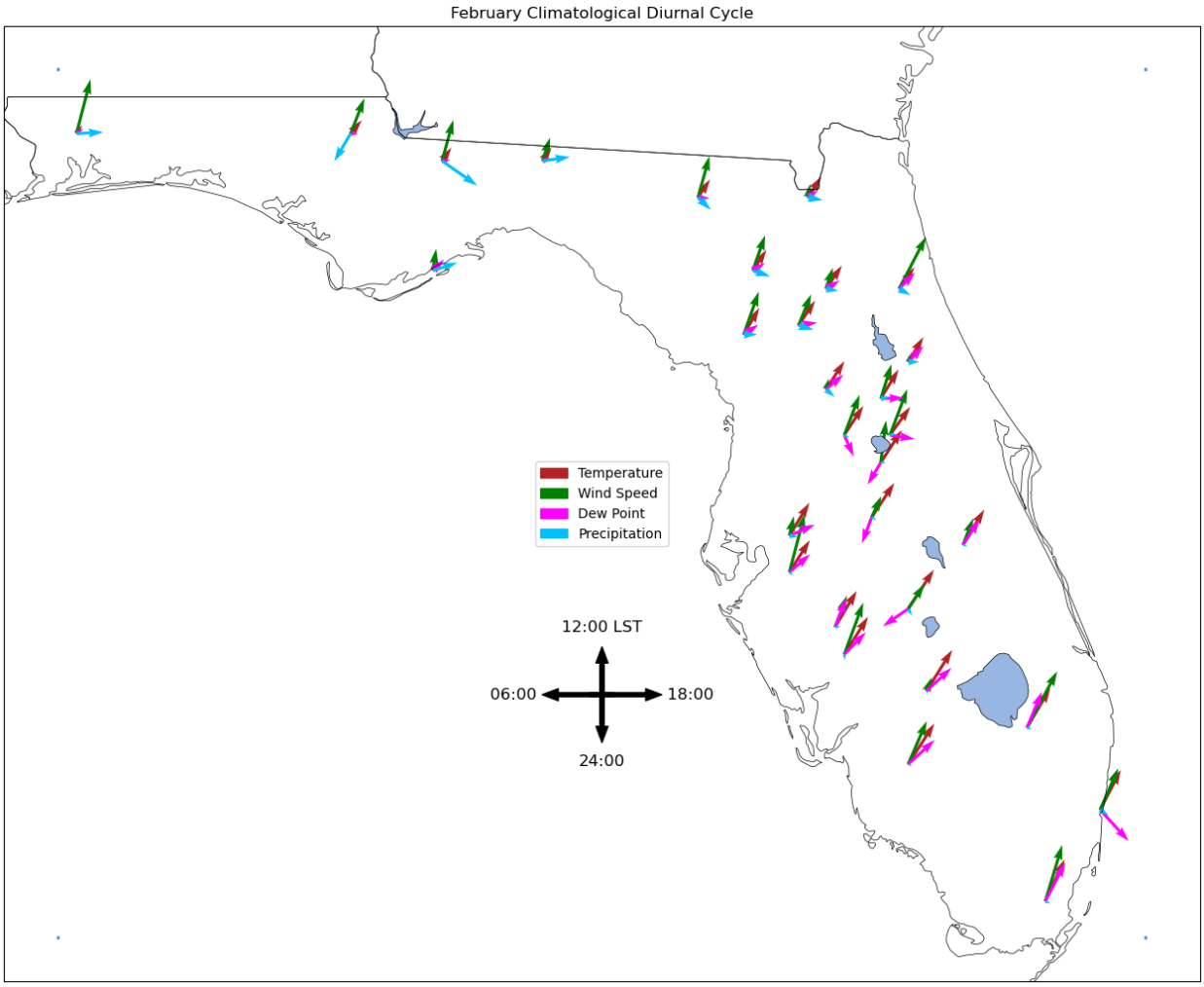

Figure 5.16. The February climatological phase (direction of arrow; Local Solar Time) and amplitude (length of arrow) of the diurnal maxima of surface temperature (red), wind speed (green), dew point temperature (magenta), and precipitation (blue) from the sum of the semidiurnal and diurnal components (IMF4+IMF5).

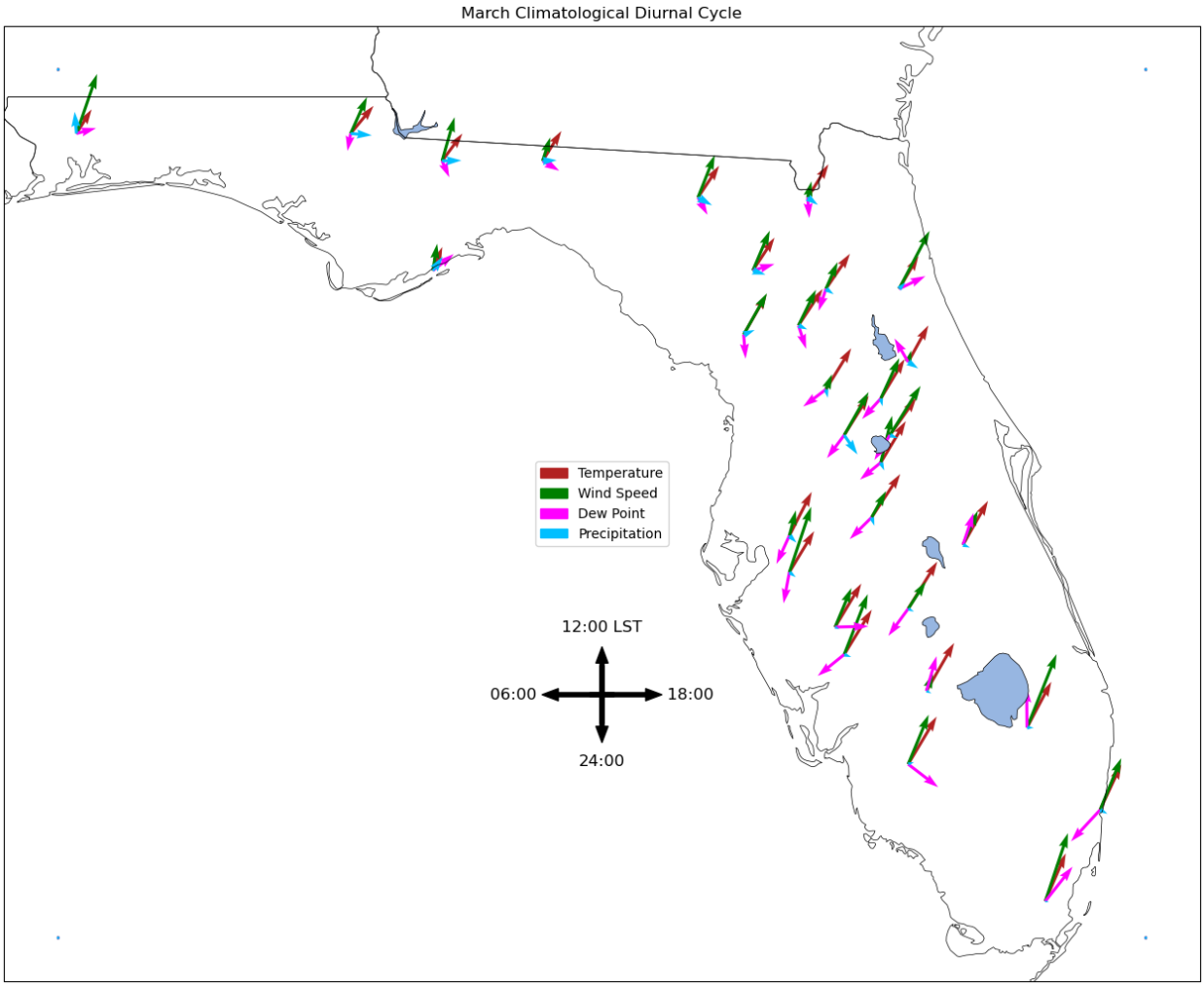

Figure 5.17. The March climatological phase (direction of arrow; Local Solar Time) and amplitude (length of arrow) of the diurnal maxima of surface temperature (red), wind speed (green), dew point temperature (magenta), and precipitation (blue) from the sum of the semidiurnal and diurnal components (IMF4+IMF5).

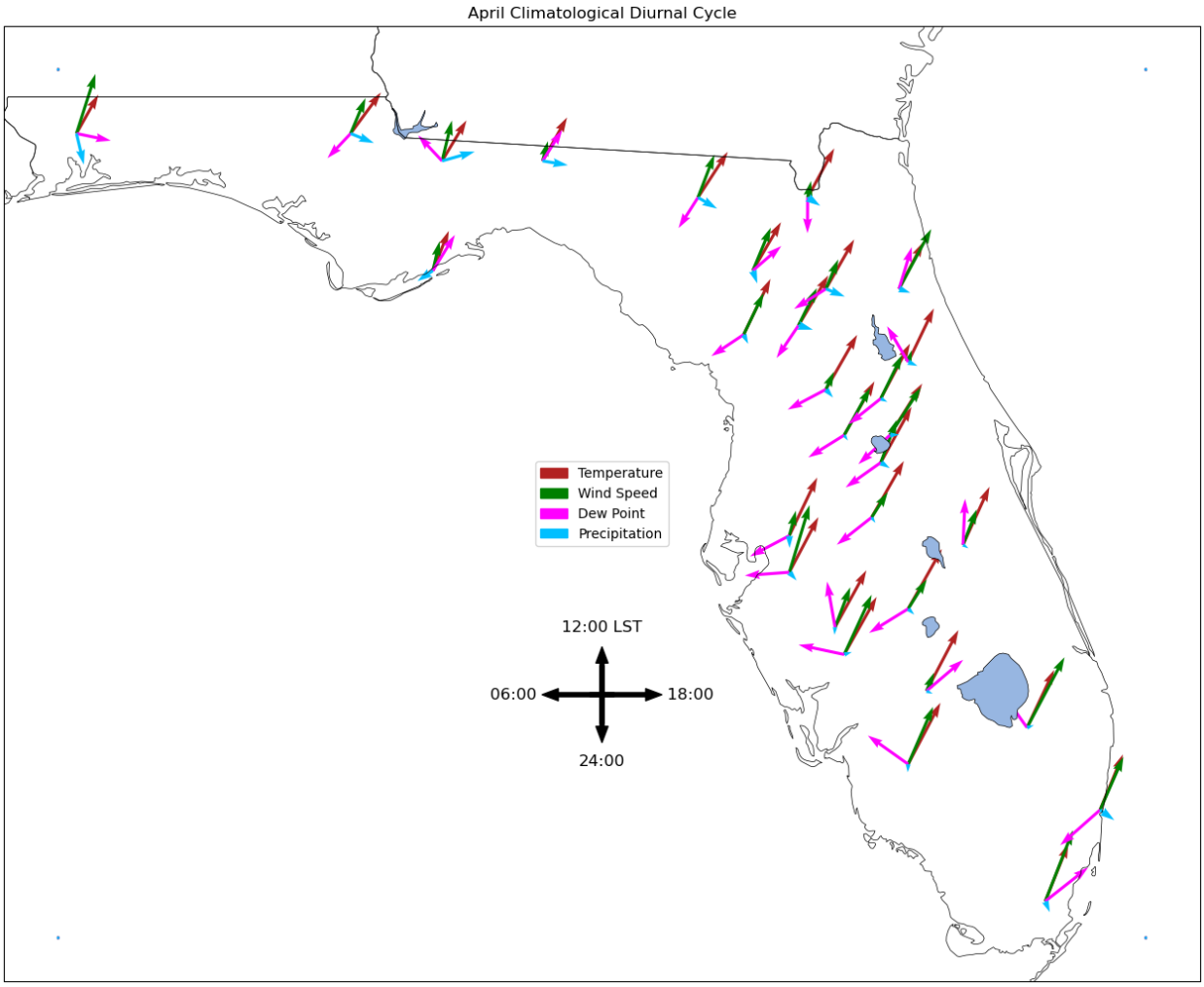

Figure 5.18. The April climatological phase (direction of arrow; Local Solar Time) and amplitude (length of arrow) of the diurnal maxima of surface temperature (red), wind speed (green), dew point temperature (magenta), and precipitation (blue) from the sum of the semidiurnal and diurnal components (IMF4+IMF5).

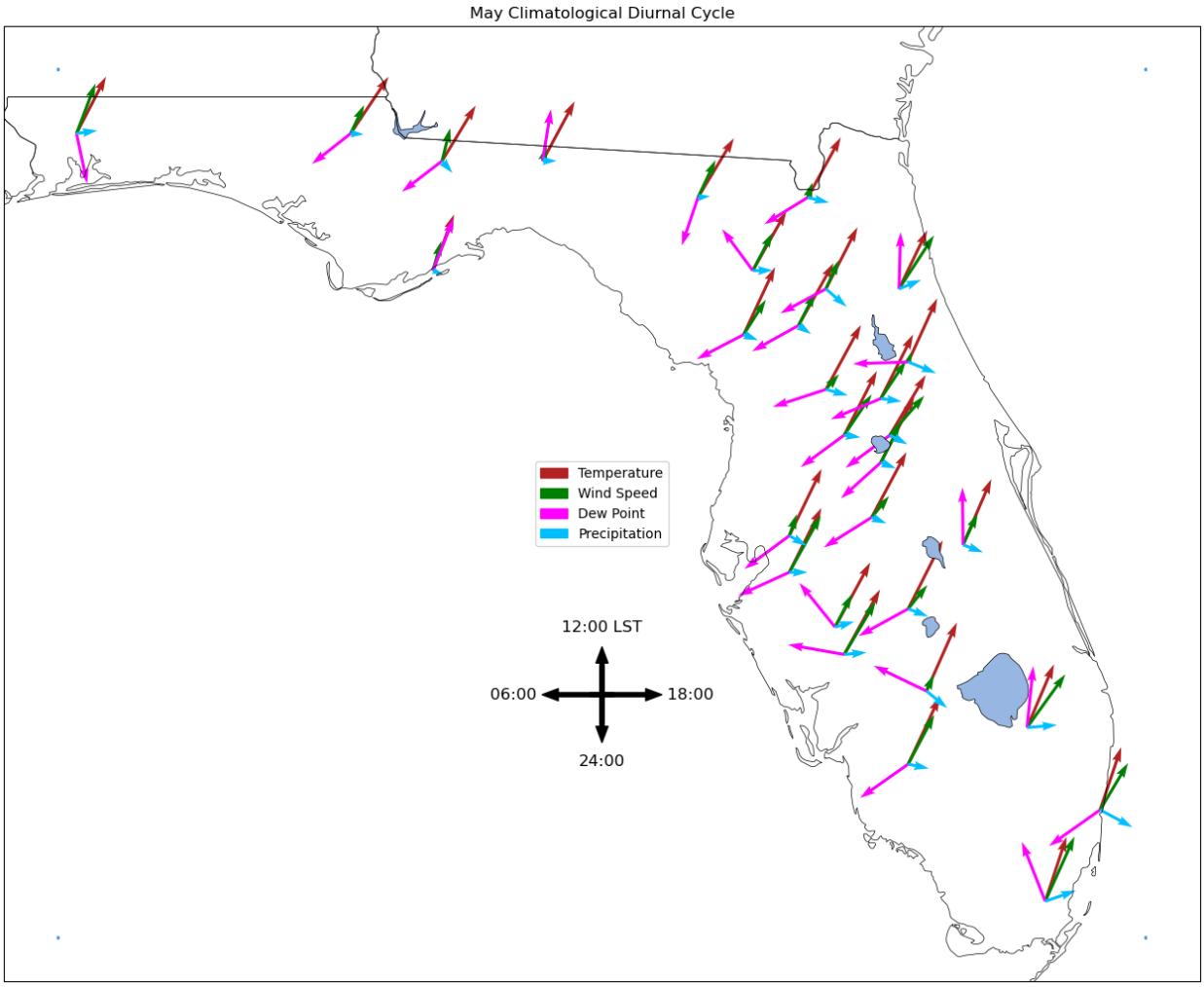

Figure 5.19. The May climatological phase (direction of arrow; Local Solar Time) and amplitude (length of arrow) of the diurnal maxima of surface temperature (red), wind speed (green), dew point temperature (magenta), and precipitation (blue) from the sum of the semidiurnal and diurnal components (IMF4+IMF5).

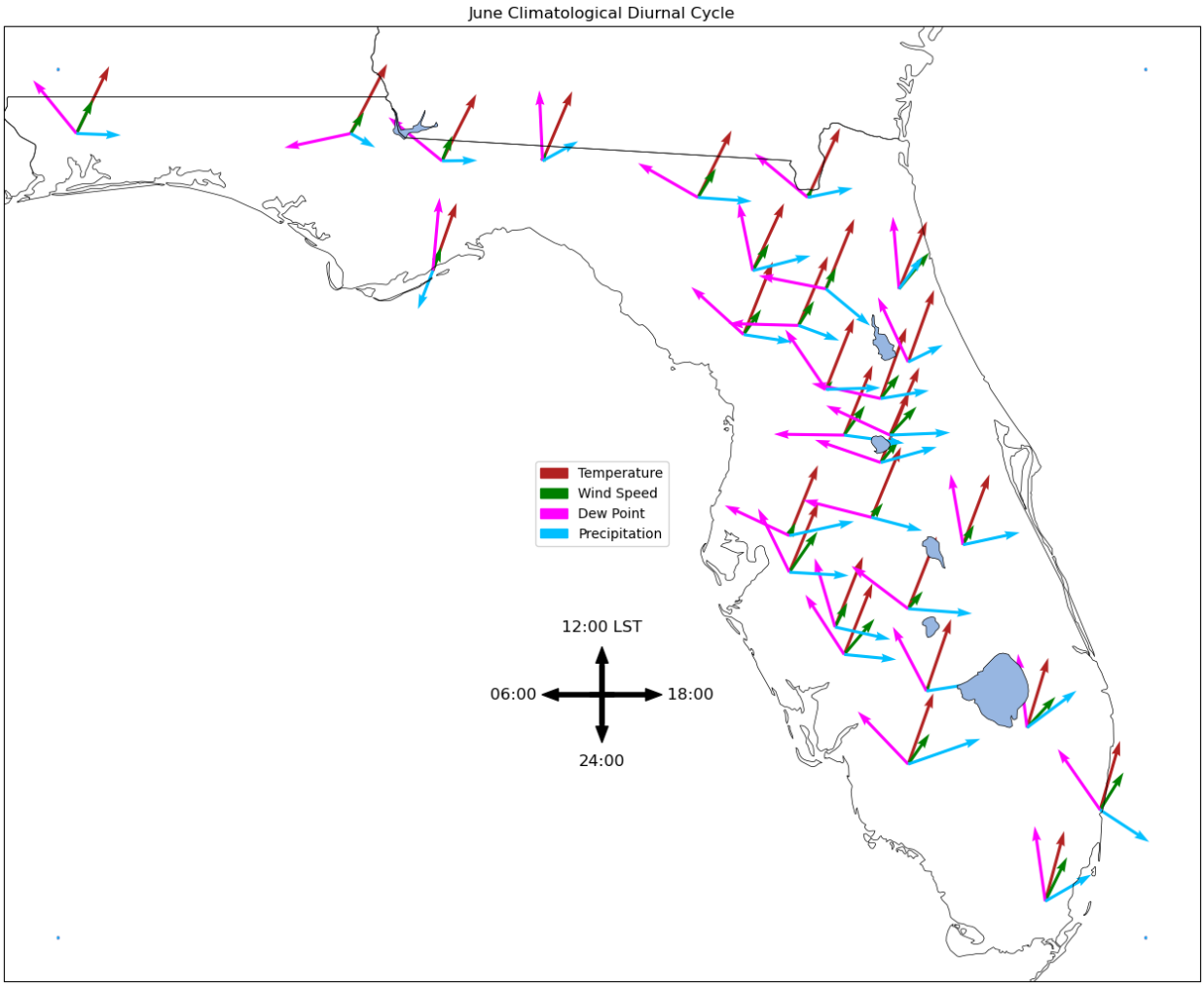

Figure 5.20. The June climatological phase (direction of arrow; Local Solar Time) and amplitude (length of arrow) of the diurnal maxima of surface temperature (red), wind speed (green), dew point temperature (magenta), and precipitation (blue) from the sum of the semidiurnal and diurnal components (IMF4+IMF5).

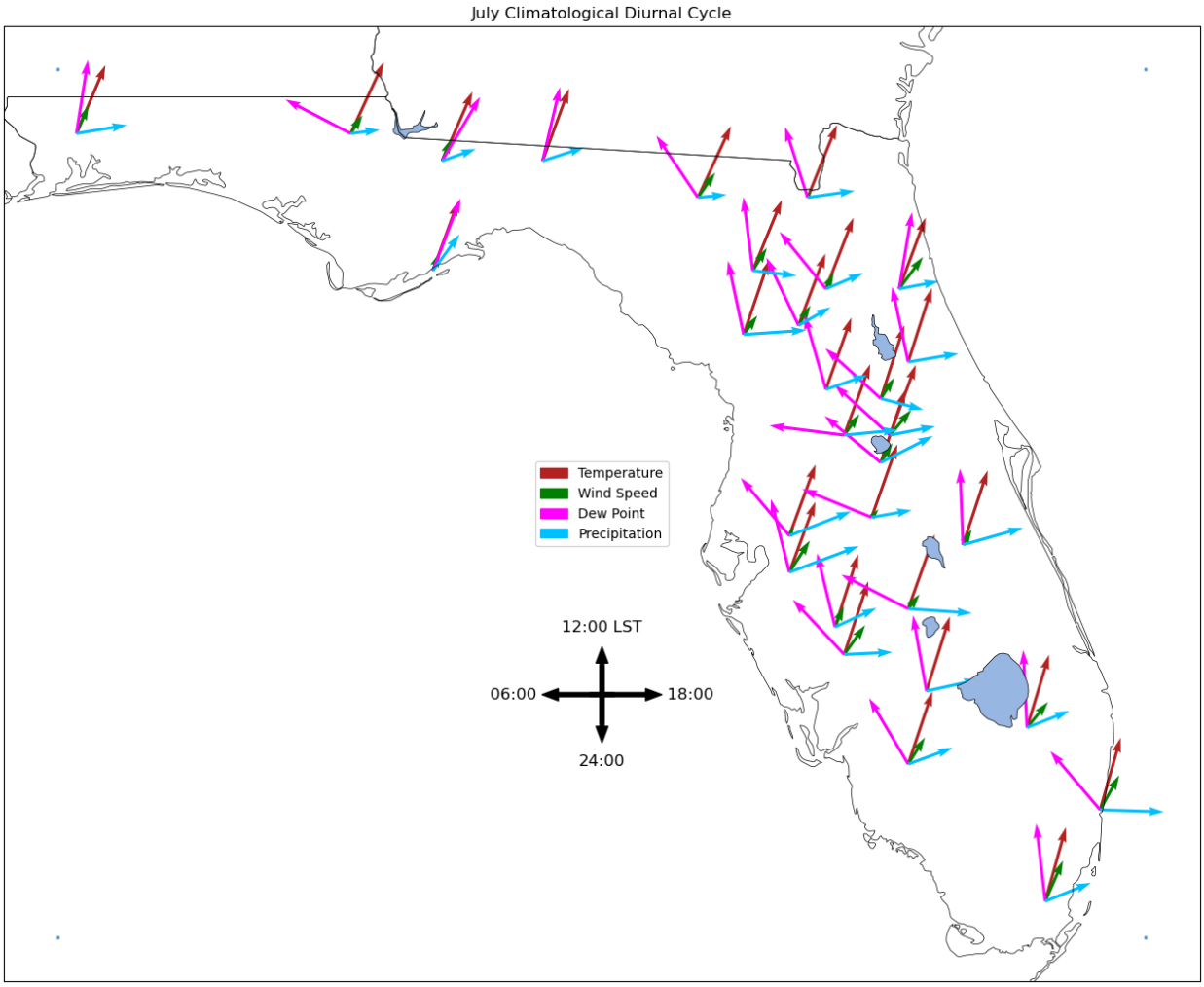

Figure 5.21. The July climatological phase (direction of arrow; Local Solar Time) and amplitude (length of arrow) of the diurnal maxima of surface temperature (red), wind speed (green), dew point temperature (magenta), and precipitation (blue) from the sum of the semidiurnal and diurnal components (IMF4+IMF5).

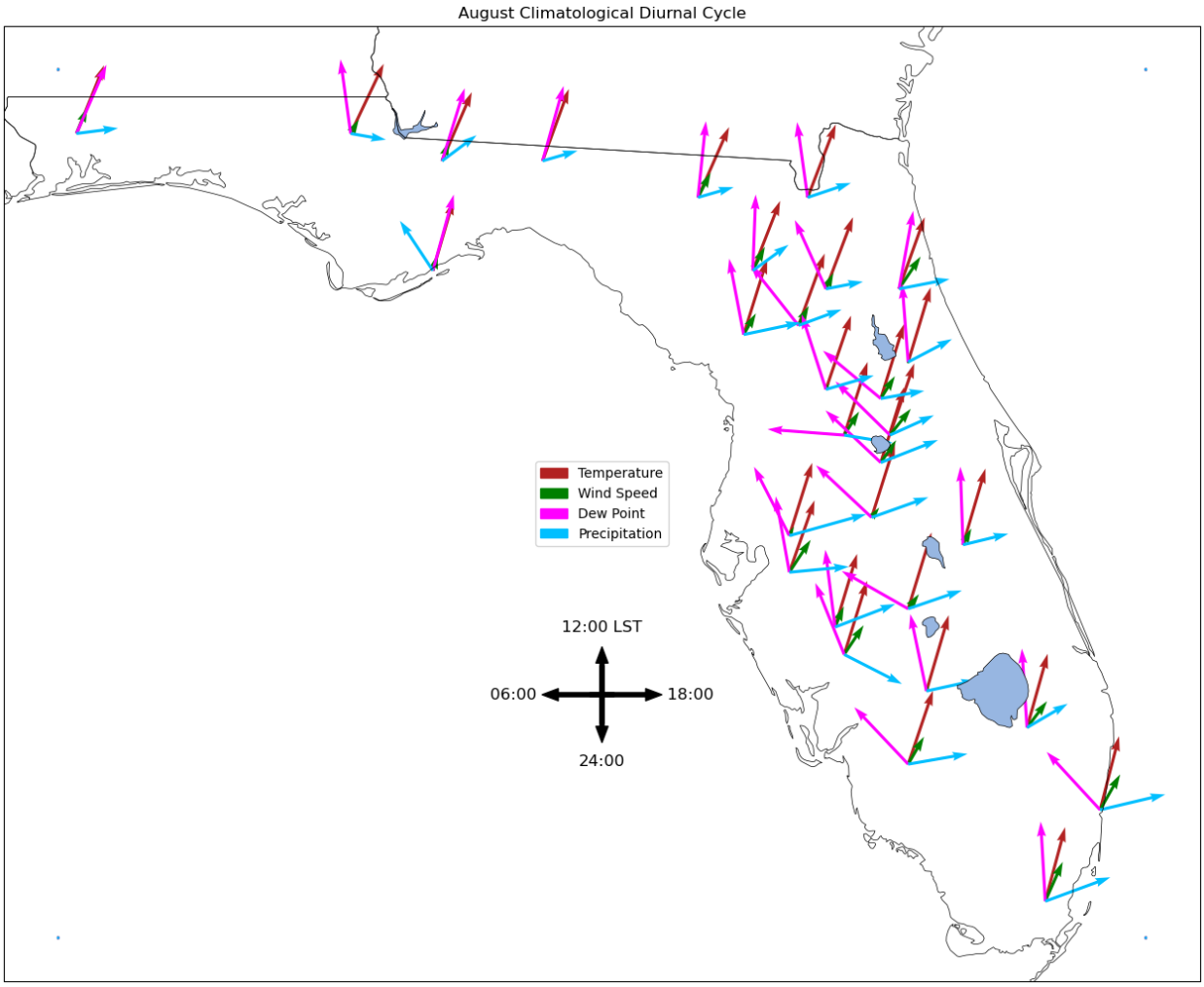

Figure 5.22. The August climatological phase (direction of arrow; Local Solar Time) and amplitude (length of arrow) of the diurnal maxima of surface temperature (red), wind speed (green), dew point temperature (magenta), and precipitation (blue) from the sum of the semidiurnal and diurnal components (IMF4+IMF5).

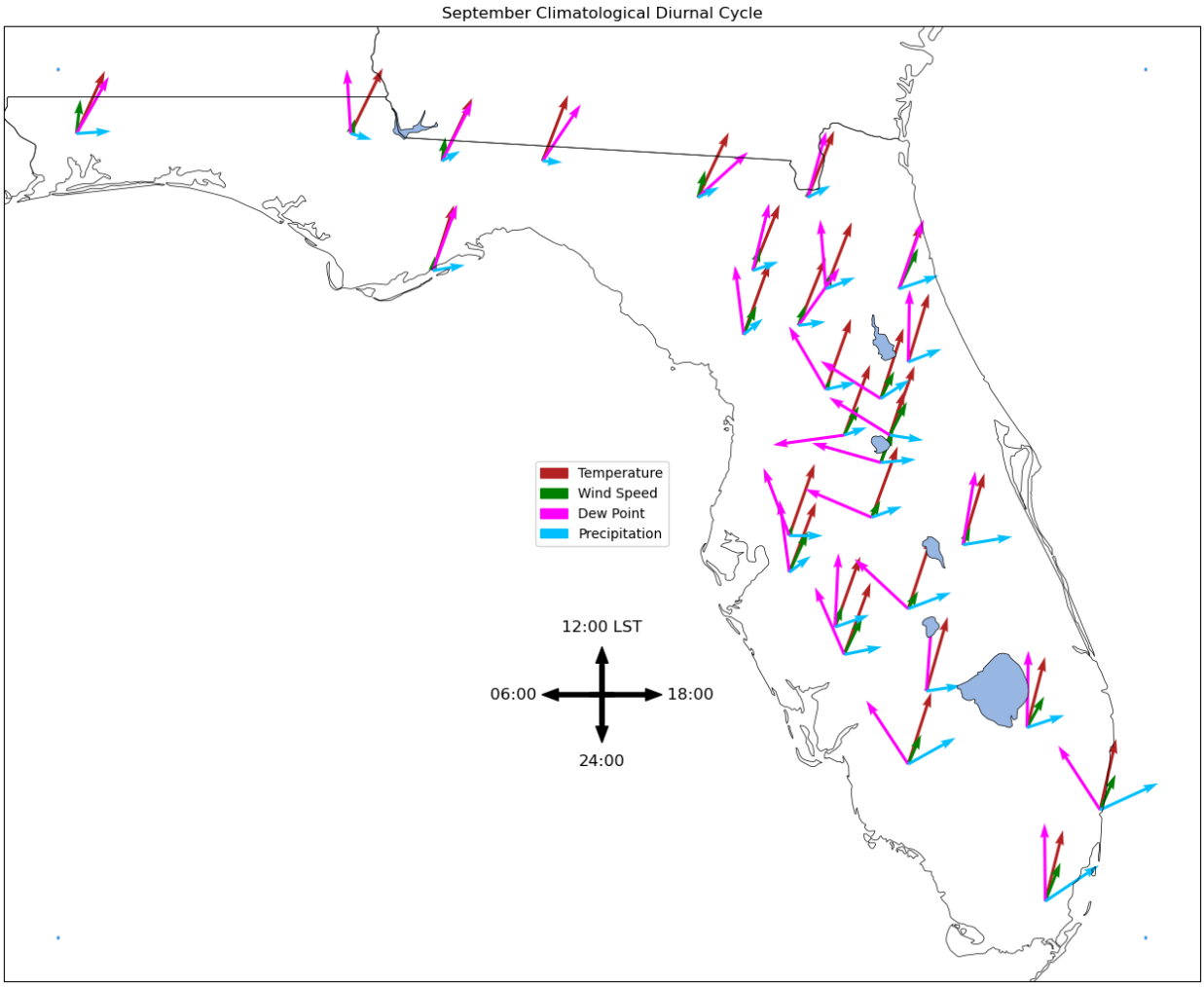

Figure 5.23. The September climatological phase (direction of arrow; Local Solar Time) and amplitude (length of arrow) of the diurnal maxima of surface temperature (red), wind speed (green), dew point temperature (magenta), and precipitation (blue) from the sum of the semidiurnal and diurnal components (IMF4+IMF5).

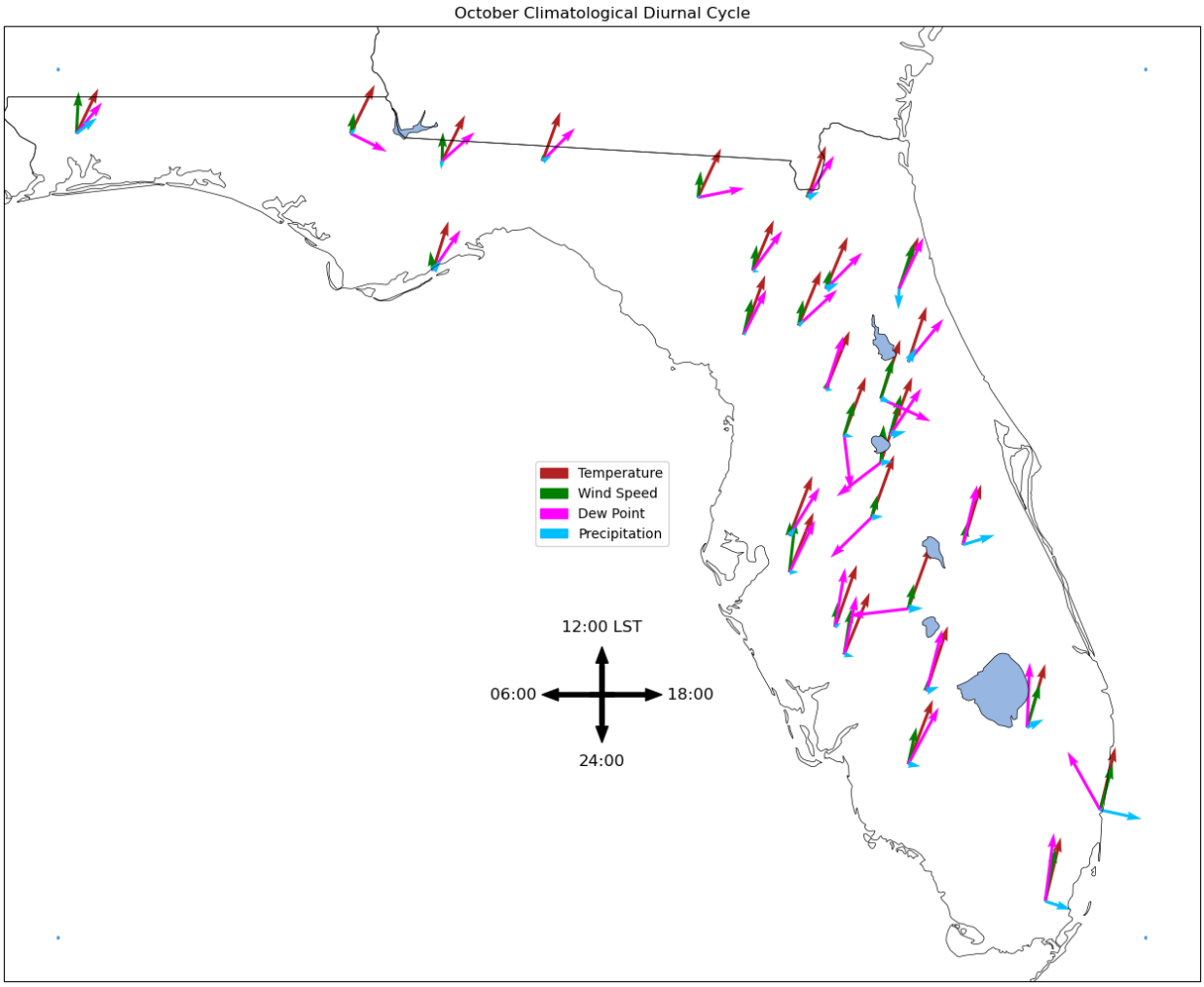

Figure 5.24. The October climatological phase (direction of arrow; Local Solar Time) and amplitude (length of arrow) of the diurnal maxima of surface temperature (red), wind speed (green), dew point temperature (magenta), and precipitation (blue) from the sum of the semidiurnal and diurnal components (IMF4+IMF5).

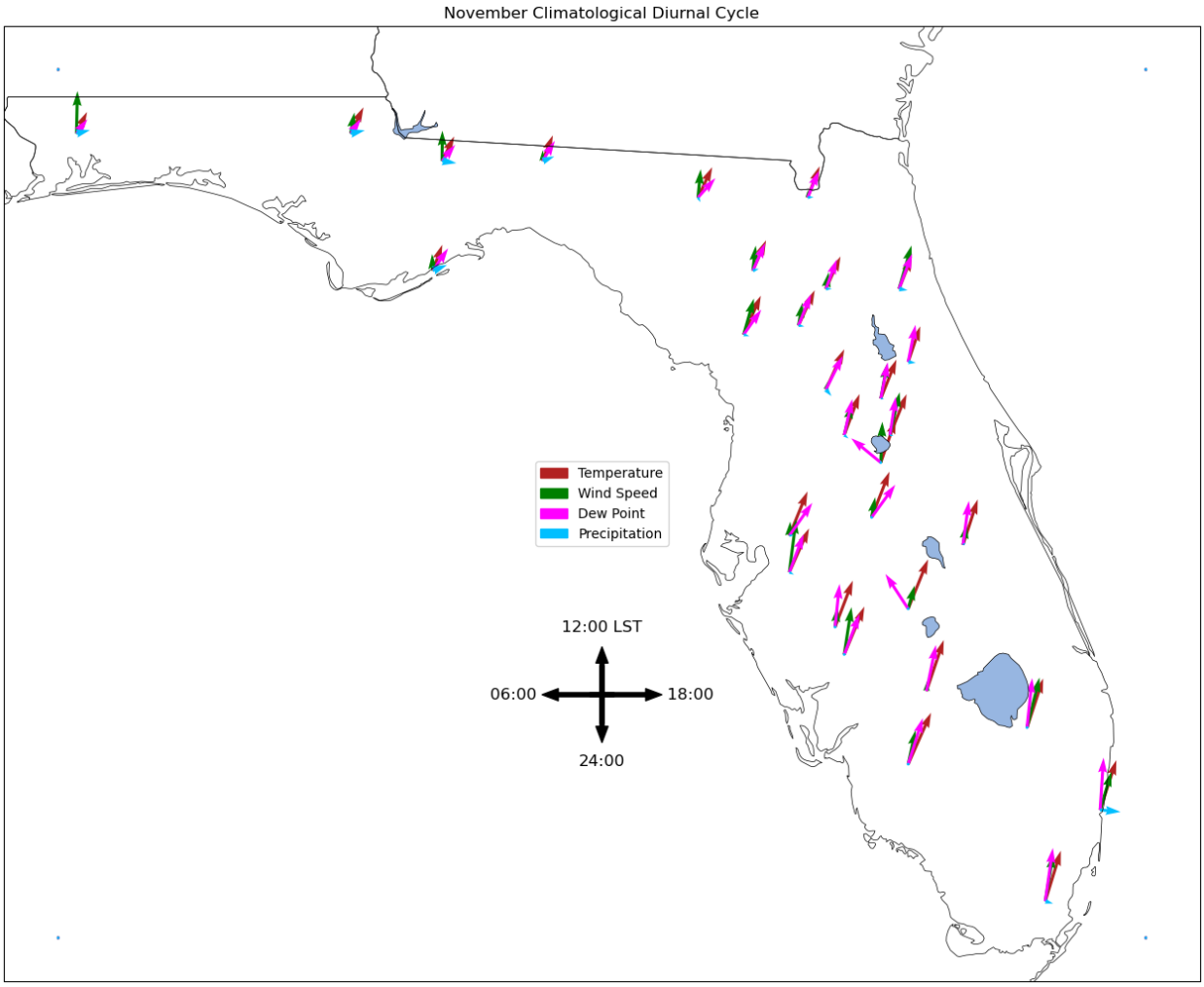

Figure 5.25. The November climatological phase (direction of arrow; Local Solar Time) and amplitude (length of arrow) of the diurnal maxima of surface temperature (red), wind speed (green), dew point temperature (magenta), and precipitation (blue) from the sum of the semidiurnal and diurnal components (IMF4+IMF5).

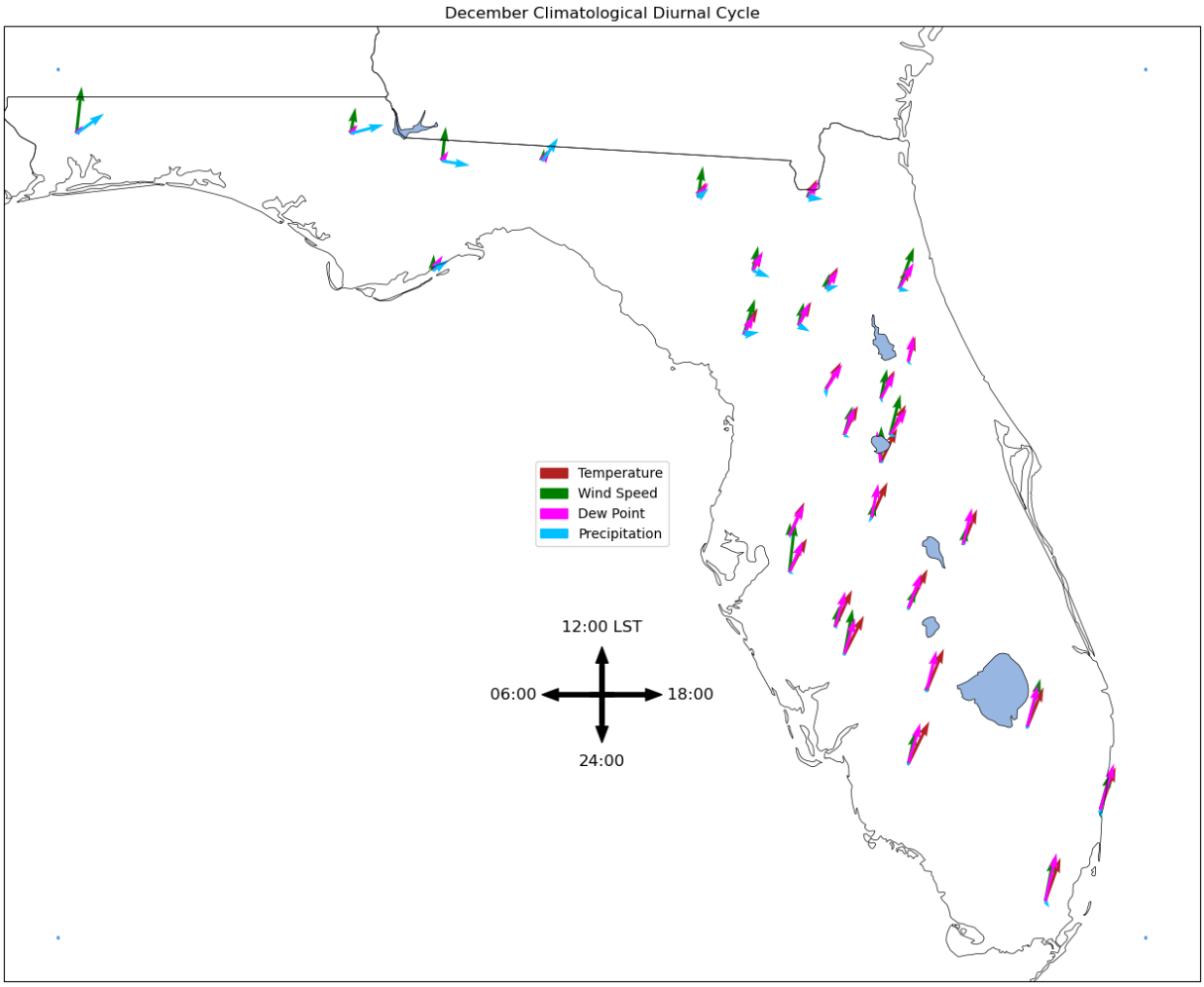

Figure 5.26. The December climatological phase (direction of arrow; Local Solar Time) and amplitude (length of arrow) of the diurnal maxima of surface temperature (red), wind speed (green), dew point temperature (magenta), and precipitation (blue) from the sum of the semidiurnal and diurnal components (IMF4+IMF5).

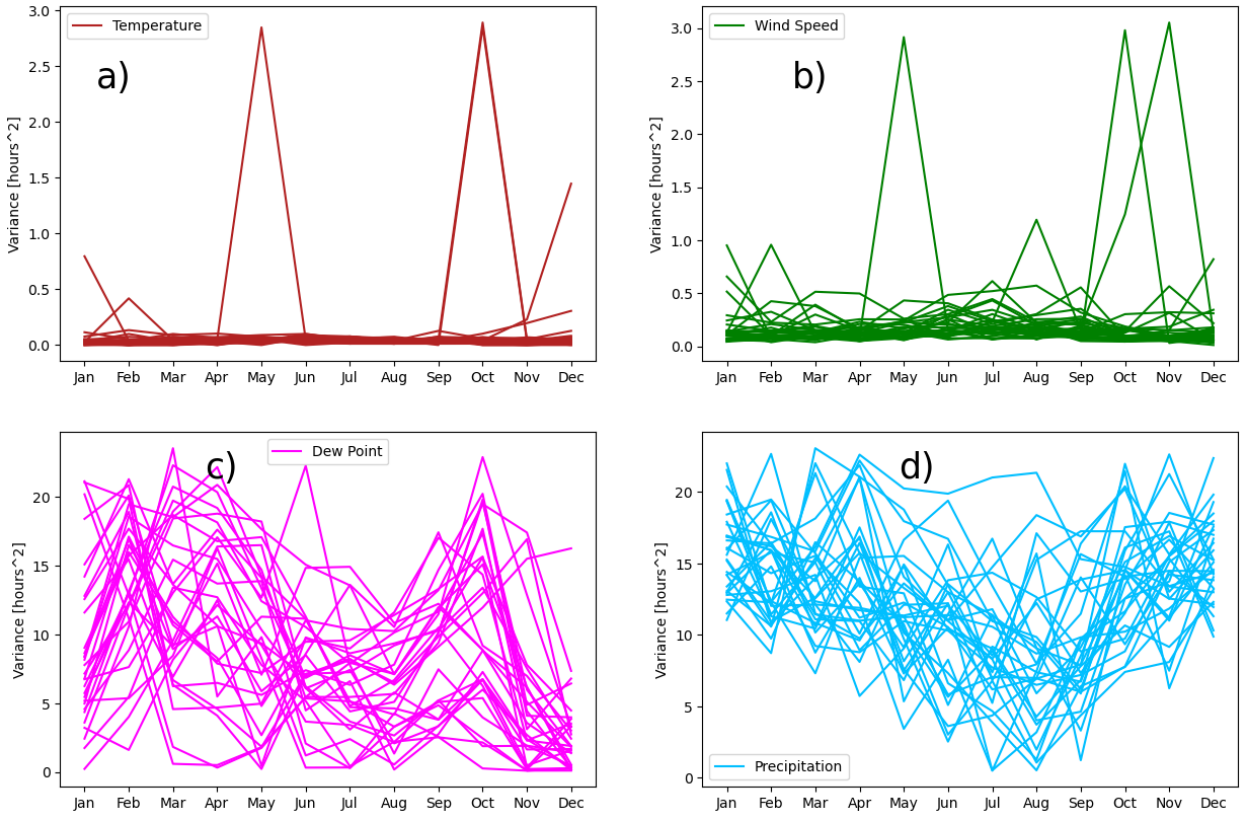

Figure 5.27. The variances of the phase (time of day) of the diurnal maxima of IMF4+IMF5 (the sum of the semidiurnal and diurnal components) of temperature (red), wind speed (green), dew point temperature (magenta), and precipitation (blue) during each month of the year. Each line represents one station.

.

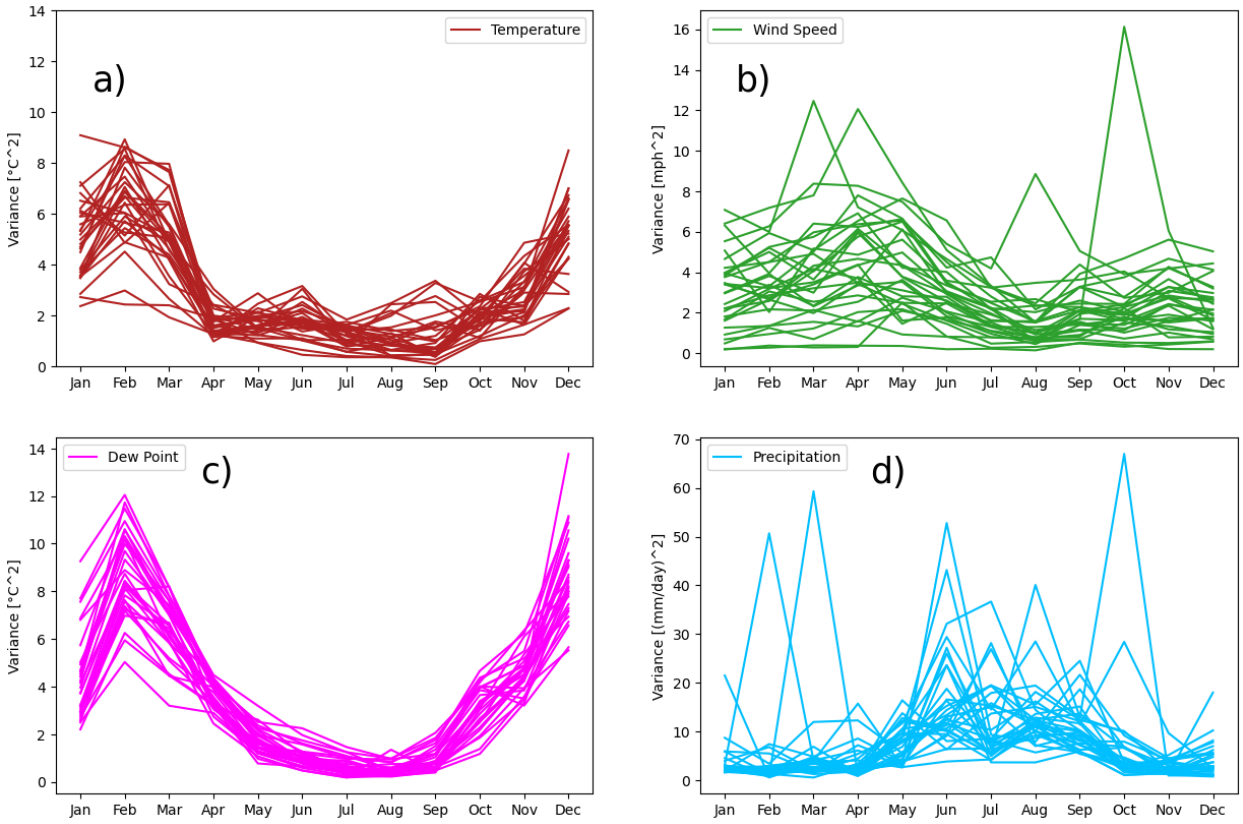

Figure 5.28. The variances of the amplitude of the diurnal maxima of IMF4+IMF5 (the sum of the semidiurnal and diurnal components) of temperature (red), wind speed (green), dew point temperature (magenta), and precipitation (blue) during each month of the year. Each line represents one station.

5.2 Validating FLAReS1.0 on the diurnal cycle of surface meteorology in Florida

5.2.1 The diurnal amplitude

The diurnal maximum amplitude of surface temperature is very well-represented by FLAReS1.0 at western Florida panhandle stations (Jay, Marianna, Quincy, and Carabelle; Figure 5.2.1). At each of these stations, RMSE is less than 1.4°C and correlation is greater than 0.99. The diurnal maximum amplitude of surface temperature is also very well-represented at the coastal south Florida stations (Homestead and Ft. Lauderdale), with correlations above 0.95 and RMSE less than 1.0°C (Figure 5.2.1). Overall, the diurnal maximum is well-represented across Florida in FLAReS1.0, although there is a cold bias of 1.76°C to 2.85°C at most stations (Figure 5.2.1). All correlation values are inflated by the ability of FLAReS1.0 to capture the annual cycle of surface temperature. The interannual variability of the diurnal peak amplitude of surface temperature validates well in FLAReS1.0 at all stations (Figure 5.2.2). However, at the western

Florida panhandle stations, FLAReS1.0 overestimates the interannual variability in December. The diurnal minimum temperature validates best in FLAReS1.0 at the central Florida stations Lake Alfred, Avalon, and Apopka, and the south Florida station Ft. Lauderdale, as the RMSE values are lowest at these stations (Figure 5.2.3). Across most of Florida, FLAReS1.0 has a warm bias for the diurnal minimum surface temperature throughout the annual cycle (Figure 5.2.3). At the western panhandle stations, FLAReS1.0 has a strong warm bias for diurnal minima of surface temperature in June—November (Figure 5.2.3). FLAReS1.0 captures the interannual variability of the diurnal minimum of surface temperature throughout the annual cycle (Figure 5.2.4).

The diurnal peak amplitude of dew point temperature validates very well in FLAReS1.0 (Figure 5.2.5). The correlation between the diurnal peak amplitudes in FLAReS1.0 and FAWN IMF5 is above 0.97 at every station across Florida. However, FLAReS1.0 tends to underestimate the diurnal peak amplitude of dew point temperature in summer, especially in August in north Florida (Figure 5.2.5). The interannual variability of the diurnal peak amplitude of dew point temperature is generally well-captured by FLAReS1.0, except that FLAReS1.0 does not reproduce the January dip in interannual variance of the diurnal peak amplitude of dew point temperature (Figure 5.3.6). As for the diurnal minimum amplitude of dew point temperature, FLAReS1.0 captures it very well in summer and fall across Florida. In January—March, however, FLAReS1.0 tends to have a moist bias when it comes to the diurnal minimum of dew point temperature (Figure 5.3.7). FLAReS1.0 generally does well to capture the interannual variability of the diurnal minimum amplitude of dew point temperature, although, again, FLAReS1.0 fails to capture the January dip in interannual variance of the amplitude of dew point temperature exhibited in the FAWN station observations (Figure 5.2.8).

In most regions of Florida, FLAreS1.0 captures the summertime increase in the diurnal amplitude of precipitation (Figure 5.2.9). Across most of Florida, the FLAReS1.0 reproduces the observed diurnal peak amplitudes of precipitation during summer and fall (Figure 5.2.9). However, in January—April, FLAReS1.0 overestimates the diurnal peak amplitude of precipitation across Florida (Figure 5.2.9). In south Florida, FLAReS1.0 also overestimates the diurnal peak amplitude of precipitation in summer (Figure 5.2.9).

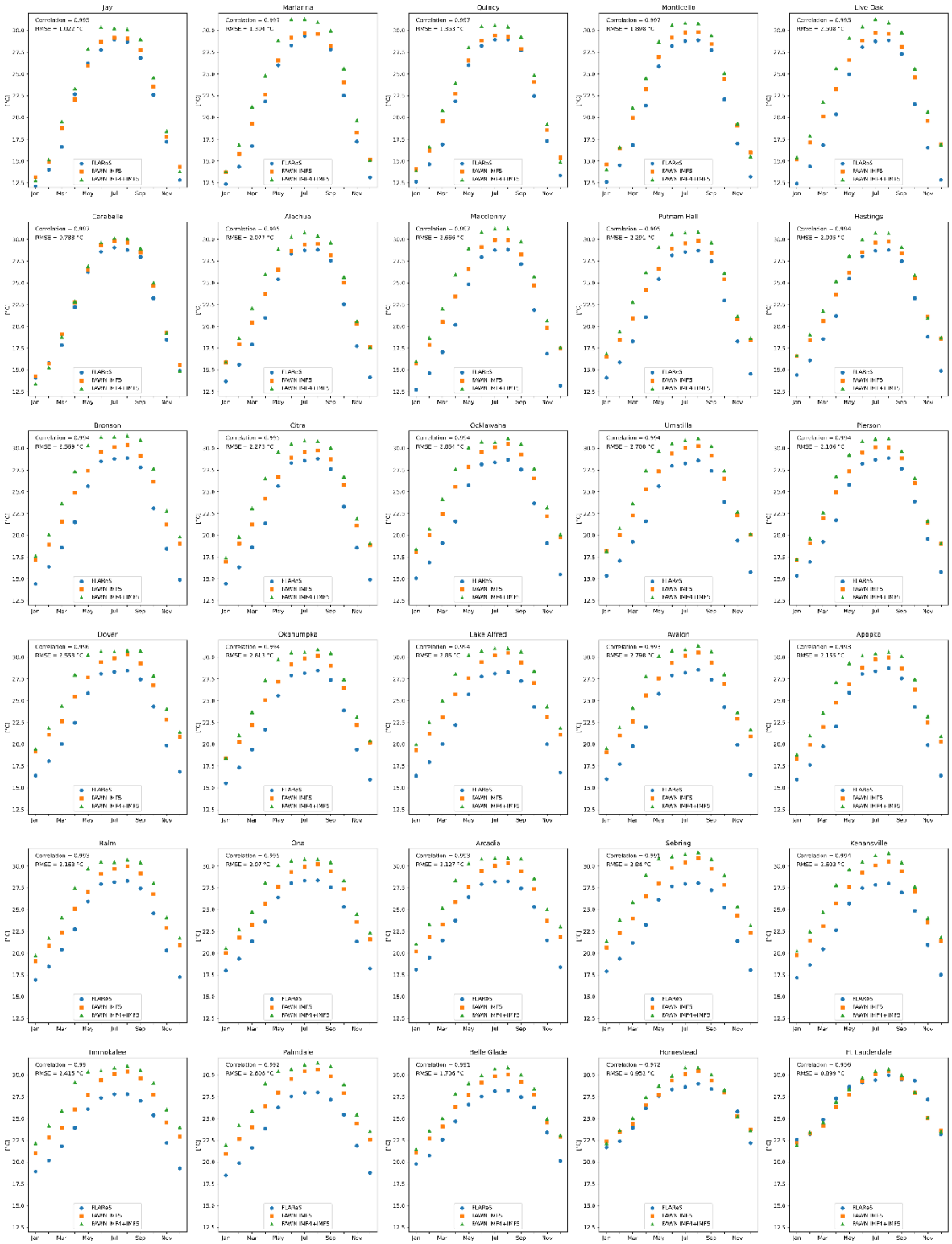

Figure 5.29. Diurnal peak amplitude of surface temperature in FAWN IMF5 (orange squares) and FAWN IMF4+IMF5 (green triangles) at 30 FAWN observational stations, and in FLAReS1.0 (blue circles) at the grid points closest to each FAWN station. The correlation and RMSE between the FLAReS1.0 diurnal amplitudes and the FAWN IMF5 diurnal amplitudes are listed in each panel.

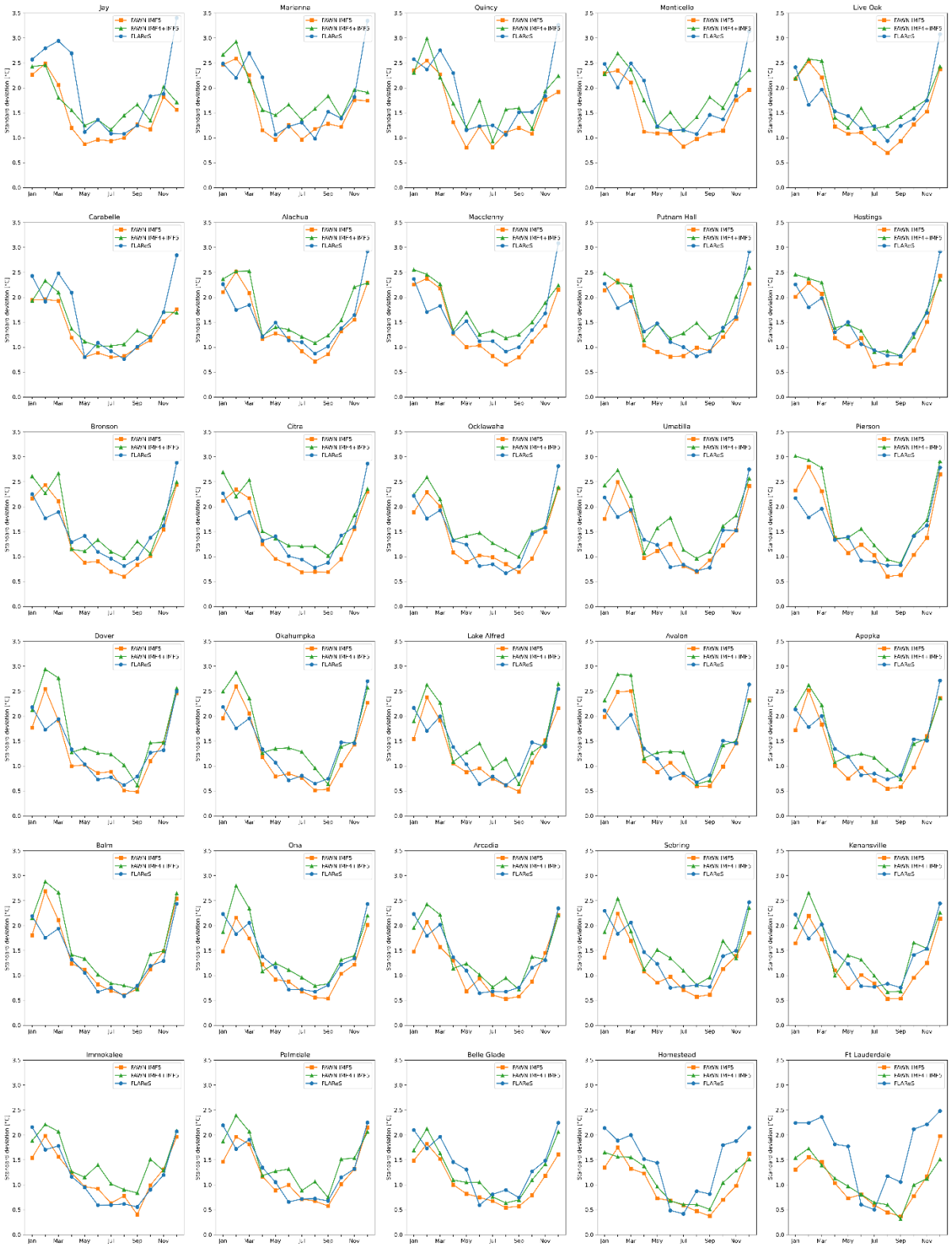

Figure 5.30. Standard deviations of the diurnal peak amplitude of surface temperature by month in FAWN IMF5 (orange squares) and FAWN IMF4+IMF5 (green triangles) at 30 FAWN observational stations, and in FLAReS1.0 (blue circles) at the grid points closest to each FAWN station.

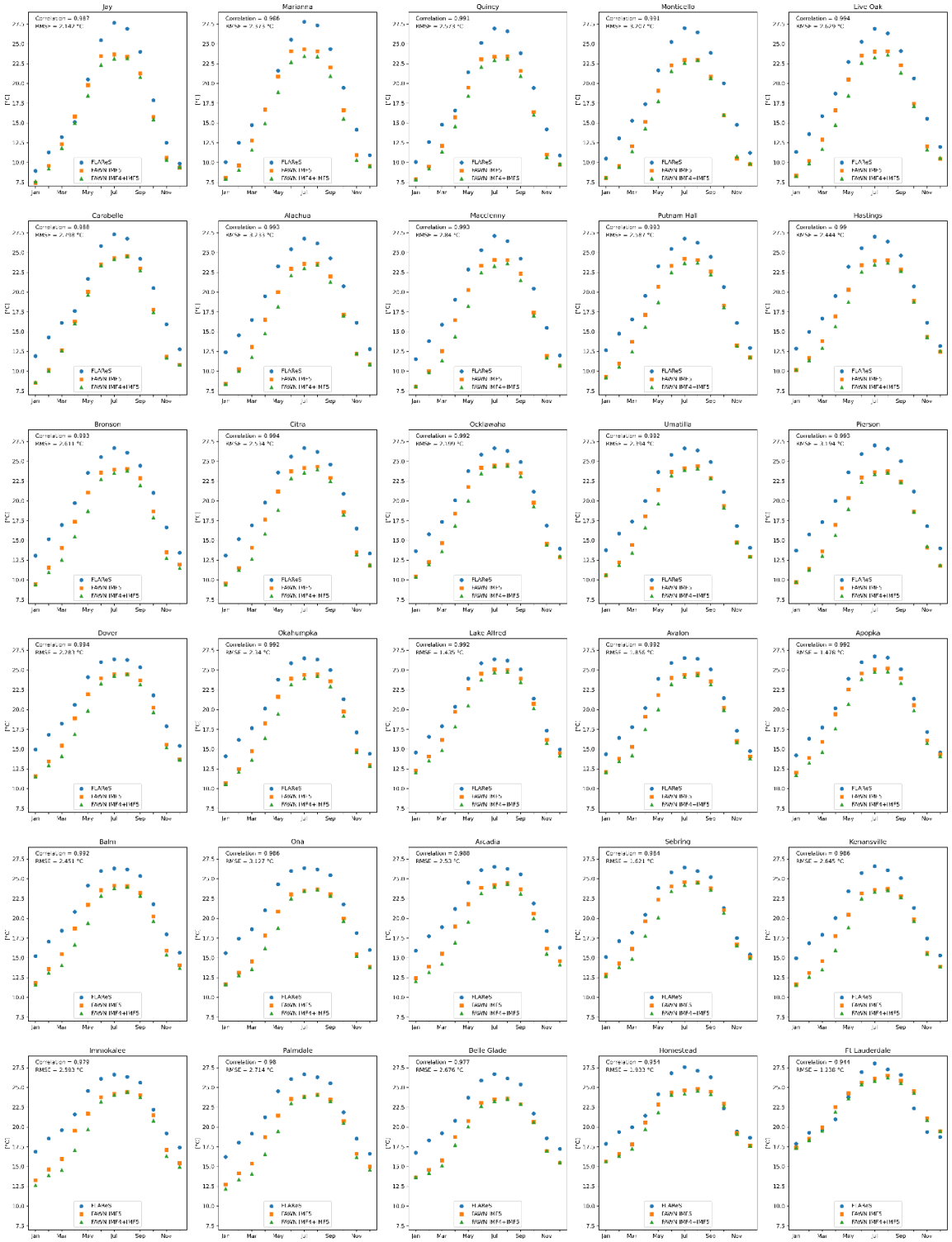

Figure 5.31. Diurnal minimum amplitude of surface temperature in FAWN IMF5 (orange squares) and FAWN IMF4+IMF5 (green triangles) at 30 FAWN observational stations, and in FLAReS1.0 (blue circles) at the grid points closest to each FAWN station. The correlation and RMSE between the FLAReS1.0 diurnal amplitudes and the FAWN IMF5 diurnal amplitudes are listed in each panel.

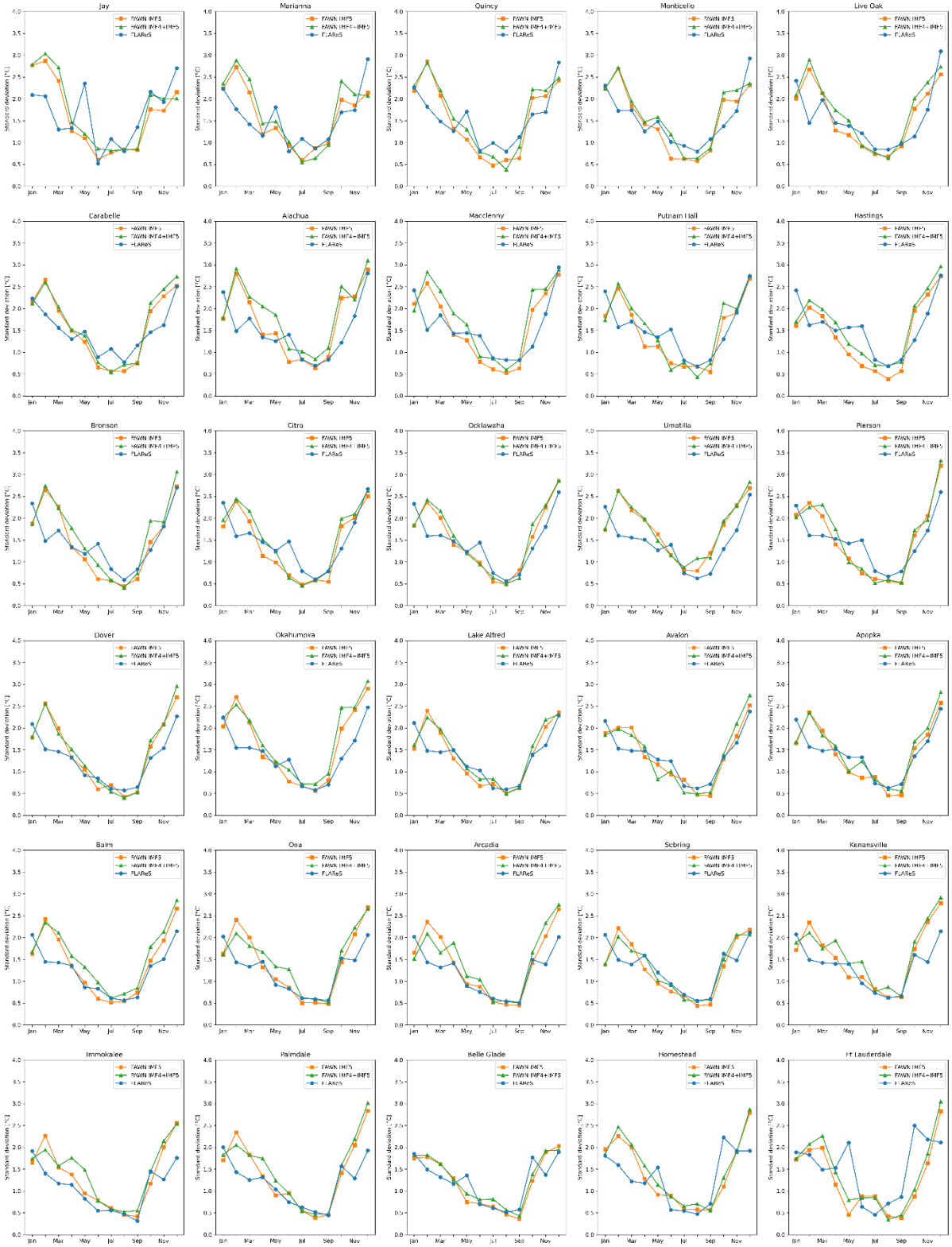

Figure 5.32. Standard deviations of the diurnal minimum amplitude of surface temperature by month in FAWN IMF5 (orange squares) and FAWN IMF4+IMF5 (green triangles) at 30 FAWN observational stations, and in FLAReS1.0 (blue circles) at the grid points closest to each FAWN station.

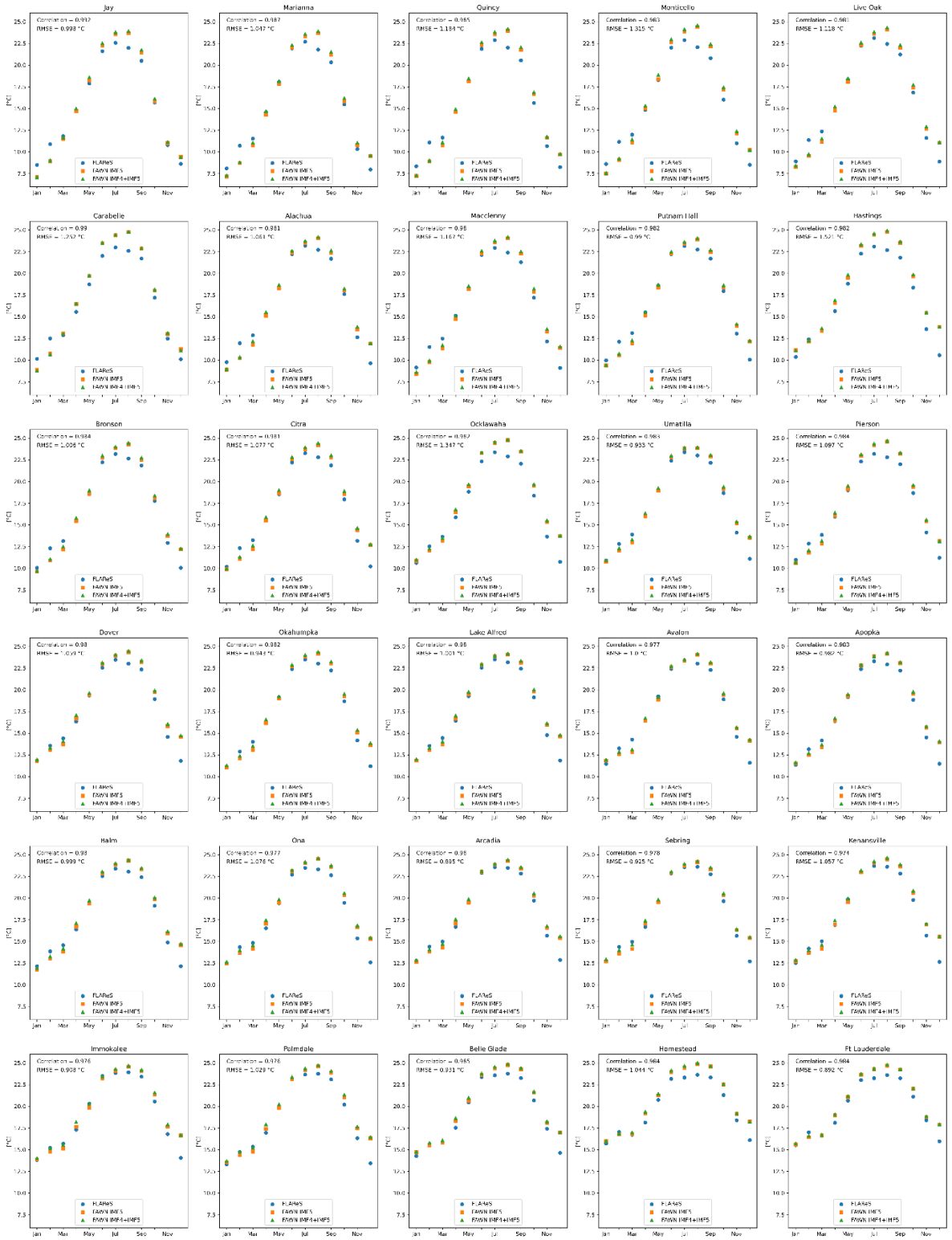

Figure 5.33. Diurnal peak amplitude of surface dew point temperature in FAWN IMF5 (orange squares) and FAWN IMF4+IMF5 (green triangles) at 30 FAWN observational stations, and in FLAReS1.0 (blue circles) at the grid points closest to each FAWN station. The correlation and RMSE between the FLAReS1.0 diurnal amplitudes and the FAWN IMF5 diurnal amplitudes are listed in each panel.

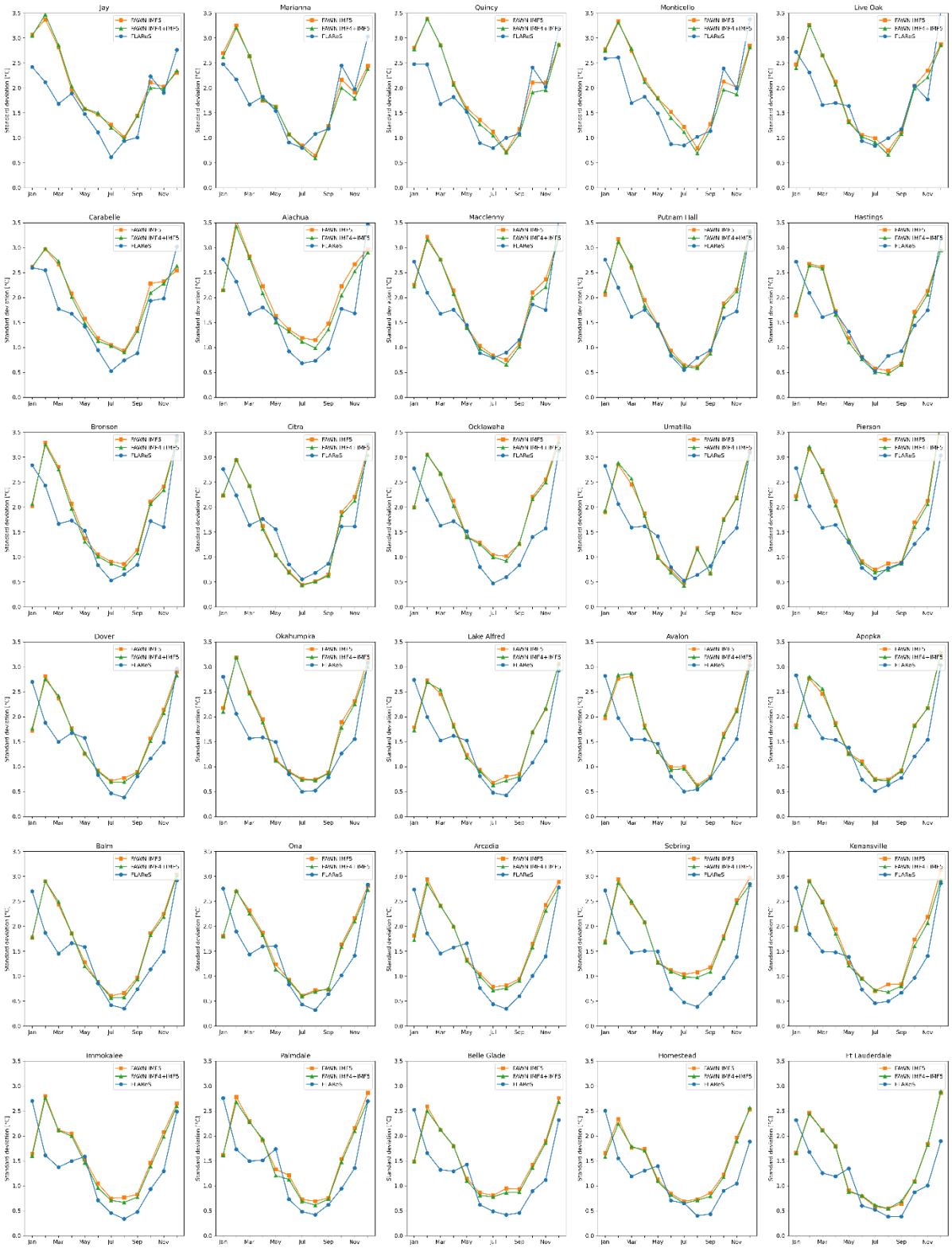

Figure 5.34. Standard deviations of the diurnal peak amplitude of surface dew point temperature by month in FAWN IMF5 (orange squares) and FAWN IMF4+IMF5 (green triangles) at 30 FAWN observational stations, and in FLAReS1.0 (blue circles) at the grid points closest to each FAWN station.

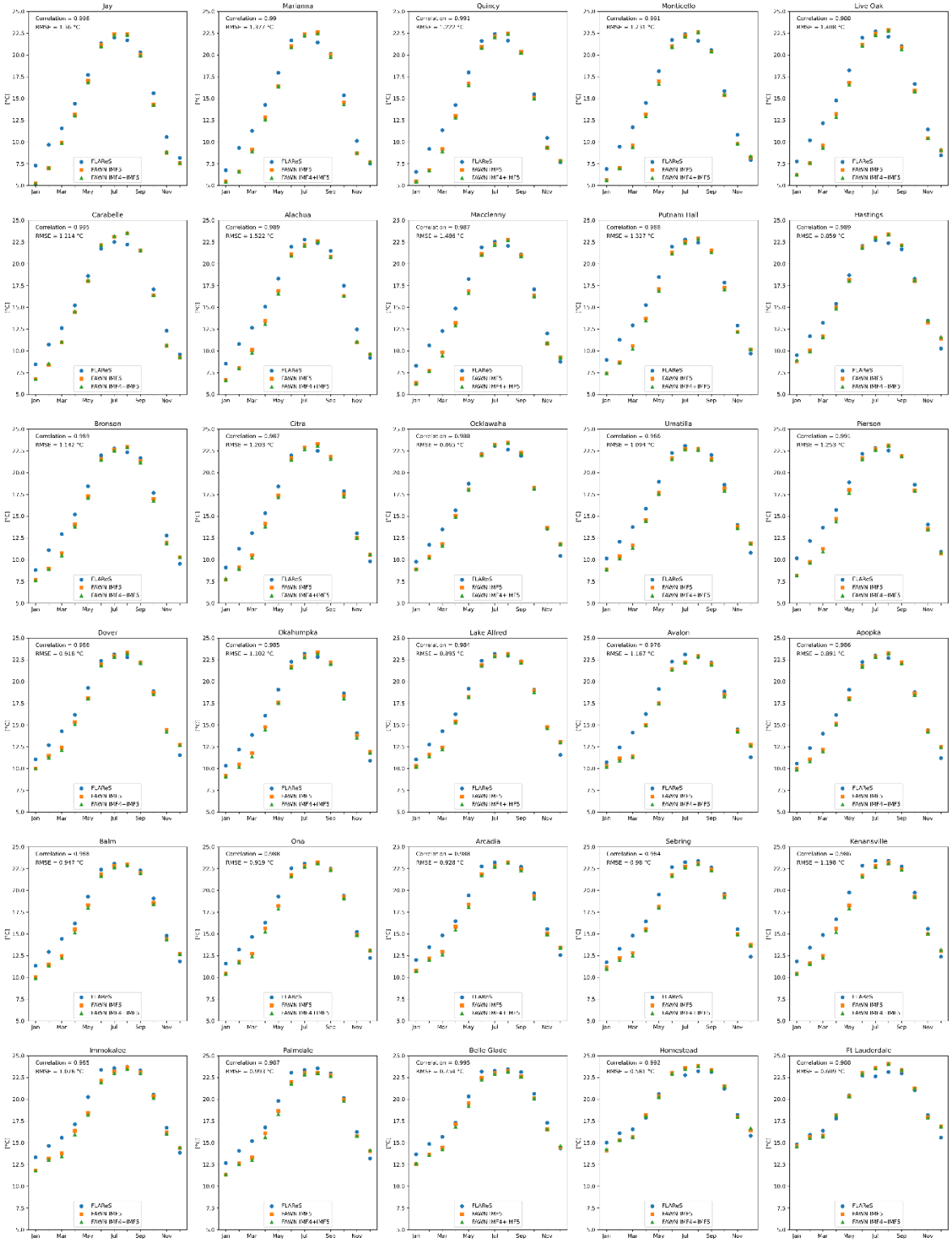

Figure 5.35. Diurnal minimum amplitude of surface dew point temperature in FAWN IMF5 (orange squares) and FAWN IMF4+IMF5 (green triangles) at 30 FAWN observational stations, and in FLAReS1.0 (blue circles) at the grid points closest to each FAWN station. The correlation and RMSE between the FLAReS1.0 diurnal amplitudes and the FAWN IMF5 diurnal amplitudes are listed in each panel.

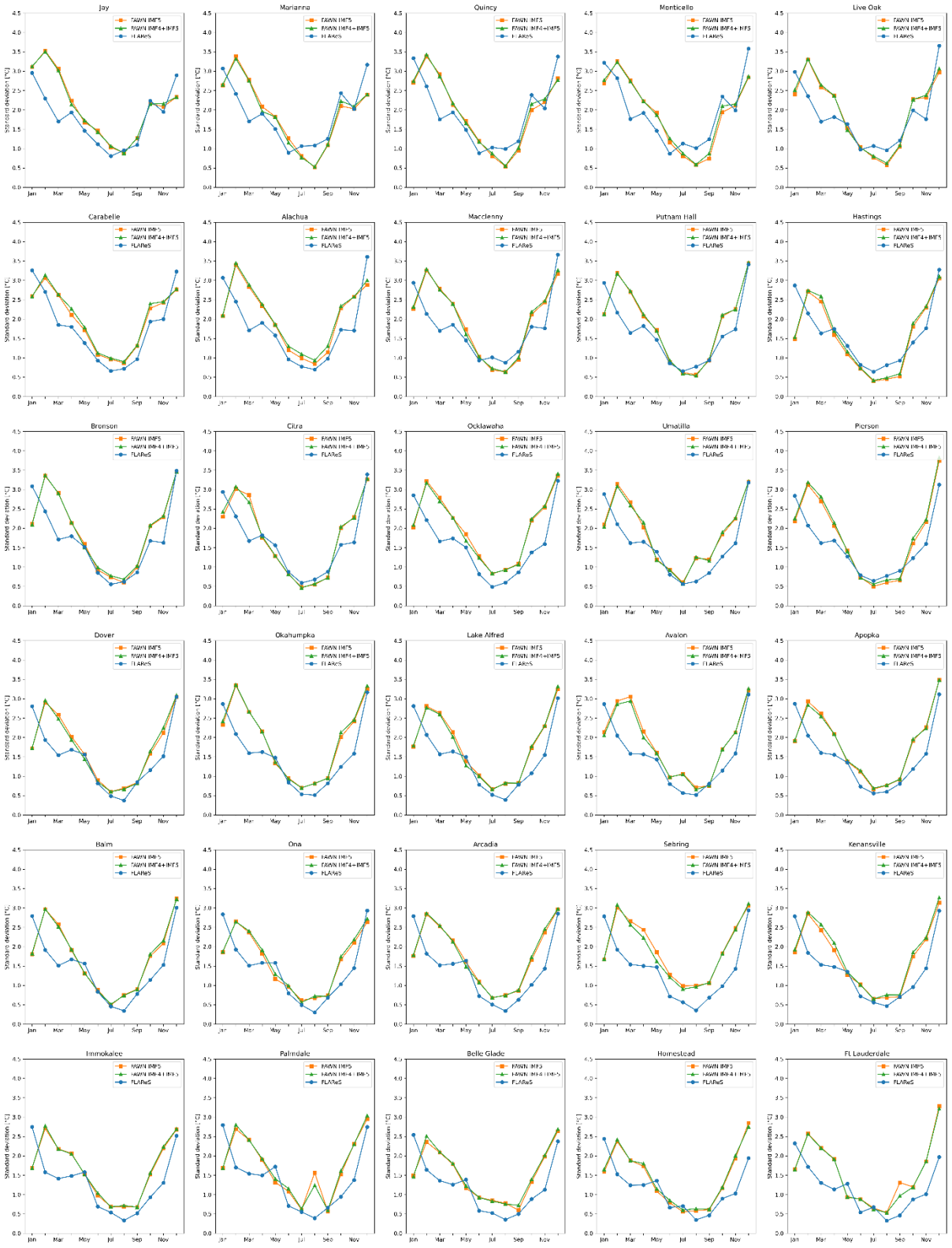

Figure 5.36. Standard deviations of the diurnal minimum amplitude of surface dew point temperature by month in FAWN IMF5 (orange squares) and FAWN IMF4+IMF5 (green triangles) at 30 FAWN observational stations, and in FLAReS1.0 (blue circles) at the grid points closest to each FAWN station.

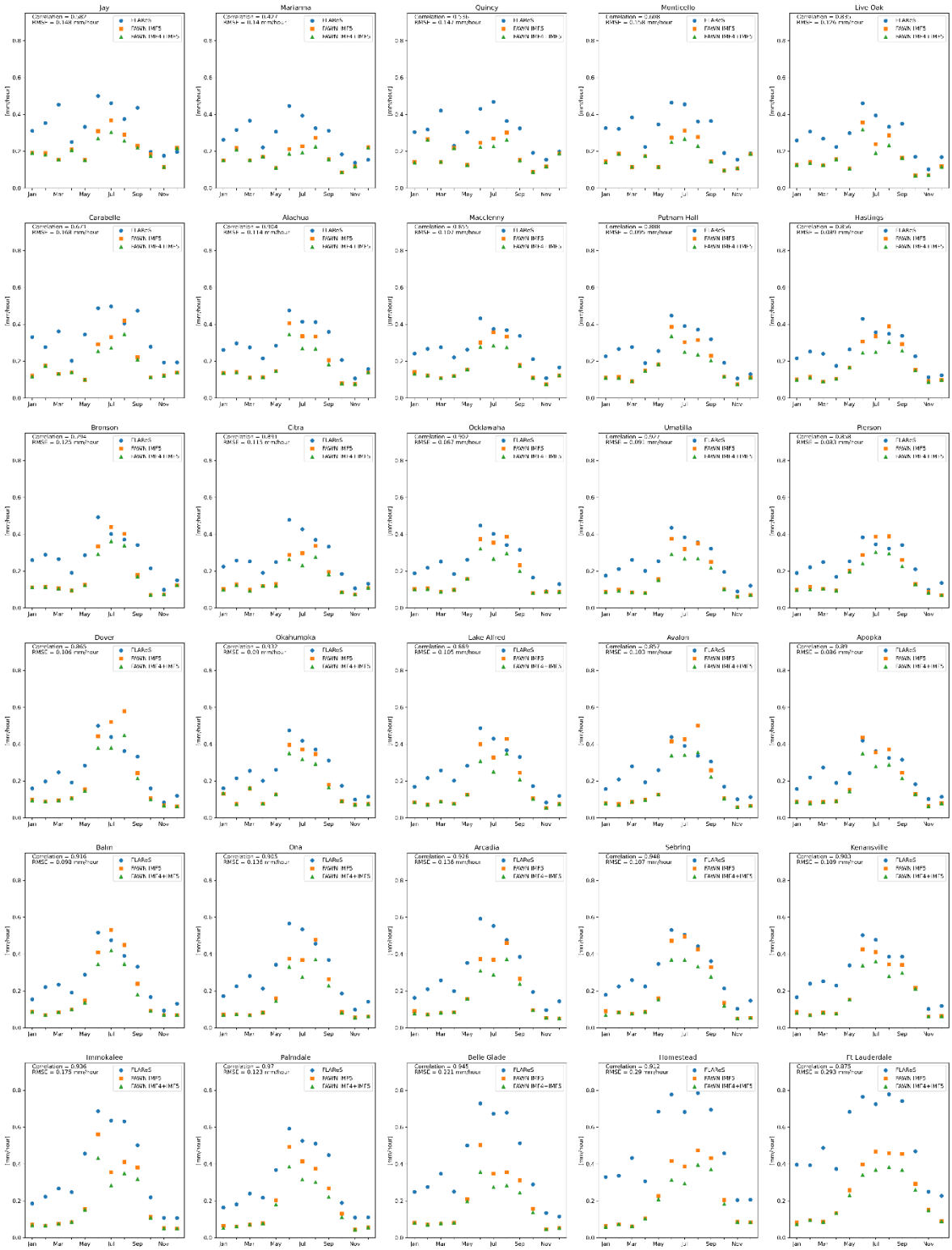

Figure 5.37. Diurnal peak amplitude of precipitation in FAWN IMF5 (orange squares) and FAWN IMF4+IMF5 (green triangles) at 30 FAWN observational stations, and in FLAReS1.0 (blue circles) at the grid points closest to each FAWN station. The correlation and RMSE between the FLAReS1.0 diurnal amplitudes and the FAWN IMF5 diurnal amplitudes are listed in each panel.

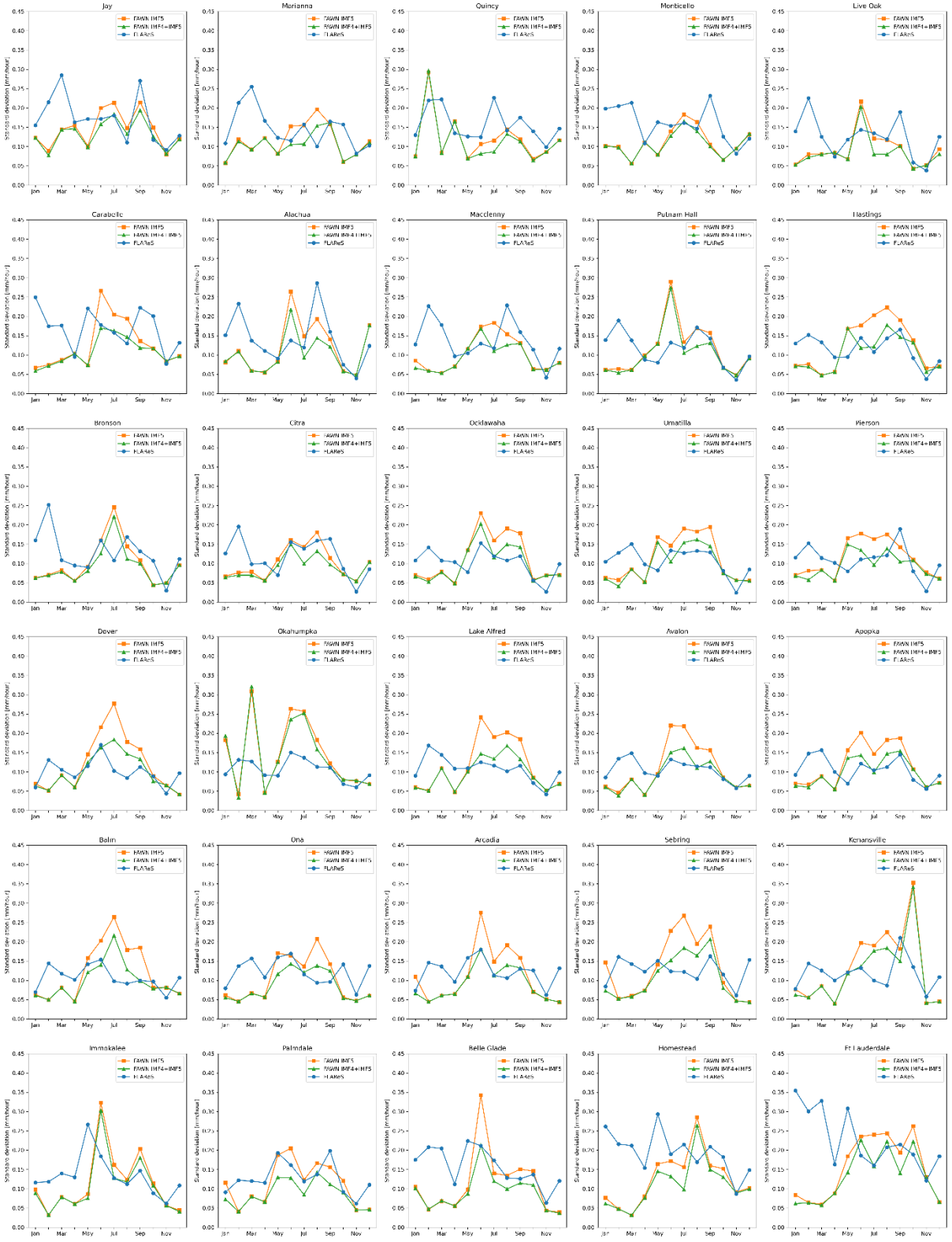

Figure 5.38. Standard deviations of the diurnal peak amplitude of precipitation by month in FAWN IMF5 (orange squares) and FAWN IMF4+IMF5 (green triangles) at 30 FAWN observational stations, and in FLAReS1.0 (blue circles) at the grid points closest to each FAWN station.

5.2.2 The diurnal phase

The observed diurnal peak phase of surface temperature is around 15:00 LST at all FAWN stations across Florida, with the diurnal peak of surface temperature occurring slightly earlier during the summer months (Figure 5.2.11). In north Florida, FLAReS1.0 reproduces this gentle annual cycle decently well, albeit with a 1-2 hour early-bias. In all of Florida, FLAReS1.0 reproduces the diurnal peak phase of surface temperature, albeit with the 1-2 hour early bias, during May—September (Figure 5.2.11-12). However, during October—April, FLAReS1.0 does not capture the diurnal peak phase of surface temperature at any peninsular Florida station (Figure 5.2.11). With few exceptions, the observed interannual variance of the diurnal peak phase of surface temperature is near zero. In general, FLAReS1.0 overestimates the interannual variance of the diurnal peak phase of surface temperature (Figure 5.2.13). The observed diurnal minimum phase of surface temperature across Florida is around 2:00 LST in summer and fall, and 3:00 LST in winter and spring (Figure 5.2.14). Generally, in north Florida, FLAReS1.0 reproduces an early-morning diurnal minimum phase of surface temperature (Figure 5.2.14). It also does so in April—September across all of Florida (Figure 5.2.14). In October—March, however, FLAReS1.0 does not capture the diurnal minimum phase of surface temperature (Figure 5.2.14). The observed interannual variance of the diurnal minimum phase of surface temperature is near zero across all Florida stations and throughout the annual cycle (Figure 5.2.16). At most stations across Florida, throughout most of the annual cycle, FLAReS1.0 overestimates this interannual variance. However, interestingly, FLAReS1.0 shows this small interannual variance in September across all stations in north and central Florida (Figure 5.2.16).

The diurnal peak phase of surface dew point temperature is represented poorly in FLAReS1.0 (Figure 5.2.17-18). The interannual variance of the diurnal peak phase of surface dew point temperature is overestimated in FLAReS1.0 (Figure 5.2.19). The diurnal minimum phase of surface dew point temperature represented poorly in FLAReS1.0, too (Figure 5.2.20-21). The observed interannual variance of the diurnal minimum phase of surface dew point temperature is relatively high in north Florida, and lower in south Florida (Figure 5.2.22). FLAReS1.0 tends to capture the high variance in north Florida and overestimate it in south Florida (Figure 5.2.22).

The diurnal peak phase of precipitation is represented poorly in FLAReS1.0 (Figure 5.2.23-24). The observed interannual variance of the peak phase of precipitation is relatively high across Florida, and FLAReS1.0 generally represents this well (Figure 5.2.25). The observed diurnal minimum phase of precipitation is in the early morning, and FLAReS1.0 generally represents that well (Figure 5.2.26-27). FLAReS1.0 also does well to represent the interannual variance of the diurnal minimum phase of precipitation (Figure 5.2.28).

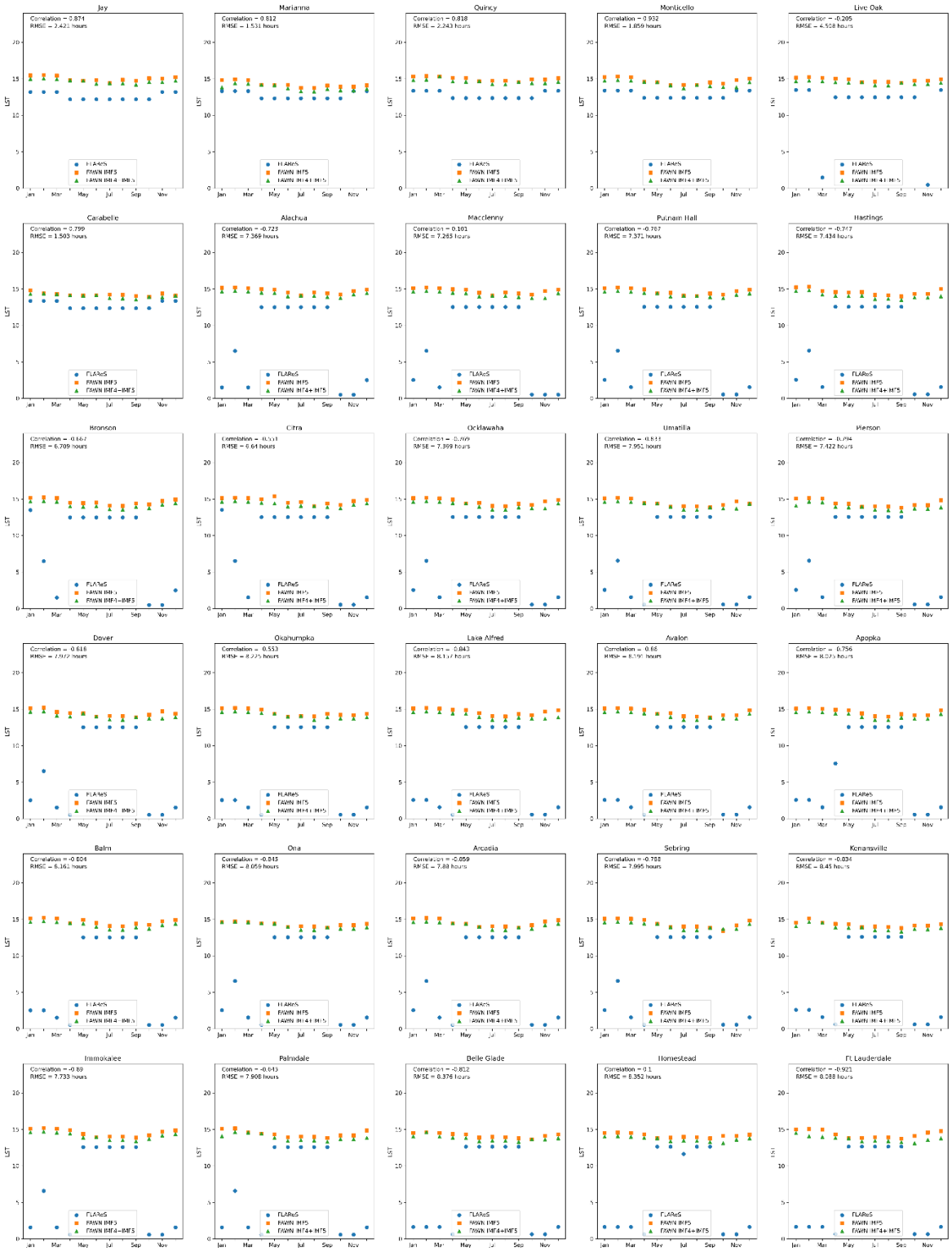

Figure 5.39. Diurnal peak phase (time of diurnal maximum; Local Solar Time (LST)) of surface temperature in FAWN IMF5 (orange squares) and FAWN IMF4+IMF5 (green triangles) at 30 FAWN observational stations, and in FLAReS1.0 (blue circles) at the grid points closest to each FAWN station. The correlation and RMSE between the FLAReS1.0 diurnal phase and the FAWN IMF5 diurnal phase are listed in each panel.

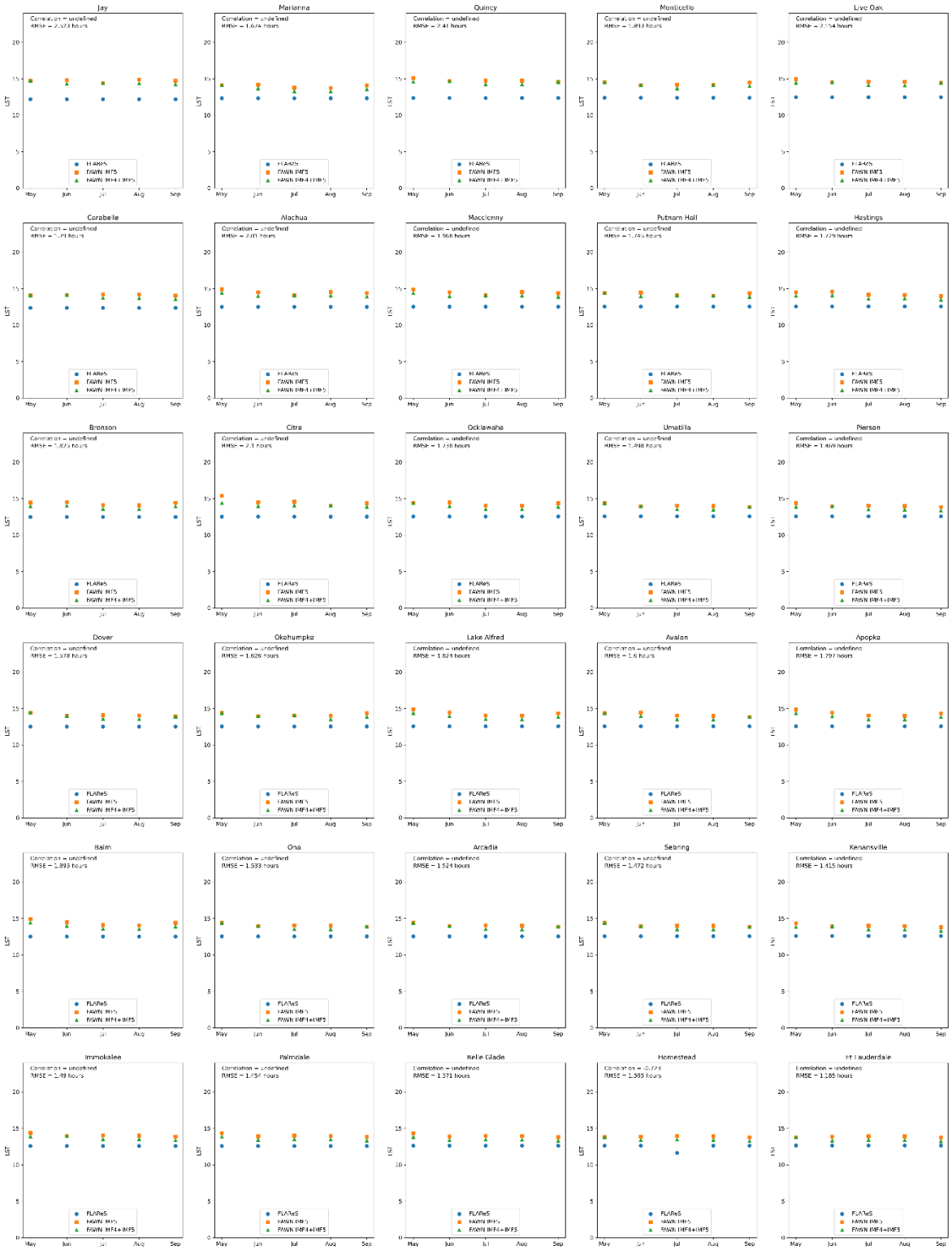

Figure 5.40. May—September diurnal peak phase (time of diurnal maximum; Local Solar Time (LST)) of surface temperature in FAWN IMF5 (orange squares) and FAWN IMF4+IMF5 (green triangles) at 30 FAWN observational stations, and in FLAReS1.0 (blue circles) at the grid points closest to each FAWN station. The correlation and RMSE between the FLAReS1.0 diurnal phase and the FAWN IMF5 diurnal phase are listed in each panel.

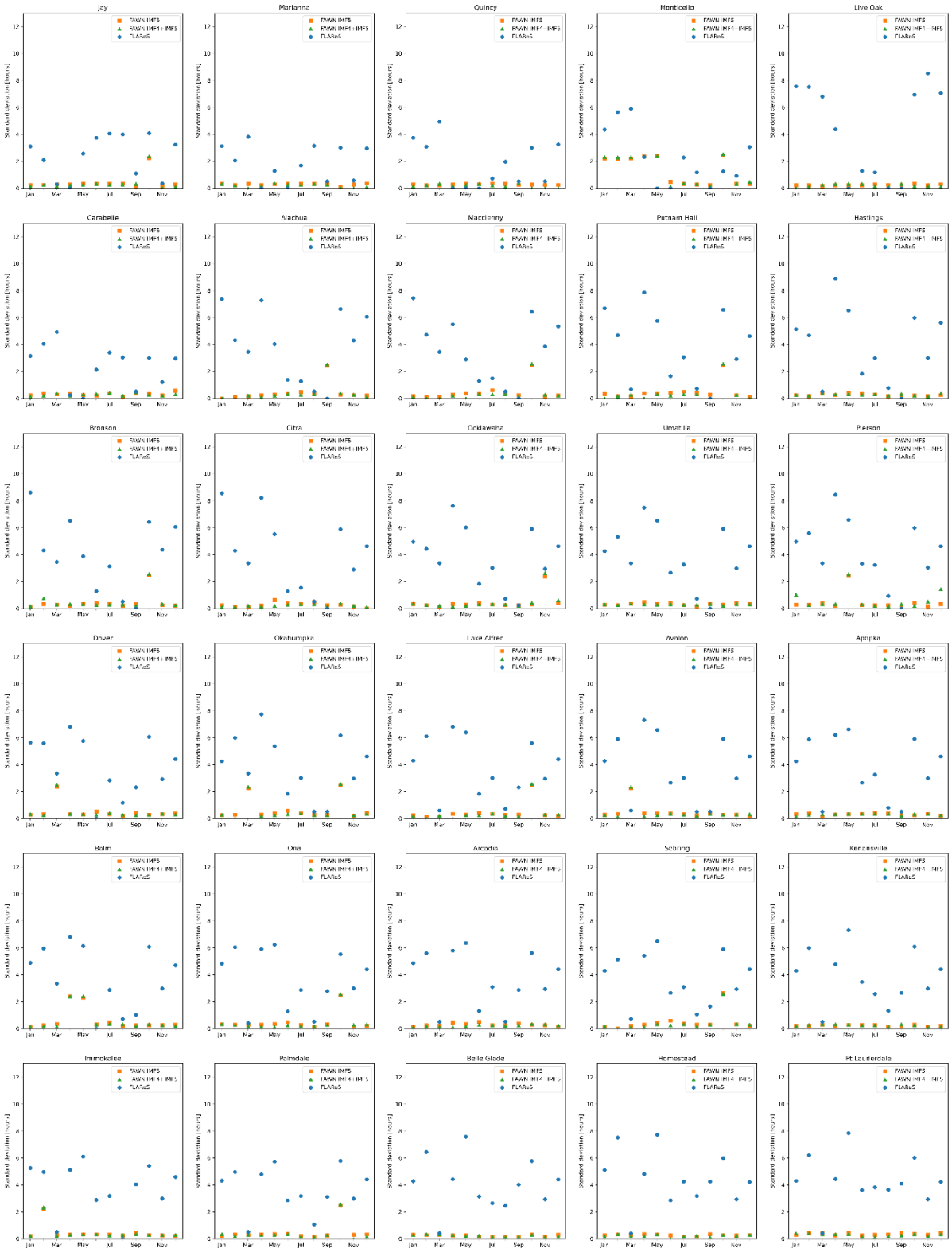

Figure 5.41. Standard deviations of the diurnal peak phase of surface temperature by month in FAWN IMF5 (orange squares) and FAWN IMF4+IMF5 (green triangles) at 30 FAWN observational stations, and in FLAReS1.0 (blue circles) at the grid points closest to each FAWN station.

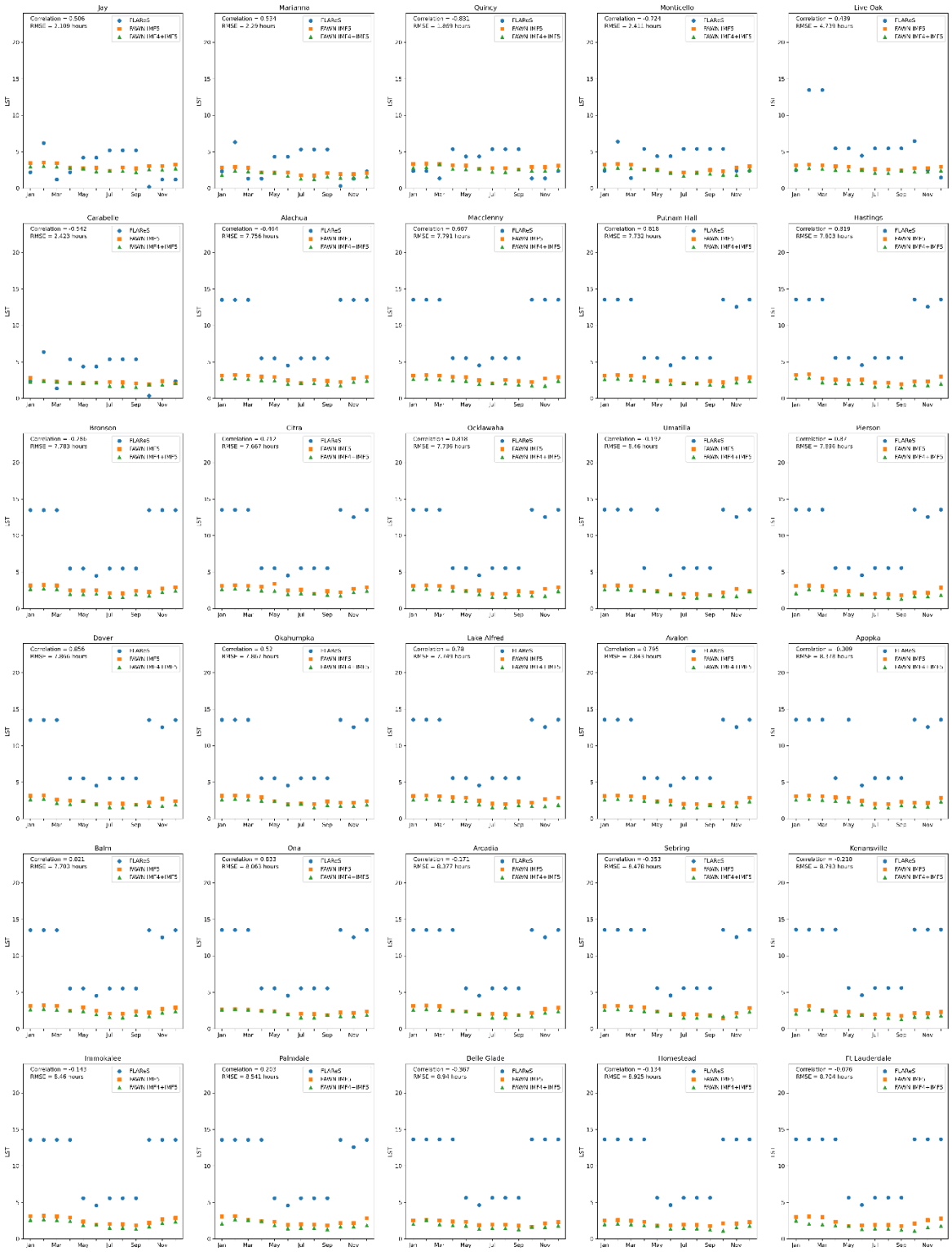

Figure 5.42. Diurnal minimum phase (time of diurnal minimum; Local Solar Time (LST)) of surface temperature in FAWN IMF5 (orange squares) and FAWN IMF4+IMF5 (green triangles) at 30 FAWN observational stations, and in FLAReS1.0 (blue circles) at the grid points closest to each FAWN station. The correlation and RMSE between the FLAReS1.0 diurnal phase and the FAWN IMF5 diurnal phase are listed in each panel.

Figure 5.43. May—September diurnal minimum phase (time of diurnal minimum; Local Solar Time (LST)) of surface temperature in FAWN IMF5 (orange squares) and FAWN IMF4+IMF5 (green triangles) at 30 FAWN observational stations, and in FLAReS1.0 (blue circles) at the grid points closest to each FAWN station. The correlation and RMSE between the FLAReS1.0 diurnal phase and the FAWN IMF5 diurnal phase are listed in each panel.

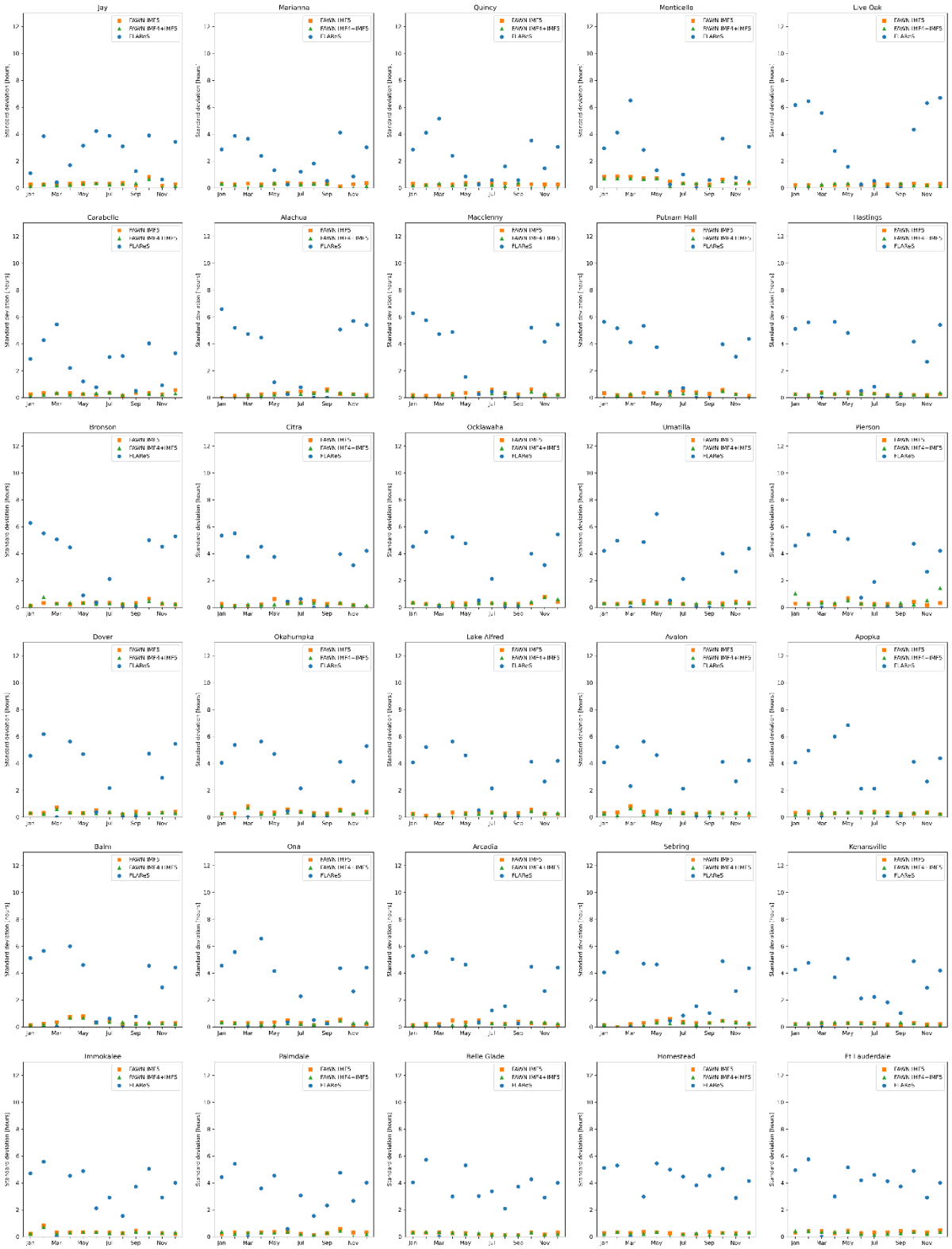

Figure 5.44. Standard deviations of the diurnal minimum phase of surface temperature by month in FAWN IMF5 (orange squares) and FAWN IMF4+IMF5 (green triangles) at 30 FAWN observational stations, and in FLAReS1.0 (blue circles) at the grid points closest to each FAWN station.

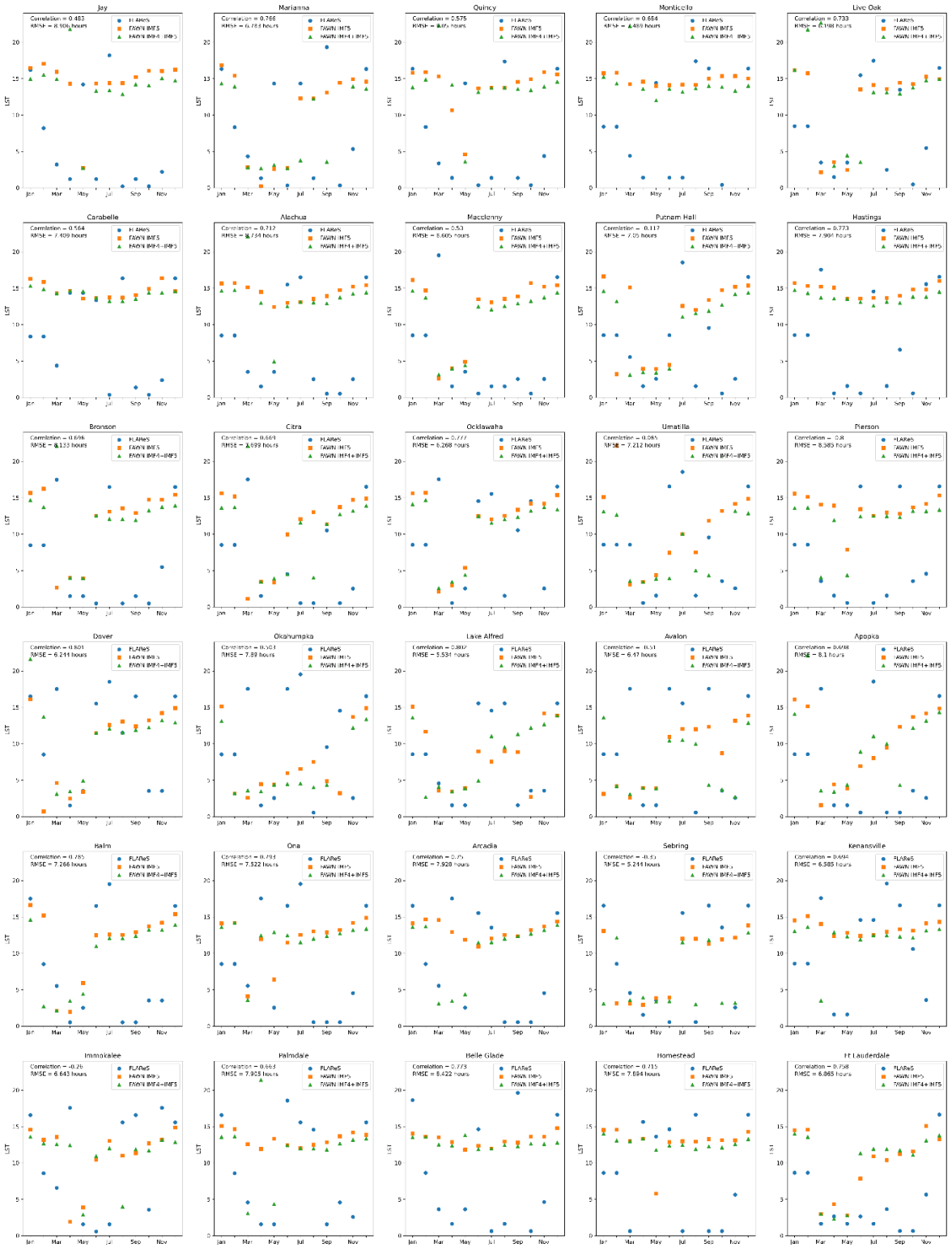

Figure 5.45. Diurnal peak phase (time of diurnal maximum; Local Solar Time (LST)) of surface dew point temperature in FAWN IMF5 (orange squares) and FAWN IMF4+IMF5 (green triangles) at 30 FAWN observational stations, and in FLAReS1.0 (blue circles) at the grid points closest to each FAWN station. The correlation and RMSE between the FLAReS1.0 diurnal phase and the FAWN IMF5 diurnal phase are listed in each panel.

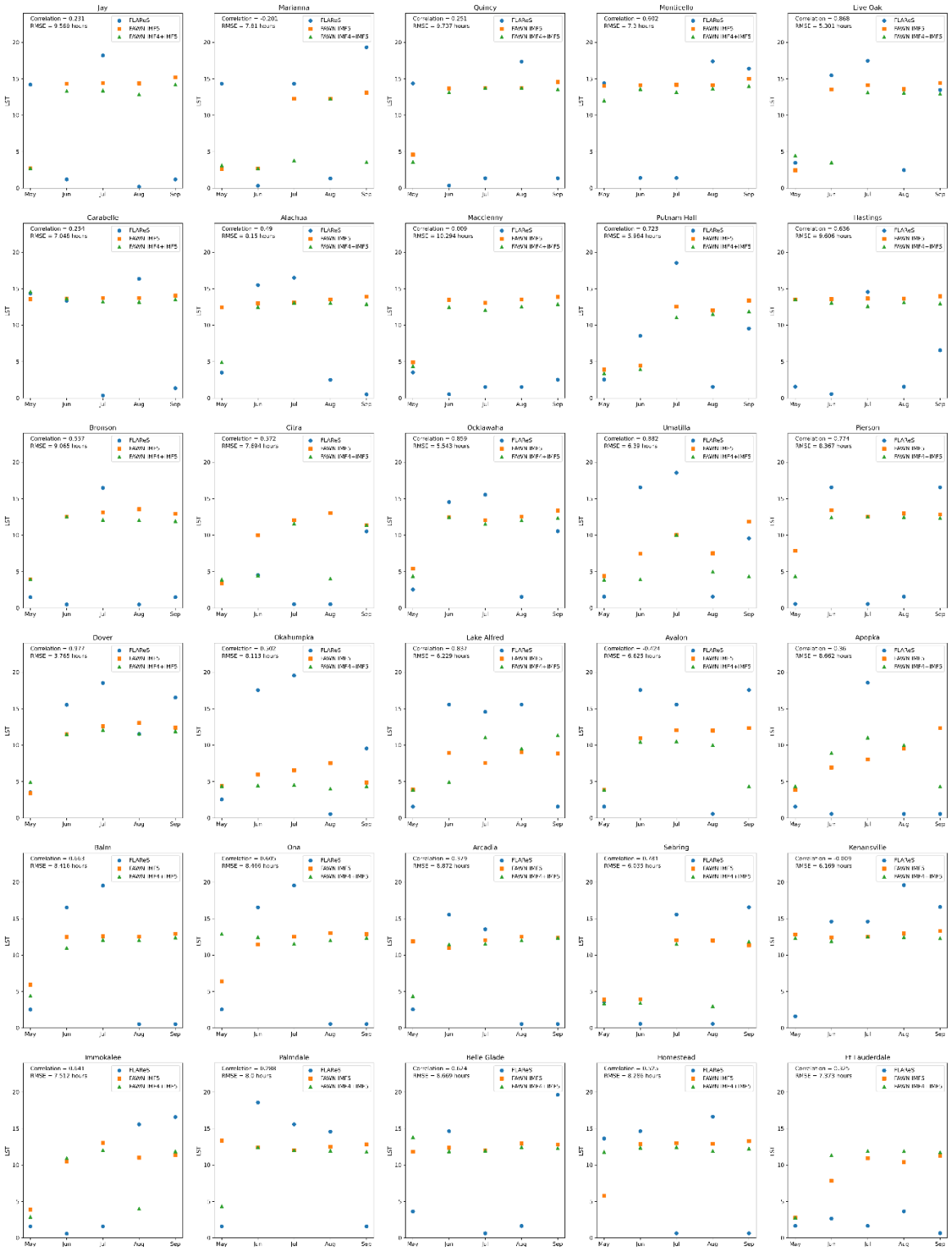

Figure 5.46. May—September diurnal peak phase (time of diurnal maximum; Local Solar Time (LST)) of surface dew point temperature in FAWN IMF5 (orange squares) and FAWN IMF4+IMF5 (green triangles) at 30 FAWN observational stations, and in FLAReS1.0 (blue circles) at the grid points closest to each FAWN station. The correlation and RMSE between the FLAReS1.0 diurnal phase and the FAWN IMF5 diurnal phase are listed in each panel.

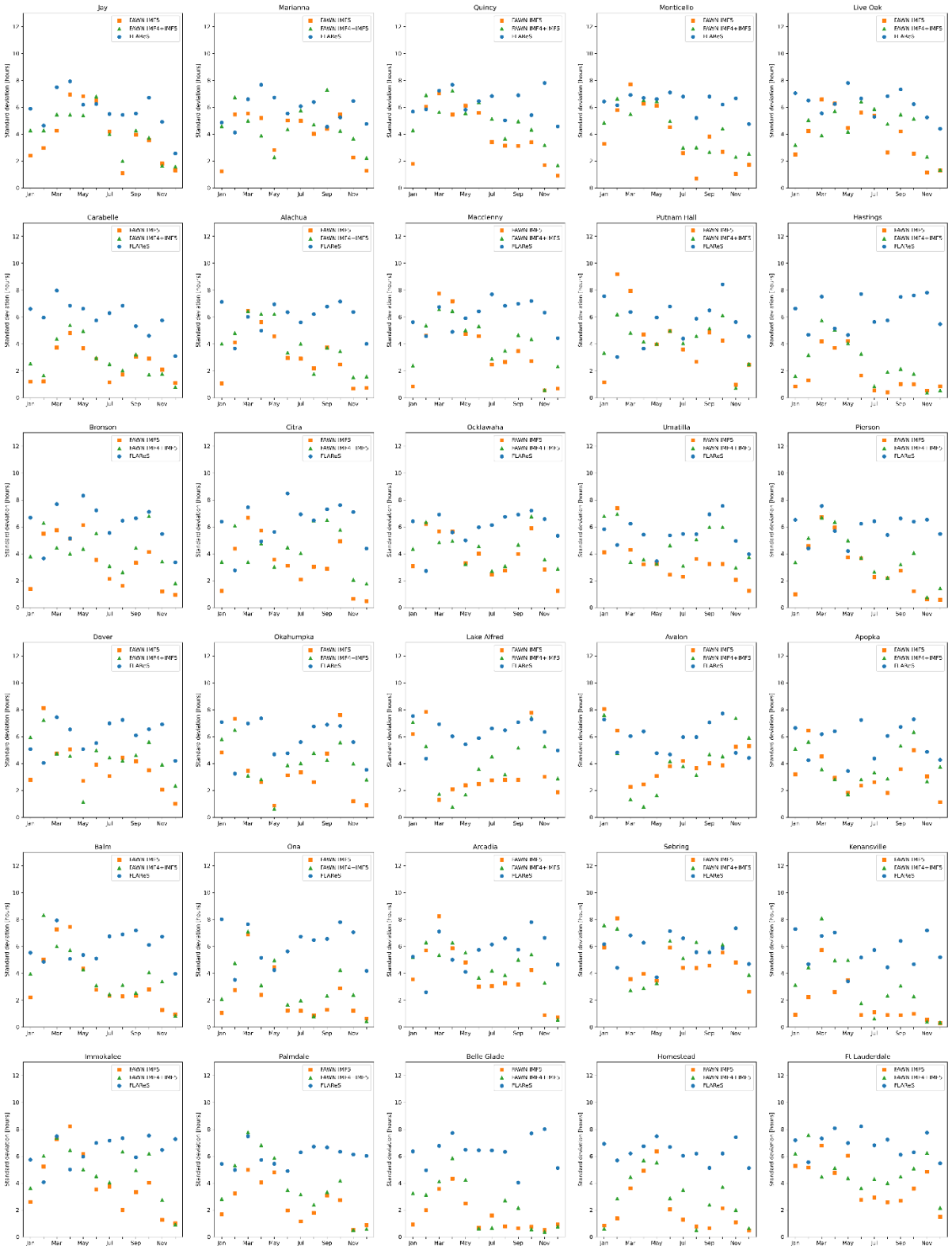

Figure 5.47. Standard deviations of the diurnal peak phase of surface dew point temperature by month in FAWN IMF5 (orange squares) and FAWN IMF4+IMF5 (green triangles) at 30 FAWN observational stations, and in FLAReS1.0 (blue circles) at the grid points closest to each FAWN station.

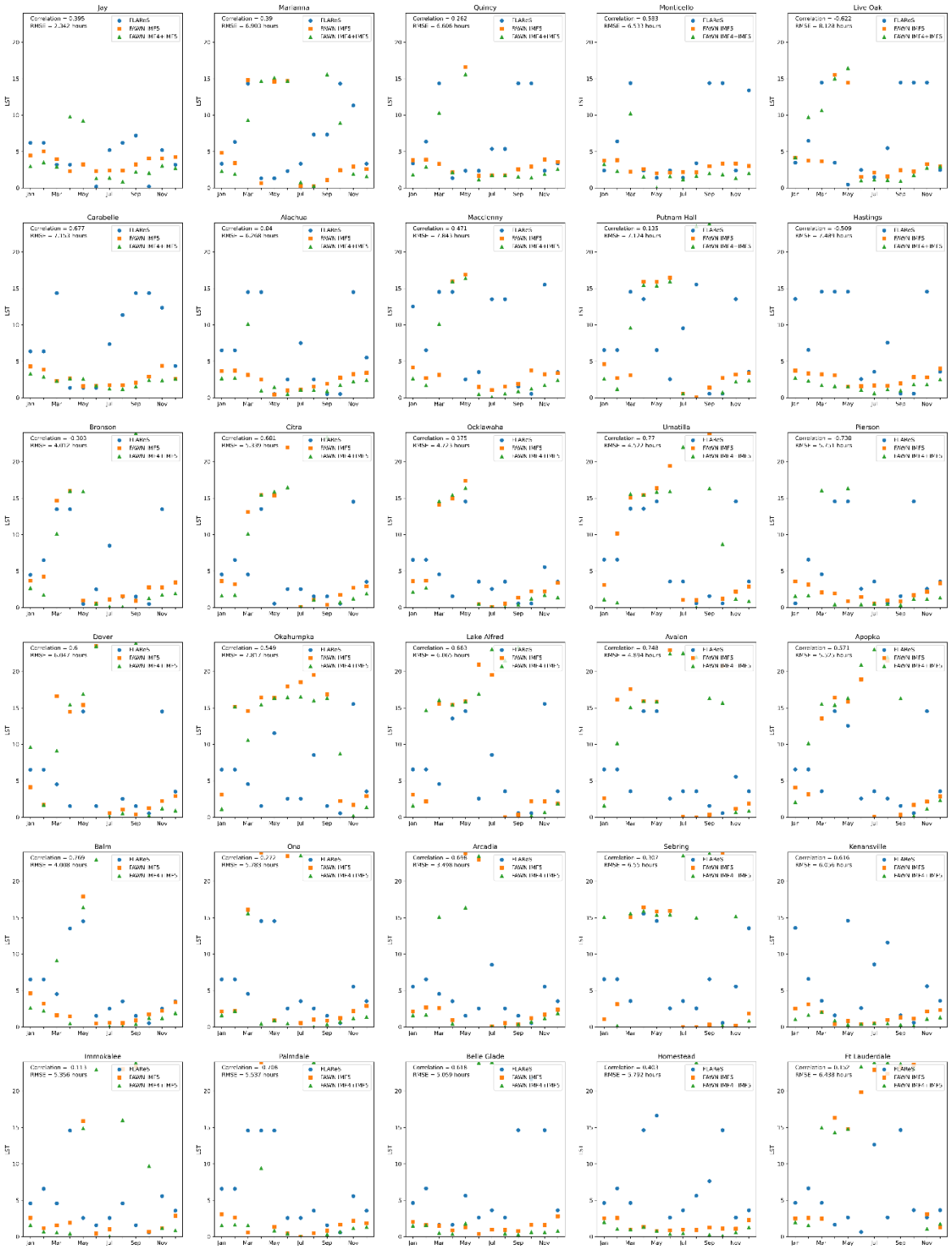

Figure 5.48. Diurnal minimum phase (time of diurnal minimum; Local Solar Time (LST)) of surface dew point temperature in FAWN IMF5 (orange squares) and FAWN IMF4+IMF5 (green triangles) at 30 FAWN observational stations, and in FLAReS1.0 (blue circles) at the grid points closest to each FAWN station. The correlation and RMSE between the FLAReS1.0 diurnal phase and the FAWN IMF5 diurnal phase are listed in each panel.

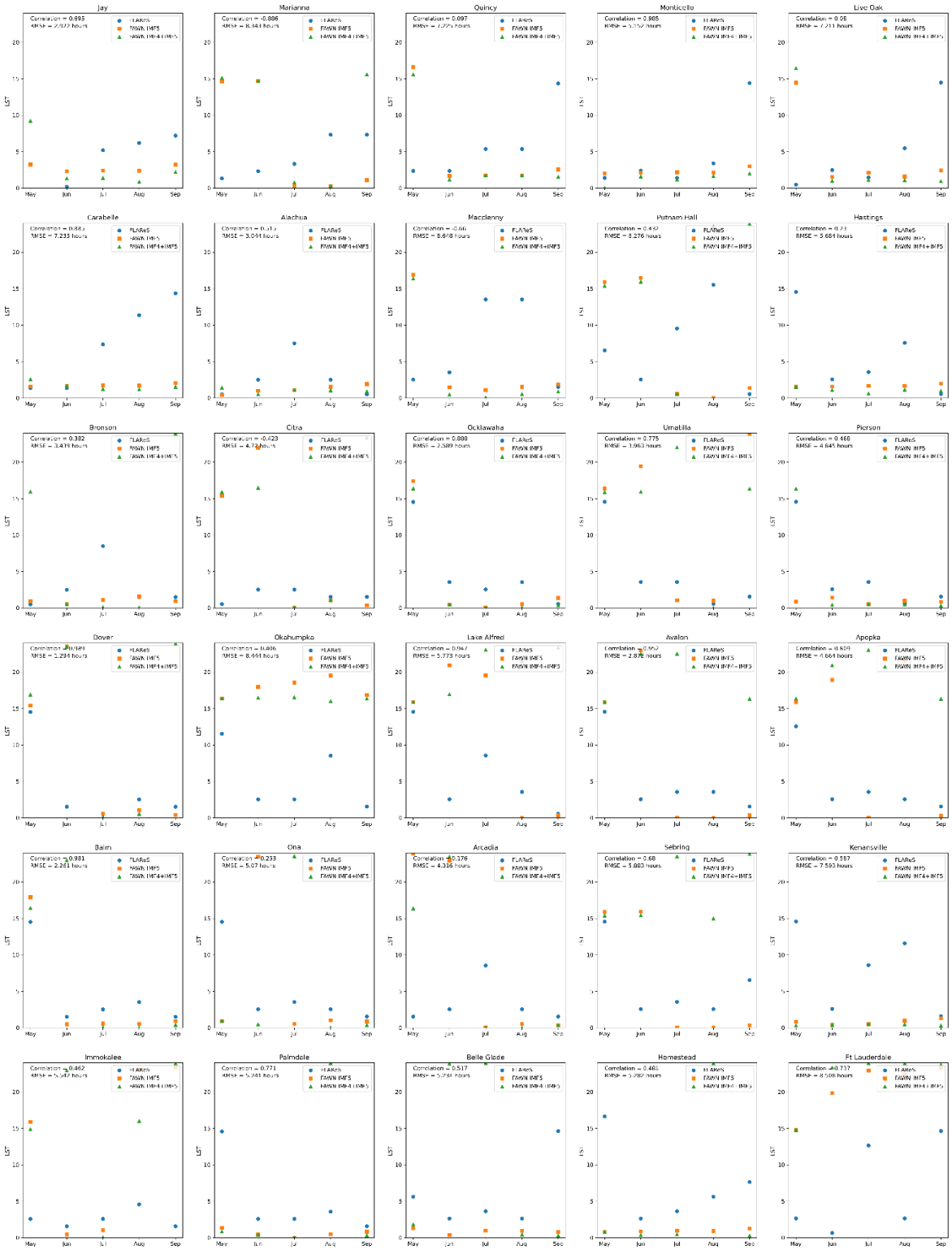

Figure 5.49. May—September diurnal minimum phase (time of diurnal minimum; Local Solar Time (LST)) of surface dew point temperature in FAWN IMF5 (orange squares) and FAWN IMF4+IMF5 (green triangles) at 30 FAWN observational stations, and in FLAReS1.0 (blue circles) at the grid points closest to each FAWN station. The correlation and RMSE between the FLAReS1.0 diurnal phase and the FAWN IMF5 diurnal phase are listed in each panel.

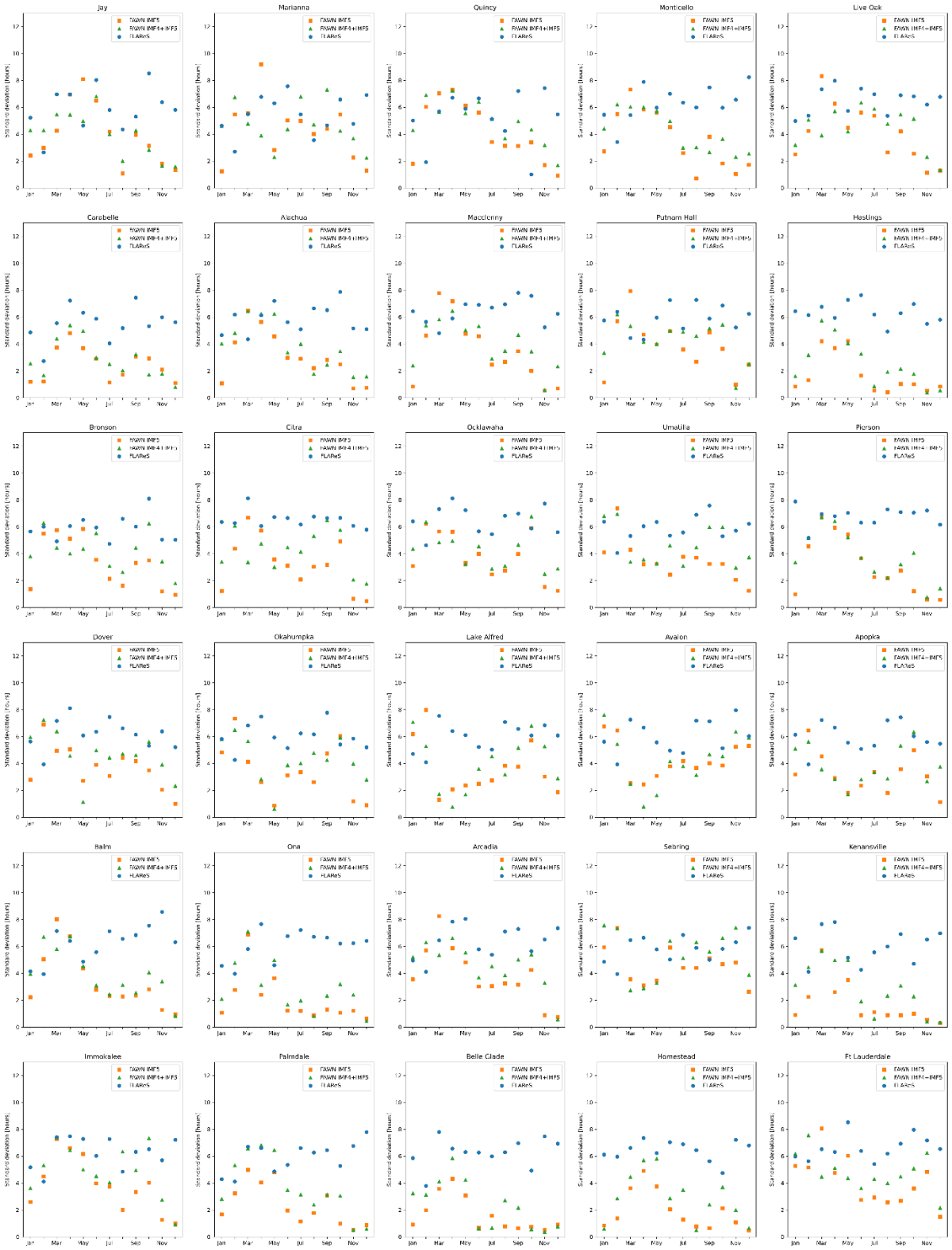

Figure 5.50. Standard deviations of the diurnal minimum phase of surface dew point temperature by month in FAWN IMF5 (orange squares) and FAWN IMF4+IMF5 (green triangles) at 30 FAWN observational stations, and in FLAReS1.0 (blue circles) at the grid points closest to each FAWN station.

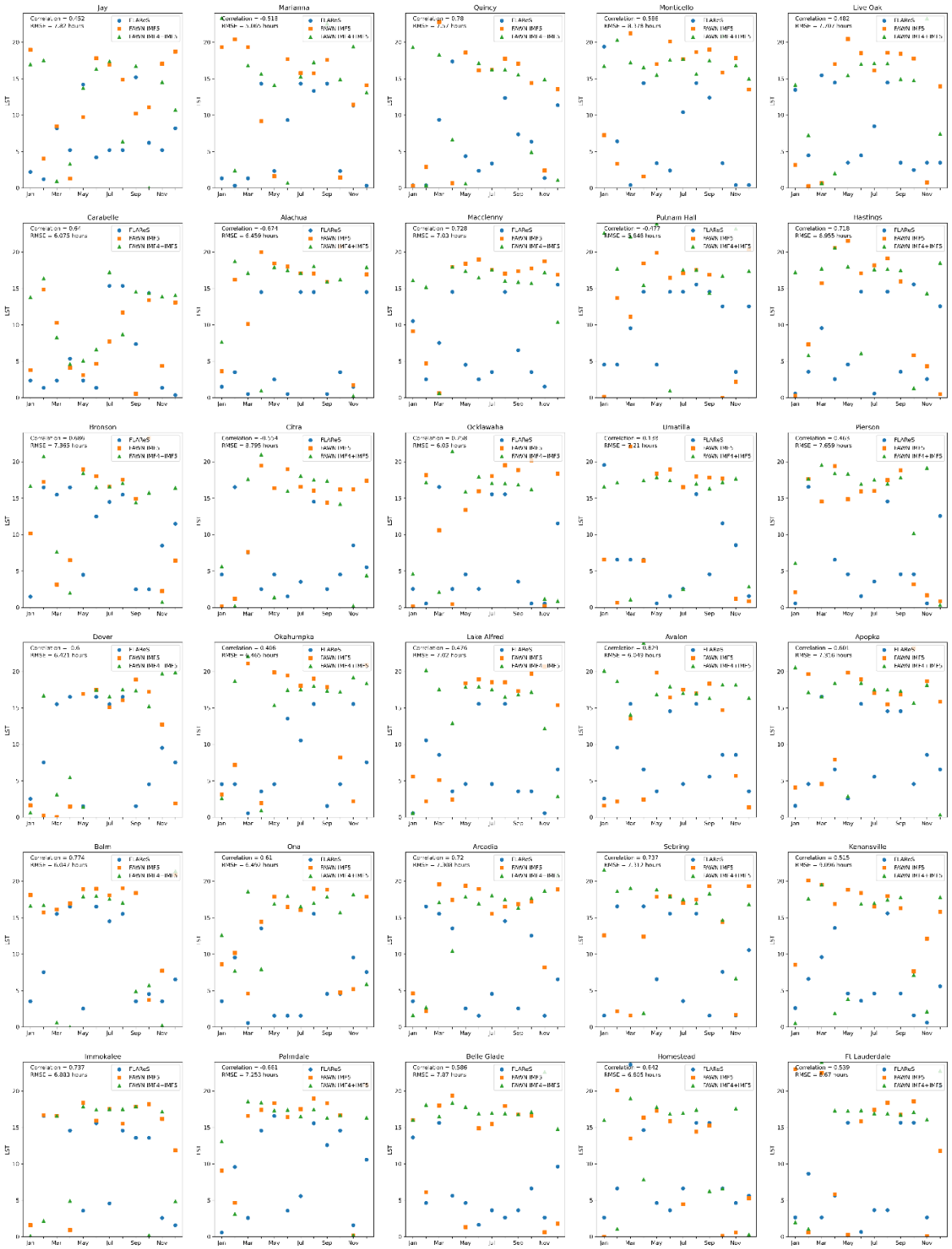

Figure 5.51. Diurnal peak phase (time of diurnal maximum; Local Solar Time (LST)) of precipitation in FAWN IMF5 (orange squares) and FAWN IMF4+IMF5 (green triangles) at 30 FAWN observational stations, and in FLAReS1.0 (blue circles) at the grid points closest to each FAWN station. The correlation and RMSE between the FLAReS1.0 diurnal phase and the FAWN IMF5 diurnal phase are listed in each panel.

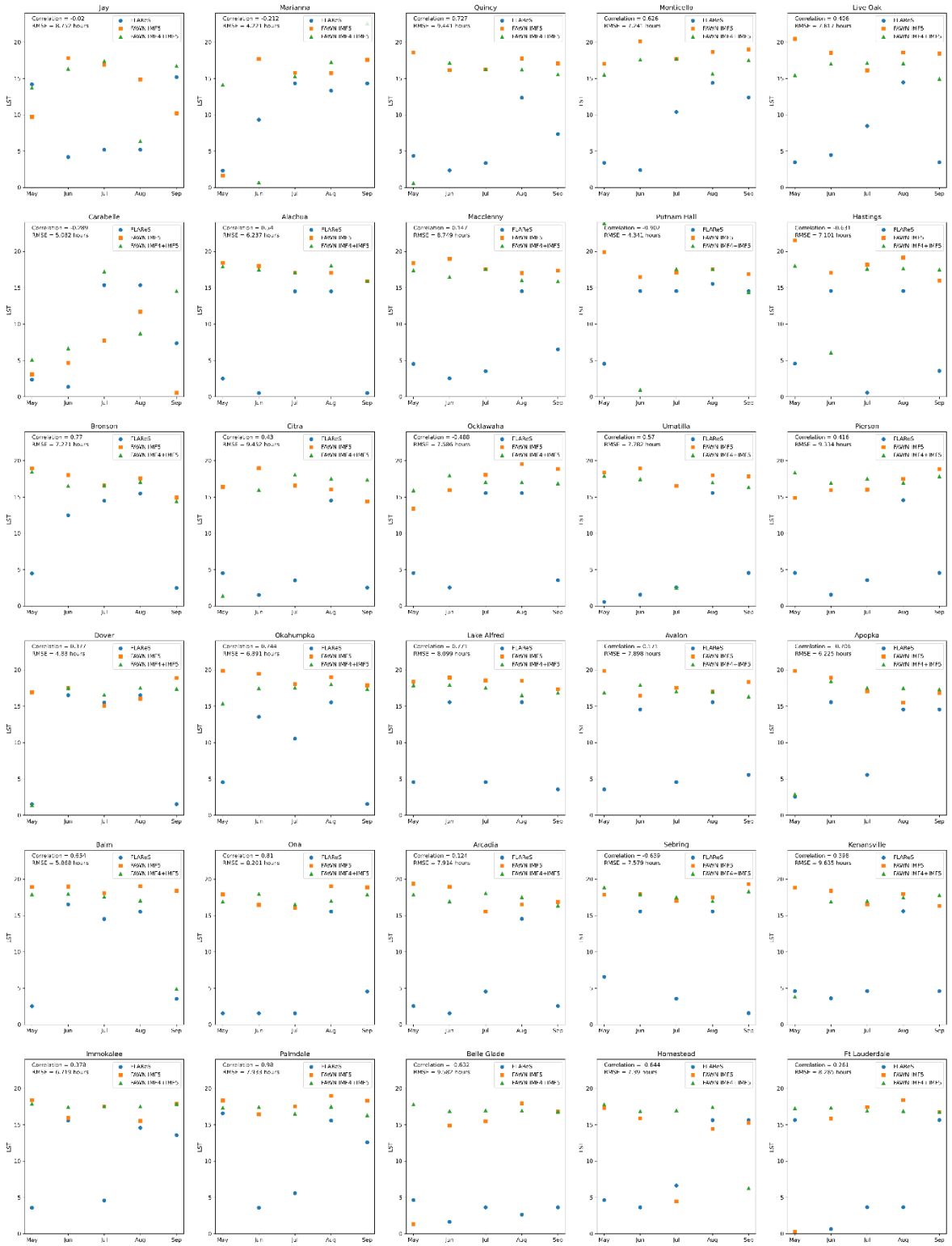

Figure 5.52. May—September diurnal peak phase (time of diurnal maximum; Local Solar Time (LST)) of precipitation in FAWN IMF5 (orange squares) and FAWN IMF4+IMF5 (green triangles) at 30 FAWN observational stations, and in FLAReS1.0 (blue circles) at the grid points closest to each FAWN station. The correlation and RMSE between the FLAReS1.0 diurnal phase and the FAWN IMF5 diurnal phase are listed in each panel.

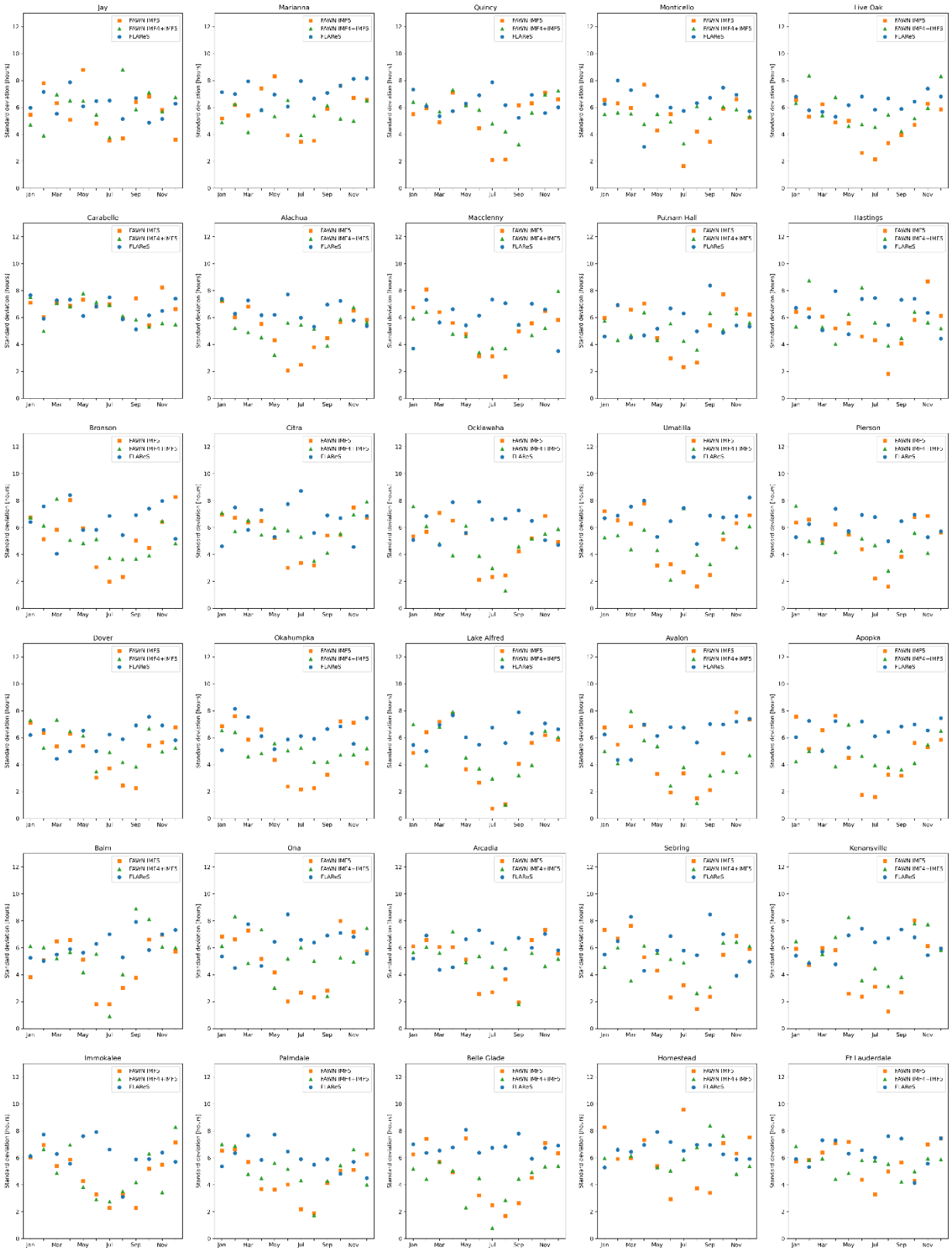

Figure 5.53. Standard deviations of the diurnal peak phase of precipitation by month in FAWN IMF5 (orange squares) and FAWN IMF4+IMF5 (green triangles) at 30 FAWN observational stations, and in FLAReS1.0 (blue circles) at the grid points closest to each FAWN station.

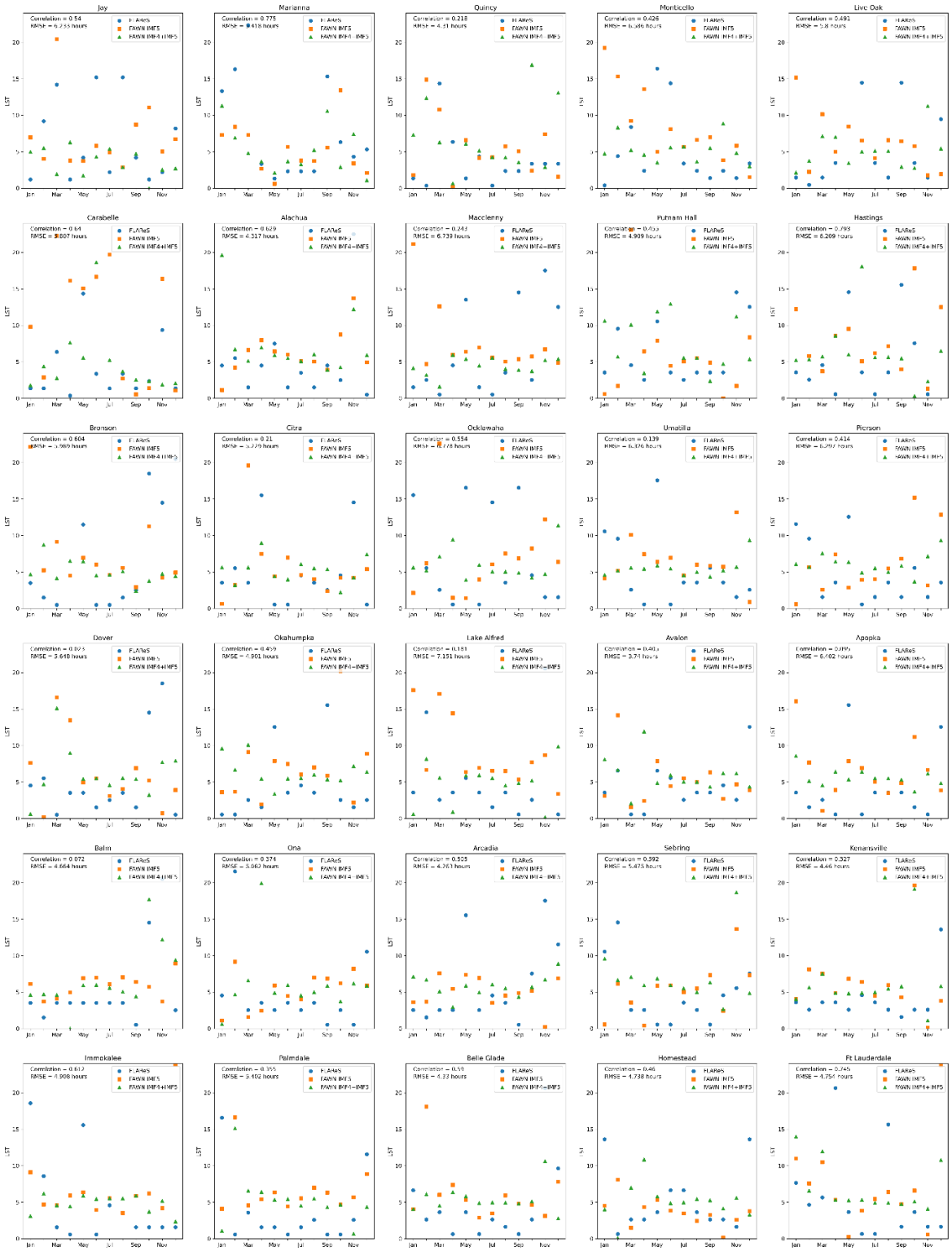

Figure 5.54. Diurnal minimum phase (time of diurnal minimum; Local Solar Time (LST)) of precipitation in FAWN IMF5 (orange squares) and FAWN IMF4+IMF5 (green triangles) at 30 FAWN observational stations, and in FLAReS1.0 (blue circles) at the grid points closest to each FAWN station. The correlation and RMSE between the FLAReS1.0 diurnal phase and the FAWN IMF5 diurnal phase are listed in each panel.

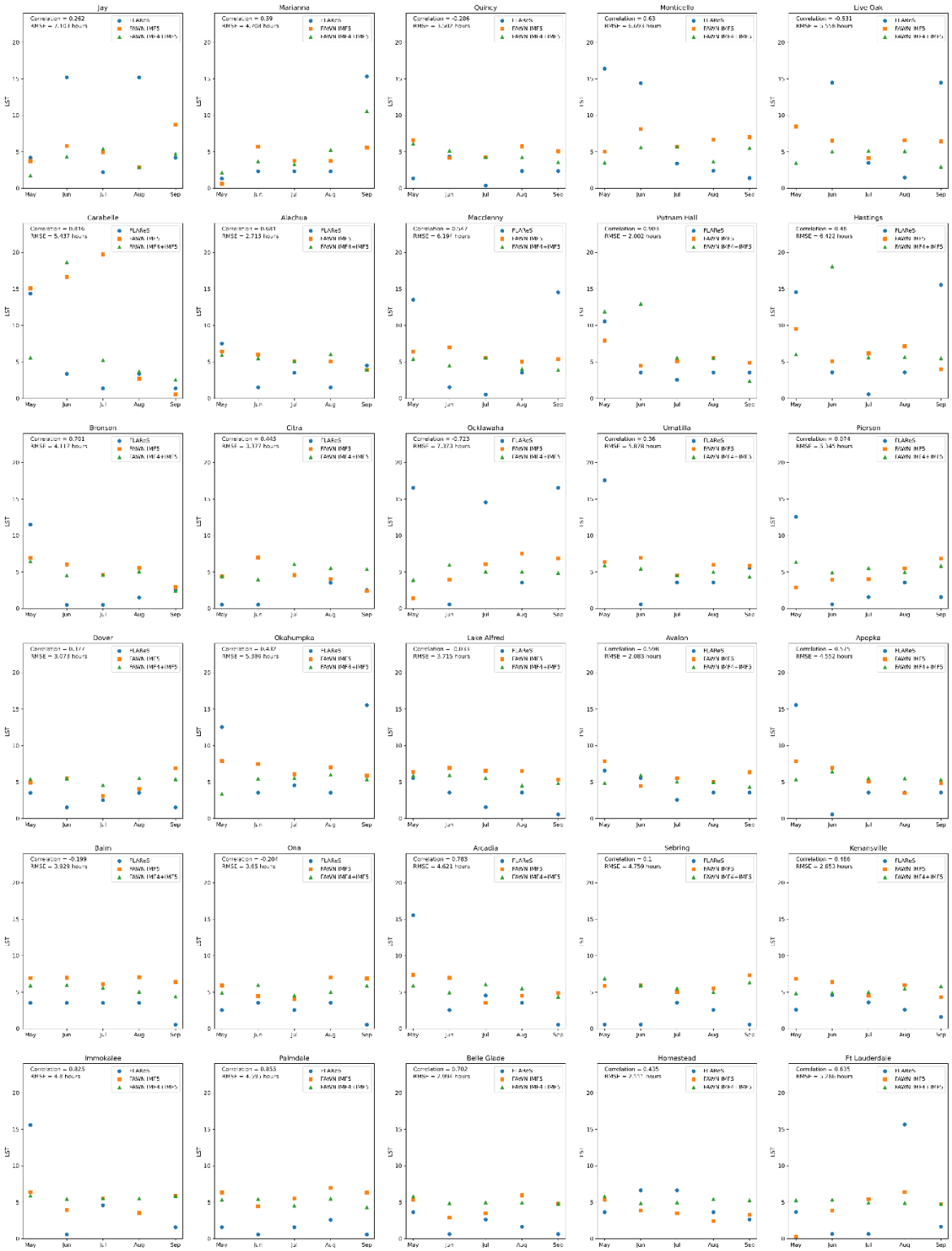

Figure 5.55. May—September diurnal minimum phase (time of diurnal minimum; Local Solar Time (LST)) of precipitation in FAWN IMF5 (orange squares) and FAWN IMF4+IMF5 (green triangles) at 30 FAWN observational stations, and in FLAReS1.0 (blue circles) at the grid points closest to each FAWN station. The correlation and RMSE between the FLAReS1.0 diurnal phase and the FAWN IMF5 diurnal phase are listed in each panel.

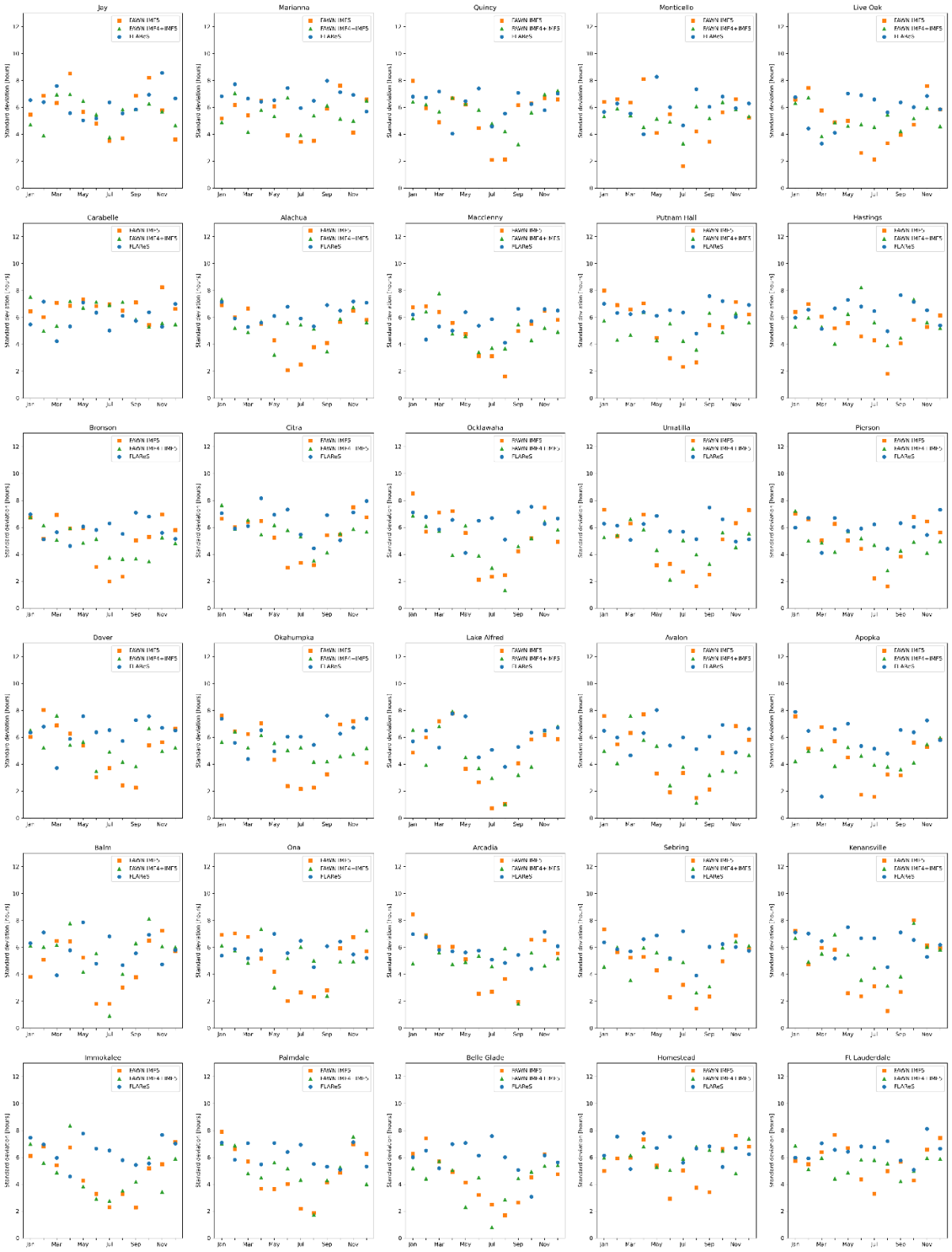

Figure 5.56. Standard deviations of the diurnal minimum phase of precipitation by month in FAWN IMF5 (orange squares) and FAWN IMF4+IMF5 (green triangles) at 30 FAWN observational stations, and in FLAReS1.0 (blue circles) at the grid points closest to each FAWN station.

5.3 Low frequency variability of diurnal variations in FLAReS1.0

5.3.1 ENSO

The relationships between the ENSO index and the surface diurnal cycle in Florida are illuminated here. There are strong relationships between ENSO and the diurnal amplitude of these surface meteorological variables. However, the relationships between ENSO and the diurnal phase are weak in most regions of Florida in most months of the year. As such, this section is focused on the relationships between ENSO and the diurnal amplitudes of the surface meteorology variables. Figures showing the relationships between ENSO and the diurnal phases of the surface meteorology variables can be found in the Appendix.

The strong relationships between the ENSO index and the diurnal amplitudes of surface temperature, surface specific humidity, and precipitation are widespread geographically across Florida and throughout the annual cycle.

There is a statistically significant negative correlation between the ENSO index and the diurnal peak amplitude of surface temperature in various areas of Florida in a few months of the year (Figure 5.3.1). This relationship indicates that during an El Niño event, the diurnal peak amplitudes of surface temperature tend to be smaller, whereas during a La Niña event, the diurnal peak amplitudes of surface temperature tend to be larger. This relationship is statistically significant in February across most of south and central Florida (Figure 5.3.1b). In March and April, the relationship is statistically significant along the coastlines of south Florida, Lake Okeechobee, and the western panhandle of Florida (Figure 5.3.1c-d). In November, the relationship is statistically significant over a large swath of north and central Florida (Figure 5.3.1k). In December, the relationship is statistically significant over most of the peninsula and north Florida, excluding the western panhandle (Figure 5.3.1l).

There is a statistically significant positive correlation between ENSO and the diurnal minimum amplitude of surface temperature in February (Figure 5.3.4b), March (Figure 5.3.4c), April (Figure 5.3.4d), September (Figure 5.3.4i), November (Figure 5.3.4k), December (Figure 5.3.4l). There is a statistically significant negative correlation between ENSO and the diurnal minimum amplitude of surface temperature in March in part of north Florida, from Live Oak to Blountstown (Figure 5.3.4c). Also in March, there is a statistically significant positive correlation between ENSO and the diurnal minimum amplitude of surface temperature at points along the western panhandle and parts of south Florida, including the oceanfront coastlines of south

Florida and the coastlines of Lake Okeechobee (Figure 5.3.4c). The statistically significant positive correlation between ENSO and the diurnal minimum amplitude of surface temperature in February is across most of central Florida and some of south Florida (Figure 5.3.4b). In April, this relationship exists in south Florida and along the panhandle coastline (Figure 5.3.4d), a signature which resembles that of March (Figure 5.3.4c). Most of the western panhandle of Florida has this relationship in September (Figure 5.3.4i). In November, the statistically significant positive correlation is present through most of north Florida (Figure 5.3.4k). In December, it is present on most of the northern peninsula, plus parts of the panhandle and parts of south Florida (Figure 5.3.4l).

The strongest relationship between ENSO and the diurnal peak amplitude of surface specific humidity occurs in March, with a statistically significant positive correlation between the two occurring across most of south and central Florida (Figure 5.3.2c) This means that in south and central Florida in March, an El Niño event tends to coincide with higher peak diurnal amplitudes of surface specific humidity, whereas a La Niña event tends to coincide with lower peak diurnal amplitudes of surface specific humidity. This statistically significant positive correlation between ENSO and the diurnal peak amplitude of surface specific humidity is also present in central Florida in April (Figure 5.3.2d) and July (Figure 5.3.2g). There is a statistically significant negative correlation between ENSO and the diurnal peak amplitude of surface specific humidity in north Florida near the Big Bend in April (Figure 5.3.2d) and May (Figure 5.3.2e). In this part of north Florida in April and May, El Niño events tend to coincide with lower diurnal peak amplitudes of surface specific humidity, whereas La Niña events tend to coincide with higher diurnal peak amplitudes of surface specific humidity. Conversely, in north Florida near the Big Bend, in January, there is a statistically significant positive correlation between ENSO and the diurnal peak amplitude of surface specific humidity (Figure 5.3.2a), indicating that the diurnal peak amplitudes of surface specific humidity tend to be higher during El Niños and lower during La Niñas in that region in January.

There is a statistically significant negative correlation between ENSO and the diurnal minimum amplitude of surface specific humidity in January (Figure 5.3.5a), March (Figure 5.3.5c), April (Figure 5.3.5d), and July (Figure 5.3.5g), and a statistically significant positive correlation in April (Figure 5.3.5d) and October (Figure 5.3.5j). The statistically significant negative correlation in January is in north Florida from the Big Bend to Jacksonville, and a small

area south of Blountstown (Figure 5.3.5a). In March, almost all of south and central Florida has this statistically significant negative correlation (Figure 5.3.5c). In April, it's in a small area north of Tampa Bay (Figure 5.3.5d). In July, this relationship is limited to part of central Florida but spans across the peninsula (Figure 5.3.5g). The statistically significant positive correlation between ENSO and the diurnal minimum amplitude of surface specific humidity is present in April in Jacksonville (Figure 5.3.5d). In October, it's present in parts of south Florida and central Florida and the western panhandle coastline (Figure 5.3.5j).

The diurnal peak amplitude of precipitation has a statistically significant positive correlation with ENSO in various parts of Florida in March (Figure 5.3.3c), April (Figure 5.3.3d), June (Figure 5.3.3f), November (Figure 5.3.3k), and December (Figure 5.3.3l). This positive correlation indicates that the diurnal peak amplitudes of precipitation are higher during El Niños and lower during La Niñas. In March, this relationship is present across the entire state of Florida (Figure 5.3.3c). In April, the relationship is present across most of north Florida and part of south Florida between Lake Okeechobee and Everglades City (Figure 5.3.3d). The western side of central Florida as well as north Florida excluding the western panhandle have this statistically significant positive correlation in June (Figure 5.3.3f). Parts of north Florida have this relationship in November as well (Figure 5.3.3k). In December, most of north Florida has this relationship, as well as parts of central and south Florida (Figure 5.3.3l).

To summarize, the relationships between ENSO and the diurnal cycles of surface meteorology in Florida are strongest in the boreal winter months of November and December and in the boreal spring months of March and April. There are some notable relationships in the boreal winter months of January and February and the boreal summer months of June and July as well. During El Niño conditions in these months, in many regions of Florida, the diurnal amplitudes of surface temperature are suppressed, while the diurnal amplitudes of precipitation and surface specific humidity are enhanced. Conversely, during La Niña conditions in these months, the diurnal amplitudes of surface temperature are enhanced, while the diurnal amplitudes of precipitation and surface specific humidity are suppressed. In November, this relationship is limited to north Florida, but spreads throughout most of Florida in December. Interestingly, the relationship between ENSO and the diurnal cycle of these surface meteorology variables is diminished in January. However, in parts of north Florida in January, the diurnal cycle of surface specific humidity is enhanced during El Niños and suppressed during La Niñas.

In February, throughout almost all of central Florida and parts of south Florida, the diurnal amplitudes of surface temperature are dampened during El Niños and enhanced during La Niñas. Then, in March, ENSO has a strong bearing on the surface meteorology through almost the entire state of Florida. On the entire western panhandle, the diurnal amplitude of precipitation is enhanced during El Niños and suppressed during La Niñas, while on the coastline of the western panhandle, the diurnal amplitudes of surface temperature are suppressed during El Niños and enhanced during La Niñas. Similarly, the diurnal amplitudes of surface temperatures are suppressed during El Niños and enhanced during La Niñas along the coastlines in south Florida, including the coastline of Lake Okeechobee. Simultaneously, in central and south Florida, the diurnal amplitudes of surface specific humidity and precipitation are enhanced during El Niños and suppressed during La Niñas. Except for the enhancement/suppression of the diurnal cycles of precipitation and specific humidity in central and south Florida, the relationships between ENSO and the diurnal cycles of Florida surface meteorology that are present in March continue into April. In June, in parts of north Florida and central Florida, the diurnal cycle of precipitation is enhanced during El Niños and suppressed during La Niñas. Then, in July in central Florida, the diurnal cycle of specific humidity is enhanced during El Niños and suppressed during La Niñas.

The suppression of the diurnal cycle of surface temperature coinciding with an amplification of the diurnal cycles of precipitation and specific humidity during El Niños indicates an increase in cloudiness which shields the downwelling shortwave flux from warming the surface during daylight hours. Similarly, during La Niñas, the amplification of the diurnal cycle of temperature coinciding with the suppression of the diurnal cycle of precipitation indicates decreased cloud cover which allows the downwelling shortwave flux to warm the surface during daylight hours and the upwelling longwave flux to escape the atmosphere overnight, cooling the surface. The results shown here are mostly consistent with the known teleconnections between ENSO and the climate of the southeast US, which have been shown to be strongest during boreal winter. The expected teleconnections during boreal winter for North America, with a focus on the southeast US, are as follows: During El Niños, especially during eastern Pacific (EP) El Niños, the Pacific jet stream is oriented zonally across the southern US, bringing wetter weather to that region. During La Niña boreal winters, the Pacific jet stream becomes situated further north and becomes more variable, with amplified ridges and troughs, creating drier and warmer conditions in the southern US for most of the winter. Boreal winter,

and the ENSO teleconnections associated with it, are generally thought to include January, yet the results shown here indicate that ENSO has a strong relationship with the diurnal cycles of surface meteorology in Florida during only the first half of winter (November-December). The relationship is diminished in January and February and is galvanized in boreal spring. For the spring months of March and April, one of the most interesting findings is the suppression/enhancement of the diurnal cycle of surface temperature along certain coastlines, including the coastline of Lake Okeechobee, possibly indicating sea-breeze induced coastal cloud formation during El Niño springs. The boreal winter relationships between ENSO and the diurnal cycle of surface meteorology in Florida are consistent with the known ENSO teleconnections, particularly those that occur during EP El Niños. As Mo (2010) indicates, the central Pacific (CP) El Niños have weaker teleconnections with southeastern US regional climate.

Here, we also isolate the interannual component of ENSO using EEMD and compute correlations between this interannual component of ENSO and the monthly characteristics of the Florida diurnal cycle (i.e., the diurnal peak and minimum amplitudes and phases of surface temperature, surface specific humidity, and precipitation) (Figures 5.65-72). This analysis reveals strong relationships between the interannual component of ENSO and the Florida diurnal cycle in January and February (Figures 5.65-72). These relationships in January and February go undetected by the simple correlation with the Nino3.4 index (Figures 5.57-64). The relationships that are revealed are enhanced amplitudes of diurnal precipitation across all of Florida in January and February during El Niños and suppressed amplitudes of diurnal precipitation during La Niñas (Figures 5.67 and 5.70-72). Additionally, there are suppressed diurnal amplitudes of surface temperature across the entire peninsula during El Niño Januarys (Figures 5.65, 5.68, and 5.71), and enhanced diurnal amplitudes of surface temperature across the peninsula during La Niñas (5.65, 5.68, and 5.72). In the analysis using the raw Nino3.4 SST index, these conditions wintertime associations (enhanced diurnal precipitation with suppressed diurnal temperature during El Niño winters, and suppressed diurnal precipitation with enhanced diurnal temperature during La Niña winters) were shown to exist in early winter (November-December), but diminished in January and February, before re-emerging in March and April. The seeming diminishment of this association in January and February was unexpected because ENSO teleconnections with the southeast US are thought to be strong through the duration of the winter.

The isolation of the interannual component of the Nino3.4 index, as we use here, reveals that these teleconnections between ENSO and the Florida diurnal cycle continue through the duration of winter. Variations of ENSO at other scales (both high frequency and low frequency) interfere with these teleconnections. Physically, these results are indicative of increased cloud cover in Florida during El Niño winters, suppressing the diurnal amplitudes of surface temperature. Conversely, during La Niña winters, there is decreased cloud cover, enhancing the diurnal amplitudes of surface temperature and suppressing diurnal scale precipitation.

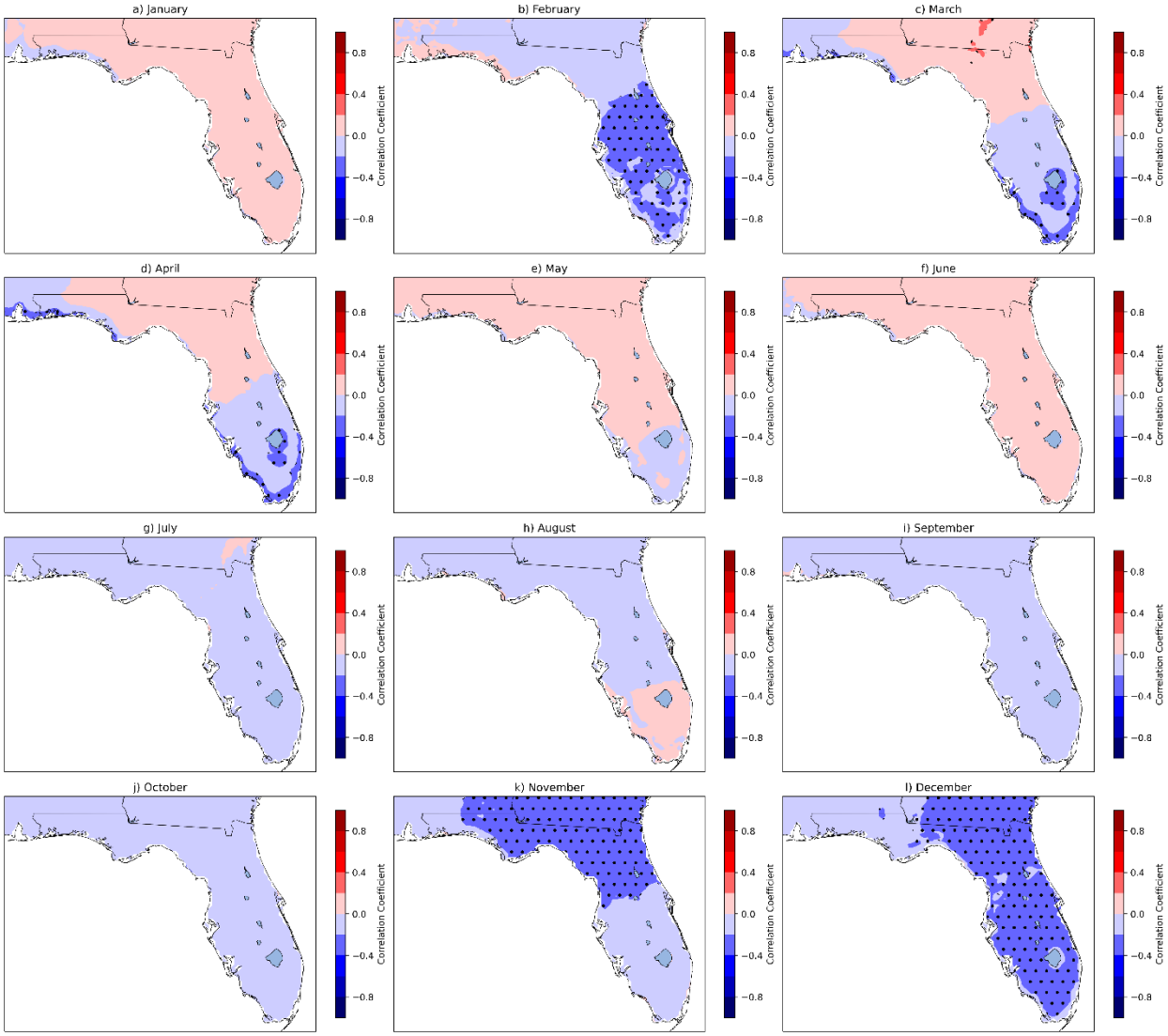

Figure 5.57. Correlation between diurnal peak amplitude of surface temperature in FLAReS1.0 and the concurrent Nino3.4 index over 1903-2004. Stippling indicates statistical significance.

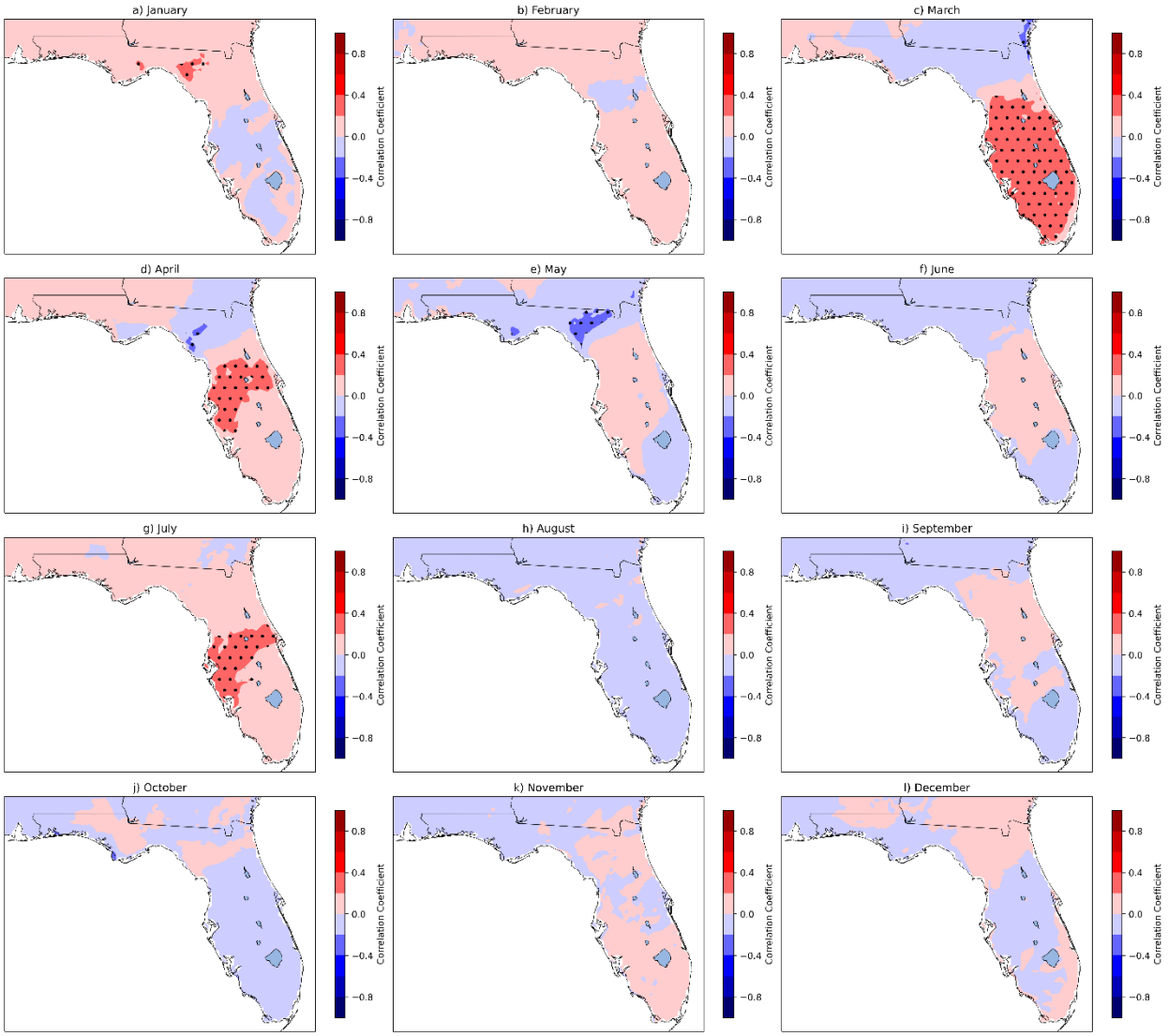

Figure 5.58. Correlation between diurnal peak amplitude of surface specific humidity in FLAReS1.0 and the concurrent Nino3.4 index over 1903-2004. Stippling indicates statistical significance.

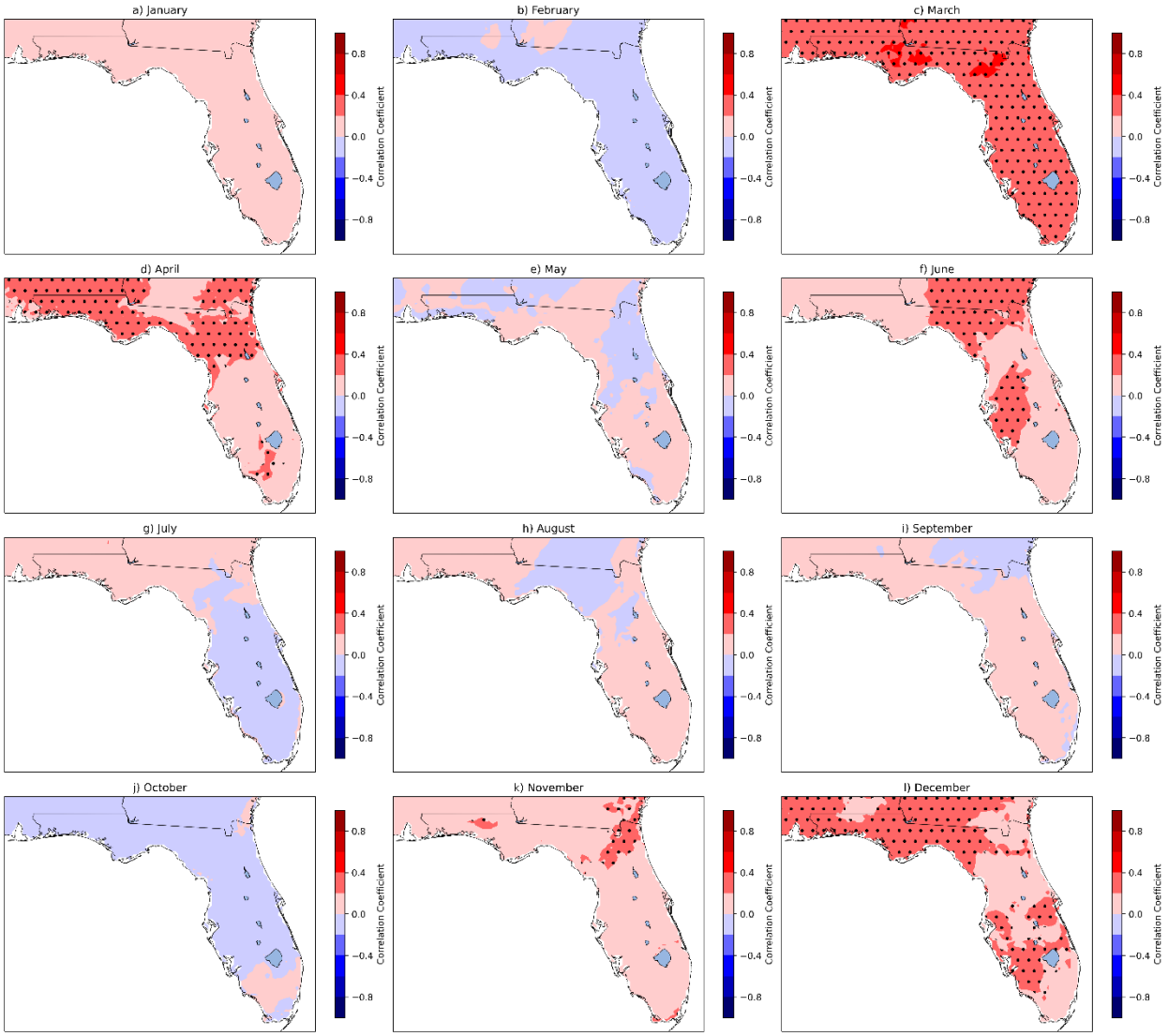

Figure 5.59. Correlation between diurnal peak amplitude of precipitation in FLAReS1.0 and the concurrent Nino3.4 index over 1903-2004. Stippling indicates statistical significance.

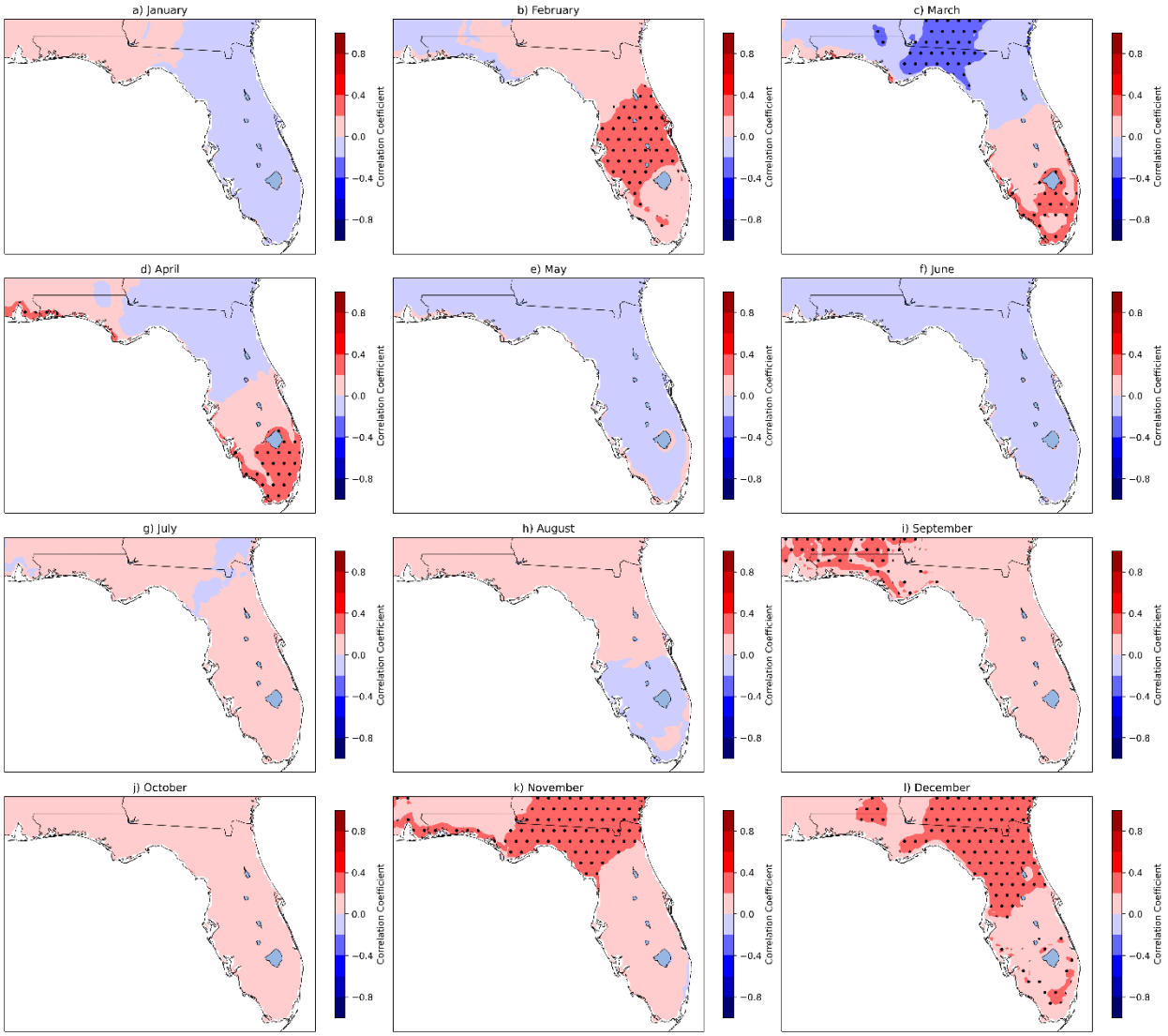

Figure 5.60. Correlation between diurnal minimum amplitude of surface temperature in FLAReS1.0 and the concurrent Nino3.4 index over 1903-2004. Stippling indicates statistical significance.

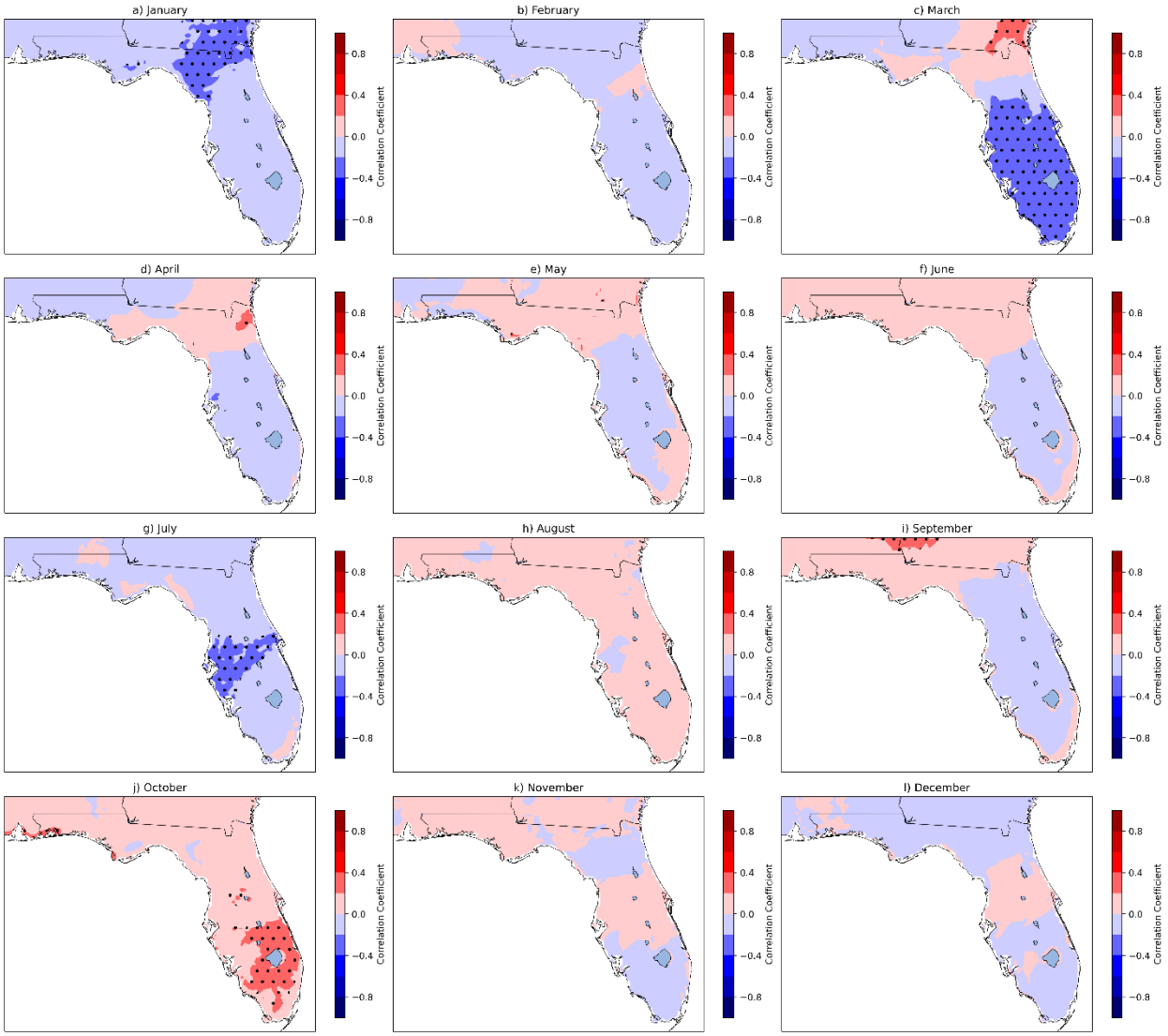

Figure 5.61. Correlation between diurnal minimum amplitude of surface specific humidity in FLAReS1.0 and the concurrent Nino3.4 index over 1903-2004. Stippling indicates statistical significance.

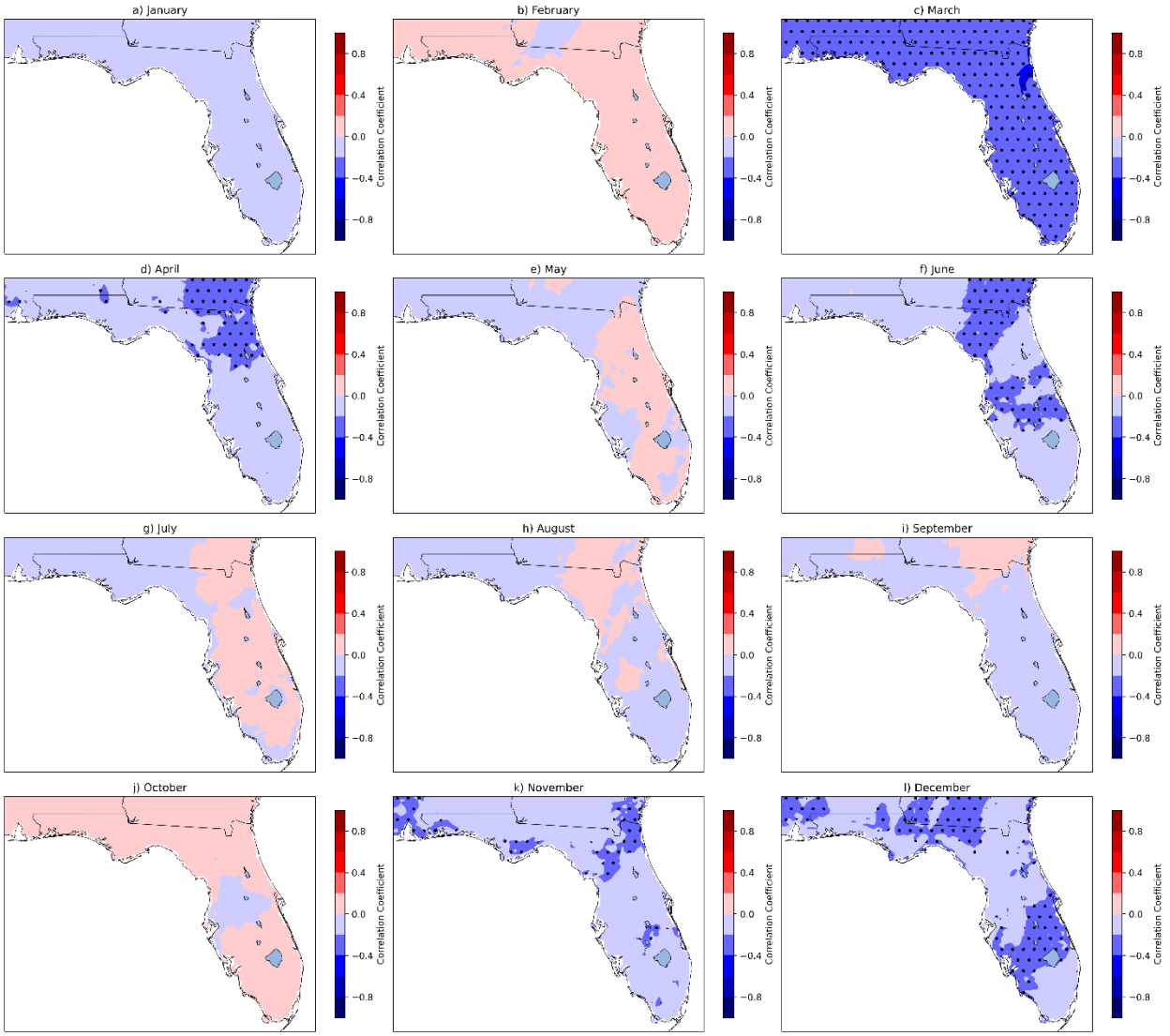

Figure 5.62. Correlation between diurnal minimum amplitude of precipitation in FLAReS1.0 and the concurrent Nino3.4 index over 1903-2004. Stippling indicates statistical significance.

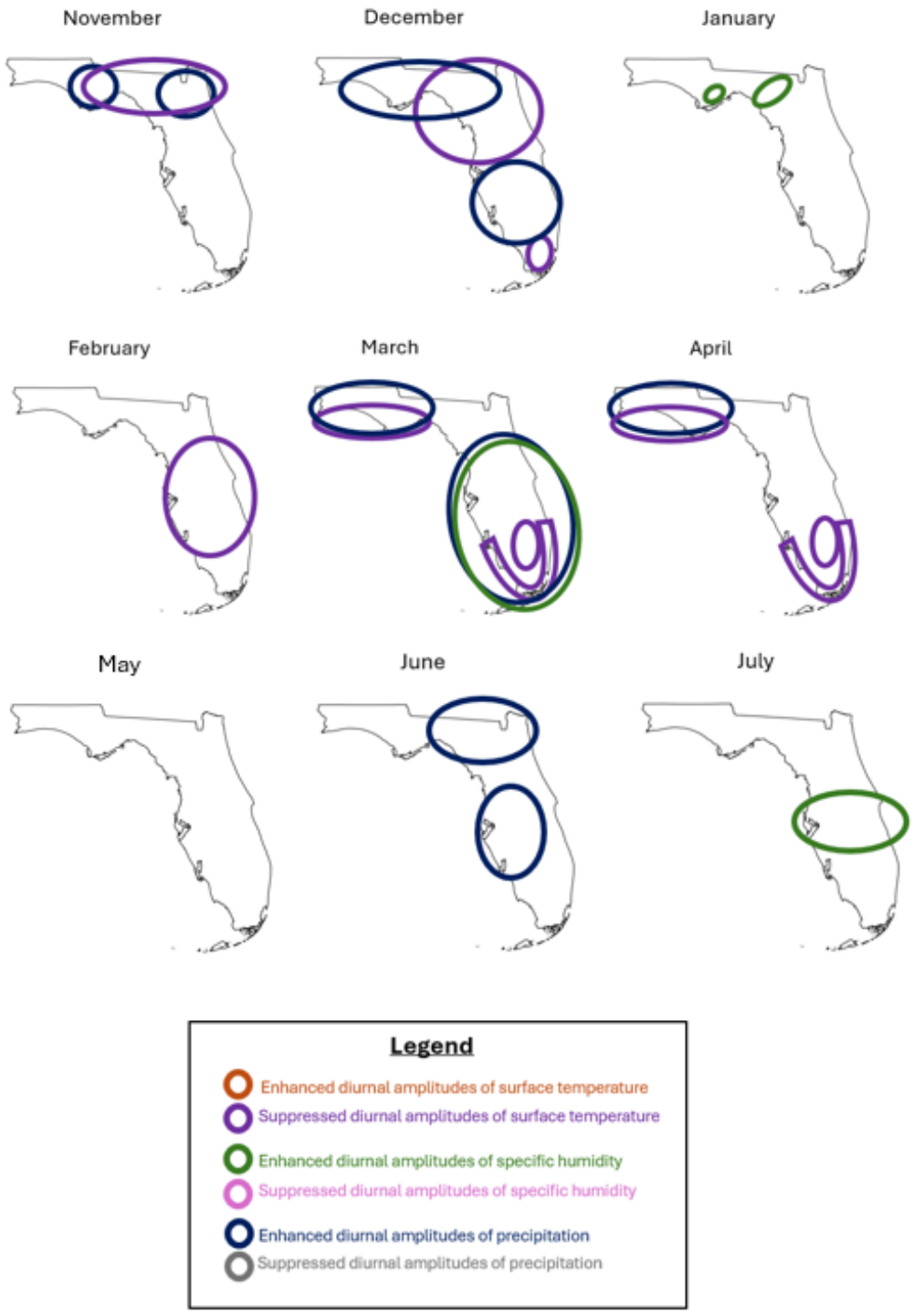

Figure 5.63. The responses of the diurnal amplitudes of surface temperature, specific humidity, and precipitation in Florida during November—July to concurrent El Niño conditions.

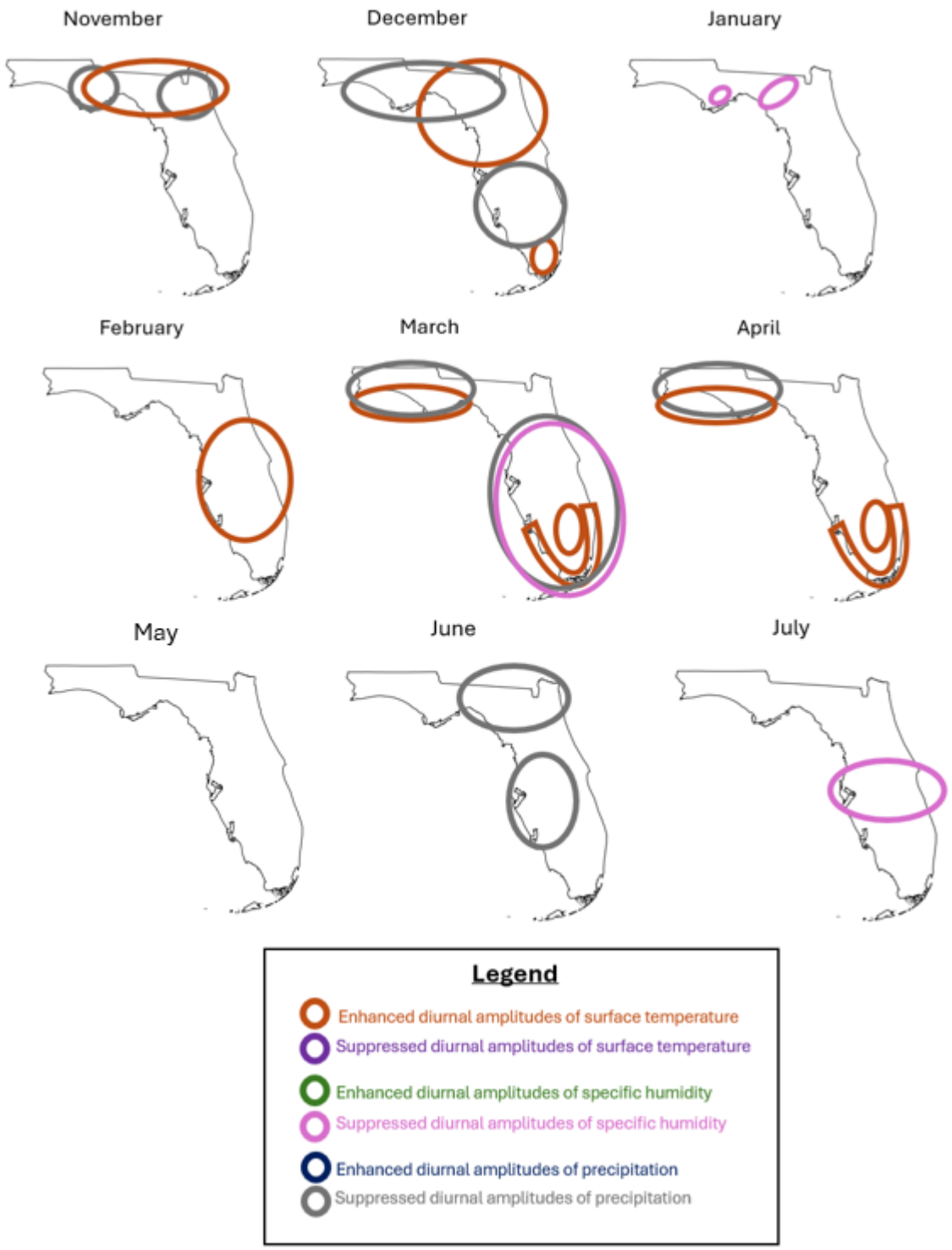

Figure 5.64. The responses of the diurnal amplitudes of surface temperature, specific humidity, and precipitation in Florida during November—July to concurrent La Niña conditions.

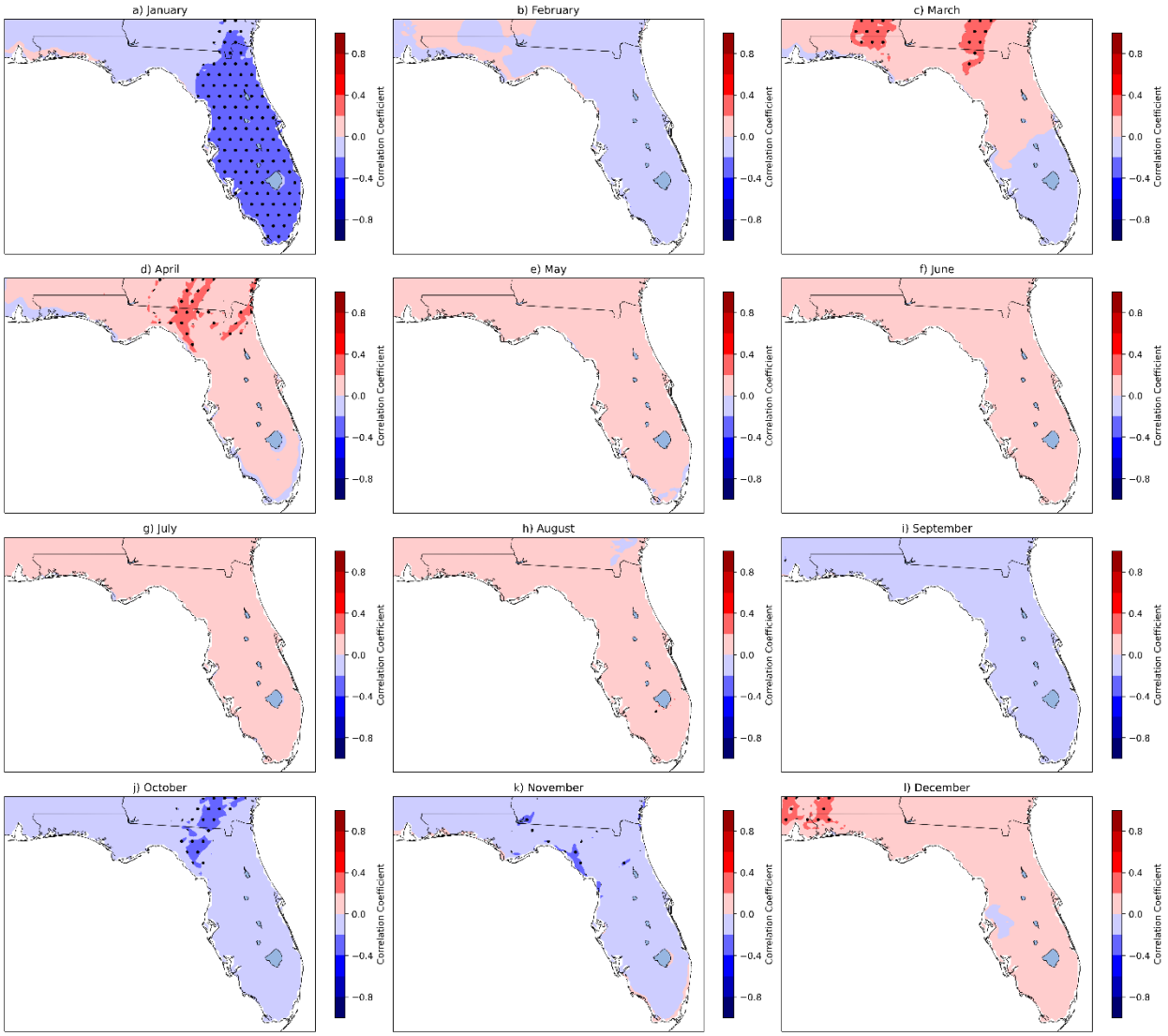

Figure 5.65. Correlation between diurnal peak amplitude of surface temperature in FLAReS1.0 and the concurrent *interannual component* of the Nino3.4 index over 1903-2004. Stippling indicates statistical significance.

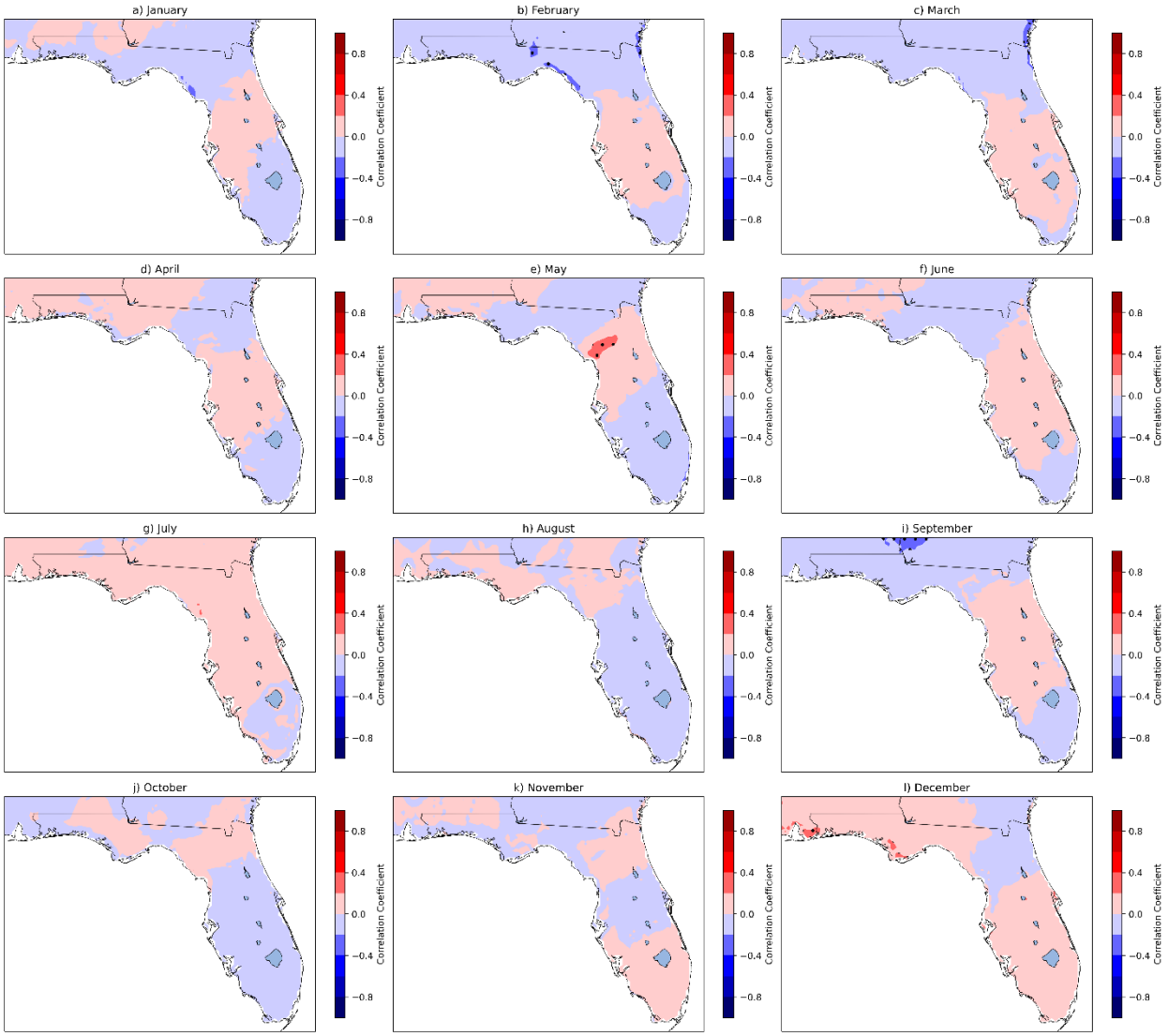

Figure 5.66. Correlation between diurnal peak amplitude of surface specific humidity in FLAReS1.0 and the concurrent *interannual component* of the Nino3.4 index over 1903-2004. Stippling indicates statistical significance.

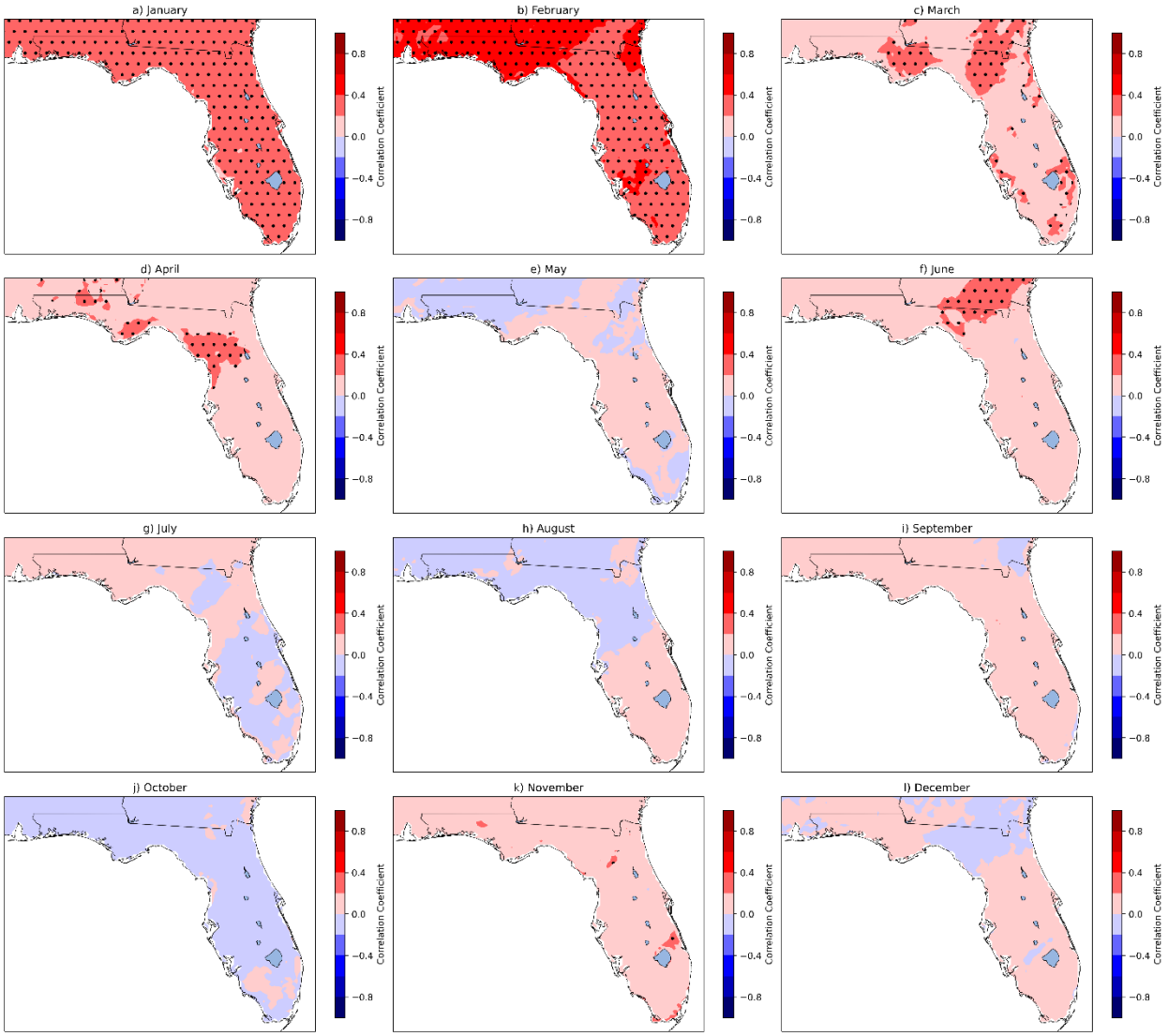

Figure 5.67. Correlation between diurnal peak amplitude of precipitation in FLAReS1.0 and the concurrent *interannual component* of the Nino3.4 index over 1903-2004. Stippling indicates statistical significance.

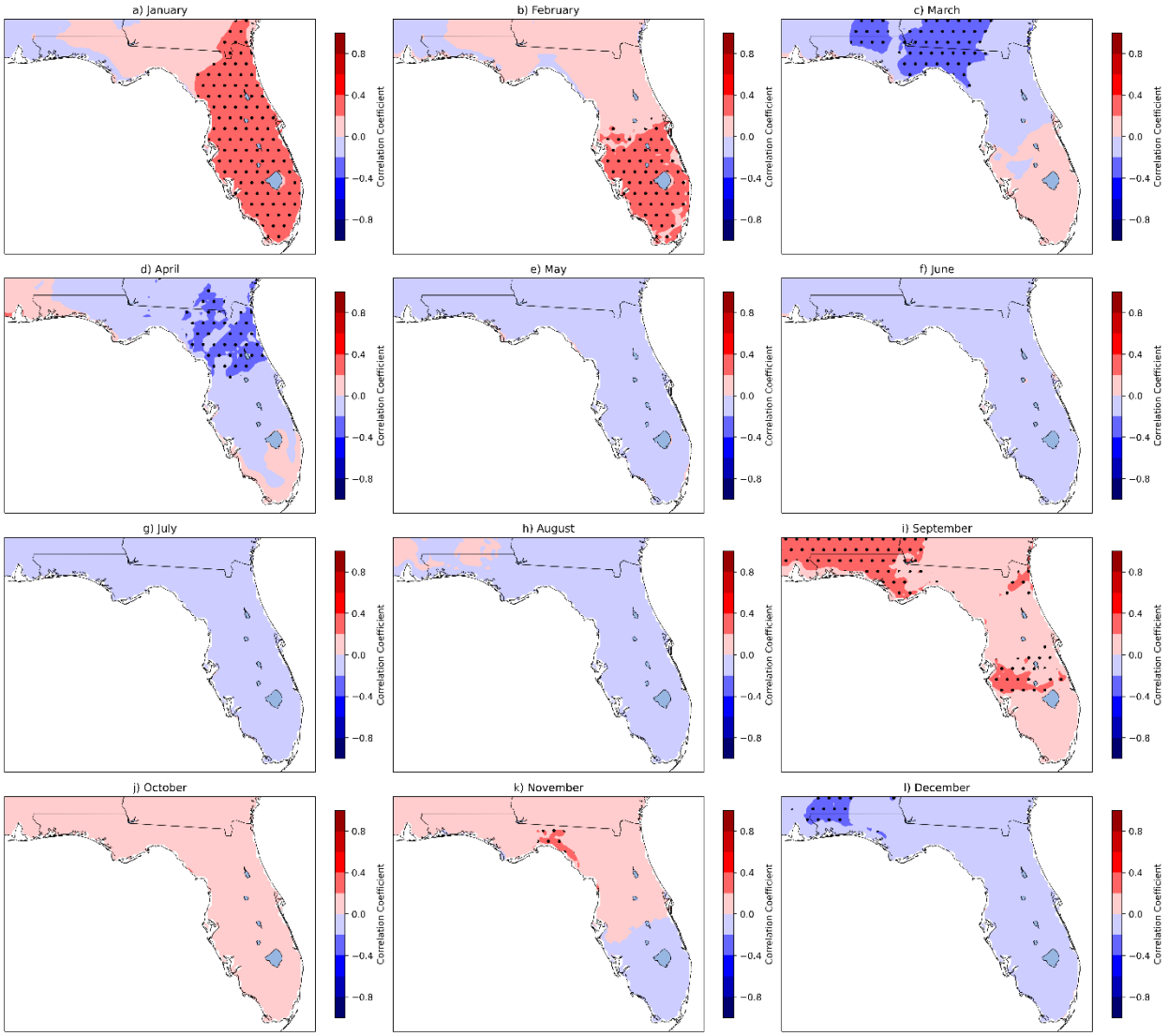

Figure 5.68. Correlation between diurnal minimum amplitude of surface temperature in FLAReS1.0 and the concurrent *interannual component* of the Nino3.4 index over 1903-2004. Stippling indicates statistical significance.

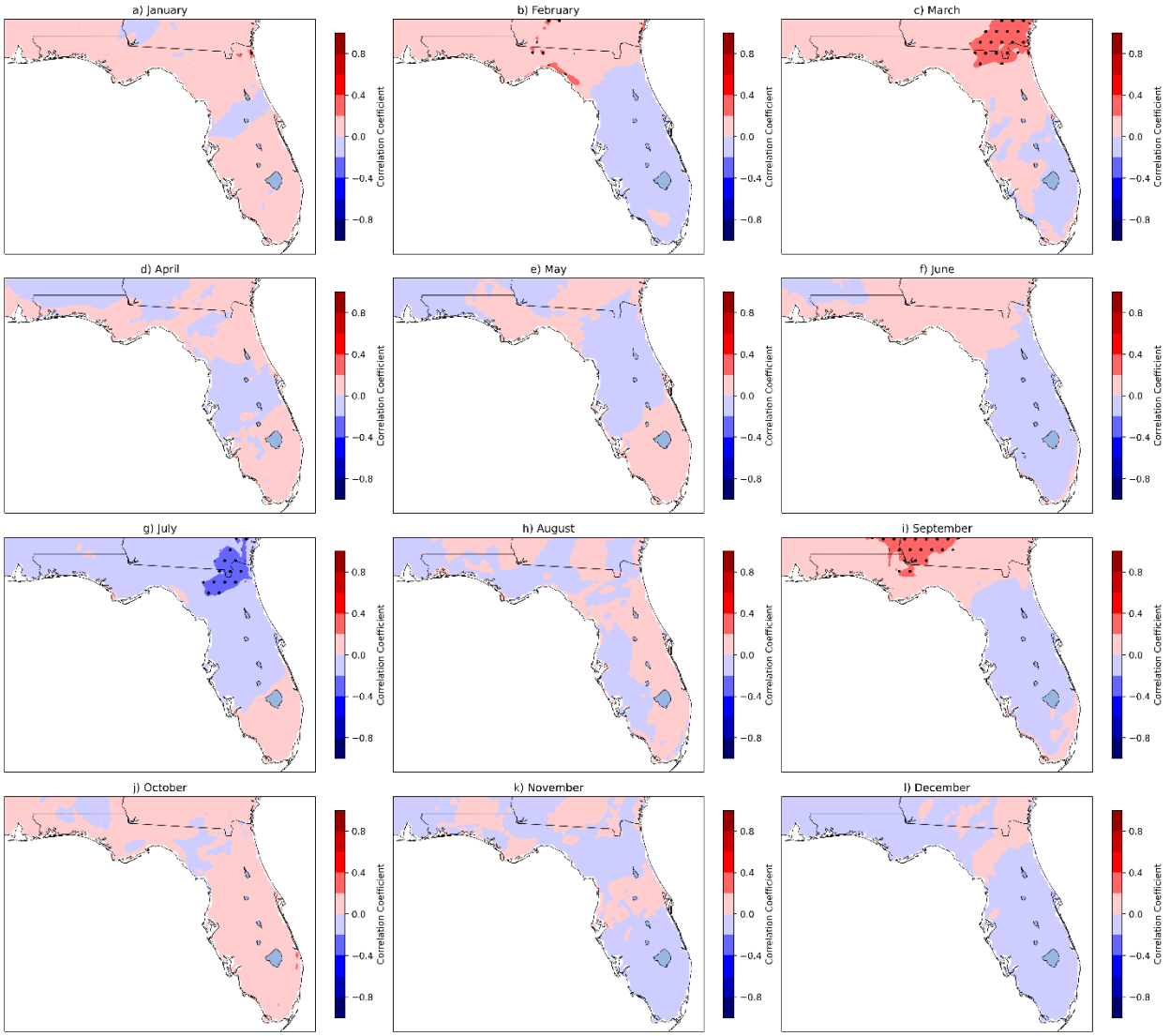

Figure 5.69. Correlation between diurnal minimum amplitude of surface specific humidity in FLAReS1.0 and the concurrent *interannual component* of the Nino3.4 index over 1903-2004. Stippling indicates statistical significance.

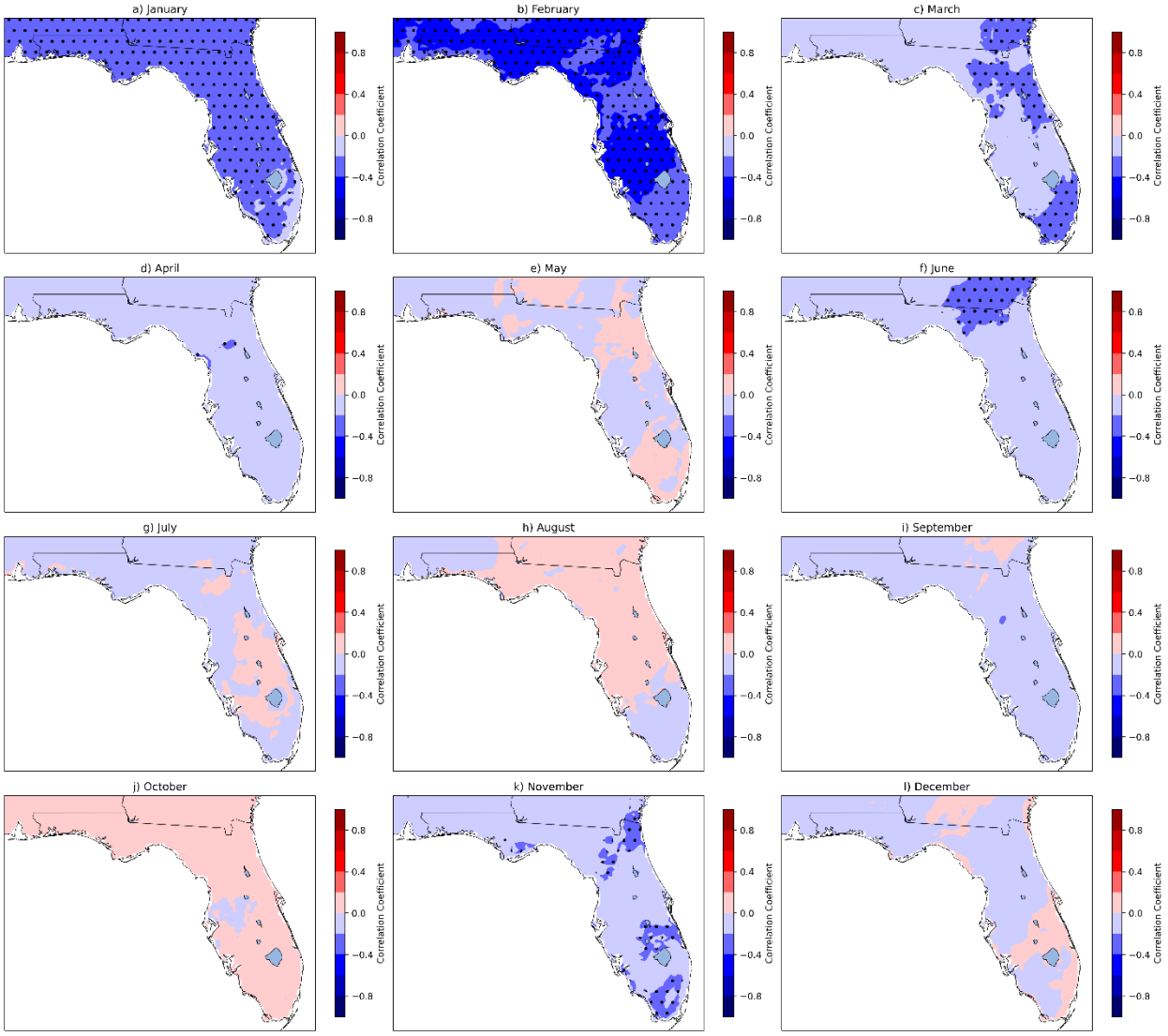

Figure 5.70. Correlation between diurnal minimum amplitude of precipitation in FLAReS1.0 and the concurrent *interannual component* of the Nino3.4 index over 1903-2004. Stippling indicates statistical significance.

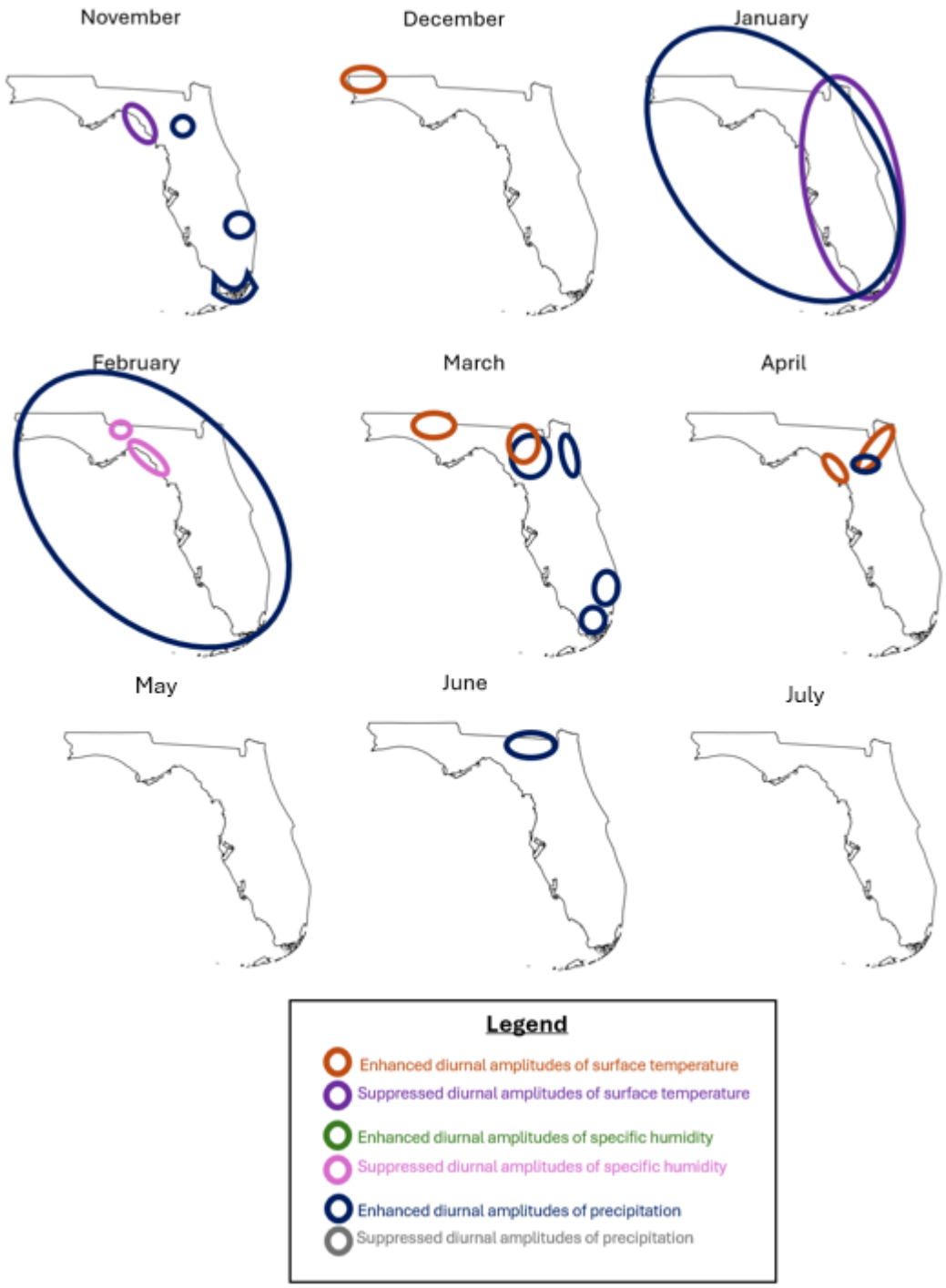

Figure 5.71. The responses of the diurnal amplitudes of surface temperature, specific humidity, and precipitation in Florida during November—July to concurrent El Niño in the *interannual component* of the Nino3.4 SST index.

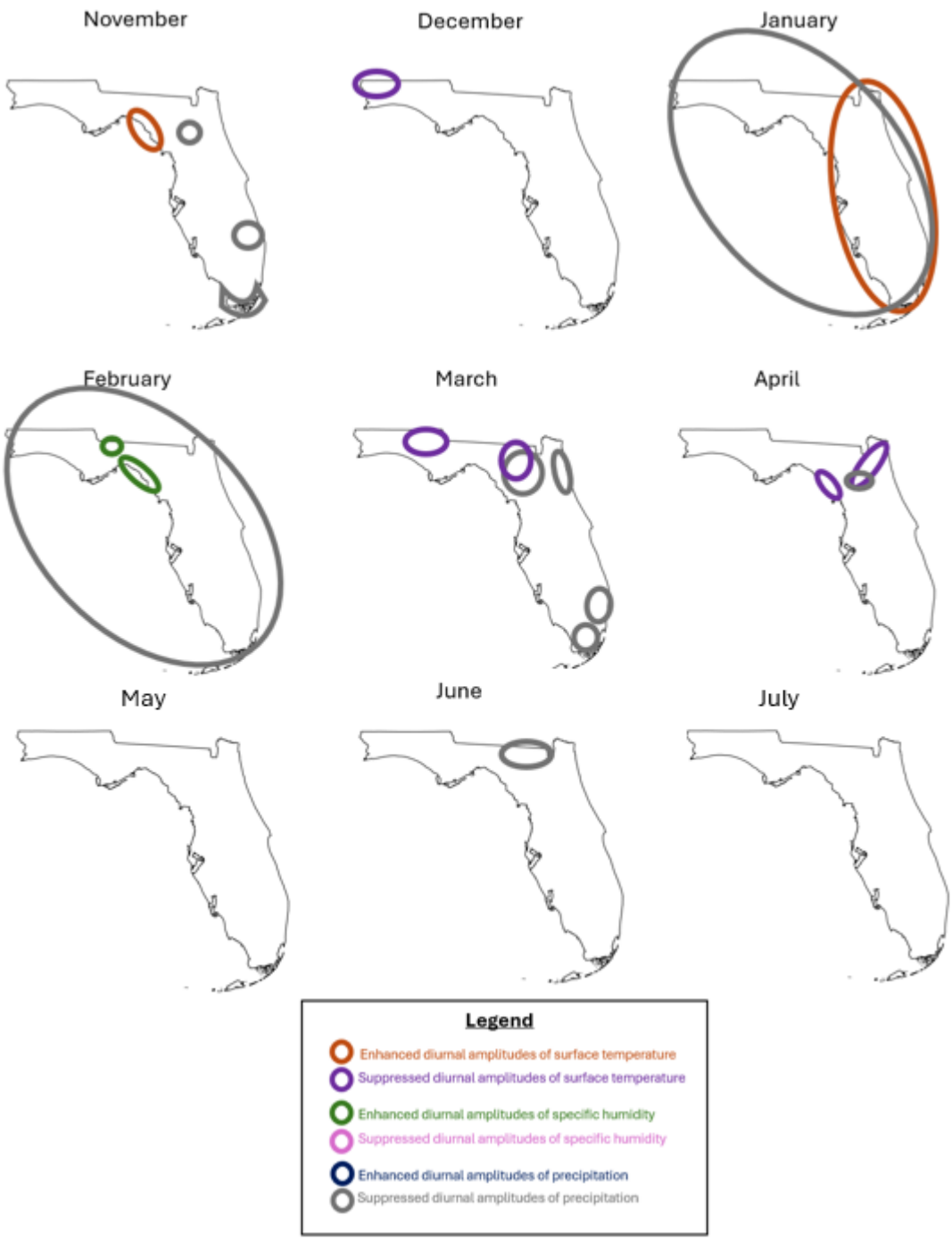

Figure 5.72. The responses of the diurnal amplitudes of surface temperature, specific humidity, and precipitation in Florida during November—July to concurrent La Niña in the *interannual component* of the Nino3.4 SST index.

5.3.2 Atlantic-Pacific interbasin SST gradient

The Atlantic-Pacific interbasin SST gradient has significant impacts on the diurnal cycles of surface meteorology in many parts of Florida in May and June, and in some parts of Florida in March, April, and July. The significant impacts are mostly on the diurnal amplitudes of the surface meteorology variables, whereas the diurnal phases of these variables are not significantly affected by the interbasin SST gradient. Figures that show the relationships between the diurnal phase of Florida surface meteorology and the Atlantic-Pacific interbasin SST gradient can be found in the Appendix. The analysis here focuses on the relationships between the interbasin SST gradient and the diurnal amplitudes of surface meteorology variables in Florida.

In March, in parts of south Florida,, the magnitude of the interbasin SST gradient affects the amplitudes of the diurnal-scale precipitation. When the magnitude of the interbasin SST gradient is small, the amplitudes of diurnal-scale precipitation are large. When the SST gradient is large, however, the amplitudes of diurnal-scale precipitation are suppressed. (Figures 5.3.9a and 5.3.12a). In April, on the western Florida panhandle coastline, the amplitudes of the diurnal cycle of specific humidity are enhanced when the interbasin SST gradient is weak, and the amplitudes of the diurnal cycle of specific humidity are suppressed when the SST gradient is strong (Figures 5.3.8b and 5.3.11b). In May, several areas of Florida are affected by the interbasin SST gradient. For instance, on the western panhandle coastline, the diurnal amplitudes of surface temperature are enhanced when the interbasin SST gradient is weak, and the diurnal amplitudes of surface temperature are suppressed when the SST gradient is strong (Figures 5.3.7c and 5.3.10c). In other parts of north Florida, near the coast, the diurnal amplitudes of precipitation are suppressed when the interbasin SST gradient is weak, and the diurnal amplitudes of precipitation are enhanced when the interbasin SST gradient is strong (Figure 5.3.9c and 5.3.12c). In north Florida, from the Big Bend northeastward to the Georgia border, the diurnal amplitudes of specific humidity are enhanced when the interbasin SST gradient is weak, and the diurnal amplitudes of specific humidity are suppressed when the interbasin SST gradient is strong (Figures 5.3.8c and 5.3.11c). Along the south Florida coastline and

the eastern coastline of Lake Okeechobee, the diurnal amplitudes of surface temperature are enhanced when the interbasin SST gradient is weak, and the diurnal amplitudes of surface temperature are suppressed when the interbasin SST gradient is strong (Figures 5.3.7c and 5.3.10c). Around Gasparilla Sound-Charlotte Harbor Aquatic Preserve, diurnal amplitudes of precipitation are suppressed when the interbasin SST gradient is weak, and they are enh anced when the interbasin SST gradient is strong (Figures 5.3.9c and 5.3.12c). In June, as in May, many areas of Florida are affected by the interbasin SST gradient. On some coastlines, including the south Florida coastline, the Jacksonville area, and the Apalachicola National Forest area, the diurnal amplitudes of specific humidity are enhanced when the interbasin SST gradient is weak, and the diurnal amplitudes of specific humidity are suppressed when the interbasin SST gradient is strong (Figures 5.3.8d and 5.3.11d). Across central Florida, the diurnal amplitudes of precipitation are suppressed when the interbasin SST gradient is weak, and the diurnal amplitudes of precipitation are enhanced when the interbasin SST gradient is strong (Figures 5.3.9d and 5.3.12d). In July, the effect of the interbasin SST gradient stretches across the Florida peninsula from the Tampa Bay area to Cape Canaveral. Specifically, the diurnal amplitudes of specific humidity are suppressed when the interbasin SST gradient is weak, and they are enhanced when the interbasin SST gradient is strong (Figures 5.3.8e and 5.3.11e).

The effect of the interbasin Atlantic-Pacific SST gradient on the Florida diurnal cycle varies seasonally and is strongest in May and June. In March and April, a strong interbasin SST gradient may suppress the diurnal cycles of precipitation and specific humidity in Florida. However, in May, the weak interbasin SST gradient may suppress diurnal precipitation on parts of the gulf coast, while enhancing the diurnal cycle of specific humidity in the Big Bend region. Similarly, in June, a weak interbasin SST gradient is also associated with a suppression of diurnal-scale precipitation on most of peninsular Florida and a simultaneous enhancement of the diurnal amplitudes of specific humidity in some coastal parts of Florida. This suppression of diurnal-scale precipitation in May and June may indicate a delayed onset of the Florida summer wet season when the Atlantic-Pacific interbasin SST gradient is weak. The relationship between the interbasin SST gradient and diurnal cycle of Florida surface meteorology wanes in July

and August, suggesting that the interbasin SST gradient has minimal influence on the diurnal cycle in Florida while the summer wet season is underway.

Here, we also isolate the interannual component of the interbasin SST gradient using EEMD and compute correlations between this interannual component and the monthly characteristics of the Florida diurnal cycle (i.e., the diurnal peak and minimum amplitudes and phases of surface temperature, surface specific humidity, and precipitation) (Figures 5.81-90).

This analysis using the interannual component of the interbasin SST gradient reinforces the robustness of the strong teleconnections between the Florida diurnal cycle and the interbasin SST gradient during May. In May, if the interbasin SST gradient is strong, there is enhancement of amplitudes of diurnal-scale precipitation in Florida, particularly along the Gulf coast (Figures 5.75, 5.78, 5.80, 5.83, 5.86, and 5.90). Additionally, in May, if the interbasin SST gradient is strong, there is suppression of the diurnal amplitudes of temperature along the Gulf coast and the east coast of Lake Okeechobee (Figures 5.73, 5.76, 5.80, 5.81, 5.84, and 5.90). Simultaneously, there is suppression of the diurnal amplitudes of specific humidity in the Big Bend region (Figures 5.74, 5.77, 5.80, 5.82, 5.85, and 5.90). A strong interbasin SST gradient corresponds to strengthened easterly trade winds. With strengthened easterly trade winds, we expect a relaxation of the onshore flow from the Gulf of Mexico onto the Gulf coast of Florida. However, the results here indicate the presence of onshore flow from the Gulf of Mexico onto the Gulf coast of Florida. Westerly flow is also indicated inland over south Florida by the suppression of diurnal temperatures on the eastern coast of Lake Okeechobee (Figures 5.73, 5.76, 5.80, 5.81, 5.84, and 5.90), which are likely explained by cloud formation on the eastern coast of the Lake. Therefore, there is most likely another mechanism, besides strengthening trade winds, responsible for the teleconnection between the interbasin SST gradient and the Florida diurnal cycle in May.

This analysis using the interannual component of the interbasin SST gradient reveals a teleconnection to the Florida diurnal cycle in April. Across most of Florida, a strong interbasin SST gradient is associated with enhanced diurnal amplitudes of surface temperature (Figures 5.81, 5.84, and 5.90), while a weak interbasin SST gradient is associated with suppressed diurnal amplitudes of surface temperature in April (Figures

5.81, 5.84, and 5.89). In the case of a strong interbasin SST gradient, the enhanced diurnal amplitudes of surface temperature over Florida could be explained by unusual quiet with respect to synoptic activity over Florida due to strengthened trade winds, thereby allowing for clear skies and daytime surface heating. Conversely, a weak interbasin SST gradient would lead to weak trade winds, which allows for more synoptic activity to impact Florida during April, thereby suppressing the diurnal amplitudes of surface temperature.

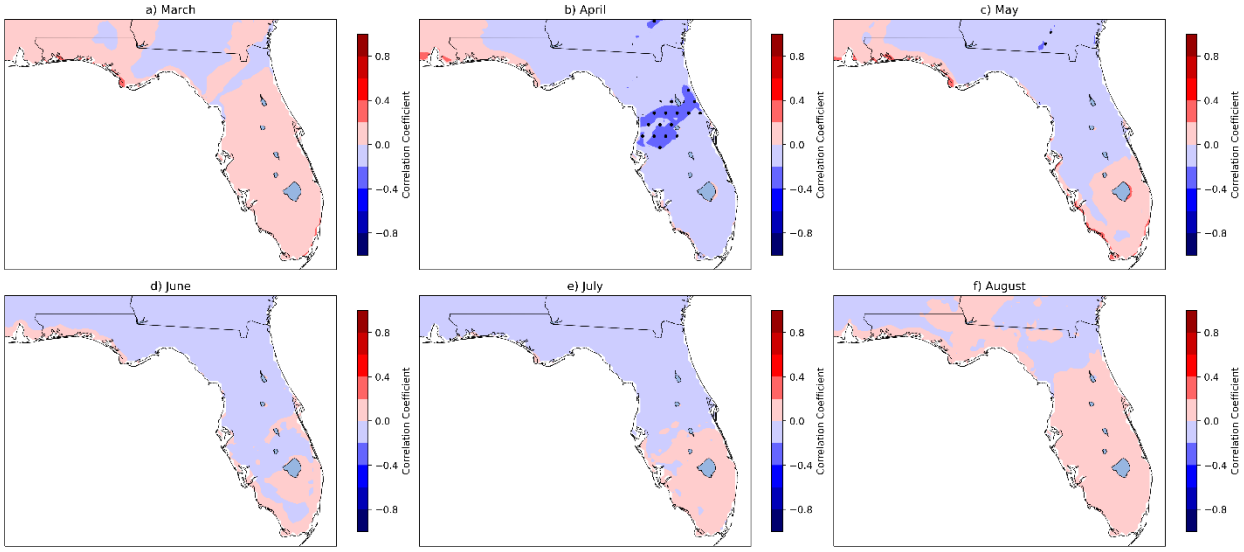

Figure 5.73. Correlation between diurnal peak amplitude of surface temperature in FLAReS1.0 and the concurrent Atlantic-Pacific SST gradient over 1903-2004. Stippling indicates statistical significance.

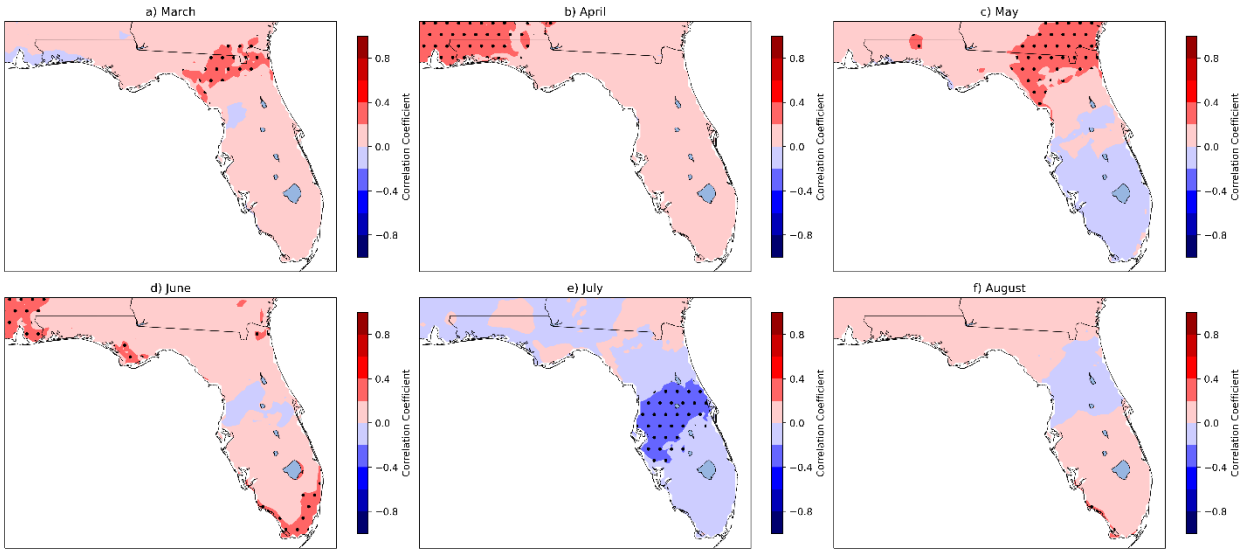

Figure 5.74. Correlation between diurnal peak amplitude of surface specific humidity in FLAReS1.0 and the concurrent Atlantic-Pacific SST gradient over 1903-2004. Stippling indicates statistical significance.

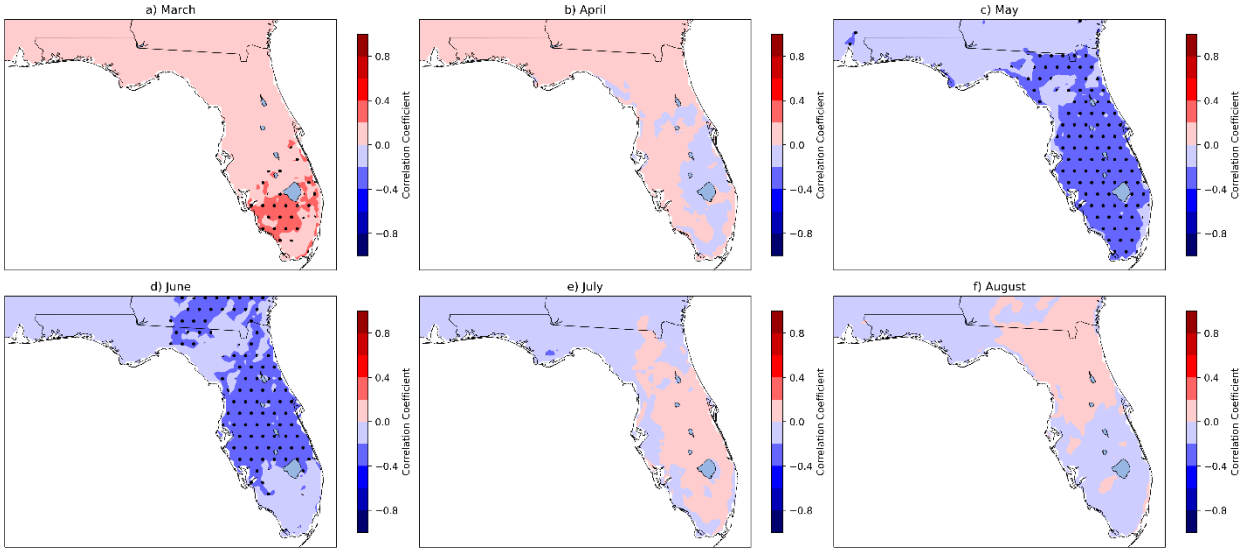

Figure 5.75. Correlation between diurnal peak amplitude of precipitation in FLAReS1.0 and the concurrent Atlantic-Pacific SST gradient over 1903-2004. Stippling indicates statistical significance.

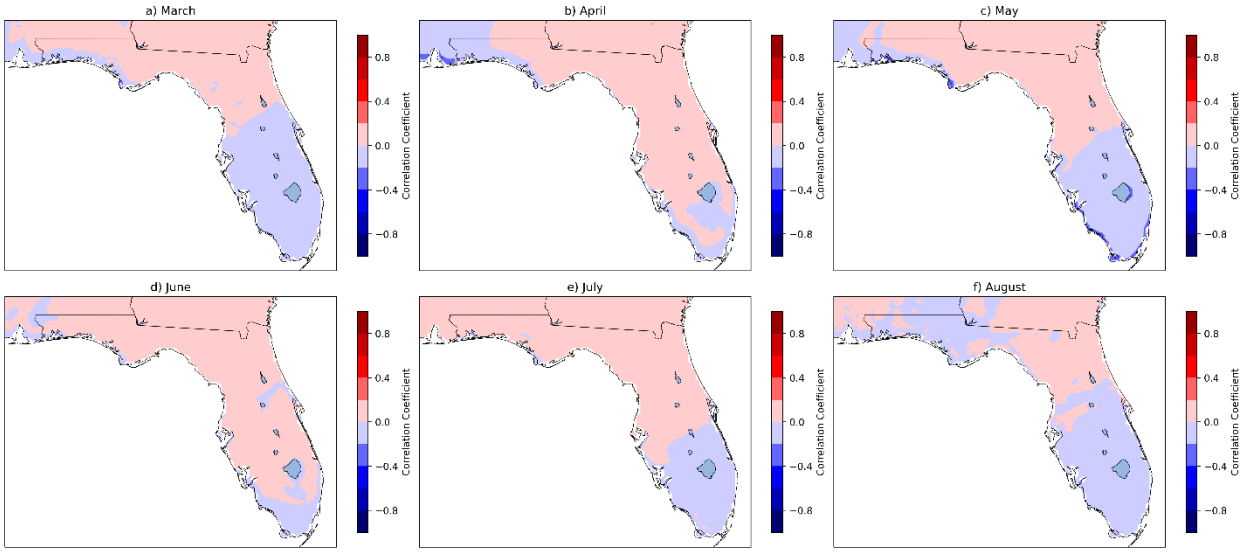

Figure 5.76. Correlation between diurnal minimum amplitude of surface temperature in FLAReS1.0 and the concurrent Atlantic-Pacific SST gradient over 1903-2004. Stippling indicates statistical significance.

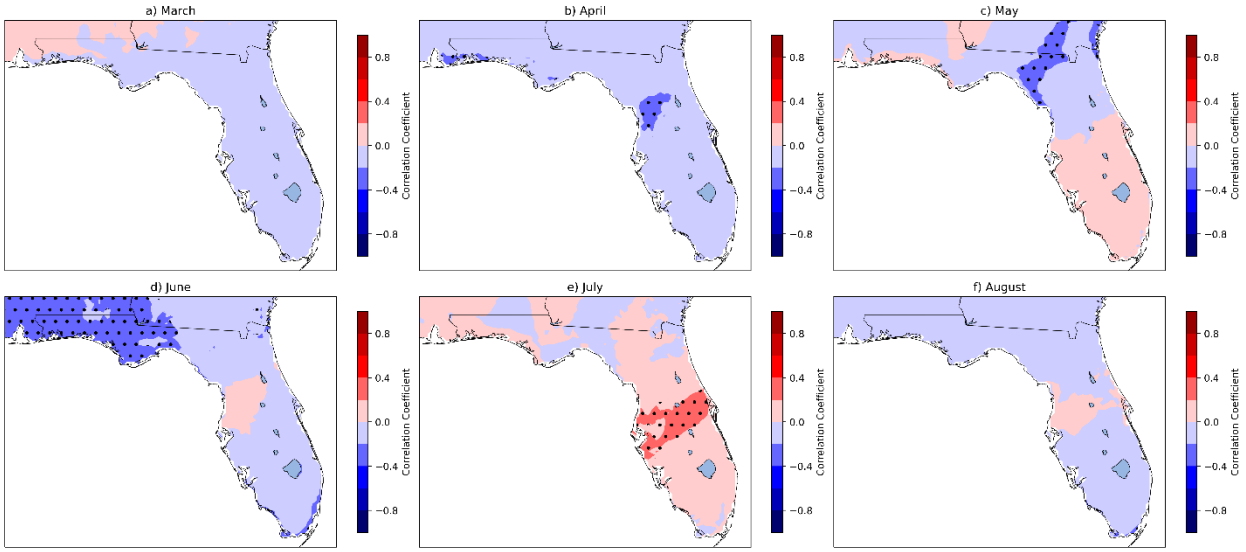

Figure 5.77. Correlation between diurnal minimum amplitude of surface specific humidity in FLAReS1.0 and the concurrent Atlantic-Pacific SST gradient over 1903-2004. Stippling indicates statistical significance.

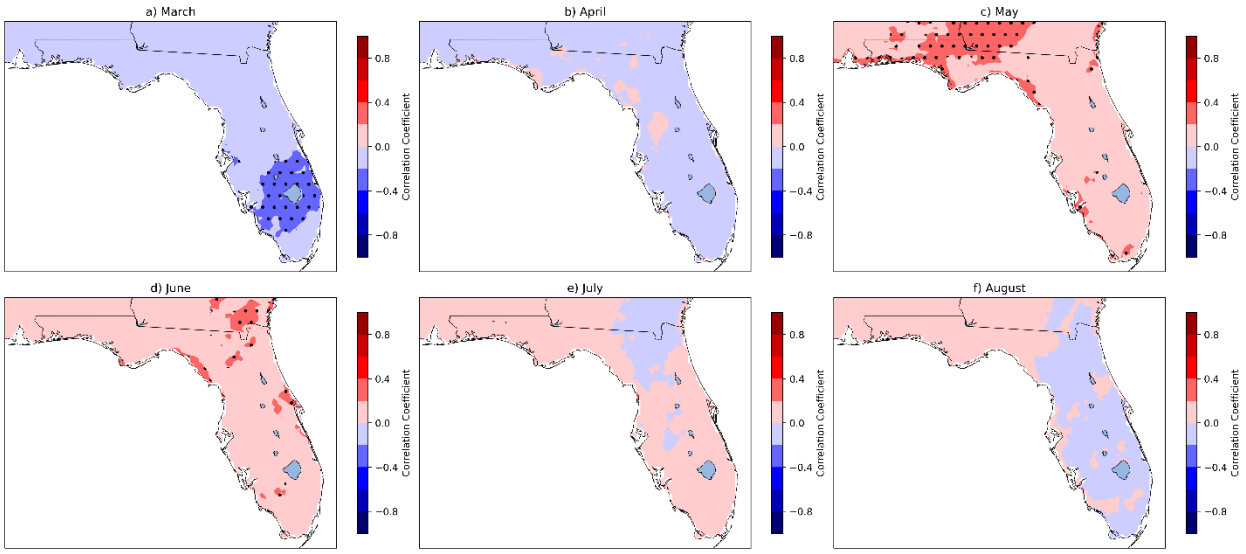

Figure 5.78. Correlation between diurnal minimum amplitude of precipitation in FLAReS1.0 and the concurrent Atlantic-Pacific SST gradient over 1903-2004. Stippling indicates statistical significance.

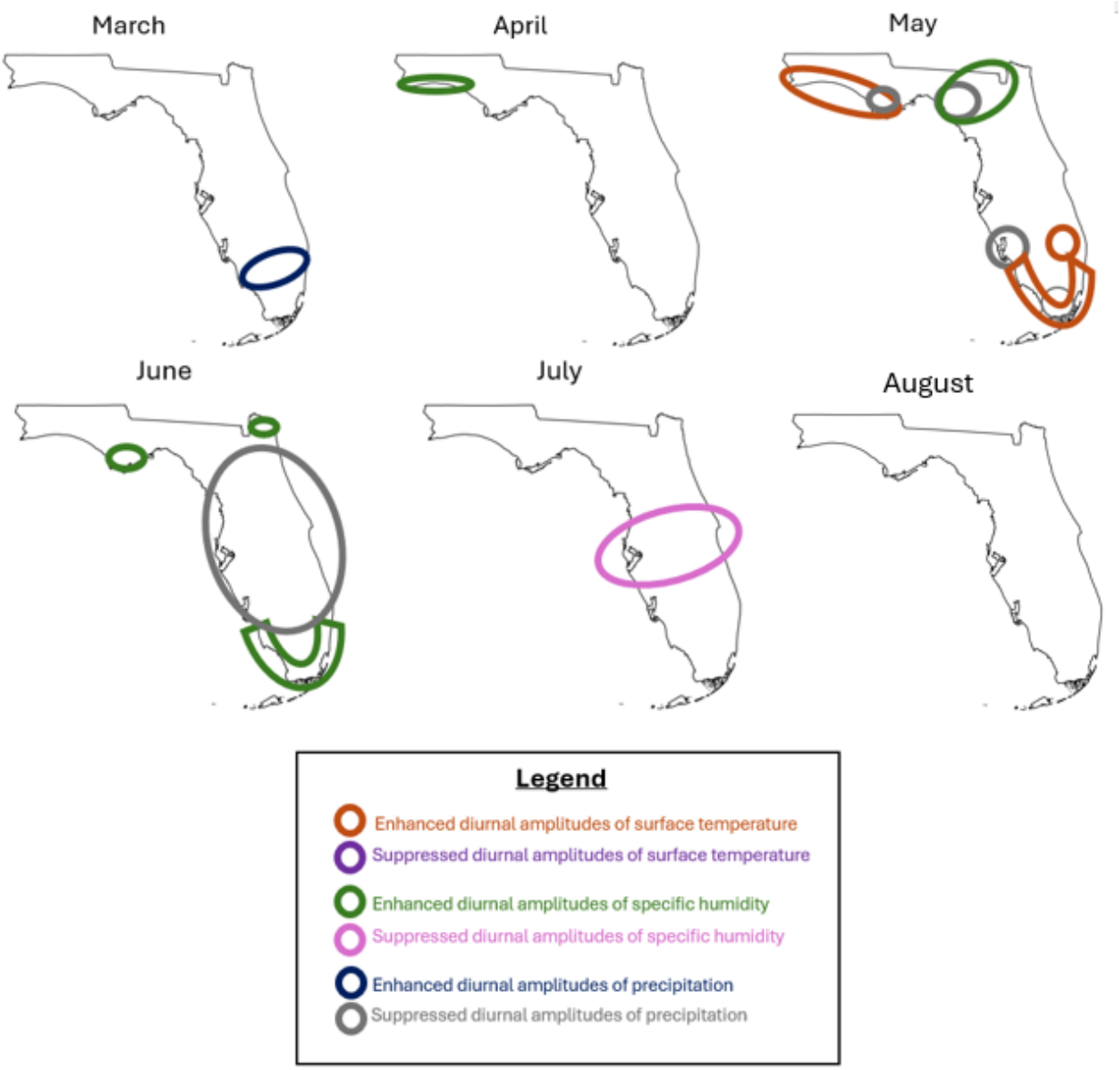

Figure 5.79. The responses of the diurnal amplitudes of surface temperature, specific humidity, and precipitation in Florida to a weak Atlantic-Pacific interbasin SST gradient during March--August.

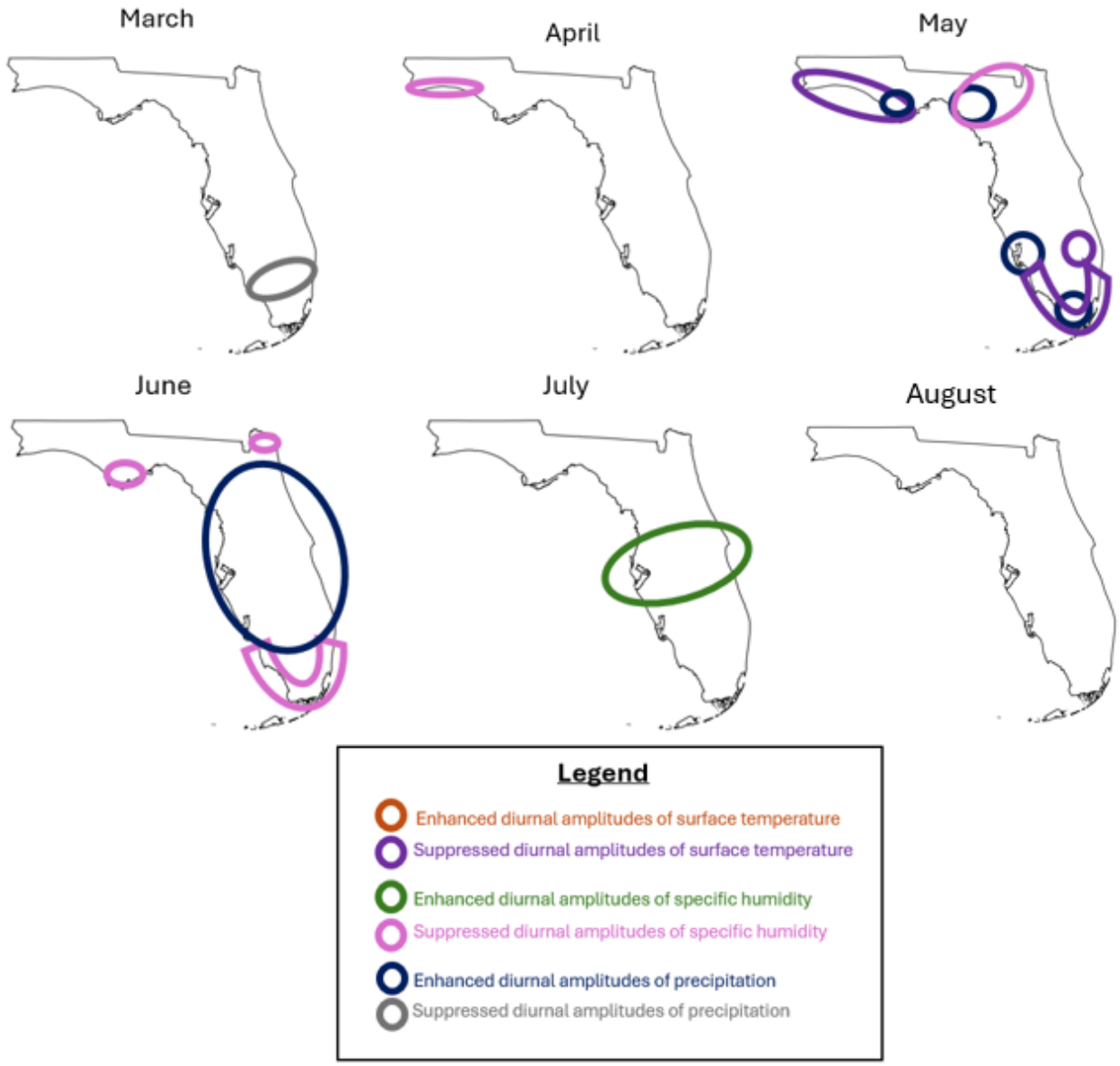

Figure 5.80. The responses of the diurnal amplitudes of surface temperature, specific humidity, and precipitation in Florida to a strong Atlantic-Pacific interbasin SST gradient during March--August.

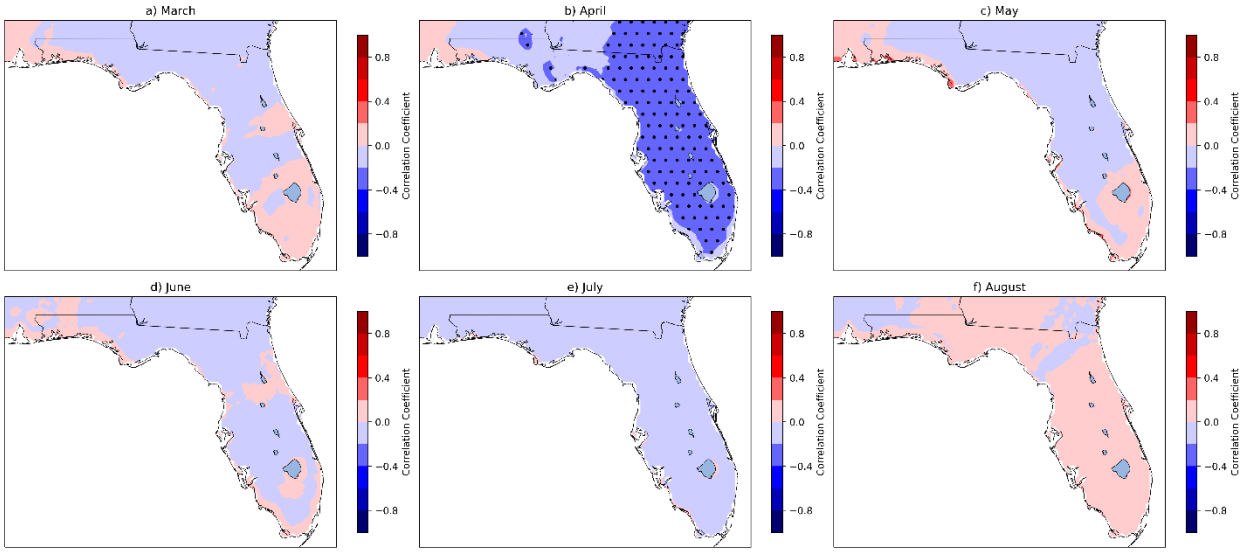

Figure 5.81. Correlation between diurnal peak amplitude of surface temperature in FLAReS1.0 and the concurrent *interannual component* of Atlantic-Pacific SST gradient over 1903-2004. Stippling indicates statistical significance.

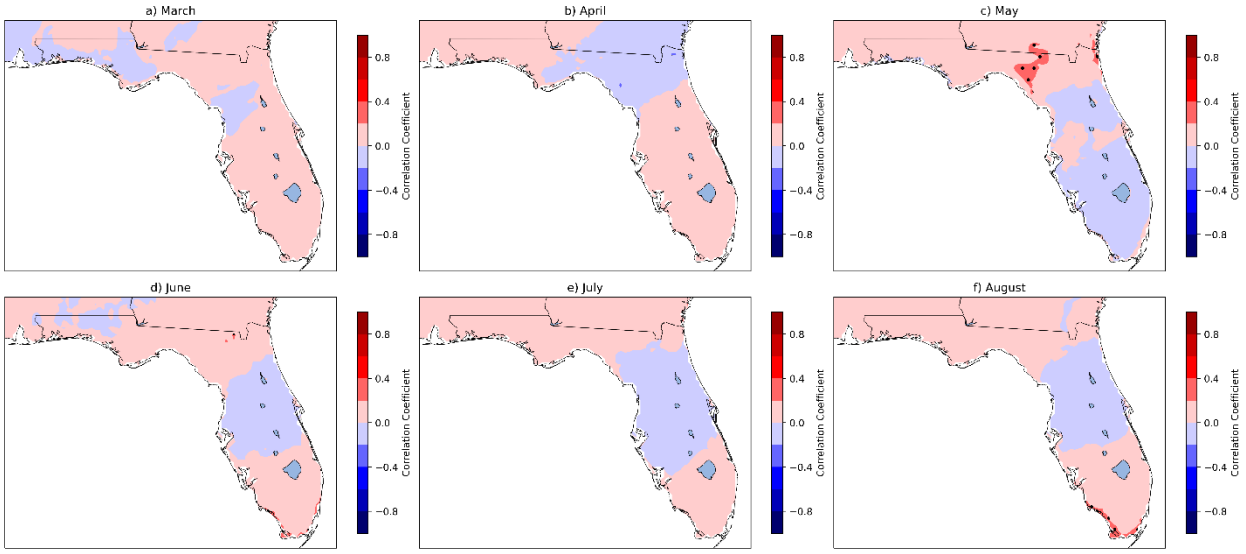

Figure 5.82. Correlation between diurnal peak amplitude of surface specific humidity in FLAReS1.0 and the concurrent *interannual component* of Atlantic-Pacific SST gradient over 1903-2004. Stippling indicates statistical significance.

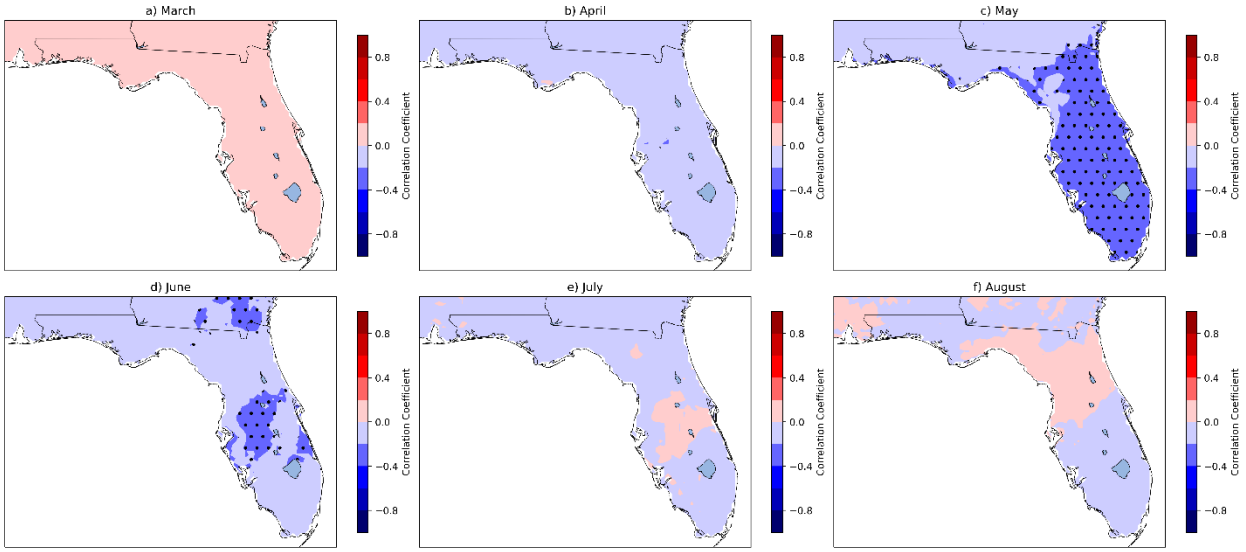

Figure 5.83. Correlation between diurnal peak amplitude of precipitation in FLAReS1.0 and the concurrent *interannual component* of Atlantic-Pacific SST gradient over 1903-2004. Stippling indicates statistical significance.

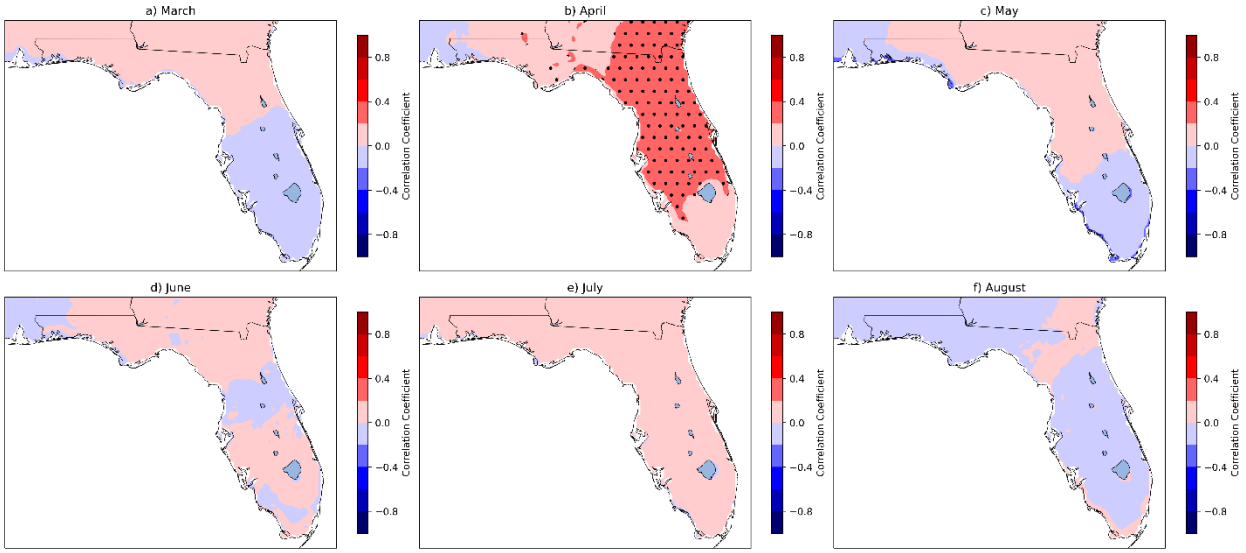

Figure 5.84. Correlation between diurnal minimum amplitude of surface temperature in FLAReS1.0 and the concurrent *interannual component* of Atlantic-Pacific SST gradient over 1903-2004. Stippling indicates statistical significance.

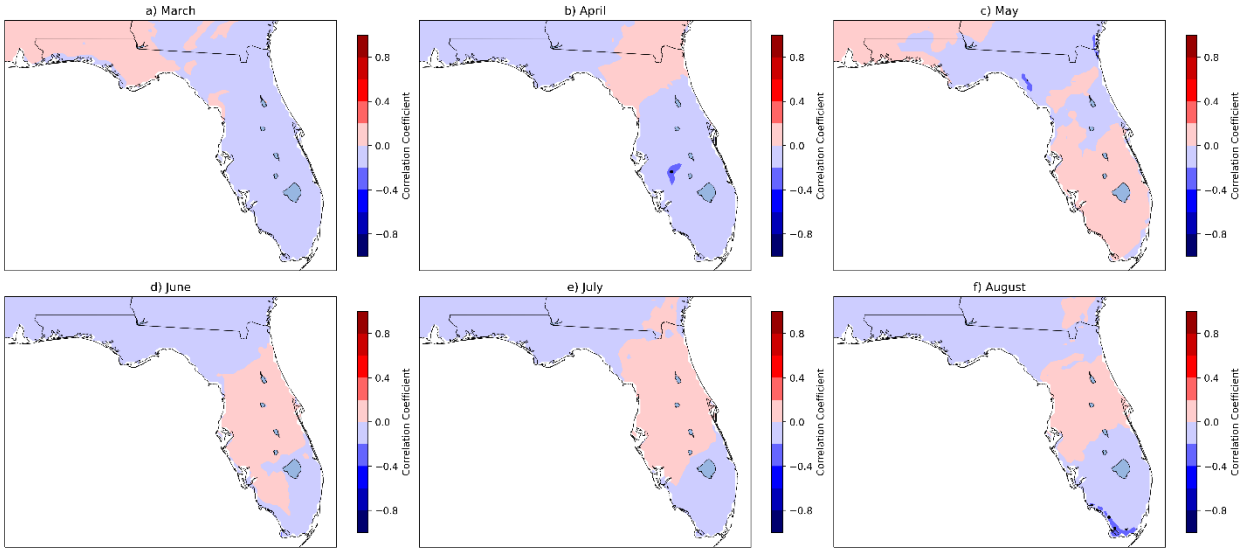

Figure 5.85. Correlation between diurnal minimum amplitude of surface specific humidity in FLAReS1.0 and the concurrent *interannual component* of Atlantic-Pacific SST gradient over 1903-2004. Stippling indicates statistical significance.

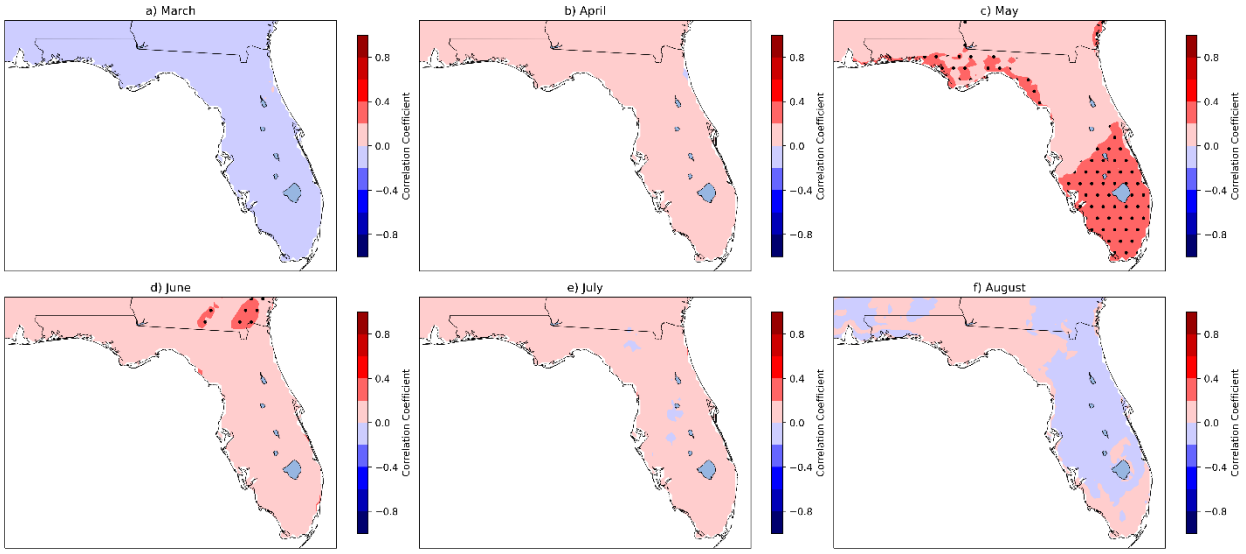

Figure 5.86. Correlation between diurnal minimum amplitude of precipitation in FLAReS1.0 and the concurrent *interannual component* of Atlantic-Pacific SST gradient over 1903-2004. Stippling indicates statistical significance.

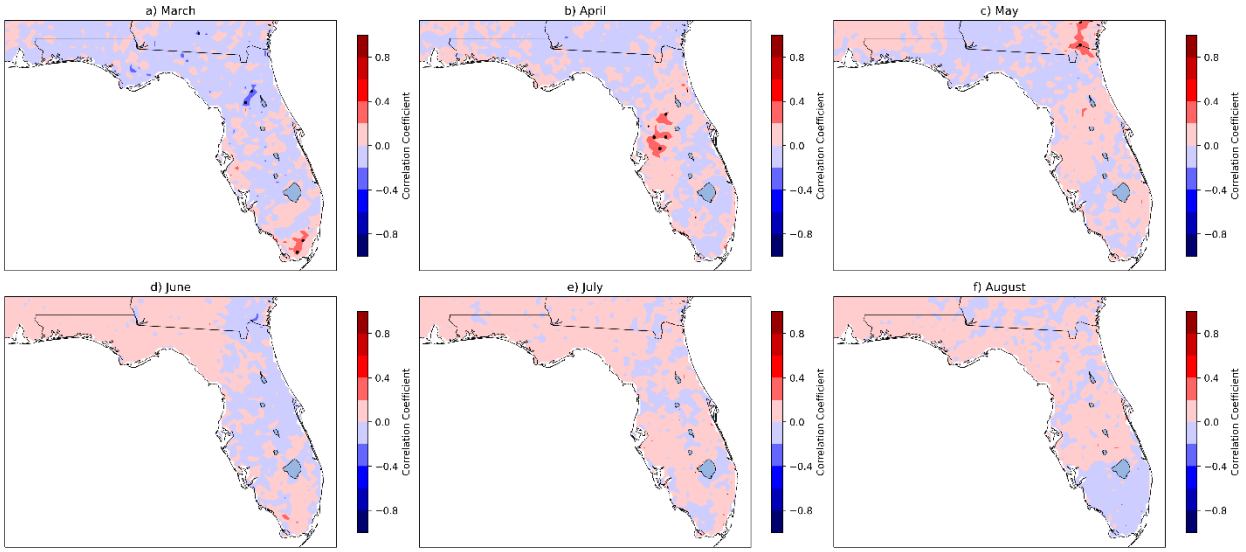

Figure 5.87. Correlation between diurnal peak phase of precipitation in FLAReS1.0 and the concurrent *interannual component* of Atlantic-Pacific SST gradient over 1903-2004. Stippling indicates statistical significance.

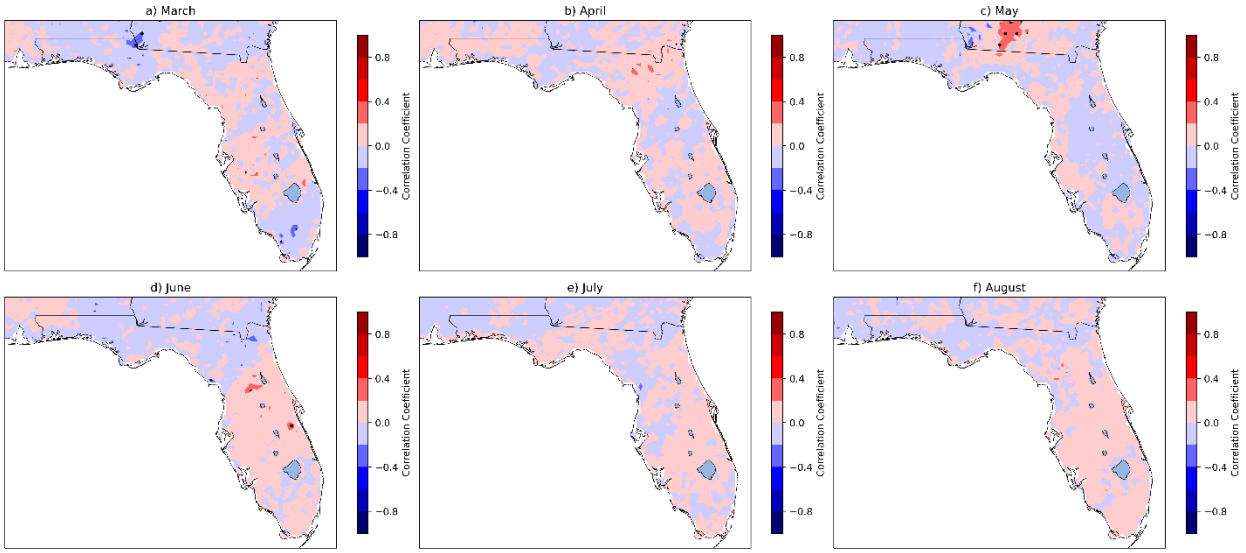

Figure 5.88. Correlation between diurnal minimum phase of precipitation in FLAReS1.0 and the concurrent *interannual component* of Atlantic-Pacific SST gradient over 1903-2004. Stippling indicates statistical significance.

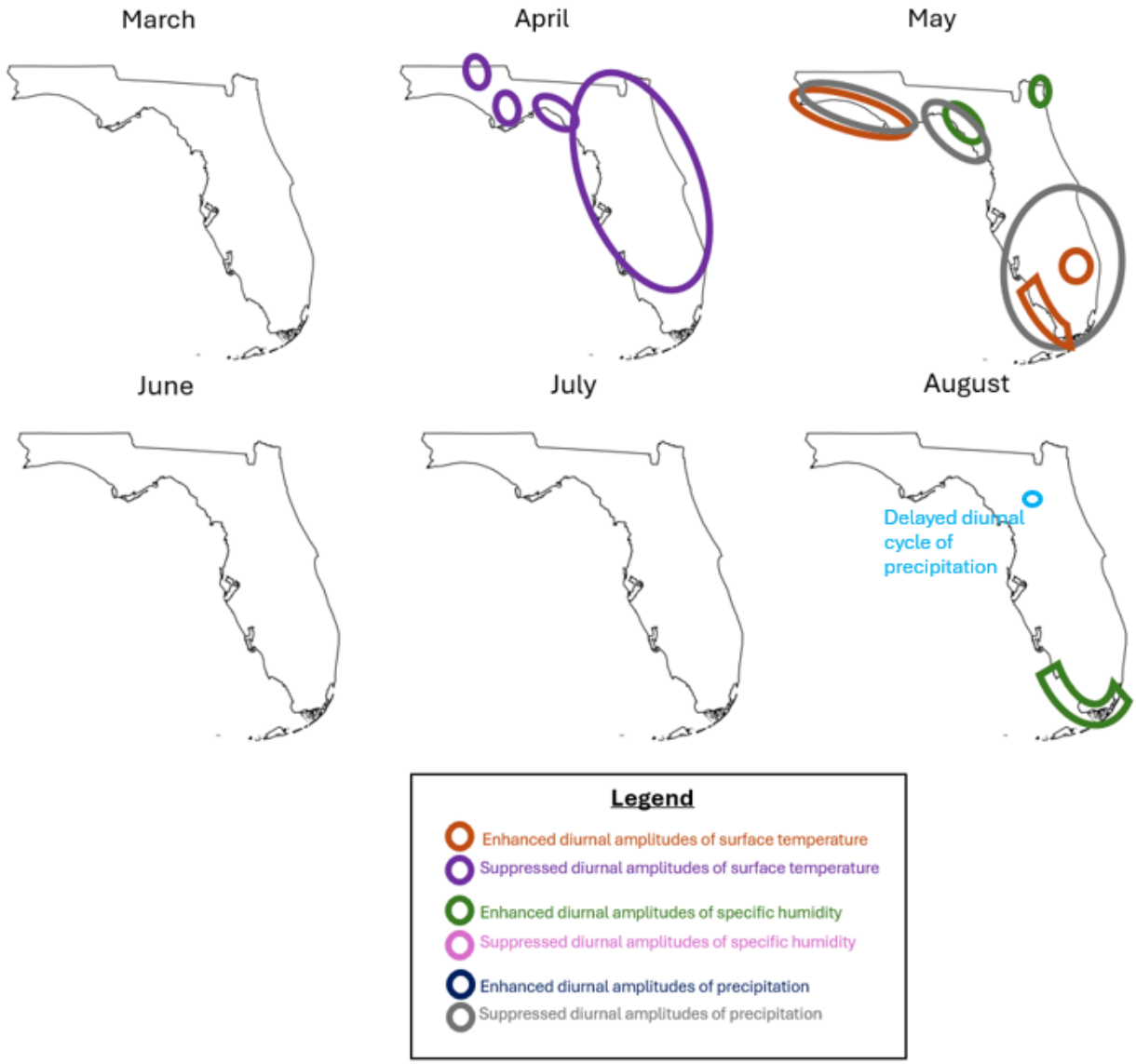

Figure 5.89. The responses of the diurnal cycles of surface temperature, specific humidity, and precipitation in Florida during March—August to concurrent weak *interannual component* of the Atlantic-Pacific interbasin SST gradient.

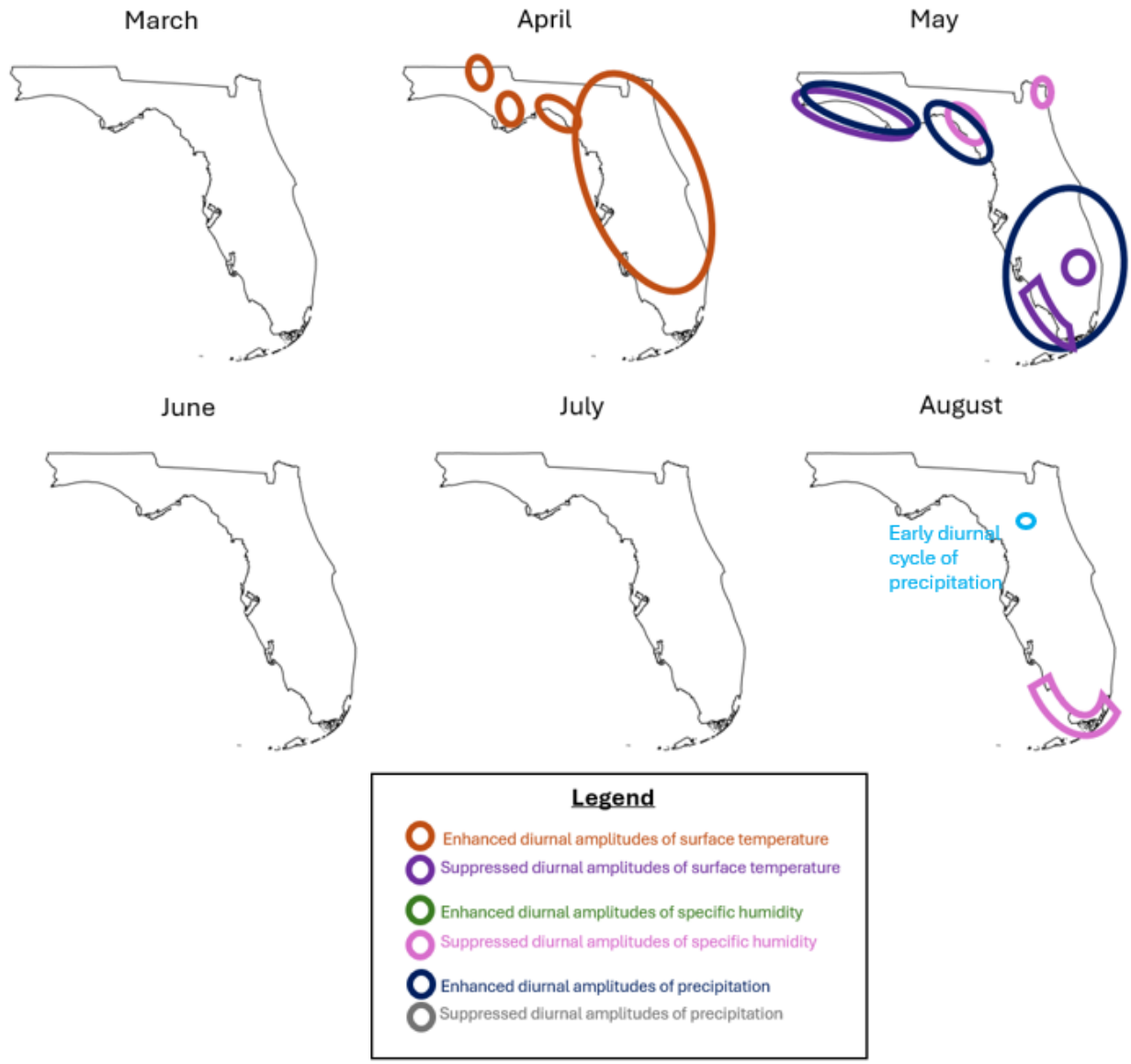

Figure 5.90. The responses of the diurnal cycles of surface temperature, specific humidity, and precipitation in Florida during March—August to concurrent strong *interannual component* of the Atlantic-Pacific interbasin SST gradient.

5.3.3 Bermuda High Index

The BHI has a strong influence on the diurnal cycles of surface meteorology variables in Florida during boreal summer. The influence of the BHI on the Florida summer diurnal cycle extends primarily to the diurnal amplitudes of the surface meteorology variables. Additionally, the diurnal phase of precipitation is influenced by the BHI, albeit in a limited capacity. The BHI is a seasonally-averaged MSLP-gradient

between 90°W, 30°N (near New Orleans, Louisiana) and 78°W, 30°N (a marine location east of Jacksonville, Florida). The BHI, seasonally-averaged over JJA, is an indicator of the westward extent of the NASH toward Florida during summer. The westward extent of the NASH varies interannually; a stronger-than-normal NASH expands further southwestward than normal (Kim et al. 2020). Therefore, high BHI corresponds to a strong NASH, whereas low BHI corresponds to a weak NASH.

Summers with a high BHI (i.e., strong NASH) are associated with enhanced diurnal amplitudes of precipitation across most of Florida (Figures 5.3.15 and 5.3.18). In June, this signal is evident in panhandle Florida as well as south and central Florida (Figures 5.3.15a and 5.3.18a). As the season evolves into July, this signal in north Florida extends further toward the east, while the signal in south and central Florida extends further toward the north, such that both signals encroach toward Jacksonville (Figures 5.3.15b and 5.3.18b). This trend continues into August, such that the high BHI is associated with amplified diurnal precipitation everywhere in Florida except the Jacksonville area (Figures 5.3.15c and 5.3.18c). In June, in the Everglades in south Florida, high BHI is associated with a delayed diurnal phase of precipitation, meaning that the diurnal peak of precipitation occurs later in the day (Figures 5.3.21a and 5.3.24a). Meanwhile, a high BHI is associated with suppressed diurnal amplitudes of specific humidity in south Florida in June, July, and August, and in north Florida in June and August (Figures 5.3.14 and 5.3.17). The response of the diurnal amplitudes of surface temperature to the BHI varies throughout the boreal summer season. In June, high BHI is associated with suppressed diurnal amplitudes of surface temperature on the western panhandle coastline (Figures 5.3.13a and 5.3.16a), suggesting sea-breeze induced cloud cover on the western panhandle coastline during high-BHI Junes. However, in July, high BHI is associated with enhanced diurnal amplitudes of surface temperature everywhere in Florida (Figures 5.3.13b and 5.3.16b), suggesting minimal cloud cover (aside from the brief rainstorms).

Conversely, summers with low BHI (i.e., weak NASH) are associated with suppressed diurnal amplitudes of precipitation across most of Florida (Figures 5.3.15 and 5.3.18). Additionally, the diurnal peak of precipitation may occur earlier in the day than usual in the Everglades in June during summers in which BHI is low (Figures 5.3.21a and

5.3.24a). Simultaneously, the diurnal amplitudes of specific humidity are enhanced in parts of north Florida and south Florida (Figures 5.3.14 and 5.3.17). Across all of Florida, in July during low-BHI summers, the diurnal amplitudes of surface temperature are suppressed, suggesting increased cloud cover in the day and night (Figures 5.3.13b and 5.3.16b).

The amplification of diurnal-scale precipitation across most of Florida, particularly along the Gulf coast, during high-BHI (i.e., strong NASH) summers is consistent with the known influence of the NASH on boreal summer US precipitation. Boreal summers during which the NASH is stronger than normal, extends further to its southwest than normal, or both, are associated with enhanced moisture flux from the Gulf of Mexico into the southern US (Kim et al. 2020).

Here, we also analyze the relationships between the *interannual component* of BHI and the characteristics of the Florida diurnal cycle (Figures 5.105-112). This analysis leads some of the relationships between the BHI and the Florida diurnal cycle to disappear, indicating that those relationships are caused by scales of variability other than the interannual scale. For example, the influences of the BHI on the amplitude of diurnal scale precipitation and specific humidity disappear in July and August when we isolate the interannual component of BHI (Figures 5.106, 5.107, 5.109-112). The relationships that remain present when we isolate the interannual component of BHI are the strong relationship between BHI and diurnal scale precipitation in June, and the relationship between BHI and the diurnal amplitudes of surface temperature across the entire state of Florida in July (Figures 5.105, 5.107, 5.108, 5.110-112). The fact that they remain demonstrates that these are robust relationships. The association between a strong NASH (relative to other years) and enhanced diurnal amplitudes of precipitation in June (relative to other years) may suggest that a strong NASH hastens the onset of the Florida summer wet season in early June.

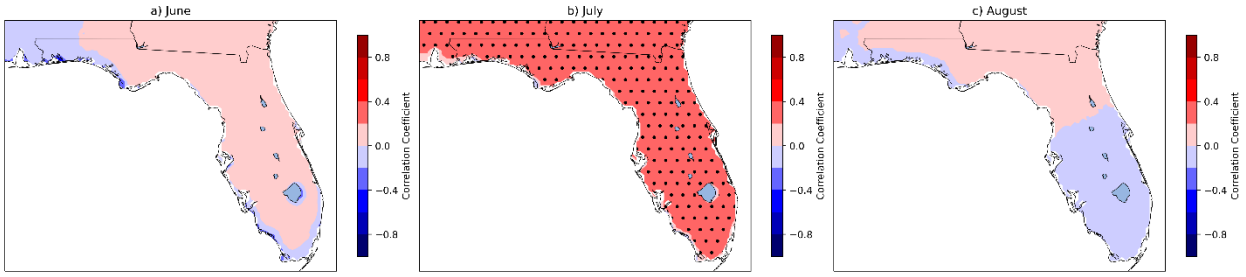

Figure 5.91. Correlation between diurnal peak amplitude of surface temperature in FLAReS1.0 and the concurrent Bermuda High Index over 1903-2004. Stippling indicates statistical significance.

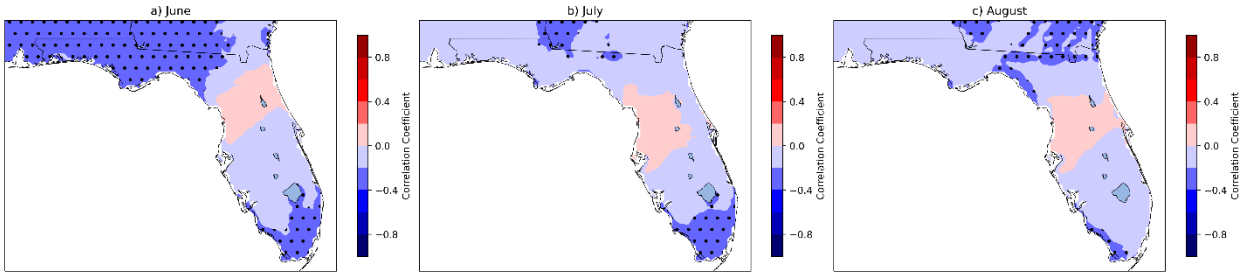

Figure 5.92. Correlation between diurnal peak amplitude of surface specific humidity in FLAReS1.0 and the concurrent Bermuda High Index over 1903-2004. Stippling indicates statistical significance.

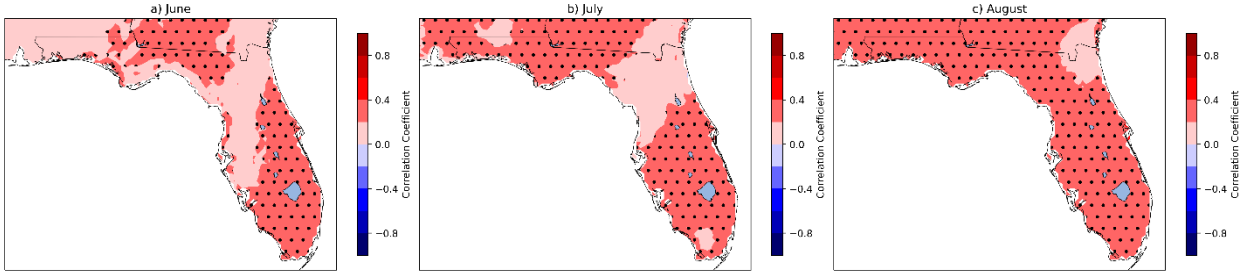

Figure 5.93. Correlation between diurnal peak amplitude of precipitation in FLAReS1.0 and the concurrent Bermuda High Index over 1903-2004. Stippling indicates statistical significance.

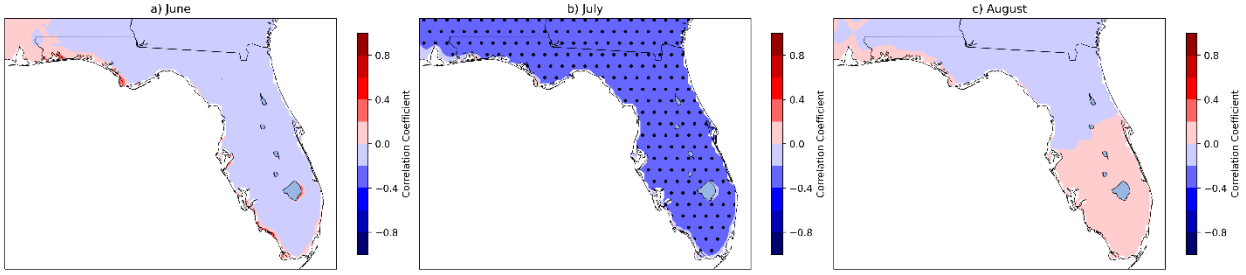

Figure 5.94. Correlation between diurnal minimum amplitude of surface temperature in FLAReS1.0 and the concurrent Bermuda High Index over 1903-2004. Stippling indicates statistical significance.

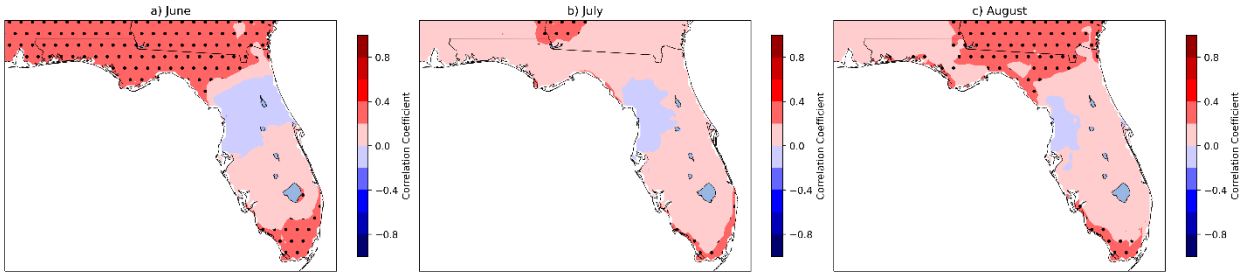

Figure 5.95. Correlation between diurnal minimum amplitude of surface specific humidity in FLAReS1.0 and the concurrent Bermuda High Index over 1903-2004. Stippling indicates statistical significance.

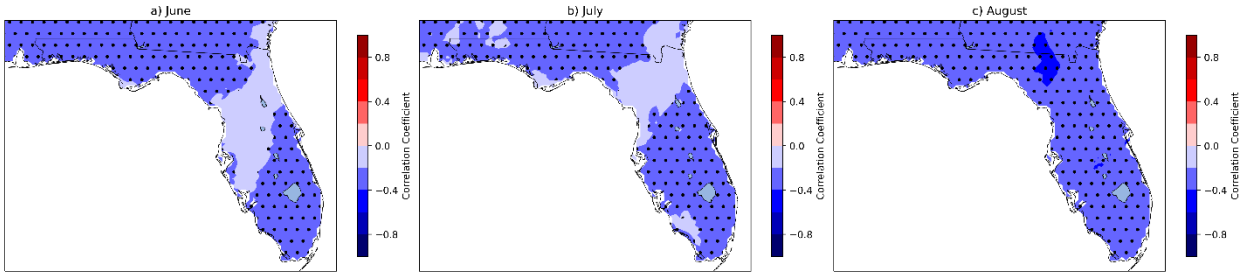

Figure 5.96. Correlation between diurnal minimum amplitude of precipitation in FLAReS1.0 and the concurrent Bermuda High Index over 1903-2004. Stippling indicates statistical significance.

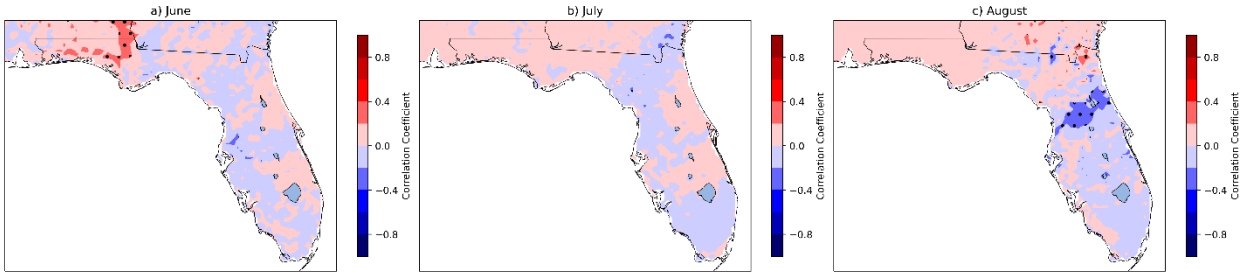

Figure 5.97. Correlation between diurnal peak phase (time of day) of surface temperature in FLAReS1.0 and the concurrent Bermuda High Index over 1903-2004. Stippling indicates statistical significance.

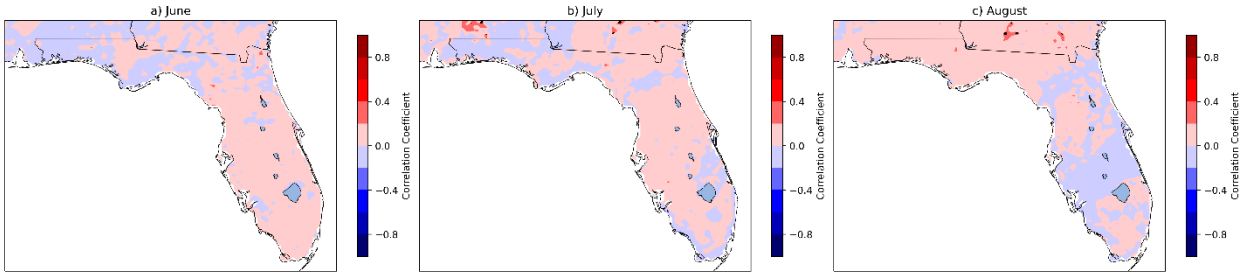

Figure 5.98. Correlation between diurnal peak phase (time of day) of surface specific humidity in FLAReS1.0 and the concurrent Bermuda High Index over 1903-2004. Stippling indicates statistical significance.

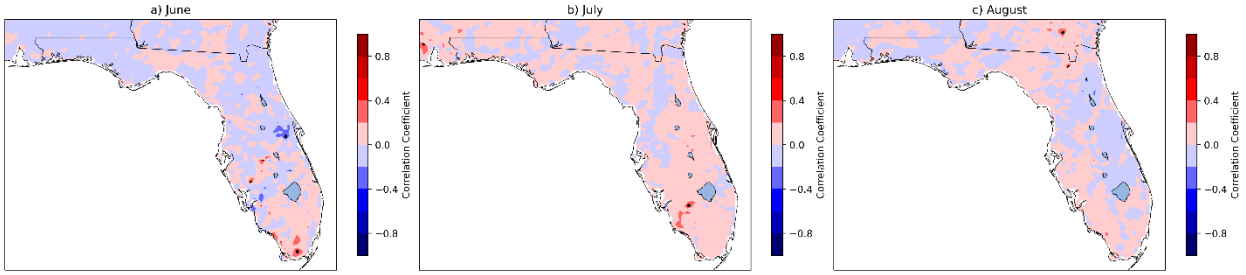

Figure 5.99. Correlation between diurnal peak phase (time of day) of precipitation in FLAReS1.0 and the concurrent Bermuda High Index over 1903-2004. Stippling indicates statistical significance.

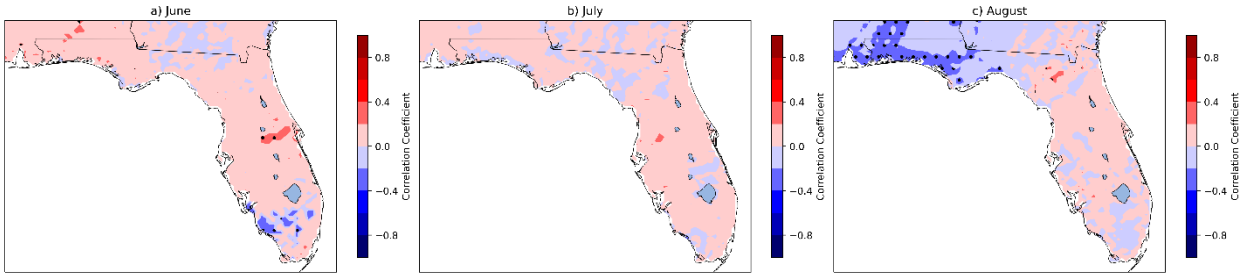

Figure 5.100. Correlation between diurnal minimum phase (time of day) of surface temperature in FLAReS1.0 and the concurrent Bermuda High Index over 1903-2004. Stippling indicates statistical significance.

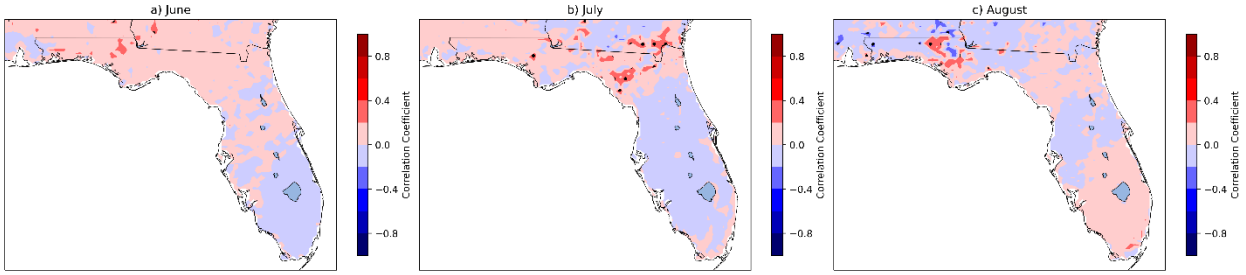

Figure 5.101. Correlation between diurnal minimum phase (time of day) of surface specific humidity in FLAReS1.0 and the concurrent Bermuda High Index over 1903-2004. Stippling indicates statistical significance.

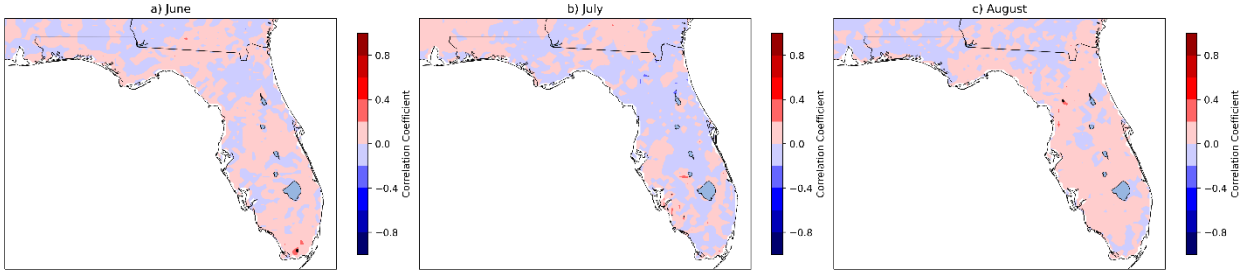

Figure 5.102. Correlation between diurnal minimum phase (time of day) of precipitation in FLAReS1.0 and the concurrent Bermuda High Index over 1903-2004. Stippling indicates statistical significance.

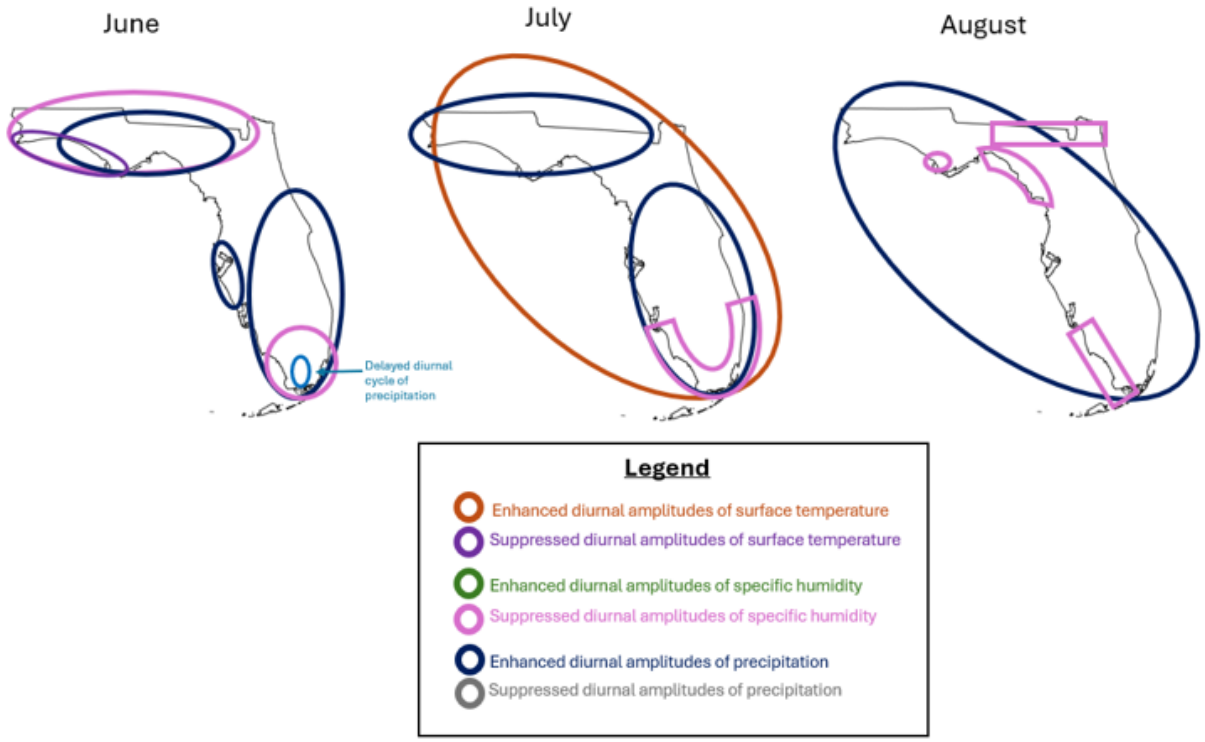

Figure 5.103. The responses of the diurnal amplitudes of surface temperature, specific humidity, and precipitation in Florida to a strong North Atlantic subtropical high during June, July, and August.

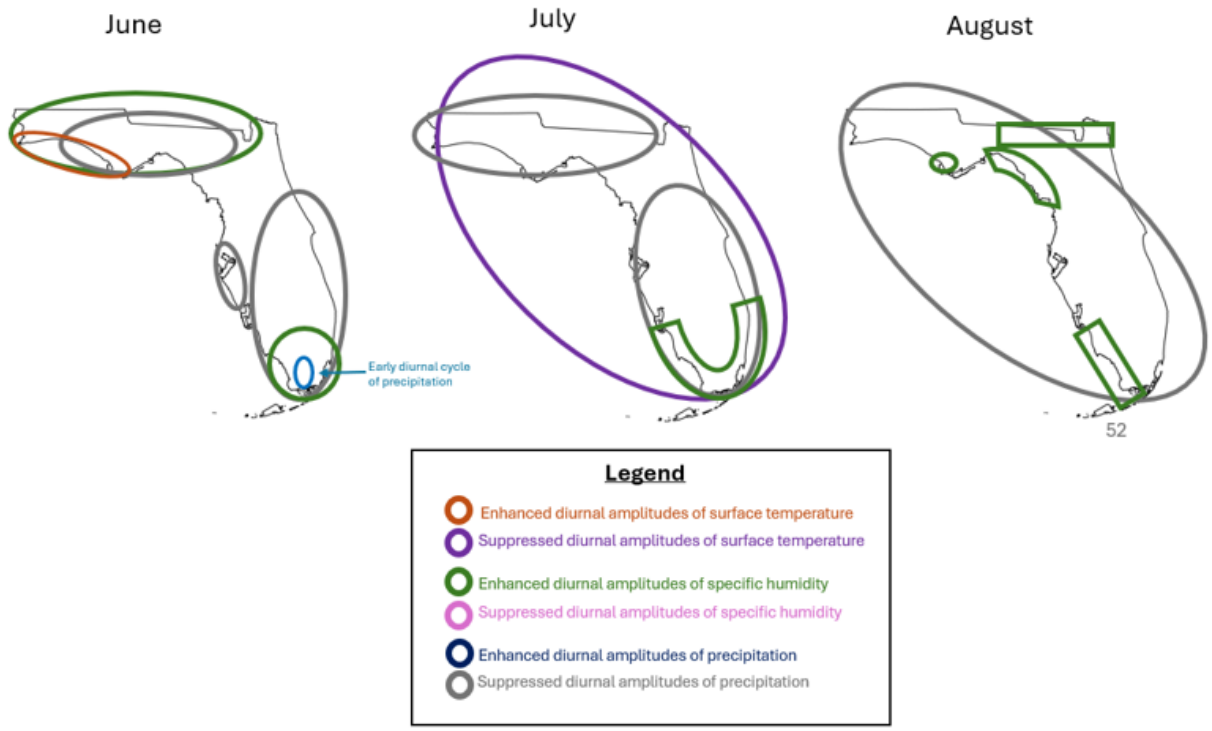

Figure 5.104. The responses of the diurnal amplitudes of surface temperature, specific humidity, and precipitation in Florida to a weak North Atlantic subtropical high during June, July, and August.

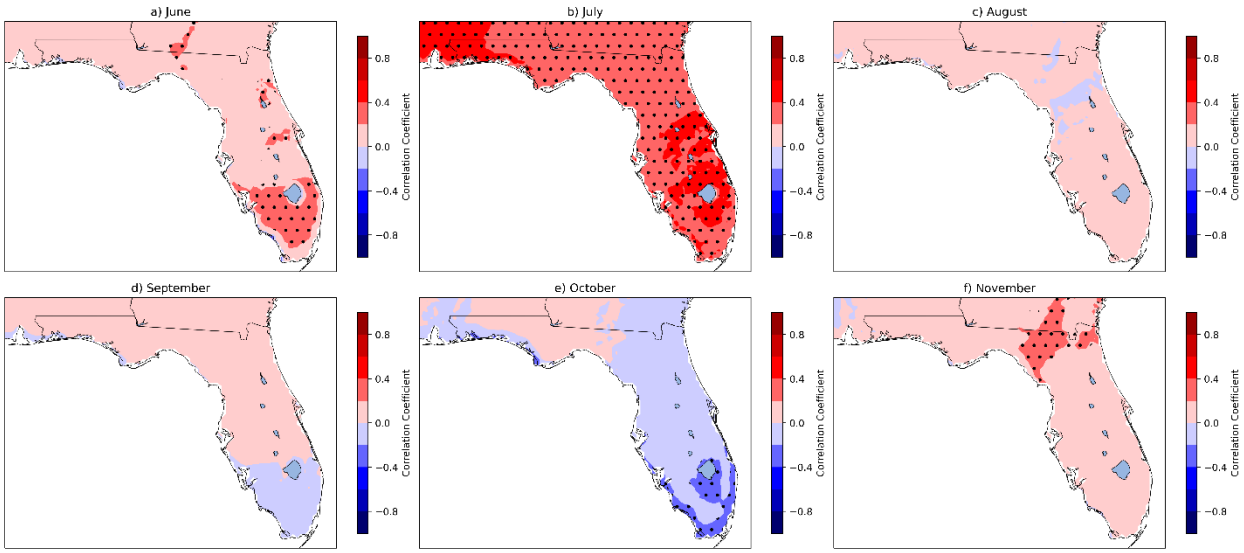

Figure 5.105. Correlation between diurnal peak amplitude of surface temperature in FLAReS1.0 and the concurrent *interannual component* of the Bermuda High Index over 1903-2004. Stippling indicates statistical significance.

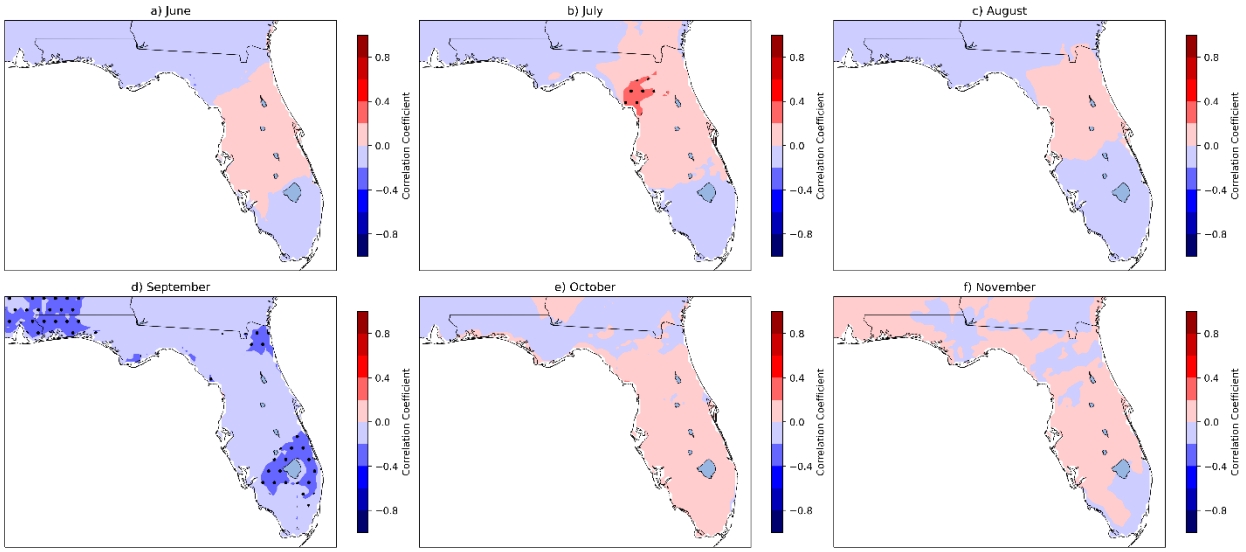

Figure 5.106. Correlation between diurnal peak amplitude of surface specific humidity in FLAReS1.0 and the concurrent *interannual component* of the Bermuda High Index over 1903-2004. Stippling indicates statistical significance.

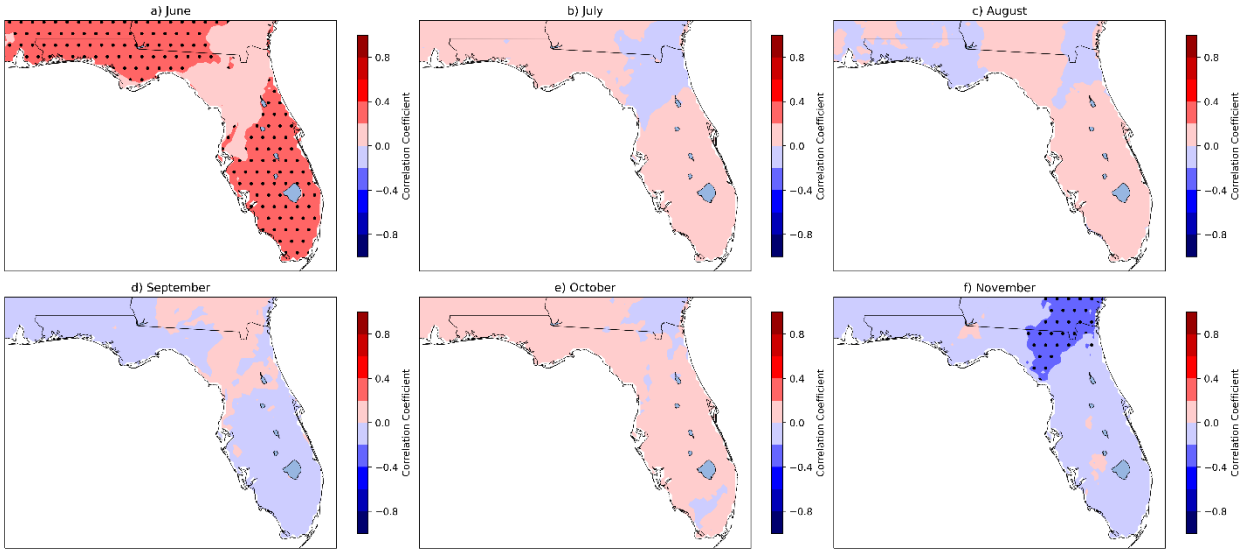

Figure 5.107. Correlation between diurnal peak amplitude of precipitation in FLAReS1.0 and the concurrent *interannual component* of the Bermuda High Index over 1903-2004. Stippling indicates statistical significance.

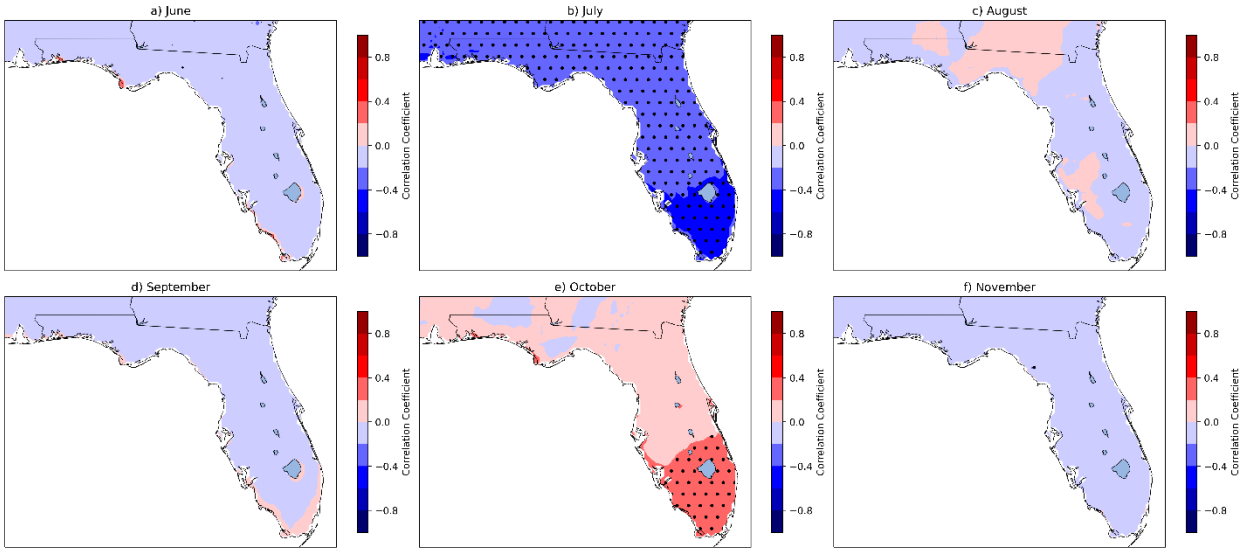

Figure 5.108. Correlation between diurnal minimum amplitude of surface temperature in FLAReS1.0 and the concurrent *interannual component* of the Bermuda High Index over 1903-2004. Stippling indicates statistical significance.

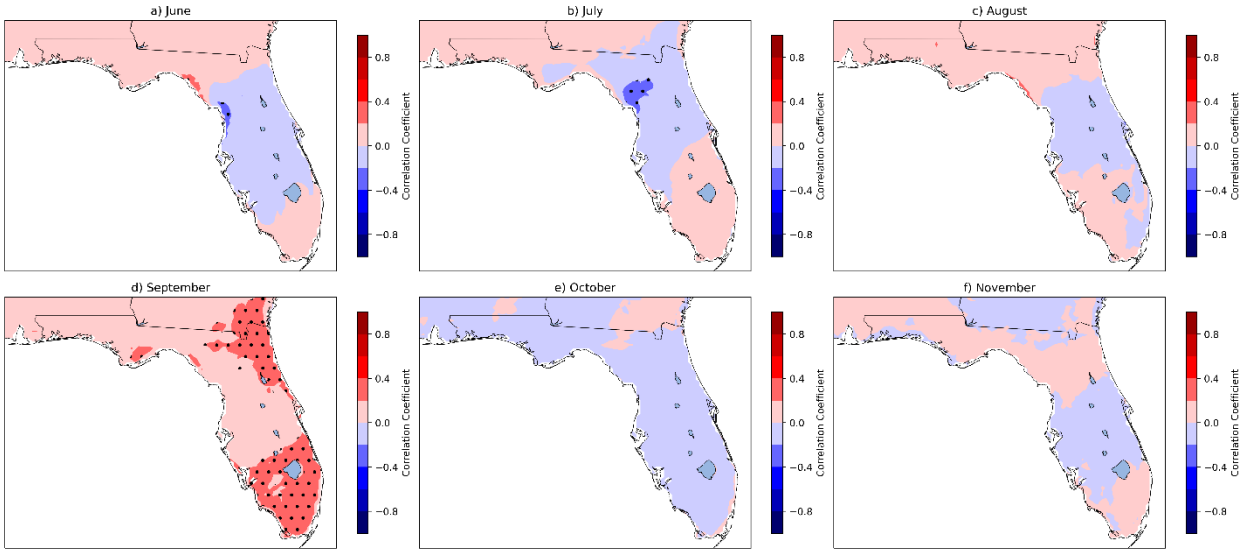

Figure 5.109. Correlation between diurnal minimum amplitude of surface specific humidity in FLAReS1.0 and the concurrent *interannual component* of the Bermuda High Index over 1903-2004. Stippling indicates statistical significance.

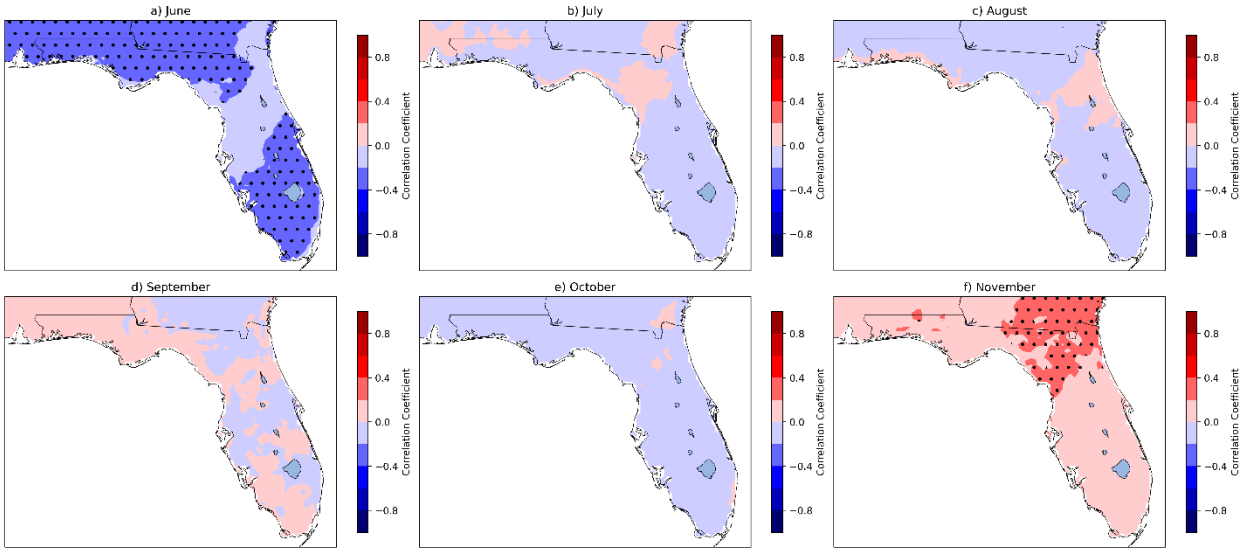

Figure 5.110. Correlation between diurnal minimum amplitude of precipitation in FLAReS1.0 and the concurrent *interannual component* of the Bermuda High Index over 1903-2004. Stippling indicates statistical significance.

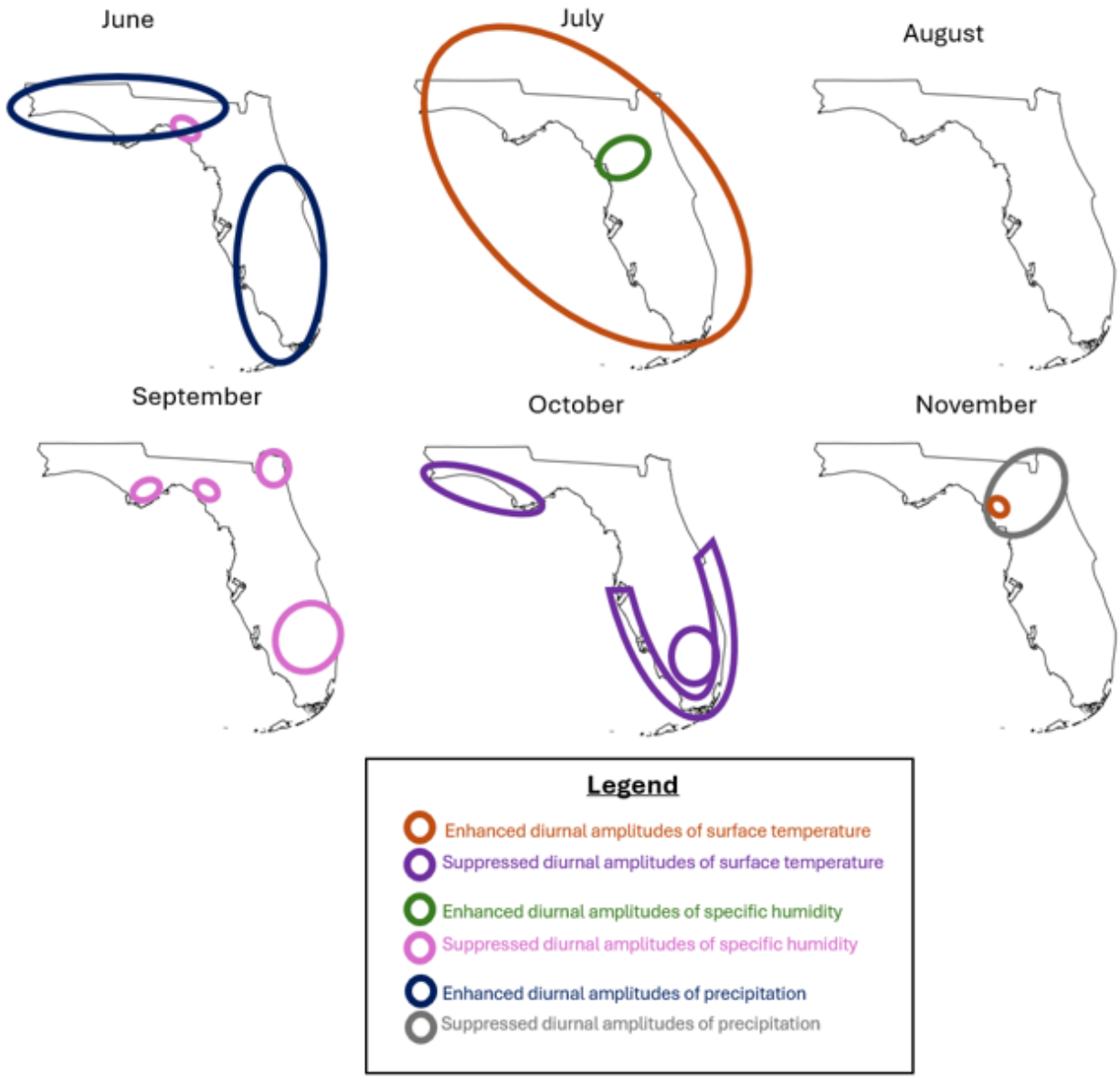

Figure 5.111. The responses of the diurnal cycles of surface temperature, specific humidity, and precipitation in Florida during June—November to concurrent strong *interannual component* of the Bermuda High Index.

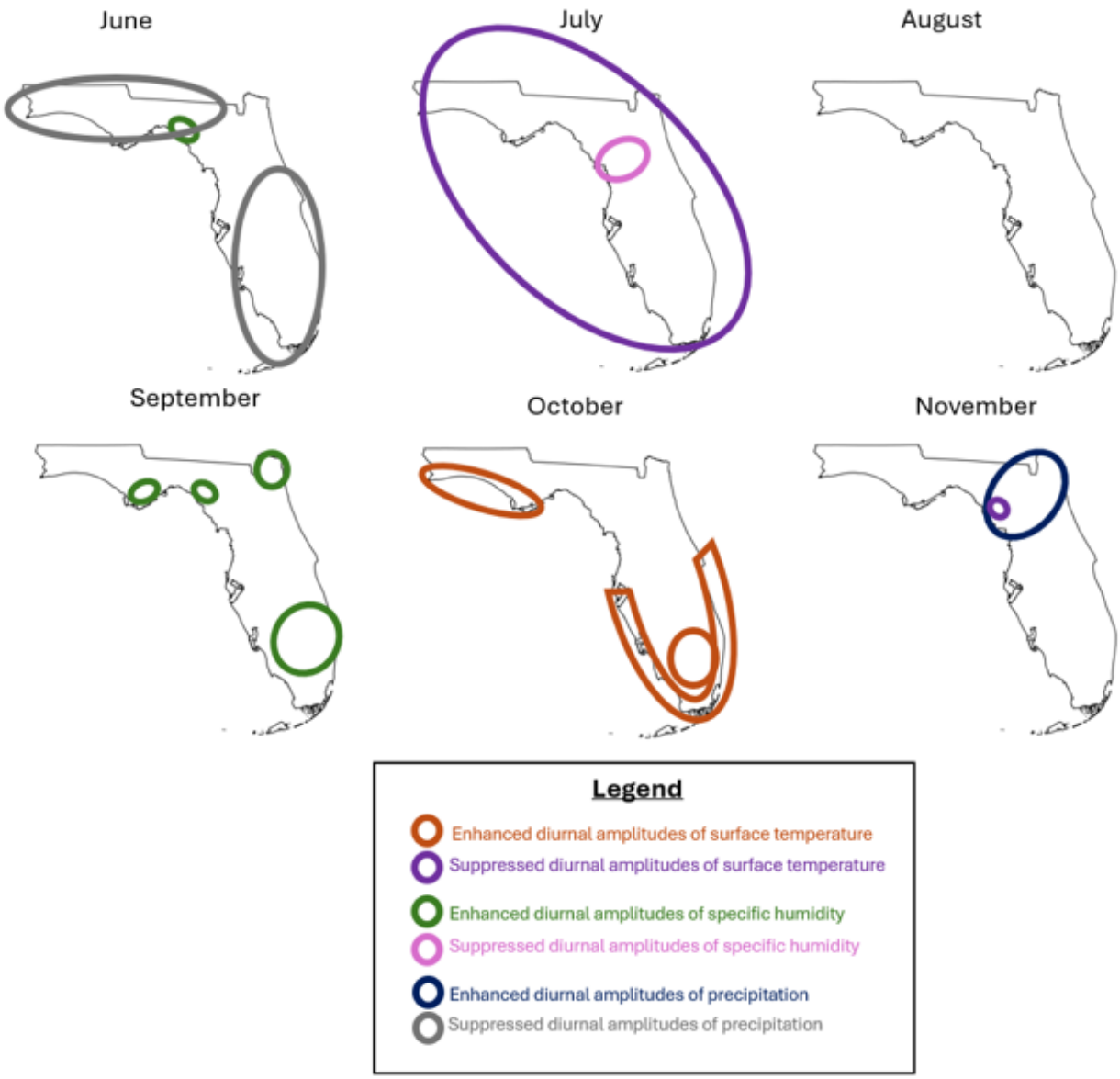

Figure 5.112. The responses of the diurnal cycles of surface temperature, specific humidity, and precipitation in Florida during June—November to concurrent weak *interannual component* of the Bermuda High Index.

CHAPTER SIX

CONCLUSIONS

The availability of the gap-filled, quality-controlled FAWN dataset at such temporal resolutions of 15 minutes spanning well over a decade is an invaluable resource for understanding diurnal variations. In addition, the dataset serves as an important source for ground validation for remote sensing products and in the validation of high-resolution model

simulations. Florida, with its subtropical and peninsular geography surrounded by relatively warm oceans, exhibits a strong diurnal cycle of hydroclimate. Given that diurnal variations is one of the fundamental modes of climate variability of the Earth system, this dataset provides a unique opportunity to examine the variations of diurnal scales across several variables observed by FAWN.

This study reports on the characteristics of the diurnal cycle in 30 discreet stations spread across Florida that observe surface temperature, dew point temperature, wind speed, and precipitation. The results of this study show that these surface variables display large diurnal variations especially in the boreal summer season. The variations in the phase of the diurnal cycle of precipitation are relatively larger outside of the boreal summer season unlike its amplitude variation which is largest during the wet (summer) season. Furthermore, we find the influence of the semi-diurnal cycle on these variables to be increasing the variance of the diurnal phase, particularly that of precipitation during summer.

The diurnal cycle of temperature is relatively consistent year-round at all stations in Florida, with only slight seasonal variability in the diurnal phase. However, there is strong seasonality in the variance of the diurnal amplitude of temperature. The interannual variability of the diurnal amplitude of temperature is high in winter and early spring, but by April, the interannual variability is drastically reduced. This suggests that afternoon high temperatures "lock-in" in April, while similarly the diurnal maximum dew point temperatures "lock-in" a month later in May, possibly helping to reliably set-up for the onset of the wet season over Florida a few weeks later.

The validation of the FLAReS1.0 downscaled reanalysis against the FAWN observations revealed strengths of the reanalysis as well as its shortcomings and biases. FLAReS1.0 generally represents the diurnal amplitudes of surface temperature, surface dew point temperature, and precipitation, and each of their variances, well. However, the analysis revealed suppressed diurnal amplitudes of surface temperature (a cold bias in the diurnal maximum amplitudes and a warm bias in the diurnal minimum amplitudes). Additionally, the analyses of dew point temperature and precipitation reveal moist and wet biases in all of Florida in spring, and a summertime wet bias in north Florida and south Florida. FLAReS1.0 presents a reasonable diurnal phase of surface temperature in north Florida year-round, and everywhere in Florida from May—September. Even under those conditions, however, the diurnal maximum has an early

bias, while the diurnal minimum has a late bias, a curious combination which may simply be a result of the suppressed diurnal amplitudes of surface temperature in FLAReS1.0. Lastly, the diurnal phases of dew point temperature and precipitation are poorly represented by FLAReS1.0.

The interannual climate modes of ENSO, the Atlantic-Pacific SST gradient, and the Bermuda High Index, have been known to influence the climate of the southeast US. This study narrows the geographical scope by homing in on Florida, and narrows the scope further through its focus on the diurnal scale variations. We find that ENSO's influence on the Florida diurnal cycle is primarily in winter and spring, whereas the influence of the Atlantic-Pacific SST gradient takes place during spring and early summer, and the BHI influences Florida climate throughout the summer. Each of these modes affect the diurnal amplitudes of surface temperature, specific humidity, and precipitation in many areas of Florida. The results also suggest that the Atlantic-Pacific SST gradient and the BHI each may influence the timing of the onset of Florida's summer wet season, an important piece of information for Florida's agricultural sector. Moreover, seeing as the results show that BHI strongly influences the diurnal-scale precipitation in Florida during summer, and seeing as diurnal scale precipitation is a substantial contributor to the summer seasonal total precipitation, the BHI is therefore an indicator of the total summer seasonal precipitation—another important piece of information for Florida's agricultural sector.

REFERENCES

Augustine, J. A., and F. Caracena, 1994: Lower-tropospheric precursors to nocturnal MCS development over the central United States. *Wea. Forecasting*, **9**, 116–135, https://doi.org/10.1175/1520-0434(1994)009<0116:LTPTNM>2.0.CO;2.

Bastola, S., and V. Misra, 2013: Sensitivity of hydrological simulations of southeastern United States watersheds to temporal aggregation of rainfalls. *J. Hydrometeor*., **14**, 1334–1344.

Blanchard, D. O., and R. E. Lopez, 1985: Spatial patterns of convection in south Florida. *Mon. Wea. Rev.*, **113**, 1282—1299, https://doi.org/10.1175/1520-0493(1985)113<1282:SPOCIS>2.0.CO;2.

Byers, H.R., and H.R. Rodebush, 1948: Causes of thunderstorms of the Florida peninsula. *J. Meteor.,* **5**, 275–280, https://doi.org/10.1175/1520-04691948)005<0275:COTOTF>2.0.CO;2.

Carbone, R. E., and J. D. Tuttle, 2008: Rainfall occurrence in the U.S. warm season: The diurnal cycle. *J. Climate*, **21**, 4132–4146, https://doi.org/10.1175/2008JCLI2275.1.

Cooper, H.J., M. Garstang, and J. Simpson, 1982: The Diurnal Interaction Between Convection and Peninsular-Scale Forcing Over South Florida. *Mon. Wea. Rev.,* **110**, 486–503, https://doi.org/10.1175/1520-0493(1982)110<0486:TDIBCA>2.0.CO;2.

Dai, A., and J. Wang, 1999: Diurnal and semidiurnal tides in global surface pressure fields. *J. Atmos. Sci.*, **56**, 3874–3891, https://doi.org/10.1175/1520-0469(1999)056<3874:DASTIG>2.0.CO;2.

Dai, A., and K. E. Trenberth, 2004: The diurnal cycle and its depiction in the Community Climate System Model. *J. Climate*, **17**, 930–951, https://doi.org/10.1175/1520-0442(2004)017<0930:TDCAID>2.0.CO;2.

Davis, R.E., Hayden, B.P., Gay, D.A., Phillips, W.L., Jones, G.V., 1997. The North Atlantic subtropical anticyclone. J. Clim. 10, 728–744.

DiNapoli, S.M., and V. Misra, 2012: Reconstructing the 20th century high-resolution climate of the southeastern United States. *J. Geophys. Res*., **117**, D19113, doi:10.1029/2012JD018303.

Frank, N. L., P. L. Moore, and G. E. Fisher, 1967: Summer shower distribution over the Florida peninsula as deduced from digitized radar data. *J. Appl. Meteor. Climatol.,* **6,** 309—316. https://doi.org/10.1175/1520-0450(1967)006<0309:SSDOTF>2.0.CO;2.

Gray, W.M., 1984. Atlantic seasonal hurricane frequency. Part I. El Niño and 30mb Quasi-Biennial Oscillation influences. *Mon. Wea. Rev.,* **112**, 1649–1668.

Hall, C. A., and R. R. Leben, 2016: Observational evidence of seasonality in the timing of loop current eddy separation. *Dynamics of Atmospheres and Oceans*, **76**, 240—267, https://doi.org/10.1016/j.dynatmoce.2016.06.002.
Hanley, D., M. Bourassa, J. J. O'Brien, S. Smith, and E. Spade, 2003: A quantitative evaluation of ENSO indices. *J. Clim*., **16**, 1249–1258.

Huang, B., P. W. Thorne, V. F. Banzon, T. Boyer, G. Chepurin, J. H. Lawrimore, M. J. Menne, T. M. Smith, R. S. Vose, and H. Zhang, 2017: NOAA Extended Reconstructed Sea Surface Temperature (ERSST), Version 5. 1903-2004. NOAA National Centers for Environmental Information. doi:10.7289/V5T72FNM [06-25-25].

Krishnamurthy, L., Vecchi, G. A., Msadek, R., Wittenberg, A., Delworth, T. L., & Zeng, F., 2015: The seasonality of the Great Plains low-level jet and ENSO relationship. *J. Clim.*, **28**(11), 4525–4544.

Klotzbach, P.J., 2011: El Niño-Southern Oscillation's impact on Atlantic basin hurricanes and U.S. landfalls. *J. Clim.* **24**, 1252–1263.

Li, W., L. Li, R. Fu, Y. Deng, and H. Wang, 2011: Changes to the North Atlantic subtropical high and its role in the intensification of summer rainfall variability in the southeastern United States. *J. Climate*, **24**, 1499–1506. DOI: 10.1175/2010JCLI3829.1.

Liang, X., L. Li, A. Dai, and K. E. Kunkel, 2004: Regional climate model simulation of summer precipitation diurnal cycle over the United States. *Geophys. Res. Lett.*, **31** (24), https://doi.org/10.1029/2004GL021054.

Lucien, G., and J. Love, 1997: Florida freeze reducing supplies of fresh vegetables. *Agricultural Outlook* (March 1997). Economic Research Service, USDA.

Lusher, W., J. Jackson, and K. Morgan, 2009: The Florida Automated Weather Network (FAWN): Ten years of providing weather information to Florida growers. *University of Florida: IFAS Extension*. SL 298.

Marshall, C.H., R.A. Pielke, L.T. Steyaert, and D.A. Willard, 2004: The Impact of Anthropogenic Land-Cover Change on the Florida Peninsula Sea Breezes and Warm Season Sensible Weather. *Mon. Wea. Rev.,* **132**, 28–52, https://doi.org/10.1175/1520-0493(2004)132<0028:TIOALC>2.0.CO;2

Martinez, C.J., Maleski, J.J., and M.F. Miller, 2012: Trends in precipitation and temperature in Florida, USA. *J. Hydrol.,* **452–453**: 259–281. doi:10.1016/j.jhydrol.2012.05.066.

Misra, V., L. Moeller, L. Stefanova, S. Chan, J. J. O'Brien, T. J. SmithIII, and N. Plant, 2011: The influence of Atlantic Warm Pool on Panhandle Florida Sea Breeze, *J. Geophys. Res*., **116**, doi:10.1029/2010JD015367.

Misra, V., Selman, C., Waite, A. J., Bastola, S., & Mishra, A. (2017). Terrestrial and Ocean Climate of the 20th Century. In Chassignet, E., J. W. Jones, V. Misra, and J.

Misra, V., A. Bhardwaj, and A. Mishra, 2018: Characterizing the rainy season of Peninsular Florida. *Climate Dynamics*, **51**, 2157–2167, https://doi.org/10.1007/s00382-017-4005-2.

Misra, V., and A. Mishra, 2016: The oceanic influence on the rainy season of Peninsular Florida. *J. Geophys. Res.: Atmos.*, **121**, 7691-7709, DOI:10.1002/2016JD024824.

Misra, V., and S. M. DiNapoli, 2012: Understanding the wet season variations over Florida. *Climate Dynamics*, **40**, 1361–1372, https://doi.org/10.1007/s00382-012-1382-4.

Misra, V., 2020: Regionalizing Global Climate Variations: A Study of the Southeastern US Regional Climate. Elsevier, 324 pp, ISBN:978-0-12-821826-6.

Misra, V., & Jayasankar, C. B. (2024). Advancing the seasonal outlook of the wet seasons of Florida. Wea. Forecasting, 39, 1751-1759. doi:10.1175/WAF-D-24-0063.1

Mo, K.C., J.E. Schemm, and S. Yoo, 2009: Influence of ENSO and the Atlantic Multidecadal Oscillation on Drought over the United States. *J. Clim.*, **22**, 5962-5982.

Mo, K.C., 2010: Interdecadal modulation of the impact of ENSO on precipitation and temperature over the United States, *J. Clim.*, **23**, 3639–3656.

Narotsky, C. D., and V. Misra, 2021: The seasonal predictability of the wet season over Peninsular Florida. *International Journal of Climatology*, 1—10, https://doi.org/10.1002/joc.7423.

National Wildlife Federation (NWF), 2019: The Everglades. Accessed 18 July 2019, https://www.nwf.org/Educational-Resources/Wildlife-Guide/Wild-Places/Everglades.

Noska, R., and Misra V., 2016: Characterizing the onset and demise of the Indian summer monsoon. *Geophys. Res. Lett.* **43**, 4547–4554.

Peeling, J.A., J. Judge, and V. Misra, 2023: Gap-free 16-year (2005–2020) sub-diurnal surface meteorological observations across Florida. *Sci Data.* **10**, 907.

Putnam, A. H., 2016: Florida Agriculture: By the Numbers., Florida Department of Agriculture and Consumer Services, Tallahassee, FL. https://www.nass.usda.gov/Statistics_by_State/Florida/Publications/Annual_Statistical_Bulletin/FL_Agriculture_Book/2016/Florida_Agriculture_by_the_Numbers_Brochure_2016.pdf

Ropelewski, C. F., and M.S,,Halpert, 1986: North American precipitation and temperature patterns associated with the El Nino/Southern Oscillation (ENSO). *Mon. Wea. Rev*., **114**, 2352–2362.

Ropelewski, C. F., and M.S,,Halpert, 1987: Global and regional scale precipitation patterns associated with the El Nin˜o/Southern Oscillation. *Mon.Wea. Rev*., **115**, 1606–1626.

Schwartz, B.E. and L.F. Bosart, 1979: The Diurnal Variability of Florida Rainfall. *Mon. Wea. Rev.,* **107**, 1535–1545, https://doi.org/10.1175/1520-0493(1979)107<1535:TDVOFR>2.0.CO;2

Slocum, M. G., Platt, W. J., Beckage, B., Orzell, S. L., & Taylor, W., 2010: Accurate Quantification of Seasonal Rainfall and Associated Climate–Wildfire Relationships, *J. Appl. Meteor. and Clim.,* **49**, 2559–2573.

Slocum, M. G., W. J. Platt, B. Beckage, B. Panko, J. B. Lushine, 2007: Decoupling Natural and Anthropogenic Fire Regimes: A Case Study in Everglades National Park, Florida, *Natural Areas Journal*, **27**, 41–55.

Srivastava, A., R. Grotjahn, P. A. Ullrich, 2020: Evaluation of historical CMIP6 model simulations of extreme precipitation over contiguous US regions, *Wea. Climate Extremes*, **29**, 100268, https://doi.org/10.1016/j.wace.2020.100268.

Stefanova, L., V. Misra, J. J. O'Brien, E. P. Chassignet, and S. Hameed, 2012: Hindcast skill and predictability for precipitation and two-meter air temperature anomalies in global circulation models over the Southeast United States. *Climate Dynamics.*, **38**, 161–173. https://doi.org/10.1007/s00382-010-0988-7.

Trier, S. B., J. W. Wilson, D. A. Ahijevych, and R. A. Sobash, 2017: Mesoscale vertical motions near nocturnal convection initiation in PECAN. *Mon. Wea. Rev.*, **145**, 2919–2941, https://doi.org/10.1175/MWR-D-17-0005.1.

Tuttle, J. D., and C. A. Davis, 2006: Corridors of warm season precipitation in the central United States. *Mon. Wea. Rev.*, **134**, 2297–2317, https://doi.org/10.1175/MWR3188.1.

Vimont, D. J., M. Newman, D. S. Battisti, and S. Shin, 2022: The role of seasonality and the ENSO mode in central and East Pacific ENSO growth and evolution. *J. Clim.*, **35**, 3195–3209, https://doi.org/10.1175/JCLI-D-21-0599.1.

Watters, D., and A. Battaglia, 2019: The summertime diurnal cycle of precipitation derived from IMERG. *Remote Sens.*, **11**, 1781, https://doi.org/10.3390/rs11151781.

Watters, D., A. Battaglia, and R. P. Allen, 2021: The diurnal cycle of precipitation according to multiple decades of global satellite observations, three CMIP6 models, and the ECMWF reanalysis. *J. Climate*, **34**, 5063—5080, https://doi.org/10.1175/JCLI-D-20-0966.1.

Wang, B., 1995: Interdecadal changes in El Niño onset in the last four decades. *J. Climate*, **8**, 267–285.

Wang, B., and S.-I. An, 2002: A mechanism for decadal changes of ENSO behavior: Roles of background wind changes, *Climate Dynamics*, **18**, 475–486.

Wang, C., and J. Picaut, 2004: Understanding ENSO physics—A review. *Geophys. Monogr.*, **147**, 21–48.

Weaver, S.J., S. Schubert, and H. Wang, 2009: Warm season variations in the low-level circulation and precipitation over the central United States in observations, AMIP simulations, and idealized SST experiments. *J. Clim.*, **22**, 5401-5420.

Wu, Z., and N. E. Huang, 2009: Ensemble Empirical Mode Decomposition: A noise-assisted data analysis method. *Advances in Adaptive Data Analysis,* **1,** 1—41, https://doi.org/10.1142/S1793536909000047.

Wu, Z.,

Xian, Z., and R. A. Pielke, 1991: The effects of width of landmasses on the development of sea breezes. *J. Appl. Meteor.*, **30**, 1280-1304.

Yang, G.Y., and J., Slingo, 2001: The Diurnal Cycle in the Tropics. *Mon. Wea. Rev*., **129**, 784-801. https://doi.org/10.1175/1520-0493(2001)129<0784:TDCITT>2.0.CO;2.

APPENDIX

SUPPLEMENTAL FIGURES

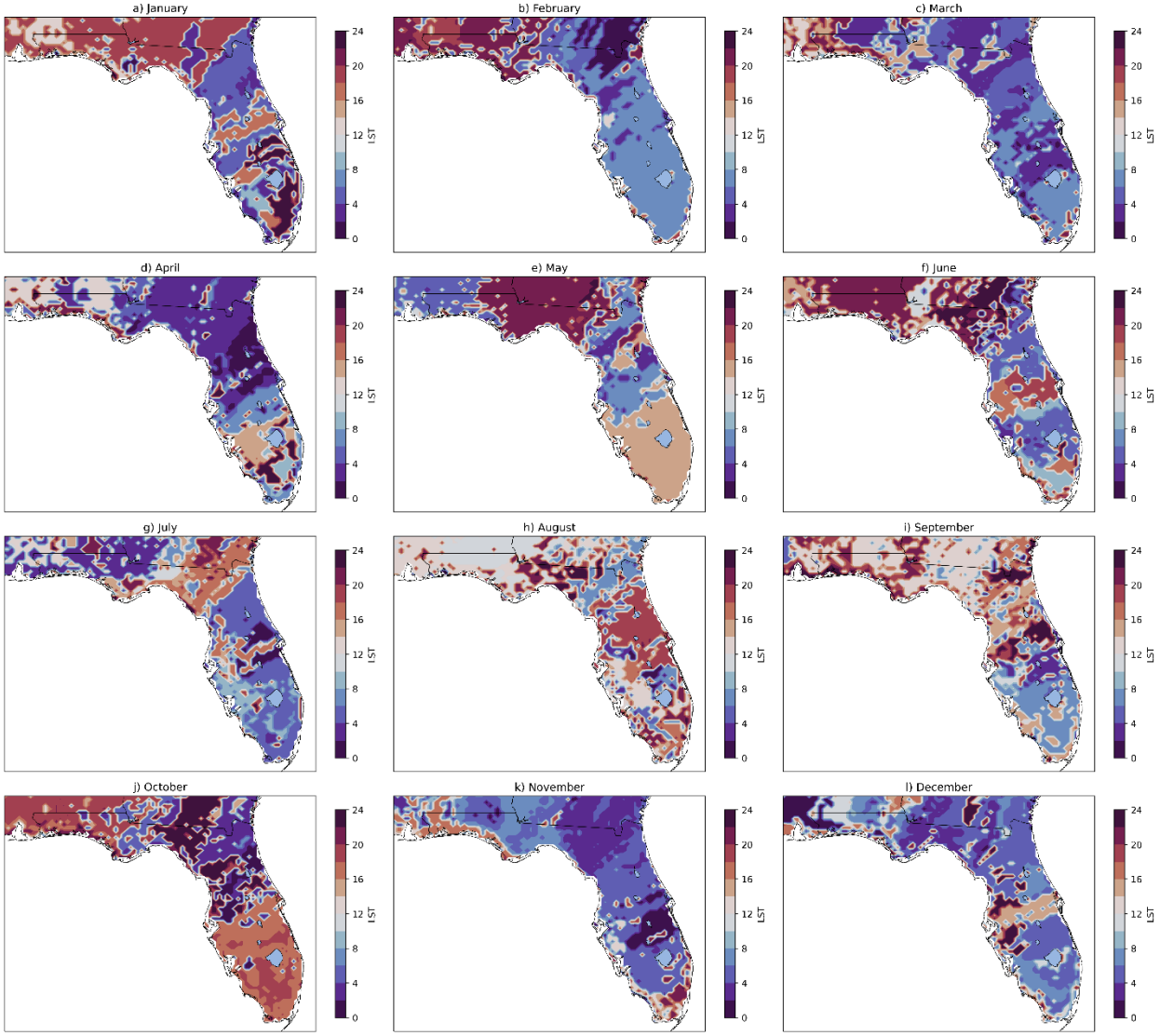

Figure A.1. The climatological mode (1903-2004) of the diurnal peak time (Local Solar Time; LST) of surface temperature in FLAReS1.0.

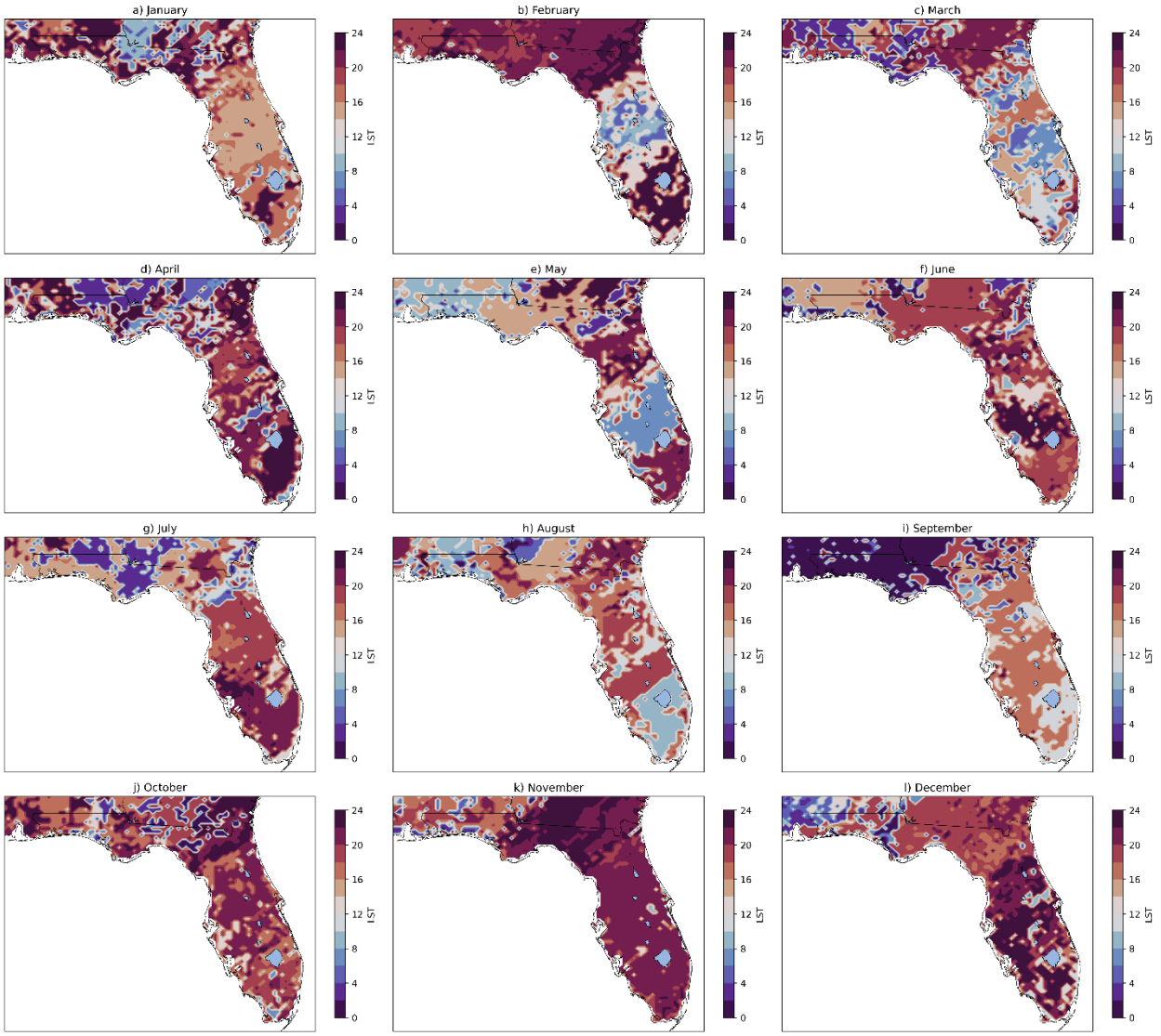

Figure A.2. The climatological mode (1903-2004) of the diurnal peak time (Local Solar Time; LST) of surface specific humidity in FLAReS1.0.

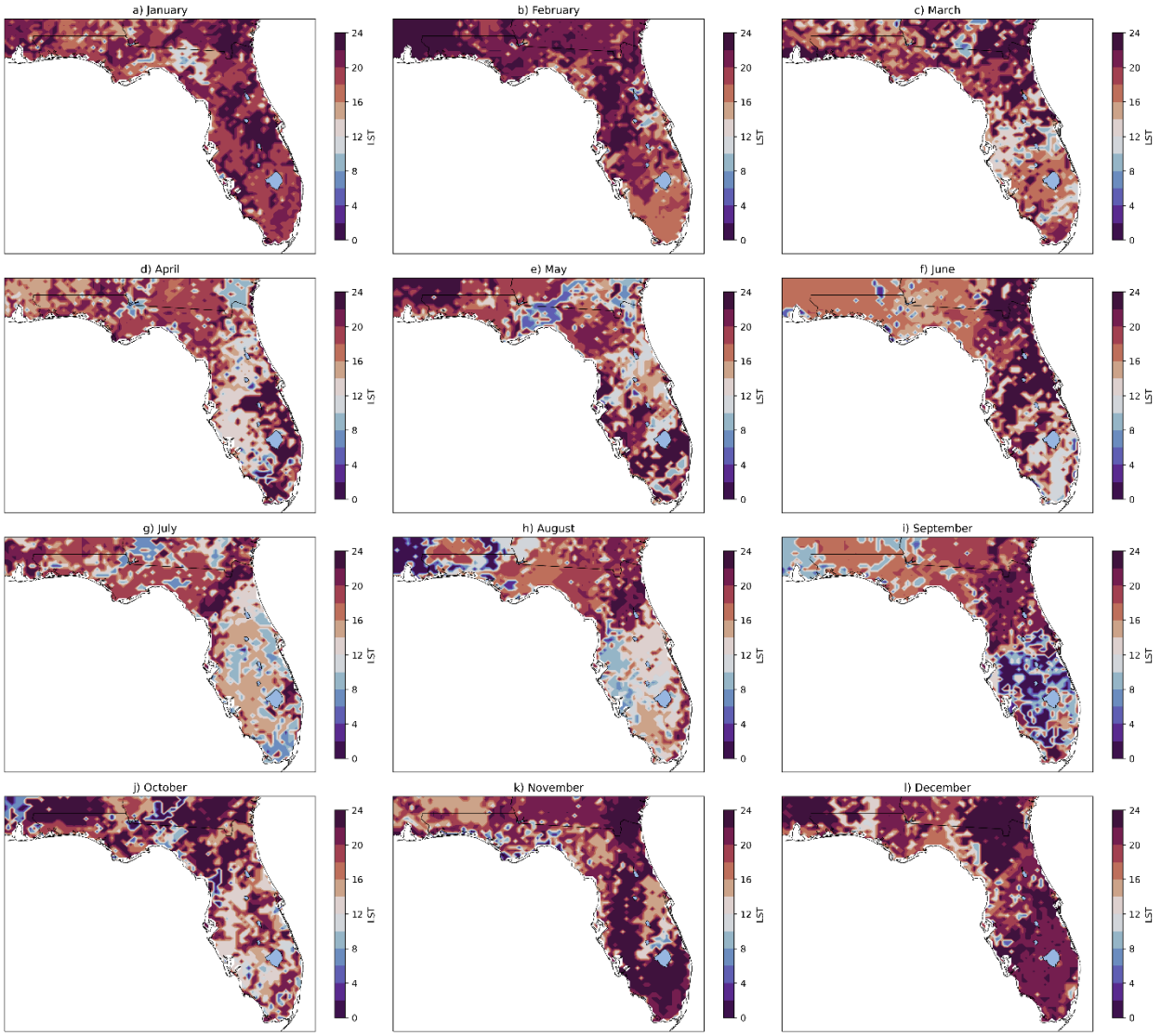

Figure A.3. The climatological mode (1903-2004) of the diurnal peak time (Local Solar Time; LST) of precipitation in FLAReS1.0.

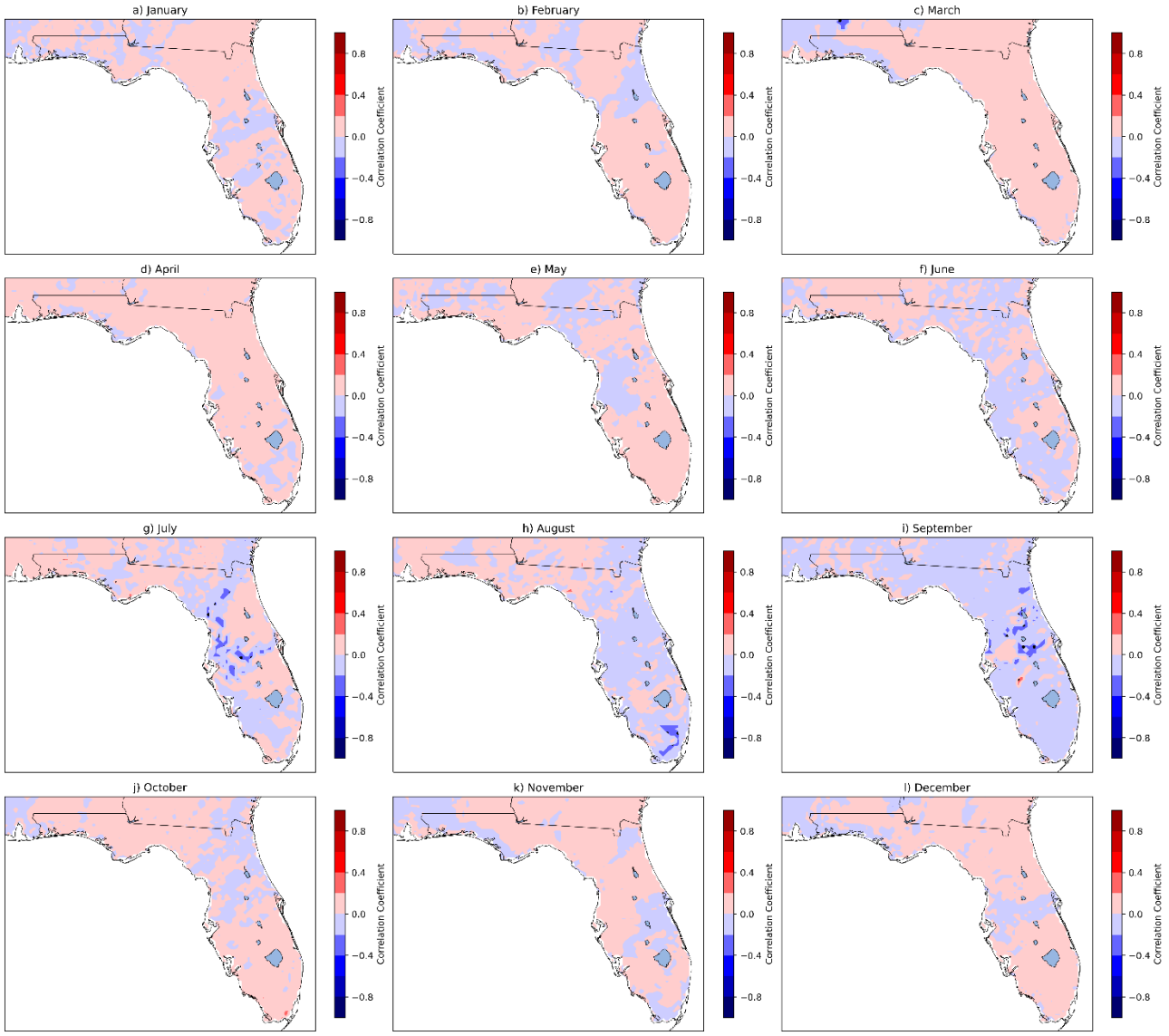

Figure A.4 Correlation between diurnal peak phase (time of day) of surface temperature in FLAReS1.0 and the concurrent Nino3.4 index over 1903-2004. Stippling indicates statistical significance.

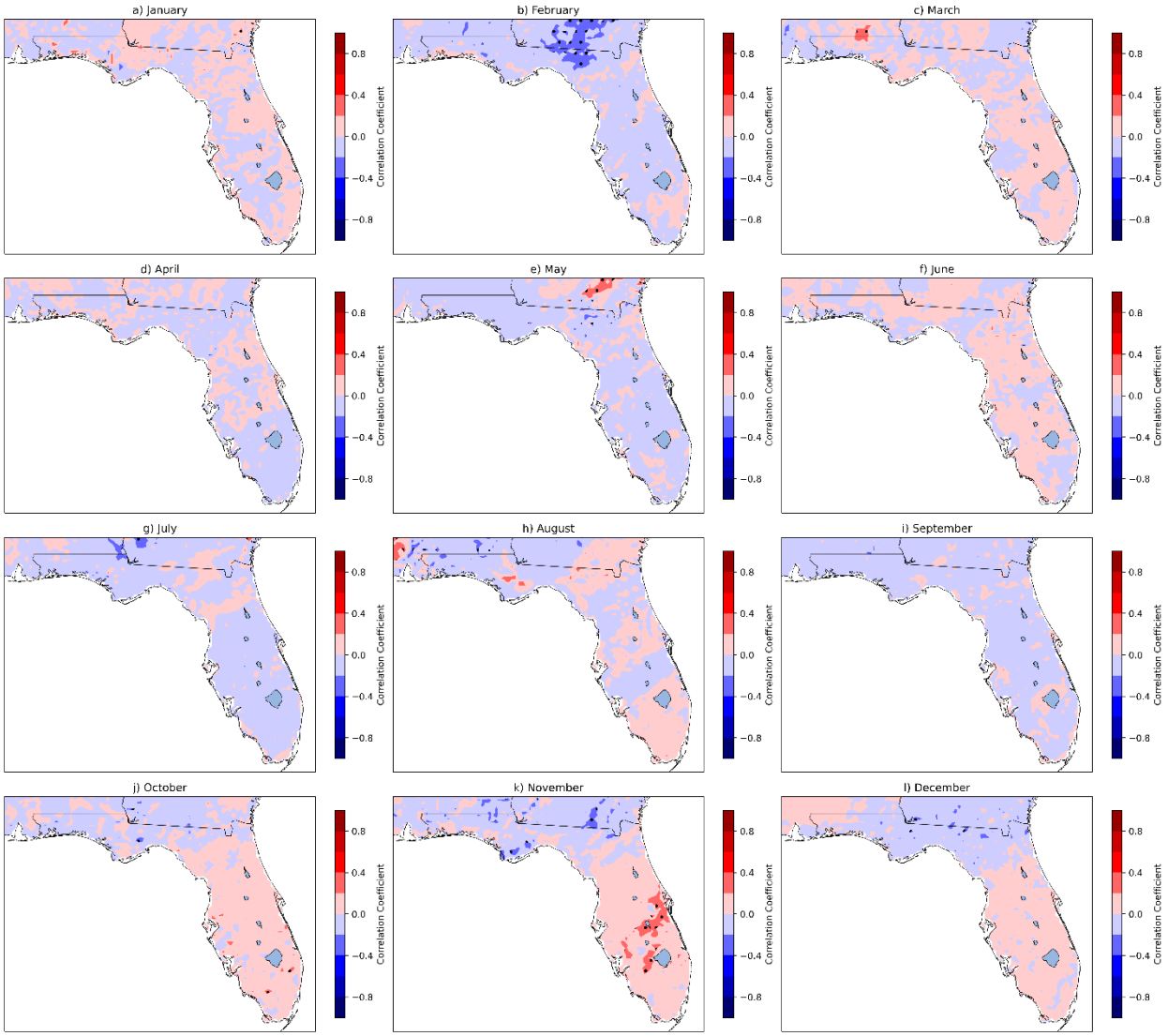

Figure A.5. Correlation between diurnal peak phase (time of day) of surface specific humidity in FLAReS1.0 and the concurrent Nino3.4 index over 1903-2004. Stippling indicates statistical significance.

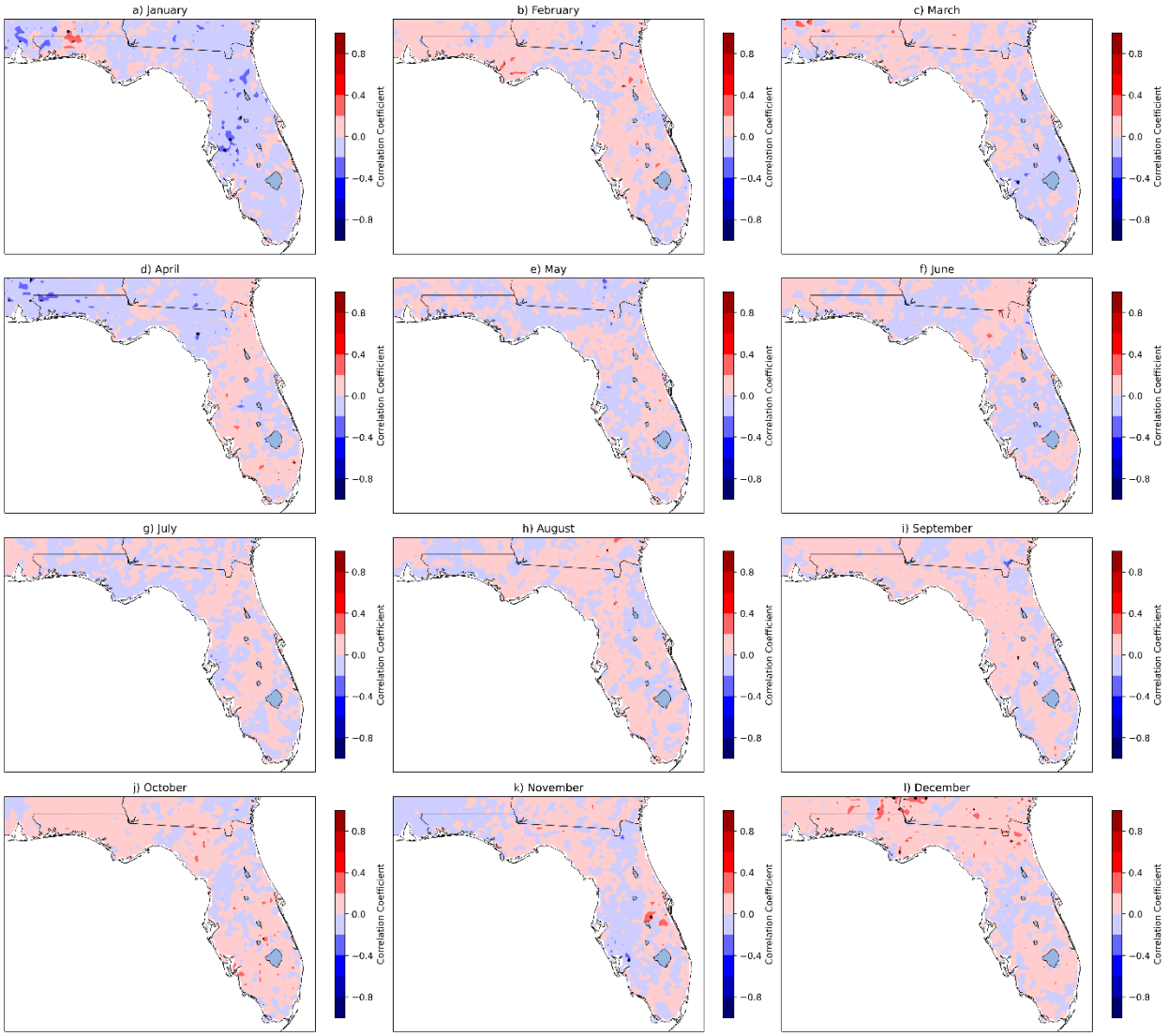

Figure A.6. Correlation between diurnal peak phase (time of day) of precipitation in FLAReS1.0 and the concurrent Nino3.4 index over 1903-2004. Stippling indicates statistical significance.

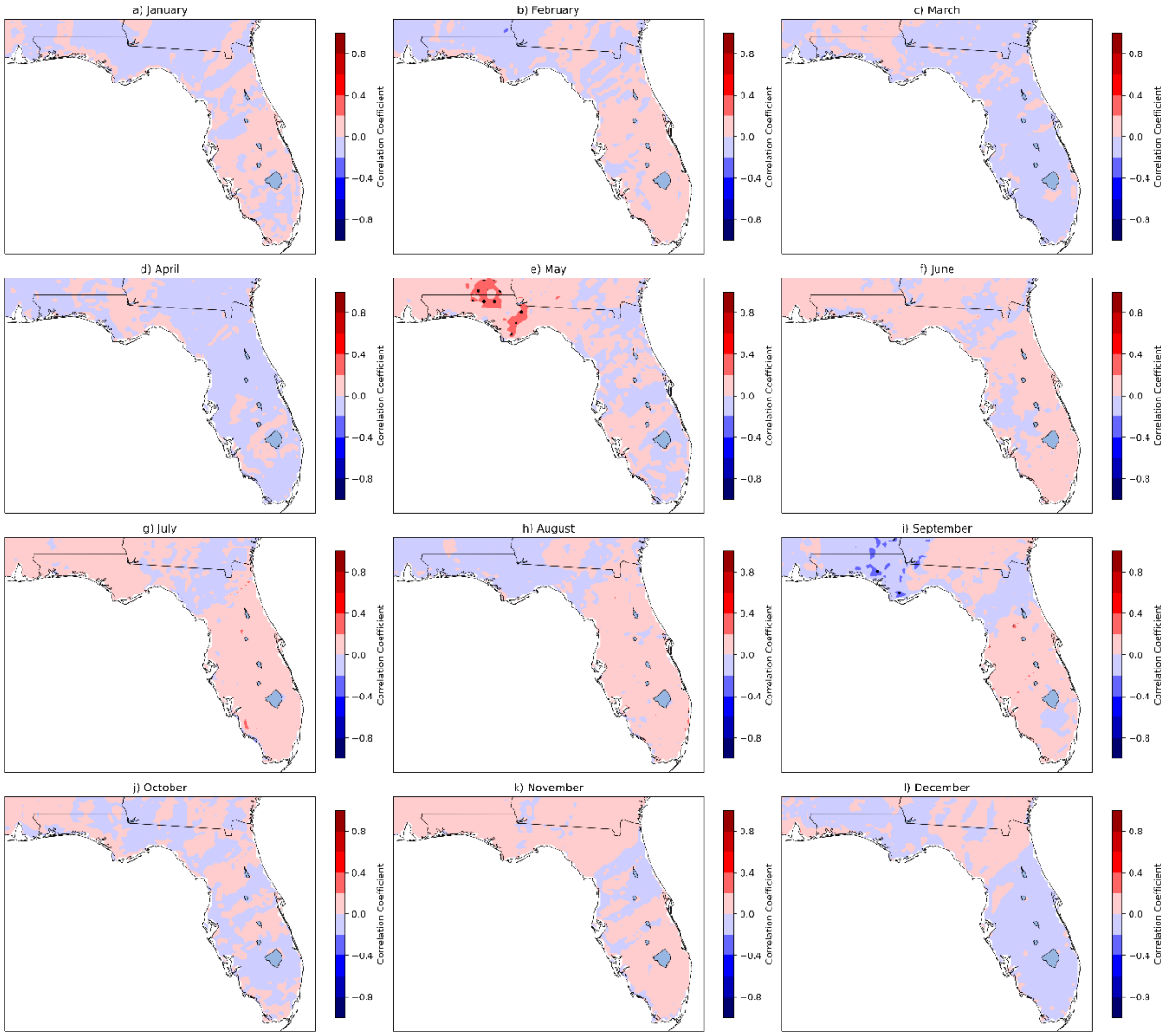

Figure A.7. Correlation between diurnal minimum phase (time of day) of surface temperature in FLAReS1.0 and the concurrent Nino3.4 index over 1903-2004. Stippling indicates statistical significance.

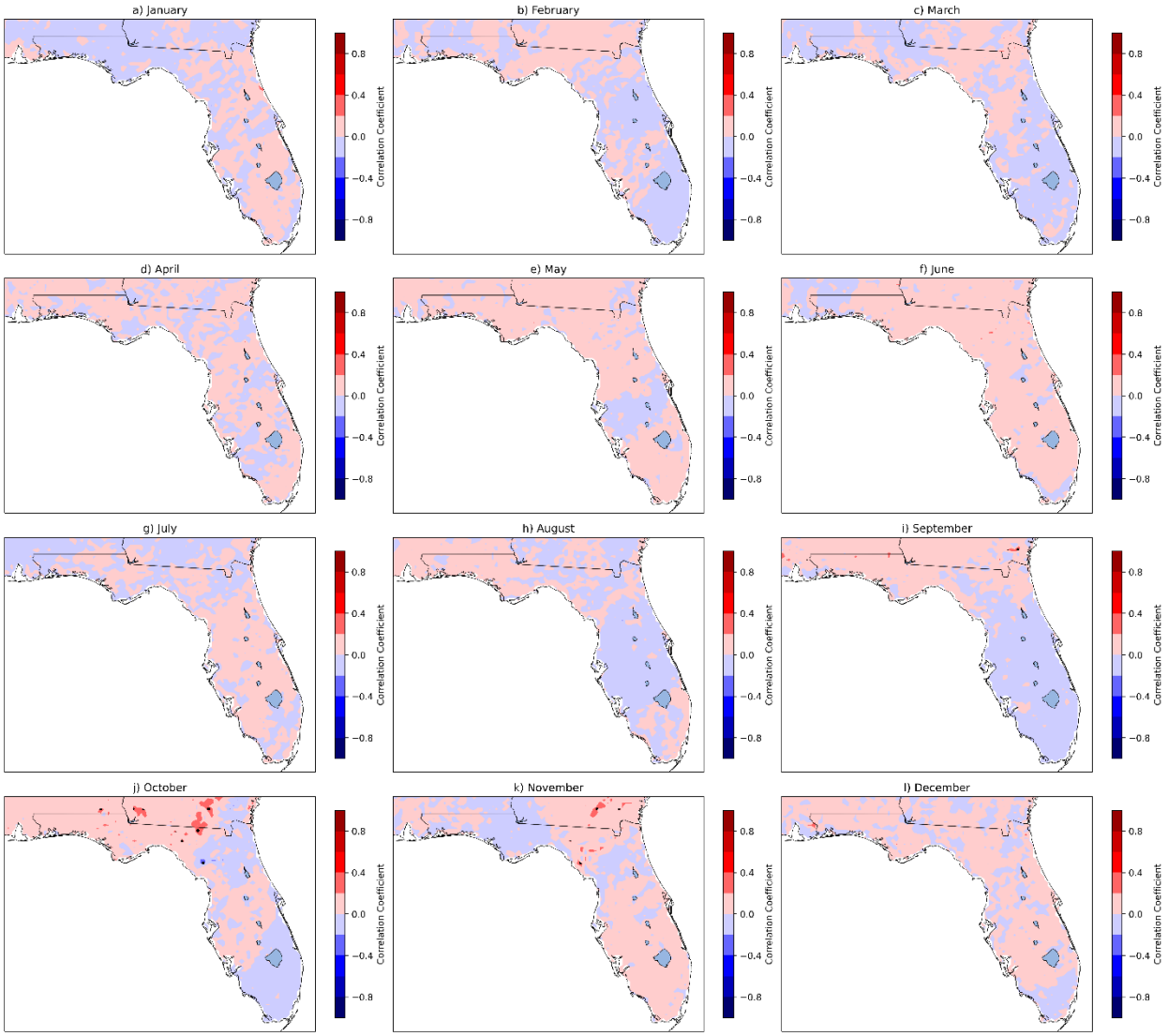

Figure A.8 Correlation between diurnal minimum phase (time of day) of surface specific humidity in FLAReS1.0 and the concurrent Nino3.4 index over 1903-2004. Stippling indicates statistical significance.

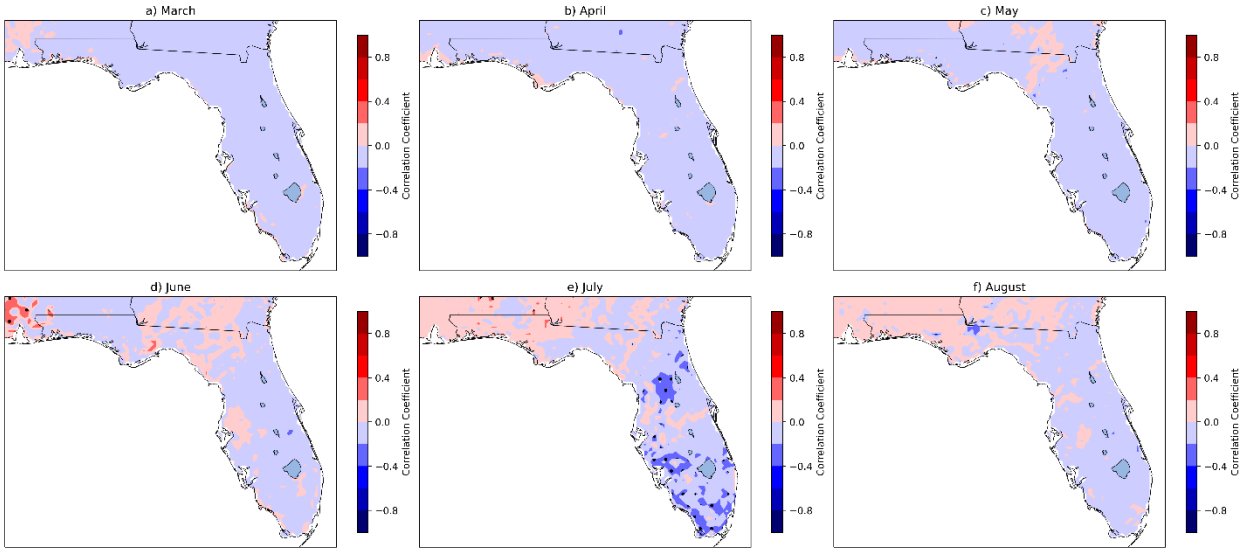

Figure A.9. Correlation between diurnal peak phase (time of day) of surface temperature in Flares1.0 and the concurrent Atlantic-Pacific SST gradient over 1903-2004. Stippling indicates statistical significance.

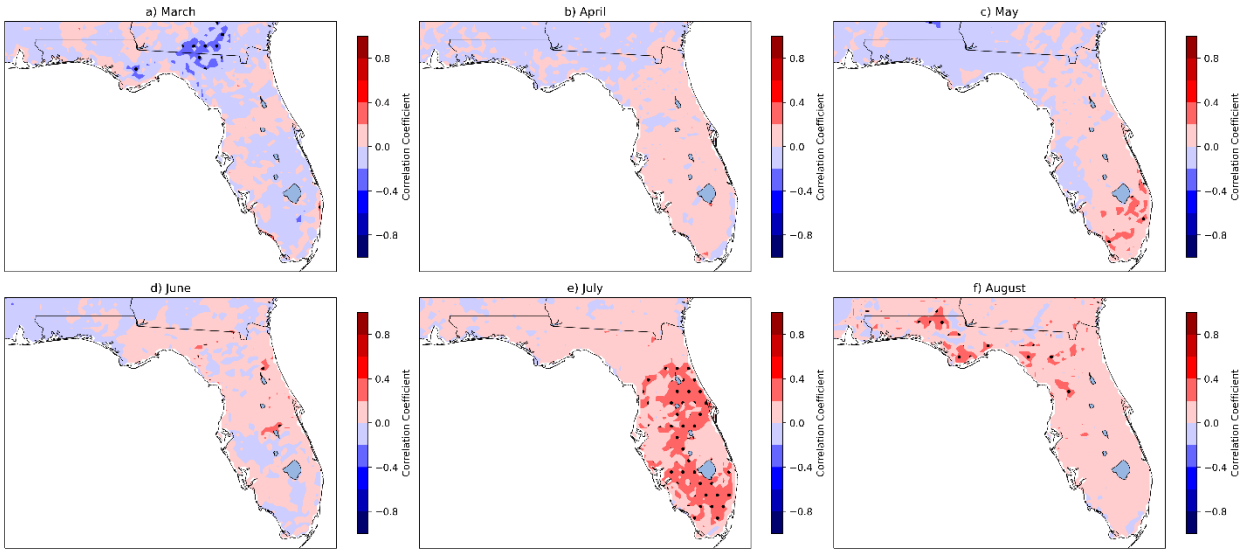

Figure A.10. Correlation between diurnal peak phase (time of day) of surface specific humidity in Flares1.0 and the concurrent Atlantic-Pacific SST gradient over 1903-2004. Stippling indicates statistical significance.

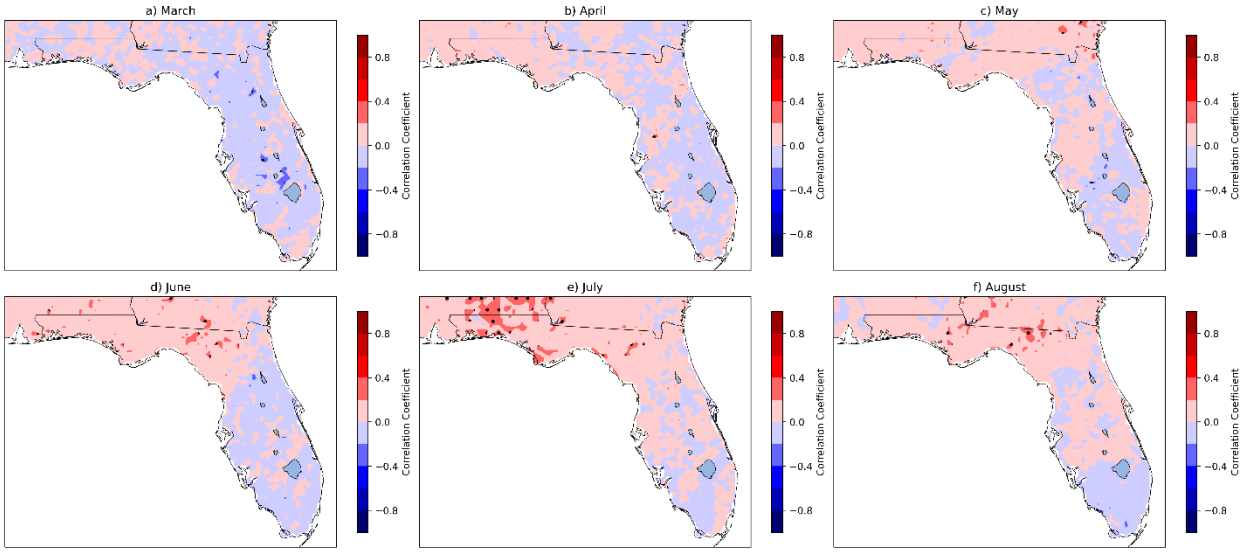

Figure A.11. Correlation between diurnal peak phase (time of day) of precipitation in Flares1.0 and the concurrent Atlantic-Pacific SST gradient over 1903-2004. Stippling indicates statistical significance.

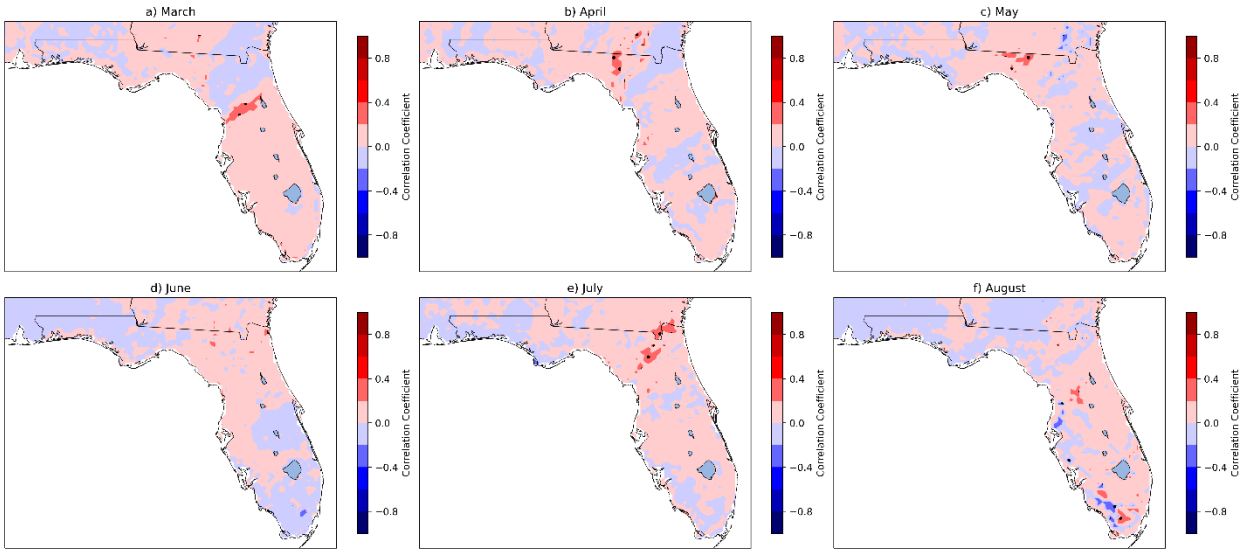

Figure A.12. Correlation between diurnal minimum phase (time of day) of surface temperature in Flares1.0 and the concurrent Atlantic-Pacific SST gradient over 1903-2004. Stippling indicates statistical significance.

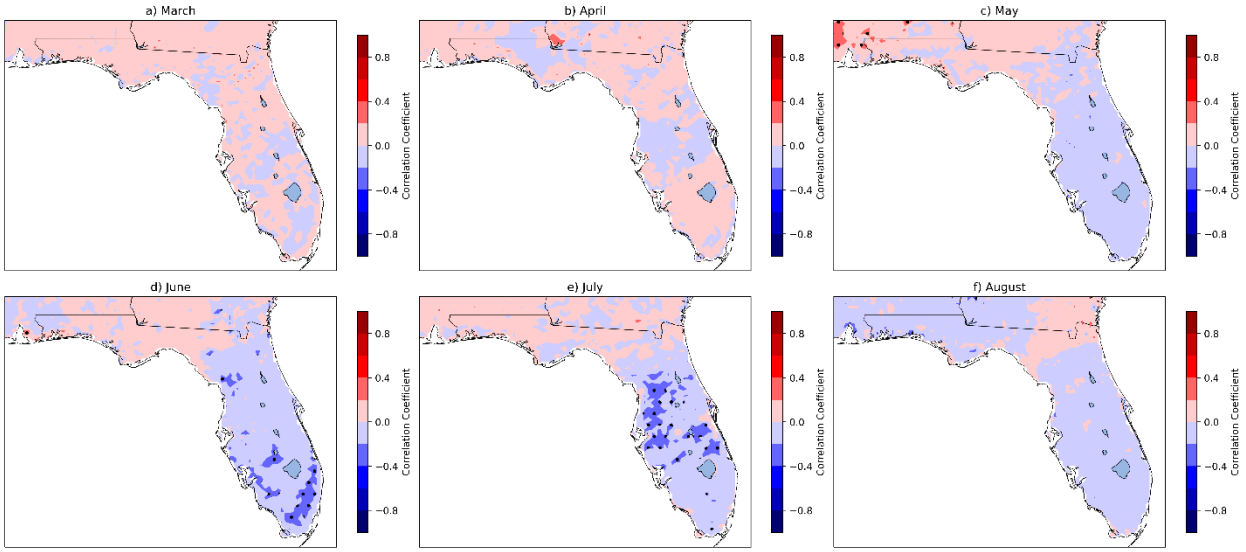

Figure A.13. Correlation between diurnal minimum phase (time of day) of surface specific humidity in Flares1.0 and the concurrent Atlantic-Pacific SST gradient over 1903-2004. Stippling indicates statistical significance.

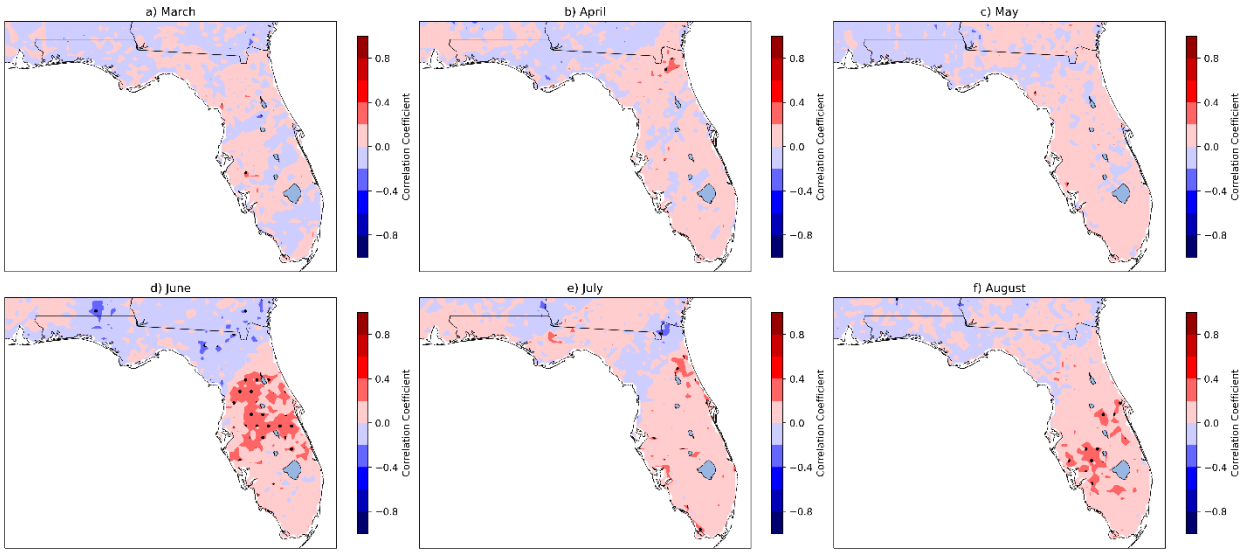

Figure A.14. Correlation between diurnal minimum phase (time of day) of precipitation in Flares1.0 and the concurrent Atlantic-Pacific SST gradient over 1903-2004. Stippling indicates statistical significance.

BIOGRAPHICAL SKETCH

Carly Narotsky was born in Durham, North Carolina in 1996 to her parents Kathy Kaufman and Mike Narotsky. As a teenager and young adult, she spent her summers working as a camp counselor at Spence's Farm for Kids and the Burgundy Center for Wildlife Studies. At the latter, she taught workshops on various nature topics; her favorite topics to teach were Weather and Butterflies. She got her start in meteorological research in the summer of 2017 at the National Weather Center Research Experience for Undergraduates (REU), working under Dr. Jason C. Furtado of the University of Oklahoma to study trends in the strength and position of the stratospheric polar vortex in the 20th and 21st centuries. Inspired by her REU experience and her younger brother's temporary move to Cañar, Ecuador, she designed and conducted a research project on the wet season of the Ecuadorian Andes with the guidance of Dr. Douglas K. Miller at the University of North Carolina at Asheville (UNCA). While a student at UNCA, she also worked as a private tutor in Atmospheric Sciences and as a field research assistant, helping to maintain a rain gauge network in Great Smoky Mountains National Park and launching rawinsonde weather balloons during wintry precipitation events in Asheville, NC. In 2018, she graduated Magna Cum Laude from UNCA with a B.S. in Atmospheric Sciences with a concentration in Climatology and a minor in Mathematics, receiving the Atmospheric Sciences Class of 2018 Academic Excellence Award and earning Distinctions in Atmospheric Sciences, as a University Scholar, and as a University Research Scholar. In 2019, she began her graduate studies at Florida State University, where, under the advisement of Dr. Vasubandhu Misra, she completed a Master's Thesis titled Predictability of the Peninsular Florida Wet Season. Beyond her academic interests, she enjoys spending time with her pet tegu Titan, playing soccer, and being outdoors.